UNICA

UNIVERSITÀ
DEGLI STUDI
DI CAGLIARI

Ph.D. DEGREE IN

Physics

Cycle XXXV

TITLE OF THE Ph.D. THESIS

Study for the scientific development of the Sardinia Radio Telescope/SDSA configured for solar observations and radio-science aimed at Space Weather and Fundamental Physics applications

Scientific Disciplinary Sector(s)

FIS/05

Ph.D. Student:	Sara Mulas
Supervisors:	Dr. Andrea Possenti, Dr. Alberto Pellizzoni, Dr. Elise Egron, Dr. M. Noemi Iacolina

Final exam. Academic Year 2021/2022
Thesis defence: February 2023 Session

UNIVERSITÀ DEGLI STUDI DI CAGLIARI
Facoltà di Scienze
Dipartimento di Fisica

Study for the scientific development of the Sardinia Radio Telescope/SDSA configured for solar observations and radio-science aimed at Space Weather and Fundamental Physics applications

PhD Thesis

Supervisor:
Dr. Andrea Possenti

Candidate:
Sara Mulas

Co-Supervisors:
Dr. Alberto Pellizzoni
Dr. Elise Egron
Dr. M. Noemi Iacolina

Academic year 2021/2022

Contents

Introduction

Our star, the Sun, is essential for the life on Earth. Also, thanks to its proximity, its study is crucial for our understanding of other stars. It reveals details we would not have easily guessed, such as spots and hot outer atmospheres. Its magnetic and radiative activity has an enormous impact on planetary magnetospheres and ionospheres ranging from subtle climate dependencies to severe radiation phenomena affecting operations and safety of our technologies on Earth (Koskinen et al. 2017). However, even after decades of studies, the Sun still presents lots of mysteries.

The Sun environment and its phenomenology can be exploited as a natural multi-disciplinary laboratory for a wide range of scientific, technological and educational applications. The physics which can be extrapolated in this context offers a rich interdisciplinary ground on astrophysics, plasma, nuclear and fundamental physics (e.g. Thompson 2014). The Sun produces radiation across virtually the entire electromagnetic spectrum. Each frequency range helps to better understand a different aspect of our star. The radio quiet Sun, compared to the emission in other spectral ranges (e.g. the EUV), has the advantage of being well understood as originating mostly from thermal bremsstrahlung in local thermodynamic equilibrium. It can thus be used as a powerful tool to characterize the physical conditions in a wide range of atmospheric layers (Shibasaki et al. 2011). Moreover, this frequency range offers valuable diagnostic potential because two of the natural frequencies of the atmosphere of the Sun, the electron plasma frequency and the electron gyrofrequency, belong to the radio band (Nindos 2020).

My PhD aims to investigate the Sun environment and its emission mechanism in the radio domain to better understand some of the complex solar phenomena, their connections and find applications as Space Weather and Fundamental Physics. This work is possible thanks to new challenging development of the radio telescopes managed by the Italian National Institute for Astrophysics (INAF) and the Italian Space Agency (ASI).

The first part of my Thesis (Part A) is dedicated to the innovative solar observation program carried out with the 64m Sardinia Radio Telescope (SRT) and the 32m Medicina radio telescope in the context of the SunDish project[1]. SunDish exploits the solar radio astronomy configuration of the SRT and has the aim to monitor and study the solar atmosphere at high radio frequencies. I contributed to the project since the beginning as junior founder member of the research program.

Chapter 1 gives an introduction on the solar radio astronomy. Starting from general characterization of the Sun, such as its structure and atmosphere, I then focus on the emission mechanism in the radio domain. The last part is dedicated to the multi-frequency solar observations and how can they be exploited for Space Weather applications and for the investigation of some of the solar open questions that are still not resolved.

Chapter 2 provides an overview on the solar observation performed in K-band (18-26 GHz) since 2018, with both SRT and Medicina radio telescopes. The first part is dedicated to the characterization of the instrumental set up and the tools for data analysis: the software

[1] https://sites.google.com/inaf.it/sundish

pipeline (SUNPIT). The studies on the pipeline gave rise to the publication of two INAF internal reports of which I am a co-author (Marongiu et al. 2021 and Marongiu et al. 2022). Then, the imaging procedure of the Sun maps is introduced. Currently, we have more than 300 maps uploaded to the SunDish archive[2]. I also present an original and innovative absolute calibration procedure with the Supernova Remnant Cassiopeia A, which is a very strong and well studied radio source in the literature. This is a challenging method since this source is extended (resolved at our frequencies) and it is currently in expansion. The results and error analysis are described in detail in my ASI technical report (Mulas et al. 2022).

Chapter 3 is concentrated on the study I performed on the solar Active Regions (ARs) and their spectra characterization. In particular, I describe the data analysis and results interpretation. I focus on the studies of free-free and gyro-magnetic emission components present in most solar ARs, providing possible applications to solar flare forecast. These results are illustrated in Pellizzoni et al. 2022. I am among the first authors of this SunDish paper.

During my PhD I was also involved in the research grant *"Study for the scientic development of the Sardinia Radio Telescope in SDSA configuration, and in configuration for radio astronomy in collaboration with INAF, for radio-science and solar observations aimed at applications of Space Weather and Fundamental Physics"*, with codes of the implementing agreements between ASI and Physics Department of the Cagliari University 2020-13-HH.0 and 2020-34-HH.0, official beginning on December 17 2019 with duration of 33 months. SRT is an ideal instrument for this Thesis project thanks to its double configuration Sardinia Deep Space Antenna (SDSA) in the implementation phase/radio astronomy for radio science experiments and solar imaging. This double configuration could allow SRT to obtain complementary information on the Sun environment and its emission mechanism, with the aid of the tracking of interplanetary spacecraft and the single dish observations. Thus, the second part of my Thesis (Part B) is dedicated to the studies I conducted for SDSA.

Chapter 4 is focused to the X-band (8-9 GHz) receiver characterization and the studies I did for a possible future configuration of the antenna to perform tracking experiments that exploits the radio science technique. These operations consist in an exchange of a radio signal between a deep space antenna and a spacecraft, also useful as a probe of the interplanetary medium and the heliosphere. These are challenging activities to perform, since the antenna should be properly equipped and meet the scientific standard required by the space mission. I also describe how the future SDSA implementations will be used in solar studies in single dish mode. Indeed, the X-band can be exploit for Space Weather applications, such as temporal variations of the Active Regions flux/brightness temperature can be used as a prognostic tool in the prediction of powerful eruptive (geoeffective) events and flares (Borovik et al. 2012). I present the thermal characterization of the receiver we have done so far. To do so, we have investigated in the literature the theoretical brightness level value the instrumentation should withstand during a solar observation. In the future, these values will be useful to design a set of solar signal attenuation to both perform radio science experiments in superior solar conjunction and direct observations in single dish mode and protect the receiver from potential solar damages.

Chapter 5 is devoted on the P-band (305-410 MHz). This frequency range is specially challenging to characterize and analyse since it is particularly affected by surrounding strong interferences (Zanichelli et al. 2022). Moreover, it is an essential band for a deep space mission which has an EDL (Entry, Descend and Landing) phase. The P-band will also help us to deepen our knowledge of the Supernova Remnant Cassiopeia A, our main calibration source for the Sun.

Chapter 6 contains a summary of the principal results I illustrated in this Thesis, which have been obtained during my PhD. I also introduce some of the planned future works.

[2]https://sites.google.com/inaf.it/sundish/sundish-images-archive/sundish-archive-summary

Part A:
Solar observations with SRT and Medicina

Chapter 1

Solar radio astronomy

1.1 Solar structure

The Sun is generally divided into several zones or layers (See 1.1). The interior is characterized by a defined structure consisting of three main regions: the core, the radiative zone and the convective zone, depending on the different nature of processes occurring in each of them. Between the convective and radiative zone there is a thin layer transition region called the tachocline (Spiegel and Zahn 1992). The **core** of the Sun is the zone where the thermonuclear reactions transform hydrogen into helium, and extends from the centre to approximately 20-25% of the solar radius. It has a density of about 150 g cm^{-3} at the centre which drops to the value of 20 g cm^{-3} at the edge, and reaches a temperature of $1.57 \cdot 10^6$ K which ensures that the matter is kept completely ionized. The **radiative zone** extends from 25% to 70% of the solar radius. In this region, the energy produced in the core is transferred to the external layers by radiative transfer, as the temperature gradient which varies from 7 million to 2 million K is less than the value of the adiabatic lapse rate. The photons mean free path in the radiative zone is a few millimeters long, due to the density of the medium, which goes from 20 g cm^{-3} at the bottom to 0.2 g cm^{-3} at the top: for this reason, a single photon takes about 30,000 years to reach the interface layer with the convective zone. Acoustic sounding of the Sun reveals that the variation of angular velocity with latitude is independent of depth in the convection zone. By contrast, deep within the radiative zone, the rotation appears to be rigid. The transition between the two rotation laws occurs in the **tachocline** (Spiegel and Zahn 1992). Beyond this thin layer there is the **convective zone**, the outer-most layer of the solar interior extending from a depth of about 200,000 km to the visible surface. The main processes occurring at this stage are atomic absorption, particularly bound-free transitions. The new conditions obstacle radiation transfer, and steep temperature gradients lead convection flows to dominate, carrying material toward the photosphere by means of thermal columns of raising bubbles in a transport mechanism which is more efficient than the one occurring in the radiative zone.

Above the convective zone there is the solar atmosphere, which is generally described as being composed of multiple layers, from the deepest, the photosphere, followed by the chromosphere, the transition region and the corona. The **photosphere** extends from the surface visible at the center of the solar disk to about 250 miles (400 km) above that. The greatest part of the photosphere surface is covered by granulation due to the activity of the convective zone below it, and the energy is transported by radiative transfer. The radiation coming from this region lies mostly in the infrared band (49%) and in the visible band (46%). A remaining amount of radiation, corresponding to 5% of the total emission, is in the ultraviolet band. The conventional definition of the photosphere is, in the optical band, that of Sun's surface. This is due to the fact that the transition from an optically thick

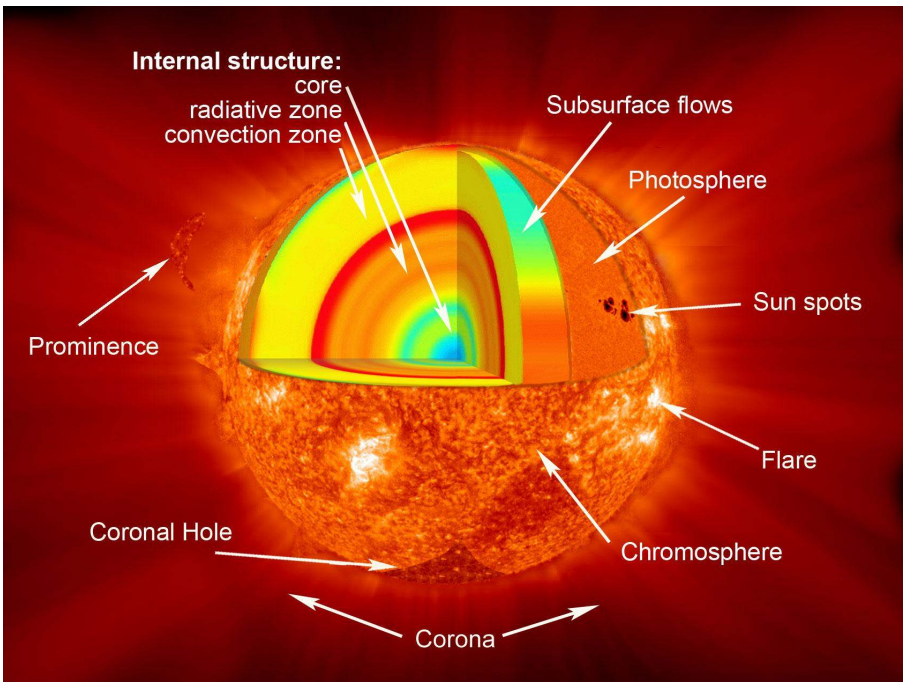

Figure 1.1: Representation of the sun layers and some features. Credits: NASA/Goddard.

to an optically thin medium occurs in this region, which occupies only 0.1% of the solar radius: for this region, the Sun does look as if it had a sharp edge. The **chromosphere** is located between 400 km and 2100 km above the photosphere. The temperature varies from 4000 K at the bottom (which is called **temperature minimum**) to 8000 K at the top. Beyond the minimum point the temperature increases going further away from the Sun, showing an opposite trend to the one observed for the internal layers. The temperature value evolves relatively smoothly in this layer (forming the chromospheric plateau), rising dramatically in the successive transition region. The hypothesis of a stationary temperature profile is suggested both theoretically, through time-dependent, dynamical models, and through observations, as cool regions appear to exist in which CO lines are observed. The energy is transported through the region by radiative transfer. The chromosphere also shows convective cell patterns comparable to the ones in the photosphere, but extended on a larger scale: this kind of pattern is called supergranulation, and it is generated by the alignment of spicules (long streams of gas) into chromospheric networks reaching the upper chromosphere and the corona. The **transition region** is a thin thermal interface layer with the thickness of about 100 km located between the chromosphere and the corona, where the temperature rises drastically from 8000 K to 500,000 K. In this highly structured and extremely dynamic region, particularly bright at far-ultraviolet wavelenghts, several fundamental transitions in the physics of the solar atmosphere take place, even if not correlated to each other. In the chromosphere, structures are modeled by the dominant action of gravity assuming horizontal extended features: in the transition layer and above, dynamic processes start to dominate, leading to a structural development in altitude. Moreover, below this layer the shape of features depends on gas pressure and fluid dynamics laws, while above it an important role is played by magnetohydrodynamics. The transition is also ratified by the change in the observed spectral lines: most of the ones formed below the transition region are absorption lines in infrared, visible light and near ultraviolet, while most of the ones formed at or above this region are emission lines in the far-ultraviolet and X-rays. The **corona** is the outermost layer of the solar atmosphere. It begins at about 2100 km above the photosphere and doesnt have a defined upper limit. Its shape is mostly determined by the magnetic field topology, which in turn is bound to photospheric driving. The temperature in the corona has a value of

500,000 K rising up to a few million K, leading to a strong emission in the X-ray spectral band. In spite of this fact, the corona contains very little thermal energy because of its extremely low density of about 10^{-15} g cm^{-3}. The emission from this region is also characterized by the presence of bright spectral lines linked to heavy elements such as calcium and iron. A wide variety of solar activity phenomena develop in this layer, mainly linked with the magnetic field activity and affected by the Sun's rotation. Around the photospheric sunspots we find the presence of coronal loops, associated with the closed magnetic field lines that connect separate regions on the photosphere surface. These dynamic structures are characterized by a stream of plasma entwined with a loop of magnetic flux, whose ends are anchored into the photosphere, and come in various sizes, from 2400 to 160,000 km. Coronal loops have a lifetime from one day to months, with an average lifetime from a few days to a few weeks: the ones which are visible for shorter periods are associated with solar flares, that will be discussed in Sec 1.3.5.

1.2 General properties of the solar atmosphere

The mean properties of the lower solar atmosphere can be well approximated by the VAL-C model (Vernazza et al. 1981; Avrett and Loeser 2008), which uses a semi-empirical approach and fits a number of spectral lines from the various atmospheric layers (Priest 2014). This one-dimensional model assumes that thermodynamic properties of the solar atmosphere are static, and only depend on the height with respect to the solar surface. The solar surface is identified as the location in the photosphere where the optical depth τ, defined by the relation:

$$I = I_0 e^{\tau} \tag{1.1}$$

is equal to unity for a wavelength of 500 nm This corresponds to the transition from an optically thick to an optically thin medium. In Equation 1.1 I_0 is the intensity of radiation at the source and I is the observed intensity at a given distance l from the source: their ratio represents the amount of radiation at l, therefore $\tau = 1$ means that at l the radiation has fallen by a factor of the Euler's number e (Priest 2014). The physical properties are subject to an extreme variation across the solar atmosphere. Fig 1.2 shows the mean plasma temperature and density calculated by the VAL-C model (Vernazza et al. 1973; Priest 2014) across the different solar atmospheric layers. The plasma density exhibits a rapid decrease of about five orders of magnitude between the lower boundary of the photosphere and the upper boundary of the chromosphere (Priest 2014). Above the temperature minimum of about 4300 K, the mean temperature gradually increases across the chromosphere, forming the so-called chromospheric plateau, and shows a sharp increase in correspondence of the transition region ($\sim$ 2100 km above the solar surface). The static thermodynamic properties assumed by the VAL-C model are associated with a thermodynamic state that is called the local thermodynamic equilibrium (LTE), which occurs when the distributions of electrons and photons in a system are in equilibrium with each other. LTE holds when the length scale over which the temperature varies is larger than the thermalisation length LT: this is defined as the distance a particle, or a photon, travels before it has undergone enough interactions that it no longer can be distinguished within the distribution. The Maxwellian velocity distribution and the Saha-Boltzmann energy levels distribution are the reference distributions for particles, while for photons this is the Planck distribution of the radiation field. As a consequence, the system can be described uniquely by the temperature and density. When LTE conditions are no longer satisfied, the system is said to be in non-LTE conditions. Non-LTE applies if the system is varying so rapidly that the electron and photon energy distributions do not

reach a thermal equilibrium, therefore the two distributions cease to be in equilibrium with each other. This also occurs for an optically thin plasma, where radiation escapes and stops providing the balance required for the basic atomic processes in LTE.

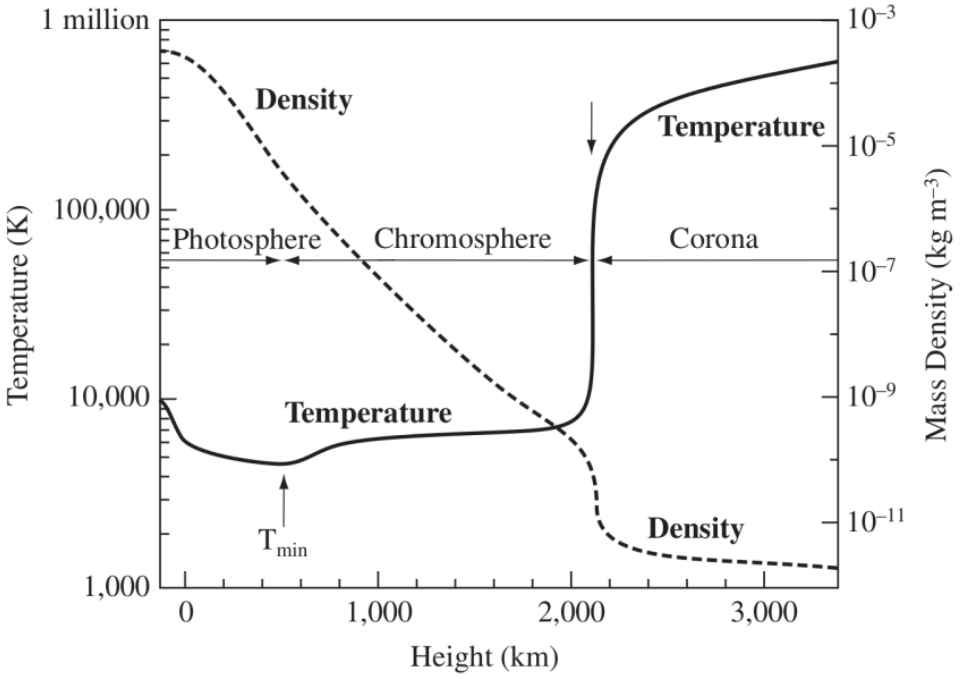

Figure 1.2: Mean variation of temperature and density with respect to the height above the solar surface, according to the VAL-C (Vernazza-Avrett-Loeser) model (Priest 2014).

1.3 Radio emission

The Sun produces radiation across virtually the entire electromagnetic spectrum. Radio frequencies offer a valuable diagnostic potential because two of the natural frequencies of the atmosphere of the Sun, the electron plasma frequency and the electron gyrofrequency, belong to the radio band (Nindos 2020). In the Sun there are no significant radio spectral lines can be observed either in emission or absorption. In fact, from millimeter to meter wavelengths pressure broadening is so high that makes such lines undetectable.

On the Sun, the free electrons dominate the radio emission mechanisms. Solar radio emission is produced from electrons with either a thermal or a non-thermal distribution, and the emission can be either incoherent or coherent. In incoherent mechanisms, no back-reaction of the emission on the electron distribution is present, and the emitted photons show no phase association while their number is proportional to the number of electrons. In coherent mechanisms, all electrons exhibit acceleration in phase; they act together to generate photons that are in phase. Coherent radiation due to wave-particle and wave-wave interactions plays an important role in transient phenomena at frequencies below 1-2 GHz. Coherent emission mechanisms are not discussed in this work, but instead, I will focus on the two classes of incoherent emission mechanisms that are important on the Sun: the free-free (or bremsstrahlung) and the gyro-magnetic.

Regarding the solar radio emission, it is usually divided in the literature into three main categories depending on the time scale of the events: (1) the quiet Sun (QS) as a background stable emission, (2) a slowly varying component mostly associated with the active regions (ARs), and (3) the one associated with occasional extreme and sudden energetic phenomena

like coronal mass ejections and flares. In the following sections (1.3.3, 1.3.4, 1.3.5) I describe the three of them separately.

1.3.1 Free-free emission

At radio frequencies, free-free emission is primarily produced by collisions between ions and thermal electrons and dominates the radio emission of the quiet Sun. Furthermore, it contributes significantly to the radio emission of non-flaring active regions and of certain flares during their decay phase. Erupting prominences and coronal mass ejections (CMEs) may also produce free-free radio emission.

From the middle chromosphere upward, the free-free emission (or bremsstrahlung) exclusively originates from electrons that are diffused in the Coulomb field of ambient ions because they are accelerated by the Coulomb force. The term free-free is due to the state of the electrons; they are free both before and after the interaction. In the classical limit, the radiation of free accelerated charged particles is described by Larmor's formula. The total radiated power is obtained after integration over the solid angle:

$$P = \frac{2q^2a^2}{3c^2} \tag{1.2}$$

where P is the power emitted by a particle of charge q, mass m, and acceleration a in the direction relative to the acceleration vector. Since a is proportional to $1/m$, the power is $1/m^2$ and the proton radiation can be ignored because it is much smaller than that of electrons. This conclusion holds for all radio emission processes. Interaction between identical charges also does not produce much radiation because the radiation power is proportional to the second derivative of the dipole moment of the system of charged particles, which does not change when two identical particles interact. Consequently, only electron-ion collisions are relevant, and significant radiation is produced by the electrons only.

Free-free absorption can result not only from interactions between ions and free electrons but also from free-free transitions of electrons in the field of hydrogen atoms. The latter mechanism is often referred to as H^- absorption (Stallcop 1974)

At most frequencies and locations, the non-flaring Sun produces radio emission via the free-free mechanism. Exceptions include regions with strong coronal magnetic fields observed at microwaves.

1.3.2 Gyro-magnetic emission

Gyro-magnetic emission is generated when free electrons are accelerated or/and change their velocity direction in a magnetic field due to the influence of the magnetic component of the Lorentz force An electron with velocity components $v_{\parallel}$ and $v_{\perp}$ parallel and perpendicular to the magnetic field, respectively, will be accelerated perpendicular to both $v_{\perp}$ and B. Its acceleration, a, is:

$$a = \omega_{ce} v_{\perp} \tag{1.3}$$

where ω_{ce} is the electron gyrofrequency

$$\omega_{ce} = \frac{eB}{m_e c} \tag{1.4}$$

For non-relativistic speeds, the total power emitted by the electron is provided by the Larmor formula (EQ 1.2) which yields:

$$P = \frac{2e^2}{3c}\omega_{ce}^2 v_\perp^2 \tag{1.5}$$

This expression requires modification when the electron speed is not small compared to the speed of light, c. Then the power of the electron is given by the relativistic Larmor formula:

$$P = \frac{2e^2}{3c}\gamma\omega_{ce}^2 v_\perp^2 \tag{1.6}$$

where γ is the Lorentz factor.

The gyro-magnetic emission is called gyro-resonance when it is produced by thermal electrons with energies that correspond to temperatures of the non-flaring corona (about 10^6 K) and plays an important role in the emission above sunspots at microwaves. The structure of gyro-resonance sources is determined to a large extent by the number of harmonics that lie above the base of the transition region. The magnetic field decreases with height and therefore higher harmonics are located above lower ones. In the case of magnetic field decreasing away from the center of a sunspot, the height of a given harmonic decreases with the distance from the center. The brightness temperature of a given harmonic layer depends on the electron temperature at the height where it is located and on its optical depth. Reviews about gyro-resonance have been provided by White and Kundu 1997, Lee 2007 and Nindos 2020.

Gyro-magnetic emission is called gyro-synchrotron when it is produced by mildly relativistic electrons having either non-thermal or thermal electron energy distributions. Gyro-synchrotron emission may arise in quite diverse solar environments: solar flares, weak transient brightenings when observed at microwaves or at decimetric and metric wavelengths for a small number of CMEs (Nindos 2020).

The properties of gyro-resonance sources have been studied by both high spatial resolution observations at a few frequencies (e.g. Tun et al. 2011; Nita et al. 2018) as well as multi-frequency spectral observations (e.g Kaltman et al. 2012; Stupishin et al. 2018)

1.3.3 Quiet Sun

The Quiet Sun (QS) brightness temperature spectrum has been modelled in several papers (e.g. Landi and Chiuderi Drago 2008; Zhang et al. 2022; Pellizzoni et al. 2022). Its radio emission comes from thermal bremsstrahlung in LTE, therefore it has the advantage to be well understood and modelled compared to other frequency bands. It can thus be used as a powerful diagnostics of the physical conditions and parameters in a wide range of atmospheric layers (Shibasaki et al. 2011). In the K-band (18-26 GHz) however, there is a lack of accurate and calibrated measurements of the brightness temperature of the QS component, since it is difficult to separate it from the contribution of the ARs. The local emission in the chromospheric layers slightly deviates from simple thermal bremsstrahlung in the optically thick regime. In fact, instead of having a flux density spectral index (α) of 2, typical of a Rayleigh-Jeans emission, it assumes a value around 1.9 due to the logarithmic dependence of the Gaunt factor on frequency.

The QS emission resulting from the combination of the chromospheric layers suggests a possible spectral change from lower to higher frequencies (Landi and Chiuderi Drago 2008), such as a flattening at 10 GHz. From the work of Landi and Chiuderi Drago 2008 the QS is predicted to have a value between 10,227-9,377 K in the 18-26 GHz interval, with an $\alpha = 1.76$. They used the data from Fedoseev and Chernyshev 1998 to fit the QS spectrum at high frequencies and while Fedoseev and Chernyshev 1998 selected the data with the highest

possible accuracy, it is known that the millimeter observations are more uncertain than the centimeter ones. In fact, it can be seen from Landi and Chiuderi Drago 2008 that the data from 35 GHz show a large scatter, which could explain the discrepancy with the α previously mentioned.

1.3.4 Active Regions

Active regions (ARs) are the totality of observable phenomena in a 3D volume represented by the extension of the magnetic field from the photosphere to the corona, revealed by emissions over a wide range of wavelengths from the radio to X-rays and γ-rays (only during flares) accompanying and following the emergence of strong twisted magnetic flux through the photosphere into the chromosphere and corona (van Driel-Gesztelyi and Green 2015).

ARs are the primary source of a broad range of solar activity phenomena: ranging from small-scale brightenings and jets to the coronal mass ejections (CMEs) and largest flares (see Sec 1.3.5). The level and type of activity is dependent on the evolutionary stage of an AR, being highest at the emergence stage and decreasing after it.

The ARs radio emission mechanism is more difficult to understand than the QS since there is an entanglement of thermal (free-free and gyro-resonance) and non-thermal emission depending on the observing frequency. In the radio domain, the gyro-resonance has been detected up to 17 GHz (see Nindos 2020 and references therein), and has its emission peak in the 2-5 GHz range (Kakinuma and Swarup 1962; Nindos et al. 2002). At higher frequencies (from 34 GHz), the ARs emission has been modelled as purely free-free (Selhorst et al. 2008), and in the range 212-405 GHz, Silva et al. 2005 as thermal bremsstrahlung. Taking into consideration the ARs flux density spectra from Silva et al. 2005, the K-band seems to be a transition region between different emission mechanisms.

1.3.5 Eruptive phenomena

Coronal mass ejections (CMEs; Fig 1.3 right panle) consist of large-scale structures containing magnetised plasma ejected from the solar corona into the interplanetary medium. CMEs and their interplanetary counterparts (ICMEs) are known to be associated with a variety of other important phenomena, such as solar energetic particle (SEP) events, interplanetary (IP) shocks, geomagnetic storms (GS), which form essential ingredients of the current Space Weather (the variations in the space environment between the Sun and Earth) research (Patel et al. 2022 and related papers). The most energetic CME events may propagate the 1 AU distance within a day, while less energetic CMEs travel the Sun-Earth distance in up to 4 days (Gopalswamy et al. 2005; Manchester et al. 2017).

ARs can often originate a flare (Fig 1.3 left panel), a powerful event consisting in a transient localised release of energy, which results in electromagnetic radiation and accelerated particle emission. The apparent characteristics of a solar flare can change depending on the observing frequency, the spatial and time resolution of the instrument used. However, there are some general characteristics that can still be deduced from the observed time variation of the electromagnetic radiation. A flare can, in general, be roughly divided into three phases: Precursor, Impulsive and Gradual Phase (Kane 1974). These three phases do not necessarily occur in all flares and some of them could be not detectable at certain radiation frequencies. Dulk 2001 reports the brightness temperature expected from a flare and the main emission mechanism involved, depending on the wavelength range: in the mm-m range from 10^6 to 10^{10} K mainly from gyro-synchrotron radiation; in the cm-dm range up to 10^{15} K from electron cyclotron maser; in the dm-km range up to 10^{17} K from plasma radiation. However,

this very strong and point-like emission is diluted in the radio beam of relatively low-spatial resolution instruments (see Pellizzoni et al. 2022).

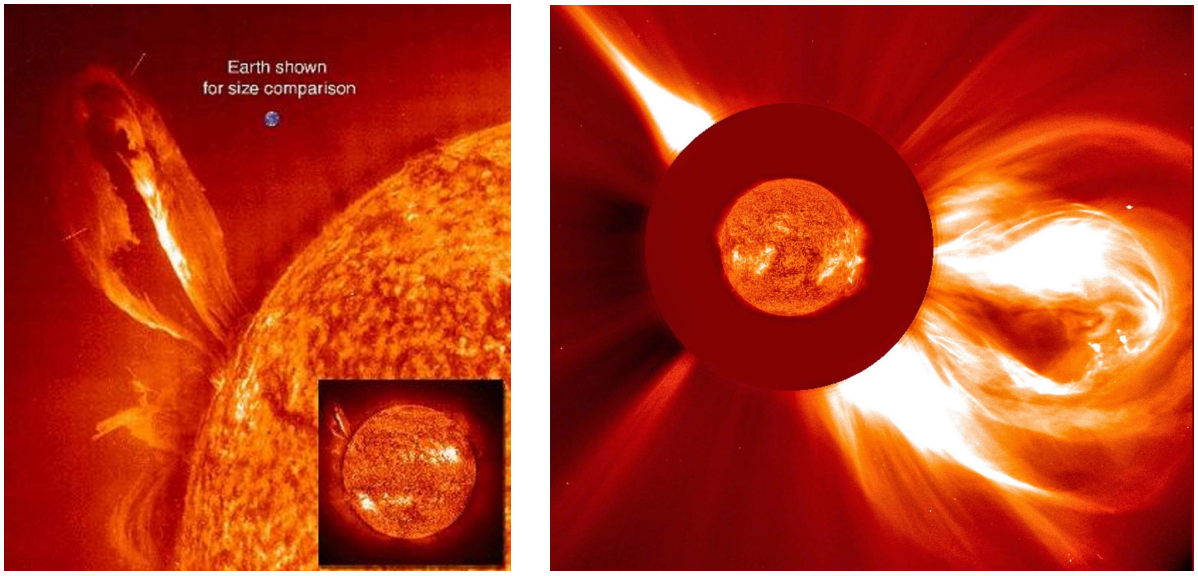

Figure 1.3: Left panel: A flare seen by the SOHO spacecraft on 24 July 1999 (Credit: SOHO/EIT). Right panel: a coronal mass ejection as captured by SOHO. A coronal mass ejection, or CME, erupts from the lower right of the sun in this composite image captured by ESA/NASAs Solar and Heliospheric Observatory on Dec. 2, 2003 (Credits: ESA/NASA/SOHO).

1.3.6 Semi-Active Regions

Aside from the previous emission components, Kallunki et al. 2020 studied the semi-active feature, an activity present in the radio domain even when the Sun appears ostensibly quiet at 37 GHz. In the study, they observed during the solar minimum, when the ARs were not present ON the disk. The semi-active featureS were found to have, at maximum, an excess above the QS level of 250 K, and for almost every sources, they found a counterpart in the EUV data.

1.4 Multi-frequency radio observations

As the opacity increases with the observing wavelength, the effective height of formation moves from the temperature minimum region to the low corona. The former is visible at sub-millimeter waves and approached by several instruments, e.g., ALMA observations (Loukitcheva, 2019), while the latter is mostly visible at meter waves, for example with LOFAR Zhang et al., 2020; Zucca et al., 2018, the Nançay Radioheliograph (NRH, Kerdraon and Delouis, 1997), and GRAPH (Ramesh et al., 1998). In between these extreme wavelengths, the chromosphere is visible at moderately high radio-frequencies (10–50 GHz) and it hosts most of the active solar features linking the photosphere to the corona, with a temperature rise of still unclear origin, being explored by a number of dedicated facilities (see, e.g., Nobeyama Radioheliograph, NoRH, Shibasaki, 1998; Metsähovi Radio Observatory, MRO, Kallunki and Tornikoski, 2017; the Expanded Owens Valley Solar Array, EOVSA, Gary et al., 2018; RATAN-600, Schwartz, 1978; SSRT, Grechnev et al., 2003; Smolkov et al., 1986; MUSER, Cheng et al., 2019). In particular, solar atmospheric models could be critically constrained by observations in the K-band (18–27 GHz) and above (see, e.g., Gopalswamy, 2016; Selhorst et al., 2005). This portion of the spectrum is suitable for detailed measurements of the chromospheric brightness temperature of the QS and to assess the rich thermal vs. non-thermal content

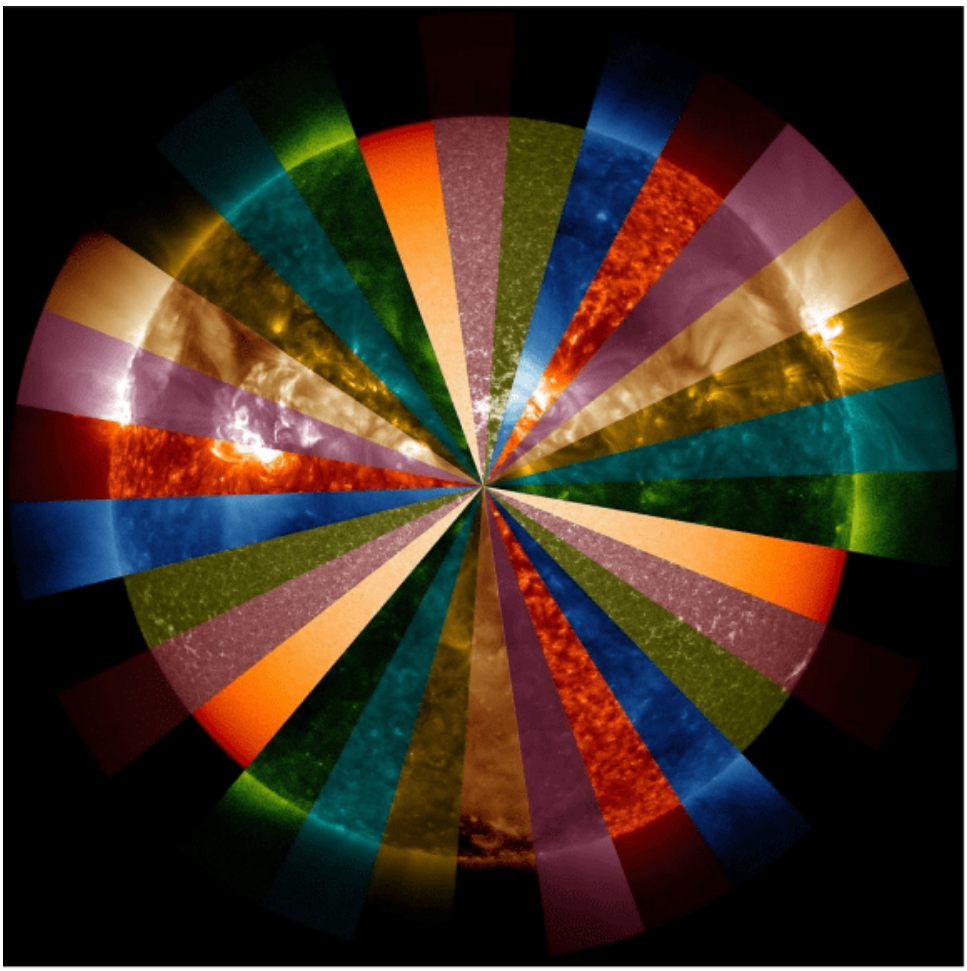

Figure 1.4: Composite image of the solar disk, performed by the Solar Dynamics Observatory (SDO). Each color represents a different wavelenght of extreme ultraviolet light. Credits: NASA/SDO/GSFC Visualization Studio.

of AR emission. At these frequencies both the QS network and gyro-magnetic variable components can be simultaneously mapped due to the relatively low instrumental dynamic range required for their observations.

For such scientific applications, single-dish radio mapping of the solar disk is as well suitable as interferometric observations in the K-band (see, e.g., Pellizzoni et al., 2019; White et al., 2017). Synthesis images of the full solar disk cannot be easily obtained in the frequency range 10–30 GHz through interferometric networks aimed at simultaneously resolving both large and arcsec-level solar features (see, e.g., Wilson et al., 2013), with the exception of dedicated short-baseline facilities, as the NoRH Shibasaki, 1998 that ceased operations in 2020 (Masuda, 2019). On the other hand, at the expenses of a coarser spatial resolution, single-dish radio mapping on relatively large and bright sources (as, for example, supernova remnants and the solar disk) offers accurate calibrated images independently from the target size, without synthesis imaging artifacts (see Loru et al., 2019, 2021; Marongiu et al., 2020; Pellizzoni et al., 2019).

1.5 Space Weather

The complex interplanetary environment surrounding the Solar System, confined by the local neighbourhood interstellar wind and permeated by the solar wind namely the heliosphere is drastically affected by high energy events of extragalactic, galactic and solar origin. Focusing on the contribution of our star only, a wide variety of eruptive phenomena such

as flares, coronal mass ejections and solar particle events severely shape the interplanetary environment and strongly interact with the Earth magnetic field, turning into an hazard for space missions and ground facilities (see Fig 1.5 for some examples).

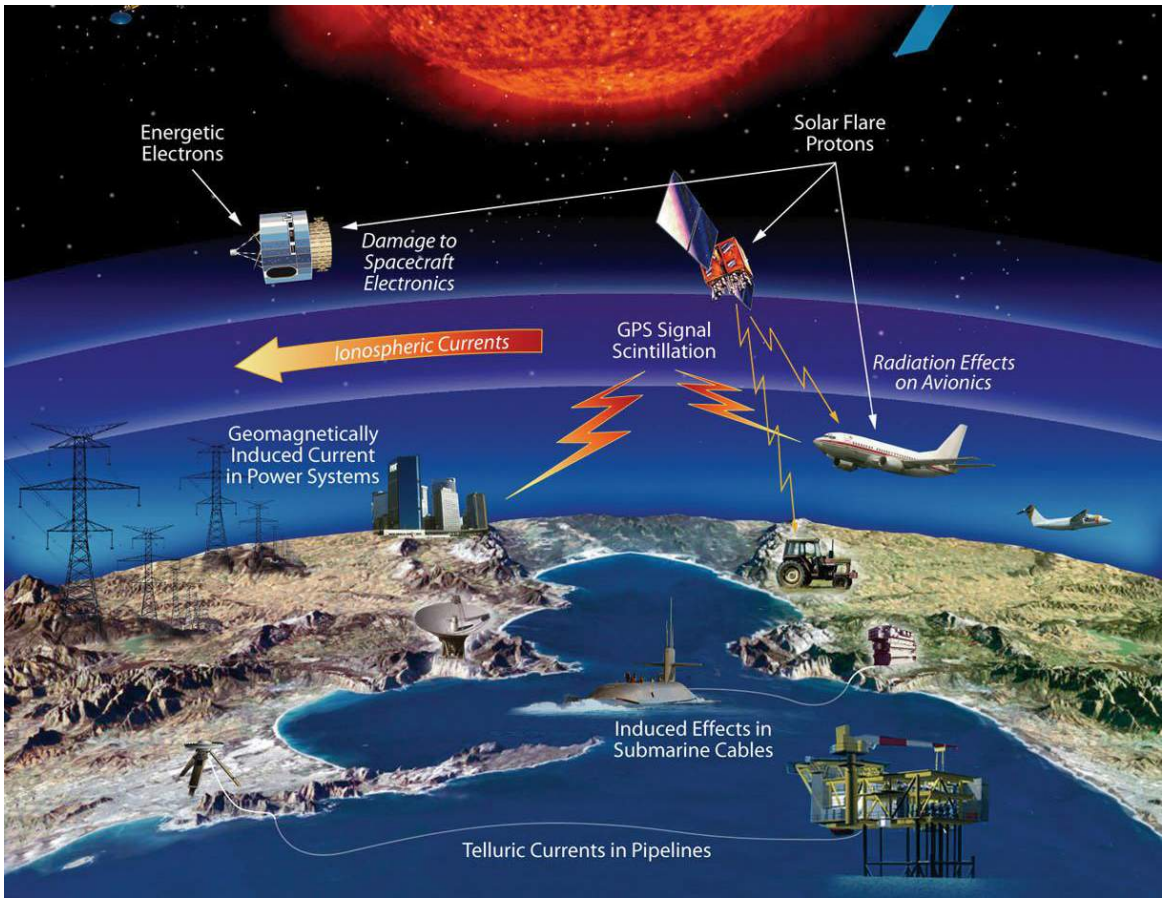

Figure 1.5: Examples of technological infrastructure affected by Space Weather events. Credits: NASA

The study of Space Weather (the variations in the physical state of the space environment between the sun and Earth) requires both short-term and long-term forecasts in multi-frequency ranges, because they can affect tasks requiring human extra-vehicular activity (EVA) and the operation of radiation-sensitive detectors. For this reason, real-time solar observations can provide useful warnings of solar activity, as large outburst events are usually associated with a strong emission of electromagnetic radiation (radio waves, soft X-rays). Through an extended set of time series of indices, based on prominent observed features, insights can be extrapolated about the long-term global behaviour of the Sun as a star and about the short-term physical state.

1.6 Open issues

There is a variety of open issues regarding the Sun and its activity. Observations in the radio domain can be helpful to shed light on the problem of the heating of the chromosphere and the corona (see, e.g., Shibasaki et al. 2011, Alissandrakis 2020), to study the electron plasma frequency and the electron gyrofrequency (Nindos 2020).

Disentanglement and quantification of the thermal (free-free and gyro-resonance) and non-thermal emission components are other open issues for radio ARs (see, e.g., Lee, 2007; White, 2004), as well as for peculiar large-scale structures such as coronal holes, loop systems, filaments, streamers and the coronal plateau, that would benefit from systematic long-term observations.

Multi-frequency observations could provide insights on the formation process of the ARs where major flares are triggered and determining the slowly varying component of the Sun over the 11-year cycle. In particular, observations of strong gyro-magnetic emission over sunspot groups can be used to test in detail the magnetic field model extrapolated from measurements at the photosphere (see Lee et al., 1998). In this frame, it is important to enlarge the sample of measurements of intensity, spectra, and size of the bright features in coincidence with the chromospheric network as a function of the frequency.

A growing number of existing facilities, surveyed, e.g, in the Community of European Solar Radio Astronomers (CESRA)[1], is working on the puzzling disentanglement of the large variety of phenomena occurring in the solar atmosphere on a wide frequency range, together with non-dedicated facilities offering more sporadic solar observations (Carley et al., 2020). A list of the facilities dedicated to the imaging observations is displayed in Fig 1.6. For a full list of the observatories dedicated also to whole-Sun dynamic spectra and radio flux or lightcurves at fixed frequencies in the CESRA community, visit the site in the footnote 1.

SunDish project (solar observations with INAF radio telescopes)	Cagliari and Bologna, Italy	**18-26 GHz**	*2D spectro-polarimetric imaging with resolution about 1 arcmin. Weekly observations (on average) since 2018*
Siberian Solar Radio Telescope (SSRT)	Irkutsk, Russia	**5.7 GHz**	*2D radio maps avaliable from 10 October 1997 till now.*
Metsähovi Radio Observatory (MRO)	Kylmälä, Finland	**37 GHz**	*Data available from 1978 till now, normally one solar map per day, at summer months special sessions up 14 hours per day. It will take about 150 seconds to make a one radio map.*
Nobeyama Radioheliograph (NoRH)	Nobeyama, Japan	**17, 34 GHz**	*17GHz (Right and left circular polarization), 34GHz (only intensity); Spatial resolution: 10 arcsec (17GHz), 5 arcsec (34GHz); Temporal resolution: 0.1 sec (Event), 1 sec (Steady); http://solar.nro.nao.ac.jp /norh/html/introduction.html*
Owens Valley Solar Array (OVSA)	Owens Valley, USA	**1.2-18 GHz**	*39 frequencies between 1.2 and 18 GHz;*
RATAN-600, SAO, Russia	Nizhnij Arkhyz, Russia	**0.7-18.2 GHz**	*Images 1-D scans at 112 frequency channels,Each day observations are between 7:00 UT to 11:00 UT. Time cadence is about 5 observations per day. Maximum is to 60 observations per day. I&V Stokes parameters at all channels with 1% frequency resolution.*
Nancay Radio Heliograph (NRH)	Nancay, France	**0.15-0.45 GHz**	*47 antennas interferometer, up to 10 frequencies*
Gauribidanur RAdioheliograPH (GRAPH)	Gauribidanur, India	**0.08 GHz**	*0.25 second cadence. Images during local meridian transit of the Sun available online since 2014. Daily observations are usually during the interval 04:00 – 09:00 UT*

Figure 1.6: List of facilities dedicated to the imaging observations. For a full list visit the site in the footnote 1.

[1] www.astro.gla.ac.uk/users/eduard/cesra/?page_id=187

Chapter 2

Solar imaging and calibration in the K-band

In this Chapter, we provide an overview on the solar observations performed in K-band in the context of the SunDish project. Starting from a description of the INAF radio telescopes used for the research program and their set up, I then describe the software pipeline (SUNPIT) utilized for the data analysis and illustrate the imaging procedure. I dedicate the rest the chapter to the calibration of the solar images and introduce an original and innovative absolute calibration procedure with the Supernova Remnant Cassiopeia A.

2.1 The INAF radio telescopes

In order to obtain valuable information on the structure of the solar atmosphere above the temperature minimum with the radio data, there is the need of reliable absolute measurements of the brightness temperature. Single-dish radio imaging (Shibasaki et al. 2011, Pellizzoni et al. 2022) represents the most suitable technique to perform accurately calibrated observations, due to inherent difficulties to calibrate solar interferometric images. We used two single-dish antennas from the INAF radio telescopes network[1]: the 64-m Sardinia Radio Telescope (SRT; Prandoni et al. 2017) and the 32-m antenna at Medicina. The SRT is also operated by the ASI for spacecraft tracking and space science (Sardinia Deep Space Antenna (SDSA); Flamini et al. 2017).

Both the SRT and the Medicina Radio Telescopes were not initially designed to perform solar imaging, therefore, from 2018 the team has started developing an imaging configurations for solar observations with both instruments in the $18 - 26$ GHz frequency range (SunDish project[2], in collaboration with INAF and ASI; Pellizzoni et al. 2019; Iacolina et al. 2019; Plainaki et al. 2020, Pellizzoni et al. 2022). In the K-band, the solar brightness is over three orders of magnitude higher than typical radio-astronomical calibration sources ($\sim$ 5000 Jy/arcmin^2). The implementation of variable attenuators for additional signal attenuation, included in the receivers amplification chain, was crucial to avoid electronic saturation in signal response and possible instrumental damage. The experimental solar observations, about on a weekly basis in the last years, have helped to establish the Italian radio telescope network as a non-dedicated solar imaging facility. In the beginning of 2022, the first paper from the SunDish team was published in Solar Physics (Pellizzoni et al. 2022), in which the implementation of the instrumental configurations for radio-continuum solar imaging and the observing techniques adopted for the solar observations is described in detail.

[1] https://www.radiotelescopes.inaf.it

[2] https://sites.google.com/inaf.it/sundish.

2.1.1 The Medicina Radio-Telescope

The 32-m Medicina radio telescope operates in frequency agility, with multiple receivers covering the range 1.3–26.5 GHz. In recent years a new control system (DISCOS[3]) was designed and produced by INAF in order to enhance the performance of this telescope – originally conceived for very long baseline interferometry (VLBI) observations – as a single-dish instrument. Fast On-The-Fly (OTF) mapping (see Sec 2.3 and Prandoni et al. 2017 for a detailed description of the technique) is now one of the built-in observing modes; its sky coverage efficiency is doubled in the case of the K-band receiver, as it is a dual-feed device. The overall K-band observable portion is 18–26.5 GHz, with an instantaneous configurable bandwidth of 2 GHz maximum. The output of each feed consists of two separate lines: LCP (Left Circular Polarization) and RCP (Right Circular Polarization) that reach an analog total-power back-end. The frequency and bandwidth actually employed may slightly vary with time, according to the incidence of RFI (Radio Frequency Interference).

Observing schedules are produced using a custom generator in turn relying on solar ephemeris computed with the NASA JPL Horizons web tool[4], as the observation of Solar system targets is currently not offered among the built-in options of the Medicina control system. Most of the maps are performed by setting the two feeds in different dynamic ranges, so as to coevally acquire data on the bright solar disk and on the much fainter emission near the limb. This is accomplished via a double layer of variable signal attenuation devices. In order to acquire spectral information, observations are carried out at the boundaries of the available radio frequency band: maps are acquired first at 18 GHz, then at 26 GHz. The two maps are obtained by scanning the desired area in Right Ascension (RA) and Declination (Dec), respectively. This choice reflects the need to reduce the total observing time, while permitting to investigate weak disk features that, in a single map, might be altered – or even created – by striping effects, usually due to fast-variable weather conditions differently affecting the many sub-scans composing the map. Radio frequency interference, RFI, might also contribute to this issue. Table 2.1 describes the mapping parameters and setup configurations used for the receiver and back-end in the vast majority of the observing sessions (except for periodic maintenance operations in order -e.g.- to check for frequency bands relatively free from strong RFI).

Flux density calibration is achieved through the observation of calibration sources, either in cross-scan or mapping mode. Mostly, the Supernova Remnant Cas A is observed producing 40×40 arcmin maps, with 2.0 scan/beamsize, in order to obtain the conversion factor from arbitrary counts to flux density units, expressed in units of Jy (see Sec 2.5.3 for calibration procedure details). The estimate of the atmospheric opacity, one for each frequency, is possible thanks to the Skydip observing mode, that measures the sky brightness at a range of elevations. Skydip scans consist in moving the telescope along a vast range in elevation, from 15° to 85° (at fixed azimuth) and require additional 12 minutes.

2.1.2 The Sardinia Radio Telescope

For our data we used the cryogenic dual-polarisation 7-beam K-band receiver ($18 - 26.5$ GHz, Gregorian focus; Verma et al. 2009, Orfei et al. 2010, Valente et al. 2022b, Valente et al. 2016, Navarrini et al. 2017, Loru et al. 2019, Navarrini et al. 2022). The radio signal is processed through the SARDARA system, a full-stokes spectral-polarimetric ROACH2-based back-end with 1.5 GHz bandwidth (Melis et al. 2018).

The 64-m Sardinia Radio Telescope (SRT) presently provides solar imaging in the 18–26 GHz

[3] https://discos.readthedocs.io/en/latest/user/index.html

[4] https://ssd.jpl.nasa.gov/horizons.cgi

Table 2.1: OTF mapping parameters and receiver/back-end configurations for observations with the Medicina radio telescope.

OTF parameter	Value	
Map dimensions	80 × 80 arcmin	
Scanning speed	6 arcmin/s	
Scan interleave	4 scan/beamsize	
Scan direction	RA for 18 GHz map	
	Dec for 26 GHz map	
Overall duration	2h 30m[a]	
Receiver/Back-end parameter	18-GHz map	26-GHz map
Frequency range (GHz)	18.20 – 18.45[b]	25.70 – 25.95[d]
	18.00 – 18.25[c]	26.00 – 26.25[e]
		(23.50 – 23.75)[f]
Beamsize (arcmin)	2.1	1.5
Sampling interval (ms)	40	40
Solar disk map on	Feed 1	Feed 1
Coronal map on	Feed 0	Feed 0

[a] *To acquire both maps*
[b] *Since 17-Jun-2018*
[c] *Until 10-Jun-2018*
[d] *Since 12-Jun-2019*
[e] *Until 6-Dec-2018*
[f] *Frequency range used in early observations*

range by the 7 feeds dual polarization K-band receiver Bolli et al., 2015; Prandoni et al., 2017, and up to 100 GHz in perspective with the planned system upgrade[5] for the whole INAF network. The radio signal is processed through full-Stokes spectral-polarimetric ROACH2-based back-end (SARDARA system, 1.5 GHz bandwidth, Melis et al., 2018).

Solar imaging observations at SRT require special hardware configuration in order to attenuate the strong solar signal in the amplification chain. At present, the need for a manual setup of additional hardware (10 dB attenuation for the 14 multi-feed chains, 7 for each polarization section) at each solar observing session restricts the use of SRT to a few solar sessions/year. A remotely-controlled attenuation level setup is under development and it will permit a quick and smart switching from standard operations to solar observing mode ("solar agility") allowing more frequent observations. The high dynamic range of the SARDARA spectro-polarimeter Melis et al., 2018 allows us to detect both the bright solar disk (chromospheric emission) and the weaker emission near the limb, in the same image. The adopted observing technique is similar to that in use with Medicina: OTF scans providing full solar mapping (both radio telescopes use the DISCOS antenna control system); with OTF scans we spanned the region on and around the source, covered by all the 7 feeds of the receiver, along the RA direction. Maps with SRT were performed at 18.8 and 24.7 GHz[6], near the edge of the K-band in order to minimize errors in spectral index measurements. OTF parameters and configuration parameters for front-end and back-end are listed in Table 2.2.

[5] https://sites.google.com/a/inaf.it/pon-srt/home
[6] After a specific test phase, we decreased the frequency at 24.7 GHz (from the initial 25.5 GHz) to match better receiver performances and avoid RFI.

Table 2.2: OTF mapping parameters and receiver/back-end configurations for SRT observations. All the map scans were performed along the Right Ascension direction.

OTF parameter	Value		
Map dimensions	90×90 arcmin		
Scanning speed	6 arcmin/s		
Scan interleave	2 scan/beamsize[a]		
Single Map duration	1h 45m		
Receiver/Back-end parameter	18-GHz map	24-GHz map	25-GHz map
Frequency range (GHz)	18.1 – 19.5	24.0 – 25.4	25.1 – 26.5[b]
Beamsize (arcmin)	1.02	0.78	0.75
Sampling interval (ms)	20	20	20
Number of frequency channels	1024	1024	1024

[a] $\times$ *7 feeds*

[b] *in a few sessions we adopted a reduced bandwidth of 0.9 GHz*

2.1.3 Observing strategies

The Medicina 32-m and SRT 64-m radio telescopes are facilities open to the scientific community. Early radio observations related to the SunDish project relied on observing time granted through INAF Guest Observer programs, Discretionary Director Time (DDT) and instrument development and testing activities (depending on the specific task/operation).

Features on the solar disk can evolve on very short timescales, thus a daily or even a more frequent monitoring is the optimal and typical choice for dedicated radio solar facilities, as for example NoRH Shibasaki, 2013 and MRO Kallunki et al., 2020. SRT and Medicina perform an almost-weekly monitoring campaign. Accounting for the bright radio ARs, which typically persist from a few days to 10–15 days, and the radio telescopes schedule constraints due to high-priority projects (such as VLBI sessions), the weekly monitoring is a good compromise for typical solar sessions with non-dedicated solar instruments in this early science phase of the project (2018–2020). A summary of the solar observations acquired with the INAF radio telescopes during the development and early science phase of the project is given in Appendix A.

2.2 SunDish Pipeline Tool (SUNPIT)

SUNPIT (SUNdish PIpeline Tool) Marongiu et al. 2022 is a pipeline designed for the imaging procedure and the data analysis of solar data acquired with some radio telescopes of the INAF Network (SRT and Medicina) in the context of the SunDish Project (PI: A. Pellizzoni)[7]. SUNPIT is composed of three independent packages:

1. **SDI (Single-Dish Imager)**, based on the programming language IDL (Interactive Data Language[8]), a commercial software with specific INAF licence[9]. This IDL Package is designed to perform continuum and spectro-polarimetric imaging, optimized for OTF scan mapping, and suitable for most receivers/backends available at the INAF radio telescopes (see e.g. Egron et al. 2017; Loru et al. 2019; Pellizzoni et al. 2019); SDI receives

[7] https://sites.google.com/inaf.it/sundish

[8] https://www.l3harrisgeospatial.com/Software-Technology/IDL

[9] Further details to obtain the Software licence are available at the ICT/INAF link https://www.ict.inaf.it/index.php/ict-inaf/software.

in input the raw acquisitions (the original subscans) obtained by these radio telescopes, and produces an output in the form of calibrated solar maps (Fig. 2.1).

2. **SDT (SRT Single-Dish Tools)**, a Python Package[10] designed for the quicklook and analysis of single-dish radio data, starting from the backends present at every Italian radio telescope.

3. **SUNDARA (SUNDish Active Region Analyser**; Marongiu et al. 2021), a Python Package aimed at the automatic data analysis of solar images processed by SDI and/or SDT; SUNDARA receives as input the solar images obtained by SDI and/or SDT. This package produces as output a complete analysis in a short time (about 5 minutes for each solar map), saving a directory containing images, plots and several tables with physical information (brightness temperatures, fluxes and spectral indices, with the respective errors) of the Active Regions (ARs) detected in all the solar maps (Fig. 2.1).

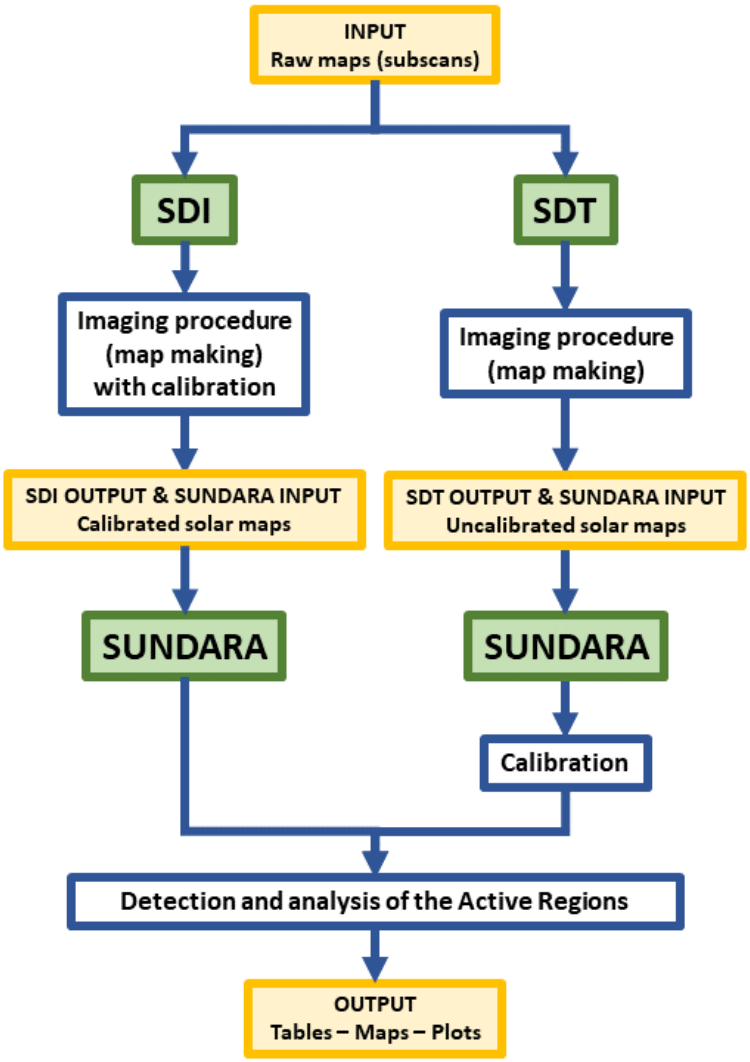

Figure 2.1: Diagram of the SUNPIT operation. Input/Output are labelled by yellow boxes, and the software packages are indicated by green boxes (Marongiu et al. 2022).

This pipeline will also be suitable – with the appropriate arrangements – for the solar images obtained with the new receivers in Q-band (33 – 50 GHz) and W-band (70 – 116 GHz, Navarrini et al. 2022) , soon installed at SRT in the context of the National Operative Programme (Programma Operativo Nazionale-PON)[11] Govoni et al. 2021; this project will

[10] https://www.python.org/

[11] https://sites.google.com/a/inaf.it/pon-srt/home

provide in the near future an upgrading with the new receivers up to 116 GHz also for the Medicina and Noto Radio Telescopes[12] Bolli et al. 2017

2.3 Solar imaging

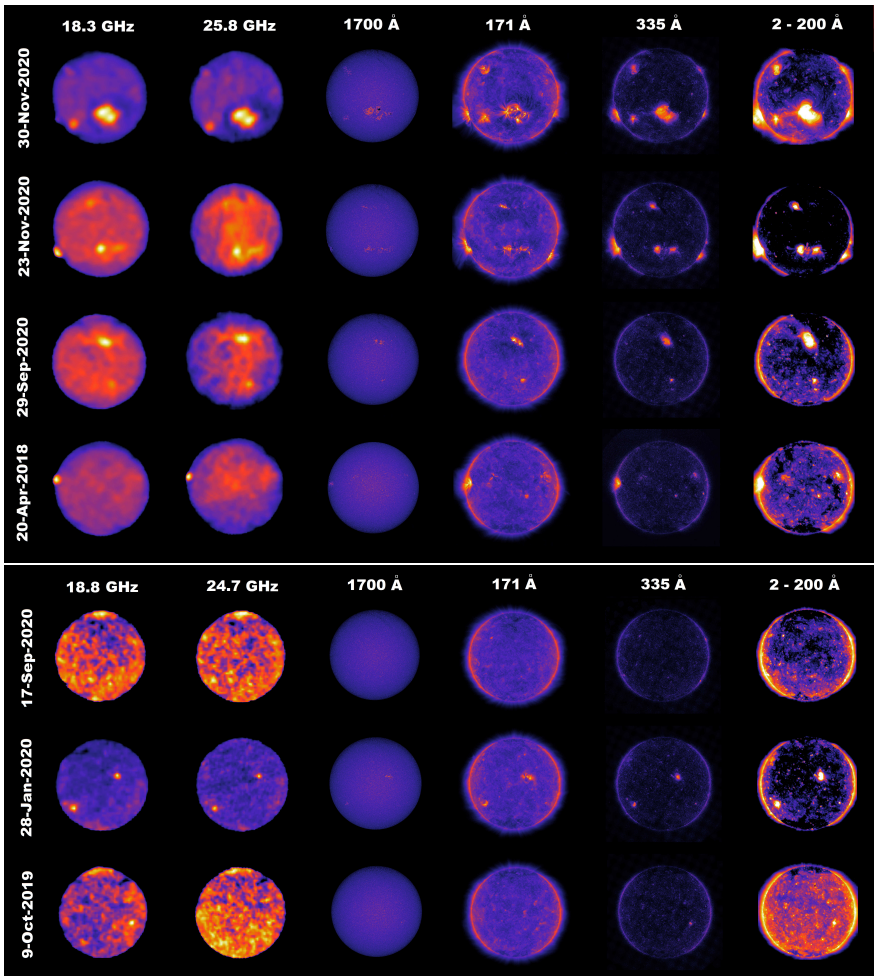

Figure 2.2: Examples of solar disk maps collected at different frequencies with Medicina (top) and SRT (bottom), in comparison with UV/EUV (SDO/AIA, Lemen et al. 2012) and X-ray (Hinode/XRT, Golub et al. 2007; Kosugi et al. 2007) images (Credits: NASA/JAXA). ARs and disk structures are clearly detected in the radio images allowing multi-wavelength spectral analysis (Pellizzoni et al. 2022).

The solar maps were acquired through OTF scans. This observing mode differs from Raster scans since the data acquisition is continuously ongoing while the antenna performs constant-speed scans across the sky, instead of tracking individual points. Usually, it produces alternatively maps along the Right Ascension (RA) and Declination (Dec) directions (Prandoni et al. 2017).

The OTF scans are binned through an ARC-tangent projection using pixel sizes of about 1/4 of the Half Power Beam Width (HPBW), which corresponds to the effective resolution of the images. Bright and adjacent point-like image features (e.g. having > 0.1 Jy flux density and a beam-size separation) associated with a Gaussian Point Spread Function (i.e. the antenna beam shape) are not distinguishable when the image pixel size is equal to the HPBW, while these are resolved when adopting a pixel size equal to the effective resolution (about $1/4 \sim$ HPBW). This arises from Gaussian beam oversampling in our mapping procedures.

[12] https://indico.ict.inaf.it/event/1515/contributions/9080/attachments/4392/9080/PON_SRT_AUDIZIONE_31MAY21.pdf

Since the apparent proper motion of the Sun in celestial coordinates is about 2.5′/hour, a blurring effect comparable to the beam size is affecting the raw images for typical mapping time of about 1.5 hours. In order to obtain corrected astrometric images, we subtracted the actual coordinates of the Sun centroid from the celestial coordinates of each OTF sample. We adopted the NASA/JPL Sun ephemeris[13] interpolated at the precise time-stamps of our measurements. This allowed us to obtain unblurred maps providing a local (helioprojective) coordinate system having its origin at the Sun centroid (Solar-X and Solar-Y, Thompson, 2006). The images are then produced in the digital file format FITS (Flexible Image Transport System) and ready for scientific analysis (e.g. image RMS/sensitivity, dynamic range, and brightness profiles) through specific packages, such as SAOIMAGEDS9 (An image display and visualization tool for astronomical data)[14], SUNPY[15] and the Common Astronomy Software Applications (CASA)[16]. A selection of typical resulting images of the solar disk is represented in Fig. 2.2.

2.4 Calibration procedure

The raw images acquired with the INAF radio telescope are obtained in counts, an electronic measurement given by the back-end in use proportional to the flux density. In order to obtain a map expressed in a physical quantity (flux density or brightness temperature), there is the need to observe a calibration source – a celestial object with a flux density, or brightness temperature, well known and studied in the literature – to calculate the conversion factor from counts to a physical unit of measurements. This factor is obtained by comparing the raw counts of the calibration sources with the theoretical flux, and it is calculated for each observing session since the counts value depends on various factors (e.g. the attenuation set up, the sky opacity, or the meteorological conditions).

Among different techniques and sources used to perform the calibration procedure, we used two different approaches: the so-called self and the absolute calibration. The first one consists of identifying the average counts of the QS in the image acquired with our telescopes and compare them with the brightness temperature published in the literature (e.g. Landi and Chiuderi Drago 2008). The latter exploits an external source for the comparison. The instrumental setup for solar observations requires several additional signal attenuation compared to non-solar radio telescope operations (see Sec 2.1). For this reason the standard calibrators (Perley and Butler 2017) are not the ideal source, since their flux is typically low. Therefore, in order to obtain accurate measurements with the absolute calibration, we implemented a new procedure using the young and strong supernova remnant (SNR) Cassiopeia A (Cas A). Compared to the standard calibrators, which are stable point like sources, Cas A is extended at our frequencies of interests and it is still expanding and changing. However its evolution is well studied in literature (see e.g. Vinyaikin 2014), therefore easy to predict.

2.4.1 Self calibration

As mentioned in the previous paragraph, a possible way to calculate the count-to-kelvin conversion factor is the self calibration method. In order to accurately estimate the average counts from the QS, we used a Gaussian fit of the image histogram (counts distribution among

[13] https://ssd.jpl.nasa.gov/horizons.cgi
[14] https://sites.google.com/cfa.harvard.edu/saoimageds9
[15] https://sunpy.org
[16] https://casa.nrao.edu/

pixels) extrapolated from the solar maps as in the example reported in Fig. 2.3. In some cases a Johnson's S_U-distribution Johnson 1949a,b would provide a better fit of the QS brightness distribution with respect to the Gaussian shape. However, this latter approximation does not significantly affect the calibration process (Pellizzoni et al. 2022). We calculated a negligible error of 0.02% in the estimation of the average QS counts. Therefore, we adopted the Gaussian fit in our data processing pipeline for the entire data set for simplicity.

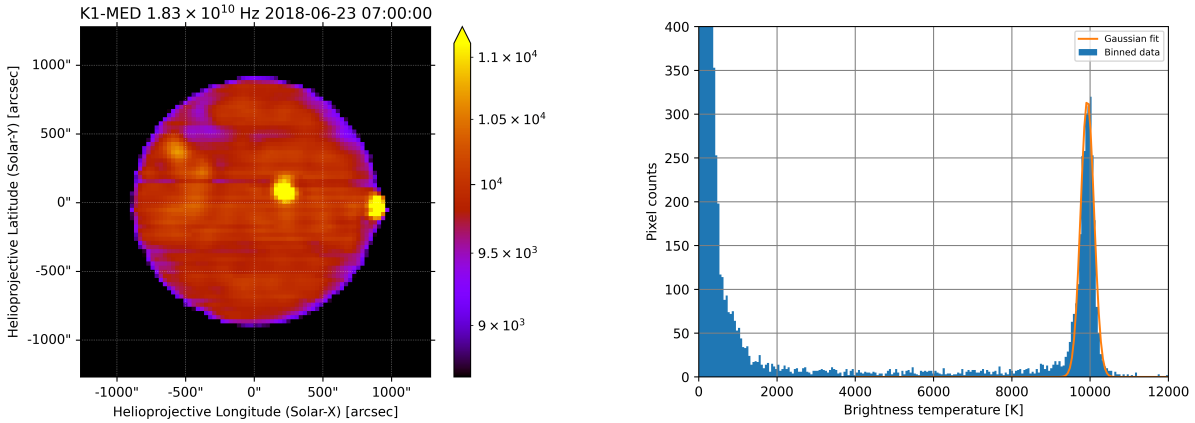

Figure 2.3: Left panel: Total intensity map of the solar disk at 18.3 GHz acquired with the Medicina Radio Telescope on 23-Jun-2018. Right panel: histogram of brightness distribution among pixels of the solar map and estimation of the average counts from the QS using a Gaussian fit (orange line) (Pellizzoni et al. 2022).

For this calibration method our brightness reference from the literature comes from Landi and Chiuderi Drago 2008. This work observed a break in the spectrum at about 10 GHz, which corresponds to a brightness temperature of about 12,000 K referred to the center of the solar disk. They obtained a spectral fit ($\chi^2 = 0.032$) for frequencies above 10 GHz characterized by a logarithmic linear relation between the brightness (T_b, in units of kelvin) and the frequency (ν, in units of Hz):

$$log_{10}(T_b) = a + b \times log_{10}(\nu) \tag{2.1}$$

where $a = 6.43$ and $b = -0.236$. Landi and Chiuderi Drago 2008 do not provide a fit error estimate, but the measurements used in their model are typically affected by $\sim 5\%$ errors in the 10-20 GHz range and a much larger measurement spread is present above 30 GHz.

Although the self calibration is a reliable method to obtain the QS value, it is worth noting that there is a lack of calibrated measurements in the literature in the $18 - 30$ GHz range in Landi and Chiuderi Drago 2008.

2.4.2 External source

As mentioned previously in Sec 2.4, the absolute calibration procedure exploits an external source in order to find the conversion factor from counts to Jy (or K). In some cases, the Moon has been chosen as the calibration source: in the work of Silva et al. 2005 the brightness temperature of the QS and ARs were calibrated against observations of the new Moon by using the values from Linsky 1973. Also in the work of Fedoseev and Chernyshev 1998 the new Moon brightness spectrum was used to calibrate the observations.

The $18 - 26$ GHz range has a few external inferences while the sky opacity (τ) plays a fundamental part in the image final quality Buffa et al. 2016. An ideal calibration source should be subjected to similar sky opacity condition as the main source, in order to minimize the error due to the opacity. The New Moon could have been a possible calibration source, however it was not easy to meet suitable visibility conditions of the Sun and the Moon for

our observing sessions. Accordingly, we searched for a bright celestial object visible during the solar sessions which could be observed with the same solar attenuation configuration while preserving a linear dynamic range. As we excluded that the standard point-like sources can fulfill this requirement, we adopted the SNR Cas A (Fig. 2.4 right panel) for our solar observations.

2.5 Absolute solar calibration with SRT

The use of the extended SNR Cas A as a solar calibrator is a new method introduced for the first time by our group Pellizzoni et al. 2022. We first calibrated the QS of each maps at the different frequencies and compare our results with the value from Landi and Chiuderi Drago 2008 in order to verify its trustworthiness.

2.5.1 Observing data

We performed several observing session tests and obtained the maps of the Sun and Cas A with SRT (see Fig. 2.4) listed in Tab. 2.3 and Tab. 2.4 at three different central frequencies: 18.8, 24.7 and 25.5 GHz.

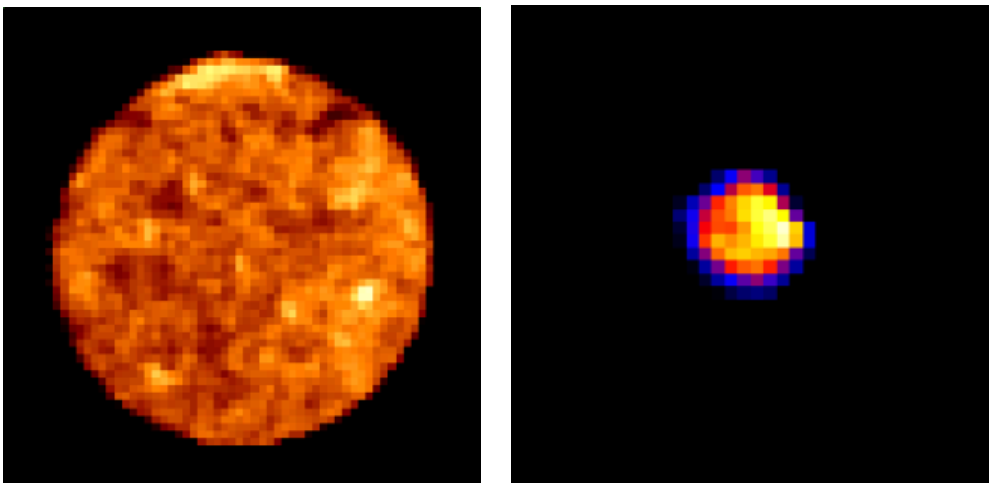

Figure 2.4: Example of a Sun and a Cas A images acquired with SRT at 18.8 GHz on 09/10/2019.

Table 2.3: List of the solar maps acquired with SRT analysed in this work

Epoch (DD/MM/YYYY)	Time (UT)	Freq (GHz)
29/10/2020	10:17-12:01	18.8
09/10/2019	11:46-13:30	18.8
09/10/2019	09:14-10:58	24.7
17/05/2019	08:40-10:24	25.5
17/05/2019	10:25-12:10	25.5

We performed another session on 28/01/2020, but the maps showed some kind of unexpected error in the synchronization of the celestial coordinates for some pixels (Fig. 2.5)

2.5.2 Data processing method

In order to produce our images we used SDI (see Sec 2.2 and Egron et al. 2017, Loru et al. 2019, Pellizzoni et al. 2019, Marongiu et al. 2020, Loru et al. 2021, Marongiu et al. 2022 and

Table 2.4: List of the Cas A maps acquired with SRT analysed in this work

Epoch (DD/MM/YYYY)	Time (UT)	Freq (GHz)
29/10/2020	12:07-12:56	18.8
29/10/2019	13:21-13:59	18.8
09/10/2019	13:40-14:37	18.8
09/10/2019	14:41-15:40	24.7
17/05/2019	13:03-14:08	25.5

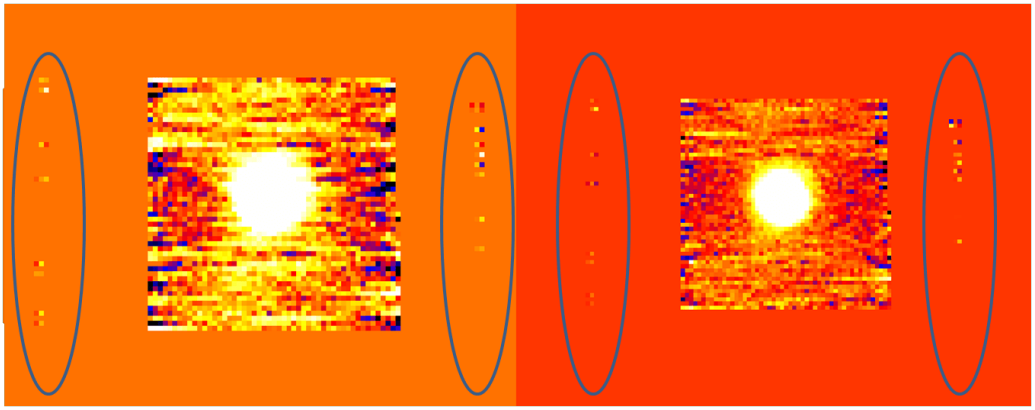

Figure 2.5: Synchronization problems of the celestial coordinate for some pixels outside the map boundaries in a Cas A image acquired on the 28/01/2020 at 18.8 Ghz.

Pellizzoni et al. 2022 for details and applications). The output files are generated as FITS images, which are suited to be further analysed with standard astronomy tools.

SDI performs an automated baseline subtraction of radio background scan by scan, using different methods adapted to each specific imaging target (see Egron et al. 2017; Loru et al. 2019, 2021). For the solar maps we adopted a simple yet robust method: a linear approximation of the baseline taken by connecting the minimum values at the beginning and at the end of the scan. For Cas A instead we used a more sophisticated baseline subtraction method due to the lower source signal (see e.g. Egron et al. 2017, Loru et al. 2019).

The K-band is influenced by a few RFIs, however the sky opacity takes an important role in the final quality of the maps. The opacity can come from different sources: the Ionosphere, the Troposphere, transient events such as clouds and fog (Nasir et al. 2013). Even without clouds and rain, the absorption and re-emission of microwave radiation is significant above 20 GHz, with a peak at 22.235 GHz in correspondence to the water vapour absorption line (Wentz and Meissner 2016).

SRT is equipped with an atmospheric monitoring and forecasting system (Buffa et al. 2016) mainly composed of a local area model based on the Weather Research and Forecasting Model[17] and a microwave radiometer. The first one gives the atmosphere and weather forecast every 3 hours starting from 00:00 UT up to 48 hours in advance. The latter provides real-time radiometer data at different time intervals from 1 to 100 GHz. For our calculations we decided to use the values from the radiometer, because even if the theoretical model gives values at a more precise frequency, the data are characterised by a large bandwidth, therefore we gave priority to a value with a more precise time interval. The only exception was the 29/10/2020 data since the radiometer was malfunctioning. We used a normalized gain curve with a τ factor to correct the raw counts before the calibration procedure and take into account not only the gain loss due to target elevation, but also the weather conditions.

To cross check the solar images processed by SDI, we used the new Python package SDT;

[17] https://www.mmm.ucar.edu/weather-research-and-forecasting-model

moreover, we carried out the automatic data analysis of solar images through SUNDARA (see Sec 2.2).

2.5.3 Data analysis

We used the imaging tool SDI and paired the calibrators and Sun maps at the same frequencies and epoch. For example, on the 29/10/2020 we have two Cas A maps at 18.8 GHz and one solar map at the same frequency. We obtained two different values of QS using the two calibrator maps on the same solar image. In the opposite case, e.g. on the 17/05/2019, we have two solar maps and only one Cas A image. We again, obtained two different values for the QS by pairing the calibrator map with the two different target images. The steps needed to obtain the value of the calibrated QS with the SDI pipeline are the following ones:

- generate a Cas A quicklook map by executing the command **`sd_ql`**;
- extrapolate the total counts from the left and right circular polarised images of Cas A with the program SAOImageDS9. One must use the same extracting region for both channels in order to obtain a coherent result. In order to obtain coherent measurements on the QS values, we decided to use *standard* extracting regions depending on the frequency, which are reported in Tab. 2.5;
- produce a Sun quicklook map by executing the command **`sd_sun_ql`**;
- without moving the file from the working directory, the user should run the command **`.r sd_sun_abscal_SaraM.pro`**;
- once compiled, the user can launch the program **`sd_sun_abscal_SaraM, c_freq, counts_0, counts_1, epoch, CasA_pixel`**, where *c_freq* is the central observing frequency expressed in GHz, *counts_0* and *counts_1* are, respectively, the Cas A total counts extrapolated from the left and right circular polarization image, *epoch* refers to the exact time at which the observing session has taken place, and finally *CasA_pixel* is the dimension of the Cas A map pixel expressed in arcmin. It is important to note that the program takes into account the most recent input parameters file uploaded with the command **`sd_init, 'inputpars_file'`**;
- if the procedure has been executed correctly, the QS value for the left and right circular polarizations, and the total intensity will be printed on the terminal.

If the users want to upload a new inputpars_file, they should run again the **`sd_init, 'inputpars_file'`** command and compile again **`sd_sun_abscal_SaraM.pro`**.

To obtain the calibrated map in units of brightness temperature ($T_{b\,i}$), it should be taken into account that in K-band the SNR Cas A appears as an extended source, so the absolute calibration procedure utilizes slightly different equations compared to a more traditional procedure with a point-like calibration source. The final expression written in our pipeline (Eq 2.9) is not an intuitive formula, therefore in the following its mathematical derivation is described. The maps are produced in counts per beam as a default value. However, from a scientific point of view we are more interested in a map expressed in counts per pixel, so to have, after the calibration, the precise flux contained in each map pixel. The passage from the two unit of measurements involves the ratio between the beam solid angle (Ω_{bm}) and the pixel solid angle of the map (Ω_{pix}):

$$C_i^{pix} = \frac{\Omega_{pix}}{\Omega_{bm}} C_i^{bm} \tag{2.2}$$

where C_i is the source counts for each pixel i in the image and *pix* or *bm* indicate if the counts are expressed over a pixel or over a beam. From Eq. 2.2 it can be seen that $\sum_i C_i^{bm} \neq \sum_i C_i^{pix}$. These relations are valid for both Cas A and the Sun.

$$C_i^{CApix} = \frac{\Omega_{pix}^{CA}}{\Omega_{bm}} C_i^{CAbm} \tag{2.3}$$

$$C_i^{SUNpix} = \frac{\Omega_{pix}^{SUN}}{\Omega_{bm}} C_i^{SUNbm} \tag{2.4}$$

where *CA* and *SUN* refer to the Cas A and Sun quantities.

We obtain the flux (Jy) contained in each pixel of a Sun map (S_i^{SUN}) by multiplying each pixel counts with the conversion factor (f), defined as the ratio between the total Cas A flux from the literature (S_{tot}^{CA}) and the the Cas A total counts expressed per pixel (C_{tot}^{CApix})

$$S_i^{SUN} = f\, C_i^{SUNpix} = \frac{S_{tot}^{CA}}{C_{tot}^{CApix}} C_i^{SUNpix} \tag{2.5}$$

If we express again the counts per pixel in counts per beam by using Eq 2.4, we obtain a formula where the beam solid angle is not needed anymore:

$$S_i^{SUN} = \frac{S_{tot}^{CA}}{C_{tot}^{CAbm}} \frac{\Omega_{bm}}{\Omega_{pix}^{CA}} \frac{\Omega_{pix}^{SUN}}{\Omega_{bm}} C_i^{SUNbm} = \frac{S_{tot}^{CA}}{C_{tot}^{CAbm}} \frac{\Omega_{pix}^{SUN}}{\Omega_{pix}^{CA}} C_i^{SUNbm} \tag{2.6}$$

To obtain the brightness temperature in each pixel ($T_{b\,i}$) we use the Rayleigh-Jeans approximation:

$$T_{b\,i} = \frac{c^2}{2\,\nu^2 k_B \Omega_{pix}^{SUN}} S_i^{SUN} \tag{2.7}$$

where c the light speed, ν is the observing frequency and k_B the Boltzmann's constant. By combining Eq 2.6 with Eq 2.7:

$$T_{b\,i} = \frac{c^2}{2\,\nu^2 k_B \Omega_{pix}^{SUN}} \frac{S_{tot}^{CA}}{C_{tot}^{CAbm}} \frac{\Omega_{pix}^{SUN}}{\Omega_{pix}^{CA}} C_i^{SUNbm} \tag{2.8}$$

we can see that the information on the Sun pixel solid angle of the map is no longer necessary. Finally, we obtain the final formula we use in our solar pipeline

$$T_{b\,i} = \frac{c^2}{2\,\nu^2 k_B} \frac{S_{tot}^{CA}\, C_i^{SUNbm}}{C_{tot}^{CAbm}\, \Omega_{pix}^{CA}} \tag{2.9}$$

All the values expressed in Eq 2.9 can be found directly from the literature or through our data, except from S_{tot}^{CA}. There are no calibrated empirical measurement at our frequency. In addition, the source is in continuous expansion. As the SNR evolves, its flux decrease appreciably over a short period of time, only a few years.

In order to obtain the theoretical flux to compare with the counts from the maps, we took two steps: we extrapolate the flux at our frequencies from a model Vinyaikin 2014 and then we recalculate the value at our epoch of interest. The Cas A fit was obtained by gathering empirical value of the SNR flux from different works that cover several decades and frequencies from MHz to GHz (for further information, see Vinyaikin 2014). All the

values were brought to a standard epoch (2015.5) by using a formula which expresses the secular variation of the radio flux of Cas A as a function of frequency:

$$d_\nu[\%year^{-1}] = -(0.63 \pm 0.02) + (0.04 \pm 0.01)\, ln(\nu) + (1.51 \pm 0.16) \cdot 10^{-5}(\nu)^{-2.1} \quad (2.10)$$

where the frequency ν is expressed in GHz and ln indicates the natural logarithm. The final expression they obtained for the fitted curve of the Cas A spectrum at the 2015.5 epoch is:

$$S_\nu^{CasA}(2015.5) = S_0 \nu^{-\alpha+\beta\, log_{10}\nu} e^{-\tau_0\, \nu^{-2.1}} \quad (2.11)$$

where $S_0 = 2190.294\ Jy = S^{CasA}_{\nu=1\,GHz}(2015.5)$, $\alpha = 0.752$, $\beta = 0.0148$ and $\tau = 6.162 \cdot 10^{-5}$.

Table 2.5: Standard selection region for each central frequency (ν_{obs}). The *center* is indicated in Right Ascension and Declination coordinates while the *radius* of the circular region is expressed in degrees.

ν_{obs} [GHz]	Center [AR/Dec]	Radius [degree]
18.8	23:23:27.567 +58:48:43.424	0.1234114
24.7	23:23:27.310 +58:48:49.582	0.1357700
25.5	23:23:25.094 +58:48:38.732	0.1199118

2.5.4 Results

In Fig. 2.6 and Tab 2.6 the QS absolute calibration values obtained after the implementation of the procedure are reported. The errors were calculated taking into account different contribution sources (see Sec 2.6) and they were propagated appropriately in order to calculate the final value for each frequency.

Table 2.6: QS brightness levels obtained from the absolute calibration procedure; ν_{obs} is the central observing frequency; *Cas* A_f lists the SNR Cassiopeia A integrated fluxes (and related observation epochs); T_{QS} is the measured QS brightness temperature; *Err* lists the percentage and absolute error obtained after our calculations; Fit_{dev} expresses the deviation from the expected value extrapolated from Landi and Chiuderi Drago 2008 in percentage and in K.

ν_{obs} [GHz]	*Cas* A_f [Jy]	T_{QS} [K]	Err [%]	Err [K]	Fit_{dev} [%]	Fit_{dev} [K]
18.8	247.9 ± 5.7 (Oct–2020)	10099	1.53	154	0.24	24
24.7	205.3 ± 4.8 (Oct–2019)	9799	2.74	268	3.24	308
25.5	201.1 ± 4.7 (May–2019)	9764	2.28	223	3.65	344

Our measurements are in good accordance with the fit from Landi and Chiuderi Drago 2008, with a maximum deviation of 3.7% and a mean relative error of 3% of our measurements for all the investigated frequencies. We are within 2 σ of deviation from the theoretical values.

The deviation from the Landi and Chiuderi Drago 2008 work at the higher frequencies could be explained in different ways. We may need better weather conditions during the observation, since the radio wave absorption is more important at 25.5 and 24.7 GHz (Wentz and Meissner 2016). In alternative, the deviation could be of physical origin. In the work of Landi and Chiuderi Drago 2008 there is a lack of empirical measurements in the K-band and the measurements at higher frequencies are more scattered than those at lower frequencies (10-20 GHz interval). The data from Fedoseev and Chernyshev 1998 (above ∼35 GHz) were carefully selected, but they could not provide an accurate measure of the QS (Landi and

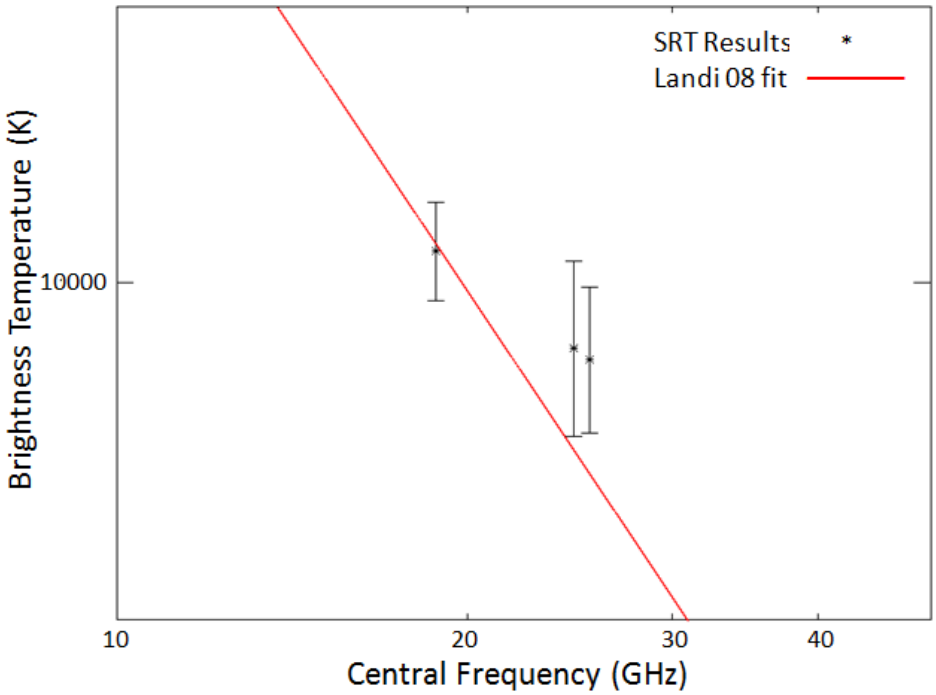

Figure 2.6: SRT value obtained with the absolute calibration procedure (asterisks) compared to the Landi and Chiuderi Drago 2008 fit (red line).

Chiuderi Drago 2008), resulting in a large scattering. With more precise data we managed to better constrain the QS value suggesting a flatter trend in the spectrum at high frequencies compared to the fit. However, our measurements are within 2σ from the theoretical brightness temperature. More data are needed to confirm if the deviation from the Landi and Chiuderi Drago 2008 fit is significant at 24.7 and 25.5 GHz.

At 18.8 GHz we have an almost perfect accordance with the theoretical value and the smaller relative error. For this frequency we had more QS calibrated values and the weather conditions had a lower impact on our final results.

In general, the deviation within 2 σ of our measurements from the Landi and Chiuderi Drago 2008 work, is a strong indicator of the trustworthiness of our method of using Cas A as a solar calibrator source.

2.6 Absolute calibration uncertainty study

The absolute calibration procedure is a complex method which involves several non-trivial steps. There are several kind of error sources to take into consideration, having a different impact on the final results that need an accurate assessment. In the following sections, we are going to analyse the most important error sources.

2.6.1 Baseline subtraction method

As described in Sec 2.5.2, we used an automated tool with a linear approximation in order to perform the baseline subtraction. If the background is not successfully eliminated in the Cas A map, the final QS value would be subjected to an error, since an excess amount of counts would be included in the conversion factor expressed in Eq 2.5, leading to an underestimation and error in the final QS evaluation.

To quantify the uncertainty induced by the procedure, we performed again the QS

absolute calibration measurement adopting different baseline subtraction parameters. In this case the Cas A extracting region included as much background as possible (e.g. Fig. 2.7 right panel) and compare the result with Tab 2.6. In an ideal case, the background has a zero mean, within the errors, therefore the counts from the background should not lead to a remarkable change in the QS final value.

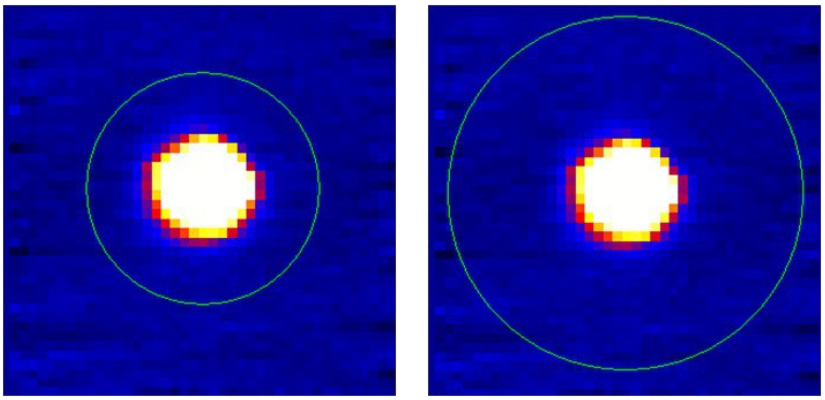

Figure 2.7: Comparison of different extracting regions on the same Cas A map (29/10/2020 at 18.8 GHz, Feed 0 left circular polarization): left panel, a standard region from 2.5, right panel, a region with as much background as possible.

For some maps it worked fairly well, the error on the QS measurements was less than 1%. However, for others, this value went up to 7%, which indicated that we needed a more precise algorithm. We introduced a more refined baseline subtraction procedure, with a series of iteration in order to identify better the linear approximation of the baseline. This method led to a decrease in the error on the QS measure, which varies from 0.24% to a maximum of 1.56%. We tried to use further more refined iterative methods, but they did not improve significantly the final result.

The results reported in Tab 2.6 were obtained with the improved baseline subtraction method.

2.6.2 Sky opacity contribution

As said in section 2.5.2, the K-band is affected by several atmospheric and environmental factors that contribute to the signal attenuation (see Nasir et al. 2013, Wentz and Meissner 2016, Navarrini et al. 2022). If the τ value changes remarkably during the acquisition of a map, it will manifests as a temperature gradient or stripes in the final image, like, e.g., in Fig. 2.8. The data from Tab 2.3 and 2.4 do not present such features, indicating that the weather conditions were stable during the observation of each map.

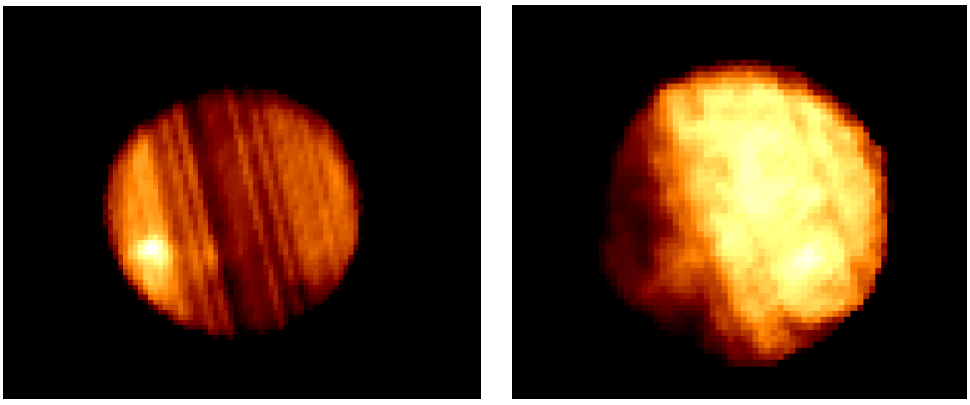

Figure 2.8: Examples of stripes (left panel) and temperature gradients (right panel) in a solar maps due to sudden changes in the weather conditions during the data acquisition.

In order to estimate an error induced by an undetected change in the weather conditions, we decided to use the values extrapolated from the theoretical model of the SRT forecast system (see Buffa et al. 2016) to be compared with the observed radiometer values. We derived sky opacity errors by analysing the scatter between these two different sources of sky opacity information. The final percentage error related to the sky opacity uncertainties varies in a range of 1% –1.6%.

It is worth noting that the sky opacity effects cannot be neglected in the analysis even in case of good weather conditions. Without considering the τ correction factor in the gain curve, the error induced by the opacity contribution in the QS calculation rises up to 6%.

2.6.3 Cas A spectral fit

For the Cas A spectrum expressed in equation 2.11, the Vinyaikin 2014 work provides a spectrum fitting of $\chi^2/(n-4) = 0.91$, without error estimation. The measurements used in the model closest to the K-band (between about 13-33 GHz, Tab 2.7) are affected by an error between 0.3% and 4.2%.

Table 2.7: Cas A integrated fluxes ($CasA_f$) in the 13-33 GHz frequency range used in the SNR spectral fit model from Vinyaikin 2014 referred to 2015.5 epoch; ν_{obs} is the central observing frequency.

ν_{obs} [GHz]	$CasA_f(2015.5)$ [Jy]	Reference
13.5	313.0 ± 13.0	O'Sullivan and Green 1999
15.5	283.0 ± 12.0	O'Sullivan and Green 1999
16.5	273.5 ± 7.5	O'Sullivan and Green 1999
22.7	219.7 ± 3.0	Weiland et al. 2011
32.9	169.4 ± 1.8	Weiland et al. 2011
33.0	171.6 ± 0.6	Hafez et al. 2008

We calculated the mean value, 2.3%, and used it as the relative error of the Cas A theoretical flux in the K-band. In perspective, it could be useful to perform independent flux measurements of Cas A with SRT and Medicina to better assess them in the frequency range of solar observations, without relying on the sparse literature data in K-band.

2.6.4 Secular decrease formula

To obtain the uncertainty induced by Eq 2.10 we firstly recalculated it by adding (Eq 2.12) and subtracting (Eq 2.13) the errors for each factor in the formula indicated in Vinyaikin 2014. We used the two equations to calculate the total flux of Cas A at our epoch for both formulas. By comparing the final values, we calculated the relative error induced in the final QS value: 0.23%.

$$d_\nu[\%year^{-1}]_{MAX} = -(0.65) + (0.05)\, ln(\nu) + (1.67) \cdot 10^{-5}(\nu)^{-2.1} \tag{2.12}$$

$$d_\nu[\%year^{-1}]_{MIN} = -(0.61) + (0.03)\, ln(\nu) + (1.35) \cdot 10^{-5}(\nu)^{-2.1} \tag{2.13}$$

2.7 Calibration problems and issues

Our absolute calibration results were very stable during the first years of SunDish observations (2018-2020). However, from the beginning of 2021 we experienced some unusual and

unexpected changes in our results: we found a deviation $\geq 3000K$ from the theoretical and our empirical values from Tab 2.6. In Tab 2.8 are reported the values obtained with the new observing session with the SRT through the 2021 year.

Table 2.8: QS brightness levels obtained from absolute calibration procedure in year 2021. ν_{obs} is the central observing frequency; T_{QS} is the measured QS brightness temperature; Fit_{dev} expresses the percentage deviation from the expected value extrapolated from Landi and Chiuderi Drago 2008.

Epoch (DD/MM/YYYY)	Freq (GHz)	T_{QS} [K]	Fit_{dev} [%]
11/06/21	18.8	11986	18.4
11/06/21	24.7	11345	19.5
05/05/21	22.8	11314	17.0
05/05/21	22.8	11128	17.2
01/04/21	18.8	12883	27.3
01/04/21	24.7	11689	23.2
04/03/21	18.8	19427	91.9
04/03/21	24.7	13209	28.4
12/02/21	18.8	13126	29.7
12/02/21	24.7	13055	37.6
02/02/21	18.8	13065	29.1
02/02/21	18.8	13673	35.1
02/02/21	24.7	13528	42.5

We started to investigate the possible causes for these anomalies. Our first hypothesis was a malfunction in the software caused by some changes in the code or updates. We ruled out this option by testing the same pipeline on 2019-2020 data and obtaining the same results as in Tab 2.6.

We can consider a possible physical origin. Semi-ARs seem to cover most of the solar disk area in some sessions. Thus, we noticed that the measured QS value could apparently fluctuate by a few hundreds K due to the increasing presence of the semi-ARs as the solar cycle is heading towards its maximum. However, the deviation reported in Tab 2.8 are irregular and of a thousand K from the expected values (an order of magnitude higher than semi-ARs contributions). We do not exclude a possible contribution of a more active active solar network, although, we think it is unlikely that such a sudden and remarkable change could come mostly from the relatively low-flux semi-ARs.

We then contemplated the possibility of a problem in the instrumental setups. As said in Sec 2.1, observing the Sun is a risky task if the instrumentation is not prepared against thermal and electromagnetic damages. The optomechanics and front-end require additional attenuation setups to guarantee instrumentation safety, ensure a linear response to the strong solar input signal impacting the systems amplification chains, and avoid electronic saturation Pellizzoni et al. 2022. Until the end of 2020, we verified that the typical variability of solar phenomenology in K-band was compatible with the available instrumental dynamic range (see Pellizzoni et al. 2019, Iacolina et al. 2019), as well as the calibration source Cas A. From 2021 some new strong interferences of unknown origins started to appear in our observations. The attenuation setups were adjusted to ensure the safety of the instrumentation. However, the new setups may have been too strong and the weaker SNR could have been attenuated too much, falling out from the instrumental dynamic range. In particular, an excessive signal attenuation could have lead to an underestimation of the calibration source counts, which in return produces an overestimation of the source flux, as it can be deduced from Eq 2.5.

Another possibility comes from the Low Noise Amplifiers (LNA) deterioration. The result could be similar to that resulting from an excessive attenuation setup, with an overestimation

of the target source signal. We also verified if these phenomena were connected to the observing elevation. We did not find a clear correlation with the anomalies.

In summary, it is plausible that the apparent QS excess temperature during 2021 could be due to a combination of a non optimal attenuation setup and LNA deterioration, with a possible minor contribution of the increasing network solar activity. New observations are needed to confirm our hypothesis.

2.7.1 Early Spectro-Polarimetric observations at Medicina

A first opportunity to shed some light to the 2021 calibration anomalies with SRT comes with the new observations made at the Medicina Radio telescope with SARDARA (Melis et al. 2018), the same back-end used for solar imaging at SRT. It is worth noting that before this new implementation, Medicina provided Total-Power solar observations, contributing to most part of the Pellizzoni et al. 2022 solar catalog. Unfortunately, these data did not allowed us to perform absolute calibration due to the relatively limited dynamic range in the Total-Power configuration.

A preliminary analysis of the new Medicina spectro-polarimetric data provided some interesting results from an absolute calibration of a solar map (2.9 left panel) acquired on the 28/06/2022 at 18.7 GHz (Tab 2.9). For this observing session we carefully selected a set of conservative attenuation parameters in order to guarantee a linear response in the lower part of the dynamic range (including Cas A flux).

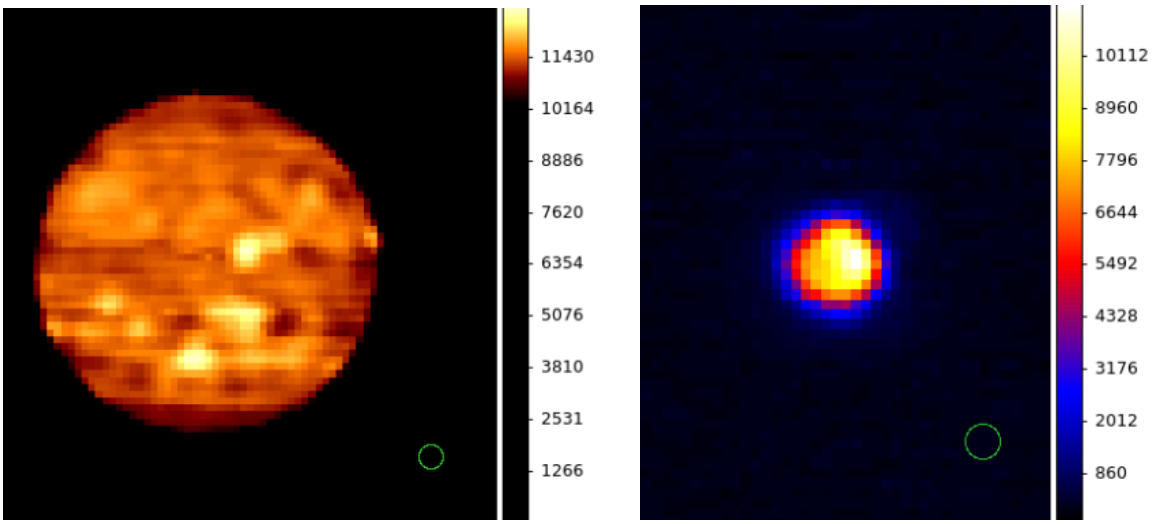

Figure 2.9: Sun (left) and Cas A (right) images acquired with Medicina on 28/06/2022 at 18.7 GHz with SARDARA back-end. The colour bar in the solar map (left panel) is expressed in kelvin, while the one for Cas A (right panel) is in counts. Both maps have 0.6 arcmin resolutions. The green circle represents the Medicina beam: 2.01 arcmin.

Table 2.9: QS brightness levels obtained from absolute calibration procedure with data acquired with the Medicina Radio Telescope on the 28/06/2022 at 18.7 GHz. T_{QS} is the measured QS brightness temperature; Fit_{dev} expresses the percentage deviation from the expected value extrapolated from Landi and Chiuderi Drago 2008.

Channel	T_{QS} [K]	Fit_{dev} [%]
Left circular polarization	11527	13.7
Right circular polarization	10085	0.5
Total Intensity	10806	6.6

The first thing we noticed was the almost perfect accordance with the Landi and Chiuderi Drago 2008 fit for the right circular polarization channel, which we did not see in the 2021

data acquired with SRT. This results strengthen the hypothesis that most problems in the 2021 SRT observing sessions could be related to LNA deterioration and/or a not optimal configuration of the attenuation setups.

The left circular polarization channel presents a deviation $> 10\%$, which is less than any result reported in Tab 2.8, but still higher than the results from Tab 2.6. The difference with the left circular polarization could comes from the LNA deterioration even at Medicina or a not ideal selection in the attenuation setups. We took into consideration a physical origin, but as we reported in Sec 1.3.3, the QS is mostly thermal bremsstrahlung in LTE (Shibasaki et al. 2011) and as stated in Dulk 2001, this emission mechanism has a near zero circular polarization. We can consider the semi-AR from Kallunki et al. 2020, however we still have not enough evidence to support this hypothesis.

This result comes from only one map, therefore is not enough to reach a definitive conclusion, but it contains precious information to help us in planning new observing sessions.

2.7.2 Future strategies

In this Chapter we obtained unprecedented and very precise calibrated measurements of the QS in the K-band with an error of $\sim 3\%$. This result can be further improved by new observation campaigns and the refinement of the procedures described in this Thesis.

Through an accurate error analysis we verified the trustworthiness of the SNR Cas A as a solar calibrator, provided that the amplification chain is properly working, the attenuation setups are correctly selected and the source is within the instrument dynamic range.

This is an extremely important results, since Cas A could be one of the few calibration sources visible at higher frequencies where the opacity has an even greater impact on the map quality. In the future we are also planning to go lower than 10 GHz in frequency where the Landi and Chiuderi Drago 2008 fit is not anymore valid, therefore the absolute calibration with Cas A will be even more crucial to obtain the physical information we need for our studies.

For our future observing sessions and analysis we will pay particular attention to the critical aspects we identified during these years:

- we will try different attenuation setups and determine the ideal parameters to include into the instrument dynamic range both the strong and weak sources;
- at present SRT is under extraordinary maintenance due to major upgrades[18]. In the near future, the SRT and Medicina Radio Telescope LNA will be replaced. We will then be able to study the impact their deterioration had on our maps;
- we plan to make other observing sessions with the aim of obtain new calibrated QS measurements and to examining the possible contribution of the semi-ARs in the results;
- we are developing in the SUNPIT pipeline a specific tool for the automatic calibration of the Sun with Cas A to simplify this procedure for an external user.

We will also investigate new possible anomalies and error sources, like the QS flux contributions from the beam secondary lobes in presence of strong ARs that were absent during the solar minimum, but could become more important with the rising solar activity.

[18] http://www.ponricerca.gov.it/comunicazione/esempi-di-progetto/potenziamento-infrastrutture-di-ricerca/srt_highfreq-potenziamento-del-sardinia-radio-telescope-per-lo-studio-delluniverso-alle-alte-frequenze-radio/

Chapter 3

Total intensity data analysis

During the first three years of the SunDish project, that included early development and observing test stages (early 2018 – December 2020), we acquired and analysed 169 solar maps with Medicina and SRT (see Appendix A). The resulting solar images are available for inspection and download in the web site dedicated to the project[1] and regularly updated.

In the first release of the image catalogue, about 20 % of the solar maps were significantly affected by RFI contamination, instrumental anomalies and/or by bad weather conditions: poor or variable sky opacity during the observations (e.g. $\tau \gtrsim 0.1$ and/or fluctuation $\Delta\tau \gtrsim 0.01$ at 18 GHz). Despite these images are still suitable for a rough estimate of AR parameters and fluxes, they typically display significant artificial brightness gradients in the QS component (see e.g. Fig 2.8) that prevent accurate calibration and affect the measurement of $\sigma_{\rm disk}$ (see Appendix A). On the other hand, about 80 % of our images sample (*high/medium quality* entries in the archive) provided typical sensitivities of a few kelvin, well below the observed physical solar disk brightness fluctuations (> 60 K), and then were suitable for accurate calibration and robust brightness and spectral analysis.

As illustrated in Chapter 2, the application of the calibration factor f (Eq 2.5) back-end counts, obtained from the peak of a Gaussian fit of the QS histogram (see Fig 2.3), provides an estimate of the QS brightness temperature at the observed frequencies. This fit is not significantly affected by ARs contributions near solar cycle minimum. We applied this procedure to a selected SRT observations with optimal weather conditions for both the calibrator Cas A and the solar map (see Sec 2.5). The Cas A flux was extrapolated to our observing epochs and frequencies from Vinyaikin 2014. We provided an accurate error analysis considering the propagation effects of different uncertainties in the calibration process: Cas A flux errors with an overall calibration errors depend on frequency and range between 1.5 and 3 % (see Sec 2.6). In this Chapter, I am going to develop the data analysis starting from the results obtained in Chapter 2.

3.1 Morphology of the obtained solar maps

The sensitivity of the obtained solar images is calculated through the background fluctuations of the brightness temperature, measured in map regions far from the solar disk emission. Image sensitivities (RMS) are typically in the range 0.7–8.5 K for Medicina and 0.1–0.3 K for SRT. Due to disk bleeding into the broad wings that slightly affects also the edge of the maps, these RMS estimations represent an upper limit of the actual image sensitivity. On the other hand, instrumental noise on the very bright solar disk is typically about an order of magnitude higher than the image sensitivity.

[1] https://sites.google.com/inaf.it/sundish

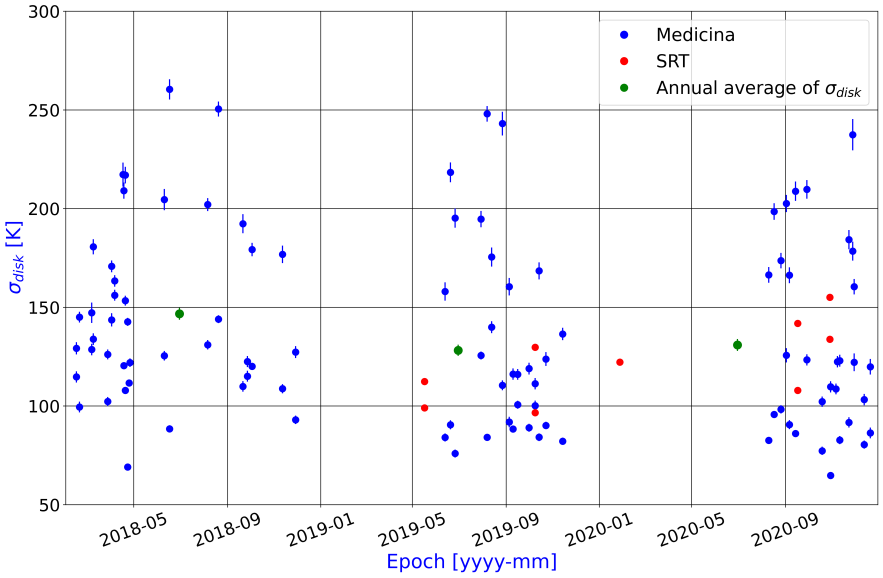

Figure 3.1: Temporal evolution of the width values σ_{disk} of the Gaussian-like shape in the histogram of brightness distribution among pixels depicted in Figure 2.3 (*orange line*). σ_{disk} represents the standard deviation of the solar disk brightness distribution with respect to the QS level reported in Table 2.6 (only measurements related to medium/high-quality images are reported in the plot). *Green circles* indicates the annual average of σ_{disk} (Pellizzoni et al. 2022).

The fit of QS brightness distribution provides σ_{disk} values (see Appendix A) higher (> 60 K) than the typical image sensitivity. These fluctuations are mostly of physical origin and possibly related to the solar activity level. In particular, the analysis of the local radiometric information allows us to estimate the apparent weather-related brightness temperature fluctuations on the solar disk. During typical observations in good/optimal weather conditions (high-quality maps) and for a typical observing period of 3 hours, these fluctuations are < 6 K at 18.8 GHz and < 18 K at 25.5 GHz. The worst case during the observations can sporadically reach apparent weather-related brightness temperature fluctuations of about 100 K, significantly overlapping with actual physical fluctuations. In these cases the effect of sky opacity fluctuations on the image is evident due to striping features (related to the OTF scanning procedures) and very different from the morphology of actual physical fluctuations on the disk (unrelated to the scanning pattern). A temporal evolution of σ_{disk} is plotted in Figure 3.1. The analysis of the possible variability of this parameter during the solar cycle requires long-term monitoring.

3.2 Data processing

the obtained scientific data products rely on calibrated brightness images of the Sun atmosphere in the K-band, centered at the solar centroid ephemeris. Image production and calibration are performed using SDI (see Sec 2.2). The core of our procedure is to fully exploit the availability of a significant number of measurements per beam (higher than Nyquist requirement) that allows us to optimize the spatial resolution with pixel size typically chosen to be about 1/4 of the Half Power Beam Width (HPBW). This oversampling permits to have a straightforward evaluation of statistical errors (through standard deviation of the measurements in each pixel), efficient RFI outliers removal and accurate background baseline subtraction. As in Chapter 2, we used SDT as a cross-check for data analysis. The major steps/procedures involved in our data processing pipeline are described in the following sections, while the tools used for scientific data analysis are reported in Sec 2.2 (for further information about our solar pipeline, see Marongiu et al. 2022).

A spectral RFI flagging, based on automated search for outliers in each scan-sample spectrum, is available for SRT when observing with the spectro-polarimetric back-end. This has been proved to be an effective method for RFI removal (see, e.g., Loru et al., 2021). However, such automated search is not available when observing with Total Power/Intensity back-ends, such as that in use at Medicina. Therefore, for most of our observations, we provide an alternative automated spatial RFI flagging procedure that consists in splitting the map into sub-regions, which correspond to adjacent solid angles in the sky. These areas have to be smaller than the beam size (typically 1/4–1/5 of HPBW) in order to avoid discarding actual fluctuations from the source, but large enough to include a significant (typically >10) number of measurements. The outlying samples presenting a count level above a standard deviation-based threshold (typically 5σ level above average) are then flagged as RFI. An additional manual/interactive RFI flagging process is then applied to remove residual artifacts. Through the above procedures, we were able to remove most of the RFI features in the images (e.g. stripes due to commercial ground-based or satellite radio links) affecting a growing fraction of our data.

Automated baseline subtraction of radio background is performed scan by scan by SDI, using different methods adapted to each specific imaging target (see Egron et al., 2017; Loru et al., 2019, 2021). Since weak solar emission is still detected over 2 degrees from the Sun centroid (well outside our typical mapping sizes), we could in principle model the outer brightness profiles through polynomial functions assuming the asymptotic value of such a fit as the background baseline. In fact, even a naive linear approximation of the baseline trivially taken by connecting the minimum values at the beginning and at the end of the scan, yield negligible discrepancies (<0.1% errors) in the image sensitivity, with respect to the above more complicated procedure. We adopted this simpler yet robust method in our data processing pipeline for the analysis of the bright solar disk emission.

3.3 ARs fluxes and spectra

Spots of enhanced radio emission due to ARs are present in most ($\sim 80\,\%$) of our 2018–2020 data set, even around the epoch of solar cycle minimum. The identification of the ARs and the definition of their parameters – e.g. the calculation of their fluxes and spectra – is a non-trivial task. It requires specific tools for pattern recognition and well-defined conventions in order to proficiently share data for multi-wavelength exploitation together with other very different solar imaging instruments.

We performed these operations through the implementation of SUNDARA (see Sec 2.2), adapted for our purposes from Marongiu et al. 2020. It is based on several Python packages, such as Photutils, usually adopted for detecting and performing photometry of astronomical sources (Bradley et al., 2019), and SunPy, an open-source package for solar data analysis Mumford et al., 2020. SUNDARA receives as input the solar images (in standard FITS format) provided by the data processing pipeline described in Sec 2.2, and in a few minute processing time it provides the identification of ARs and the estimation of their brightness temperatures, fluxes and spectral indices.

The SUNDARA procedure unearths AR candidates rising from the QS brightness level through different algorithms that search for patterns consistent with an elliptical 2D-Gaussian kernel (see Marongiu et al. 2021, for details). AR candidates are short-listed accordingly to a brightness threshold of $2\sigma_{\rm disk}$ (see Appendix A) of the QS level; this threshold was proven to avoid fake AR detection, providing enough sensitivity for the identification of known AR that are already included in public archives, and that typically exceeds the QS brightness level in our band of $T_{\rm ex} > 1000\ {\rm K} > \sigma_{\rm disk}$.

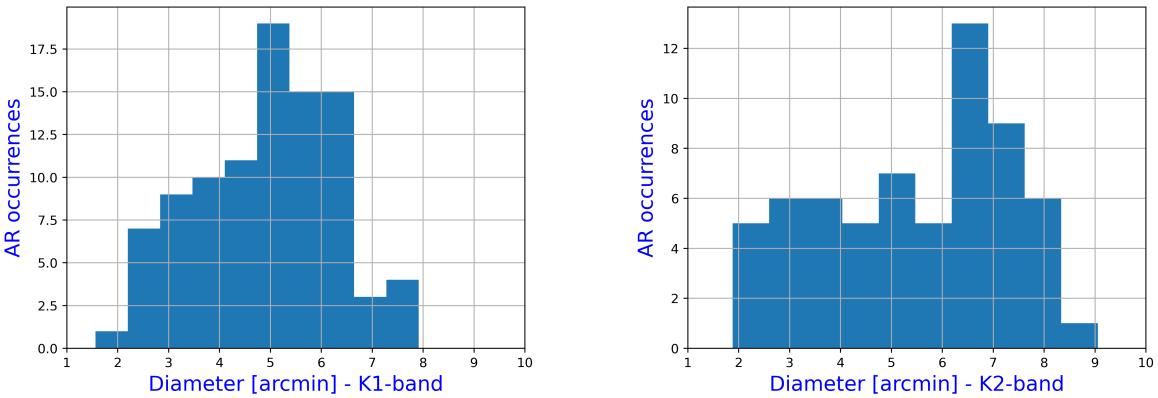

Figure 3.2: Histogram of AR mean diameters in the 18–23 GHz (K1-band, *left panel*) and 23–26 GHz (K2-band, *right panel*) frequency ranges (Pellizzoni et al. 2022).

Each AR candidate is then modelled through an elliptical 2D-Gaussian with noise, as described in Marongiu et al. 2020, where the free parameters are the AR helioprojective coordinates (Solar-X and Solar-Y; Thompson 2006), the amplitude (peak brightness), the size (semi-axes and rotation angle of the ellipse), and the background noise (related to QS level local fluctuations).

Considering that usually the size and location of ARs detected in radio domain have a good coincidence with those observed in the high-frequency part of the electromagnetic spectrum (e.g. Efanov et al., 1972; Righini-Cohen and Simon, 1977; Silva et al., 2005), ARs are then associated or identified in terms of spatial position with known features (if any) provided by the multi-wavelength standard catalog Heliophysics Event Knowledgebase (HEK, Hurlburt et al., 2012). These results applied to our first solar image catalog are included in "ar_id" column of Appendices B and C. To compare AR sizes with their parameters typically described in the literature (e.g. Silva et al., 2005), we conventionally take the mean diameter (expressed as FWHM, in units of arcmin) obtained through the sum of semi-axes of the elliptical 2D-Gaussian fit. A histogram of the AR mean diameters is depicted in Figure 3.2 for the 18–23 GHz (K1-band hereafter) and 23–26 GHz (K2-band hereafter) frequency ranges. These diameters are approximately the same at both radio bands as expected from our data resolution, and their values range from 1.6 to 9.1 arcmin, with a mean and standard deviation of 4.9 ± 1.4 arcmin at K1-band, and 5.5 ± 1.8 arcmin at K2-band, respectively. The average size and standard deviation of our ARs[2] are 30.4 ± 16.2 arcmin^2 for K1-band, and 37.8 ± 23.0 arcmin^2 for K2-band. These AR mean diameters are compatible with those obtained from other radio/mm observations (Silva et al., 2005; ValleSilva et al., 2020) with NoRH (17 GHz), ALMA (107 and 238 GHz, Wootten and Thompson, 2009), and the Solar Submillimeter Telescope (SST, 212 and 405 GHz, Kaufmann et al., 2008). Thus, ARs are typically resolved in our images.

The excess brightness temperature of ARs above QS levels, T_{ex}, is trivially defined as $T_b - T_{b(QS)}$, where T_b and $T_{b(QS)}$ are the maximum brightness temperature of the AR and the QS temperature, respectively. The error on T_b is provided by the calibration uncertainties described in Sec 2.6 ($\sim 3\,\%$ error on average, depending on frequency). Statistical errors are typically of the order of $\sim 0.1\,\%$ due to very high signal-to-noise-ratio ($> 10^4$) of solar disk brightness (typical image sensitivity < 10 K). The obtained T_{ex} distributions are reported in Figure 3.3. At both K1 and K2 bands, T_{ex} values range between ~ 200 and over 2000 K, with median values of 430 and 560 K at K1 and K2-band, respectively. AR emissions in our

[2]SUNDARA calculates the AR area considering the modeled 2-σ standard deviation along the semimajor/seminor axes of the 2D-Gaussian function for each AR candidate.

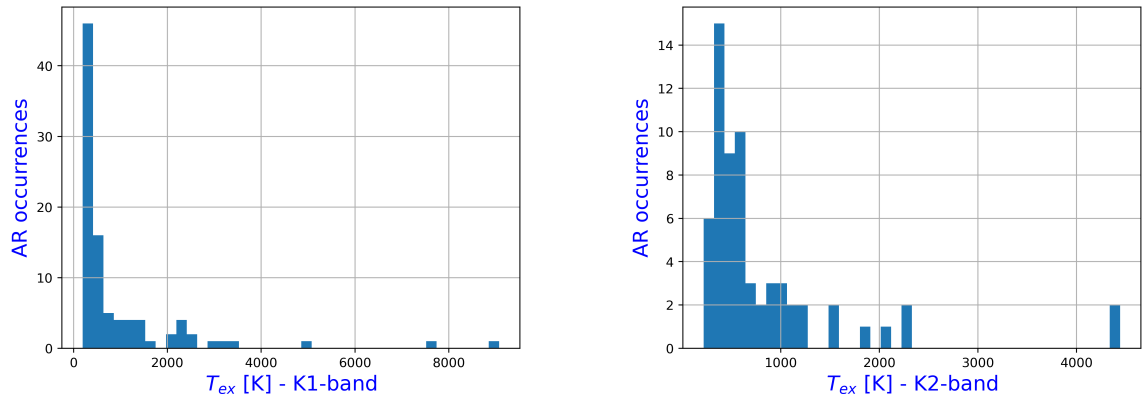

Figure 3.3: Histogram of the AR occurrences with excess brightness temperature T_{ex} above QS values in K1-band (18–23 GHz, *left panel*) and K2-band (23–26 GHz, *right panel*) (Pellizzoni et al. 2022).

2018–2020 data set exceed the QS brightness level up to a factor ~ 2, although the average T_{ex} is only $\sim 5\,\%$ of QS intensity (Pellizzoni et al. 2022).

The AR total fluxes $S_{\nu(\mathrm{AR})}$ (sfu units) are extracted from an elliptical region doubling the semi-axis of the 2D-Gaussian fit. They are calculated through the integration of the AR brightness inside that region. Together with their uncertainties, they are given by:

$$S_{\nu(\mathrm{AR})} = 10^{22}\frac{2k_B\nu^2}{c^2}\Omega_{\mathrm{pix}}\sum_{\mathrm{pix}} T_b \ [\mathrm{sfu}], \tag{3.1}$$

$$\sigma_{S_{\nu(\mathrm{AR})}} = S_{\nu(\mathrm{AR})}\sqrt{(\sigma_{f_{\mathrm{cal}}}/f_{\mathrm{cal}})^2 + (\sigma^{\mathrm{stat}}_{T_b}/ < T_b >)^2/N_{\mathrm{pix}}} \sim \frac{S_{\nu(\mathrm{AR})}\sigma_{f_{\mathrm{cal}}}}{f_{\mathrm{cal}}} \ [\mathrm{sfu}], \tag{3.2}$$

where N_{pix} the number of pixels (with solid angle Ω_{pix}) associated to the AR region, $\sigma_{f_{\mathrm{cal}}}/f_{\mathrm{cal}}$ the calibration fractional error, and $\sigma^{\mathrm{stat}}_{T_b}$ the statistical error corresponding to the image RMS.

In Appendix B we provided ARs peak brightness and fluxes (in units of sfu) both in terms of total emission (including the QS component contribution) and as spatially integrated brightness excesses with respect to the QS flux level; the AR flag "C" in the "Note" column indicates ARs located inside a confused region[3].

For the observations where AR brightness/flux information (including lower and upper limits) is available at two or three frequencies ($\sim$ 80 solar maps, characterized by high/medium quality), we provided spectral index ($S_\nu \sim \nu^\alpha$) measurements for ~ 90 ARs (see Appendix C). We performed the spectral index analysis of all the detected ARs comparing their peak brightness temperature with and without the inclusion of the QS component (see Figures 3.4 and 3.5, respectively); we also provided flux densities spectral index values (Figure 3.6). For the calculation of these latter values, we used the same extraction area for the fluxes estimated at different frequencies. As extraction area, we considered the minimum AR size detected among the same ARs identified at the same epoch (and radio telescope) at different observing frequencies; this criterion allows us to prevent possible biases due to overestimated AR sizes, possibly characterized by a complex morphology.

From the histograms of the spectral indices (Figure 3.6) we note the presence of values significantly outlying the main distribution. Most of them correspond to actual physical values after discarding those partially ascribable to data analysis biases as: (1) observing noise caused by weather conditions (such as clouds) near the AR that might have contaminated the

[3]This flag is connected with the quality of the background (the solar disk) around the extraction region (AR), in terms of the percentage variation P_v between the fluxes obtained through the extraction region corresponding to $n = 2$ and $n = 5$ times the fitted semi-axes level; in particular, C flag appears when $P_v \geq 30\,\%$.

analysis (such as in the case of the 25.8 GHz map on 1-Oct-2019, where there is SD-AR M00037 characterized by $\alpha_{T_{ex}} > 4.1$), (2) background contamination around ARs (e.g., the AR SD-AR M00051 observed on 19-Oct-2020 with $\alpha_{T_{ex}} > 4.3$, characterized by a high AR extraction region of > 50 arcmin^2), (3) AR detection on the edge of the solar disk (for example in the case of the AR NOAA 12778 / SPoCA 24770[4] observed on 30-Oct-2020 with $\alpha_{T_p} = 1.5$).

3.4 Discussion

Despite INAF radio telescopes being facilities not dedicated to solar monitoring, we were able to perform weekly observations on average in this early science phase of the project, with good performances. The sensitivities of our solar images in the 18–26 GHz frequency range are of a few kelvin or less, with an instrumental noise and sky opacity fluctuations on the bright disk usually < 10 K (Sec 3.1), about one order of magnitude lower than the typical standard deviation of the QS brightness distribution (see Appendix A and Figure 3.1).

We accurately measured QS brightness levels through the adoption of the very bright SNR Cas A as a flux calibrator (see from Sec 2.5); in good observing conditions, the overall calibration errors do not exceed 3 %, and this accuracy can be improved with further calibration campaigns. This robust image calibration procedure allows us to perform a systematic analysis of the radio parameters of ARs detected in most of our observing sessions.

SUNDARA (Sec 2.2) has successfully identified excess brightness regions in about 70 % of solar observing sessions characterized by maps with medium/high quality (see Appendix B and C). Such structures included both known ARs and other radio unidentified areas (with unclear reference in the literature). In order to measure the AR size and total excess flux we relied on our algorithms, and chose a specific convention Marongiu et al., 2021. Since other observatories could employ different methods, a common convention and a data extraction method are crucial in order to perform a careful multi-frequency spectral analysis together, and hence to obtain coherent and standardized results.

Comparing these AR features with those reported at other frequencies[5], we note that AR details and substructures – as the complex AR morphology McIntosh, 1990 and magnetic structures Jaeggli and Norton, 2016 – are typically not resolved in our data (see Figure 2.2), while the bulk emission of many ARs is typically slightly larger than our spatial resolution (see radio beam width in Tables 2.1 and 2.2). On the other hand, we typically detect rich network structures on larger scales, compatible with the"semi ARs" described in a recent work by Kallunki et al. 2020, based on single-dish radio observations at 37 GHz; they claimed that these "semi ARs" – detected even during the minimum phase of the solar cycle – can be indicative of persistent solar activity in the radio domain, suggesting that these weak radio brightenings are mostly related to coronal hole features and magnetic bright points. The brightness excess temperatures with respect to the QS level (T_{ex}) are below ~ 1000 K in most cases (see Figure 3.3); this suggests that in our data the chromospheric network shows typical temperature fluctuations of < 10 %, except from sporadic ARs with total emission nearly doubling the QS brightness level.

The analysis of 169 solar maps in the frequency range 18–26 GHz (Appendix C)provides important clues about AR spectra. In Figure 3.4 we report the spectral index distribution obtained by comparing AR peak brightness temperatures (including the QS component) at different frequencies, while in Figure 3.6 we plot the AR spectral distribution related

[4]Spatial Possibilistic Classification Algorithm (SPoCA) is a multi-channel unsupervised spatially-constrained fuzzy clustering algorithm Barra et al., 2005; Delouille et al., 2012; Verbeeck et al., 2014, developed to segment the Extreme Ultra Violet (EUV) images of the Sun into 3 categories (QS, AR and coronal holes).

[5]EUV and optical data are obtained thanks to facilities on-board several missions, such as Hinode (`www.isas.jaxa.jp/home/solar/`), and Solar Dynamics Observatory (`http://sdo.gsfc.nasa.gov`)

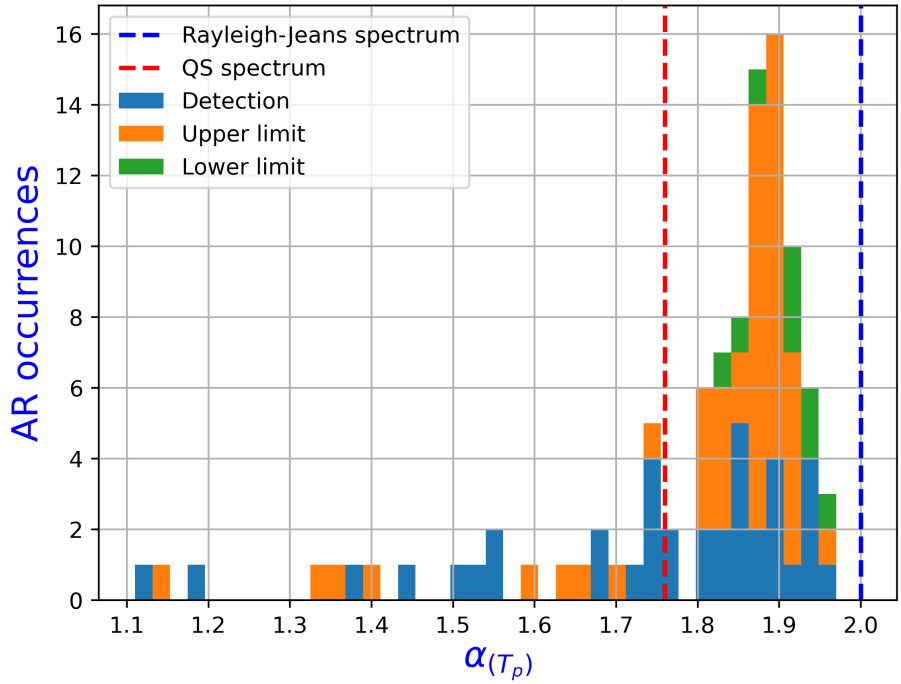

Figure 3.4: Histogram of the spectral index values calculated from the maximum brightness temperature T_p. The data are binned in 40 bins. *Blue counts* indicate detections; *orange and green counts* show upper limits and lower limits, respectively. *Dashed lines* indicate the spectral indices of Rayleigh-Jeans (blue), and of the QS-level as estimated by Landi and Chiuderi Drago 2008 (compatible with our QS measurements) (Pellizzoni et al. 2022).

to integrated total fluxes. These distributions, peaked between the Rayleigh-Jeans (RJ) and the QS spectrum ($\alpha_{QS} \sim 1.75$ in our frequency range) as derived from Landi and Chiuderi Drago 2008, suggests the presence of emission significantly deviating from simple thermal bremsstrahlung in the optically thick regime ($\alpha_{RJ} = 2$) as observed in ARs at higher frequencies Giménez de Castro et al., 2020; Silva et al., 2005; ValleSilva et al., 2020. We note that our distribution in Figure 3.4 peaks around $\alpha_{T_p} \sim 1.9$; optically-thin spectral index from thermal bremsstrahlung is generally regarded as closer to this value than to 2.0 due to the logarithmic dependence of the Gaunt factor on frequency.

The fact that many of the detected spectral indices in Figure 3.4 are higher ($\alpha_{T_p} > 1.8$) than QS values could suggest a thermal gradient within the vertical structure of typical ARs that differs from QS emission models. Furthermore, in addition to thermal bremsstrahlung, the concurring presence of sporadic gyro-magnetic components in the AR emission could contribute to spectral softening. In fact, gyro-resonance emission has been proven to peak up to $\sim$ 20 GHz (see, e.g., Selhorst et al., 2008), although in most cases this component is observed at lower frequencies (2–5 GHz; Kakinuma and Swarup, 1962; Nindos et al., 2002). The presence of strong gyro-synchrotron emission is unlikely in our data due to the low chance of observing a flare during the scans, although small-scale energy release events (nanoflares) cannot be excluded. More AR statistics is needed to precisely assess the actual distribution of unusually soft spectra, also considering the presence of many upper limit measurements.

The AR spectral index distribution in Figure 3.5, based only on the weak brightness excesses with respect to QS component (obtained by subtracting the QS level itself) emphasizes the characteristics of ARs emission and their non-thermal components. Figure 3.5 shows that a significant number of spectra are relatively flatter than the thermal bremsstrahlung emission, corroborating the possible presence of gyro-magnetic emission components. We

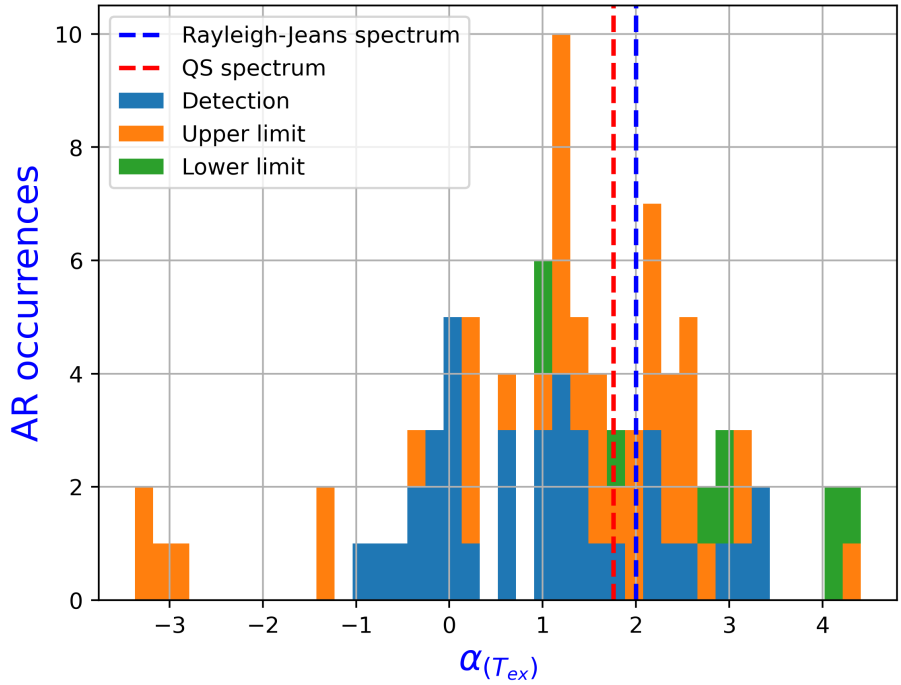

Figure 3.5: Histogram of the spectral index values calculated from the maximum brightness temperature excess T_{ex}. See the caption of Figure 3.4 for a full description of the histogram. (Pellizzoni et al. 2022)

could explain these spectra of peculiar AR events considering the contribution of a steep high-frequency tail provided by gyro-resonance emission peaking slightly below our frequency range. It is important to note that the measured spectral indices represent an average value within the beam and thus differ from the actual values rising from the smaller-scale unresolved regions that emerge from the diffuse free-free emission. For example, an hypothetical steep tail of gyro-resonance emission with spectral index $\alpha = -7$ and contributing to $\sim$50 % of the total brightness at 18 GHz will result in an apparent flat spectral index when averaged with the free-free thermal emission covering the whole radio beam.

The gyro-resonance emission at radio frequencies has been studied by many authors in order to estimate the coronal magnetic fields, up to the 15–17 GHz range (e.g. Akhmedov et al., 1982; Alissandrakis et al., 1993; Kundu et al., 2001; Nindos et al., 2000; Shibasaki et al., 1994; Vourlidas et al., 2006; White et al., 1995). They showed that the gyro-resonance emission for radio frequencies $\gtrsim$ 10 GHz is produced in regions of magnetic fields with intensities of hundreds mT (located close to the transition region), and that at 17 GHz the lower limit for the magnetic field intensity to produce this emission (due to the third harmonic) is $\sim$ 2000 G at the photospheric level; moreover, the enhancement of gyro-magnetic effects when leaving the minimum of solar activity could cause a significant increase of the AR average brightness up to $\sim 10^5$ K, and beyond.

In Figure 3.5 we also note a significant number of spectra harder than RJ emission. This could be related to gyro-resonance emission peaking above our frequency range (rising part of the spectral component) and requiring very high magnetic fields $>$ 2000 G and/or higher-harmonics components. Imaging observations above 30 GHz reported in the literature are not conclusive about the possible presence of gyro-resonance spectral contributions in addition to free-free emission Selhorst et al., 2008. In theory, at these frequencies gyro-resonance emission characterized by a typical magnetic field intensity of $\sim$ 2000 G (at the photospheric level) is allowed for high harmonics (6–7); typical emission in the gyro-frequency lower harmonics (2–4) is more difficult to observe, because uncommonly high magnetic field

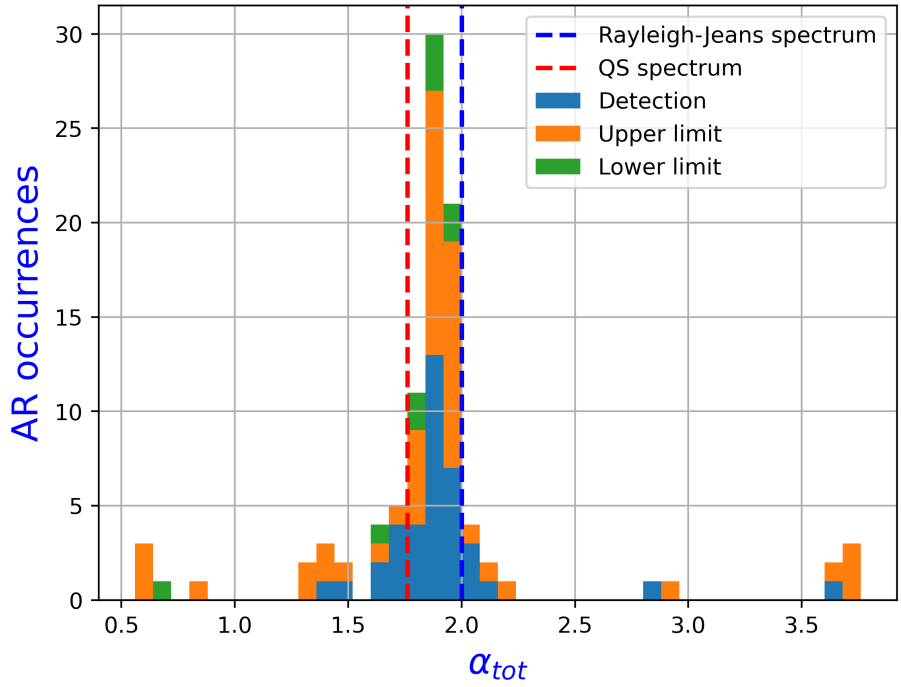

Figure 3.6: Histogram of the flux density spectral index values $\alpha_{\rm tot}$. See the caption of Figure 3.4 for a full description of the histogram (Pellizzoni et al. 2022).

intensities ($\sim 3000 - 6000$ G) would be in principle required (e.g., Nindos, 2020; Selhorst et al., 2008; Valio et al., 2020).

A possible physical context about these spectral outliers could be related to local eruptive events inside ARs – including flares and coronal mass ejections (CMEs) – crucial to investigate the AR dynamics. A gyro-magnetic emission enhancement could be a precursor of flaring gyro-synchrotron emission from the region of anomalous energy release with a sub-relativistic plasma in moderate magnetic fields Vatrushin and Korzhavin, 1989, and modelled according to several approaches (e.g. Podgorny and Podgorny, 2012; Somov, 1986). Broadband analysis of these eruptive events shows changes – a few days prior to the event – in their microwave/radio spectra, suggesting both the emergence of a new AR photospheric magnetic field and shifting movements of the sunspots Abramov-maximov et al., 2013; Bogod et al., 2012; Borovik et al., 2012; Shibasaki et al., 2011. These changes can be used as a predictive criterion for eruptive events on the Sun associated with geomagnetic disturbances.

Several papers (e.g. Abramov-maximov et al., 2013; Borovik et al., 2012) show a correlation between changes in the magnetic field configuration of the ARs and the eruptive events that have taken place one or two days prior in the same region. This could lead to a change in the balance between the thermal and non-thermal emission component, with a prevalence of the gyro-magnetic emission that - for example - can produce an inversion from positive to negative values in the spectral index. In fact, on November 23rd 2020, we observed a very soft spectrum ($\alpha_{T_p} < 1.1$ and $\alpha_{tot} < 0.6$) in AR NOAA 12786 / SPoCA 24827 and just a few hours later a C-class flare occurred arising from the same AR (Figure 3.7). Extensive correlation studies with the eruptive events are needed in order to support this hypothesis.

It is worth noting that anomalous spectral indices could be also related to sudden temporal variations of AR brightness between the non-simultaneous observation at different frequencies that are typically taken $\sim$ 1–2 hours from each other. A recent work by Kazachenko and Hudson 2020 shows that ARs observed in EUV band are characterized by temporal variability of irradiance of $\sim 3\,\%$ in a daily timescale. Moreover, currently SUNDARA is not

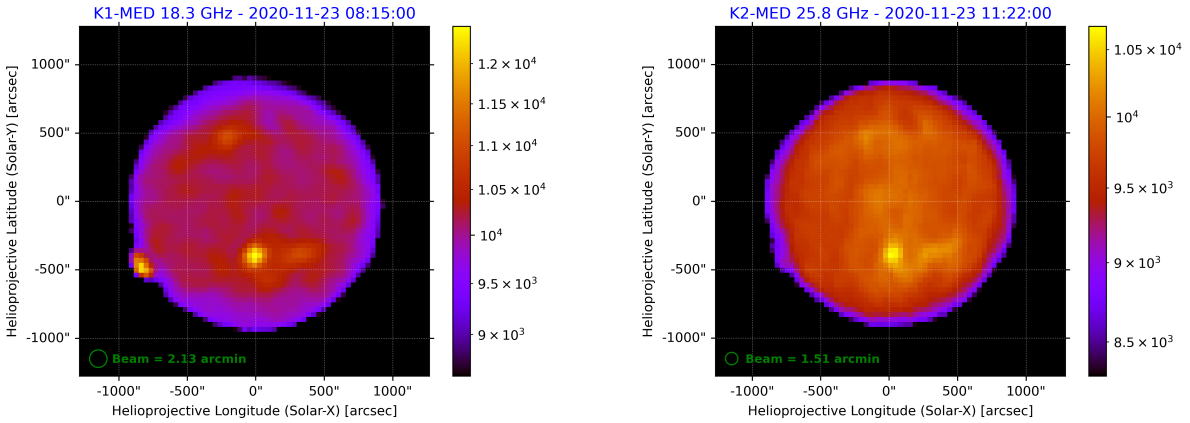

Figure 3.7: Total intensity map (in units of kelvin) of the solar disk at 18.3 GHz (*left*) and 25.8 GHz (*right*) obtained with the Medicina Radio Telescope on November 23th 2020. AR NOAA 12786 / SPoCA 24827 is visible only at 18.3 GHz at the edge of the solar disk near the solar limb. It represents a typical example of AR with very soft spectrum that can anticipate a subsequent C-class flare emission (Pellizzoni et al. 2022).

able to distinguish two (or more) very close ARs with angular distance less than 2 beams of the receiver[6].

Our results are consistent with other multi-frequency radio analysis of ARs (e.g. Silva et al., 2005; ValleSilva et al., 2020), where the contribution to $T_{\rm ex}$ is at least partially attributable to gyro-resonance emission at frequencies $\lesssim 50$ GHz, while thermal bremsstrahlung is the only emission component seen at high frequencies (100–400 GHz). Silva et al. 2005 show that in the total flux density spectra (α_{tot}) of ARs the cm-millimetric emission (17 and 34 GHz) exceeds systematically the expected fluxes from the optically thick free-free emission; this is due to the concurring presence of (1) gyro-resonance emission at 17 GHz Castelli and Clemens, 1966; Kaufmann, 1968; Tapping and Zwaan, 2001, (2) optically thick thermal free-free emission from the upper chromosphere, and (3) optically thin thermal emission from the transition region and coronal sources. A 3D solar atmospheric model, developed to reproduce the brightness temperature of a specific AR characterized by a high degree of polarization (85 %) with radio observations at 17 and 34 GHz from NoRH Selhorst et al., 2008, showed that at 17 GHz the emission was successfully modeled as gyro-resonance, while at 34 GHz the emission was attributed to free-free radiation only.

In summary, the variety of AR spectra that we observed in the 18–26 GHz frequency range could be related to the variable contribution of gyro-resonance components that peaks in this range or in neighborhood frequencies. Our findings seem to provide clues of gyro-resonance lines even slightly above 26 GHz, possibly associated with part of the ~ 33 % of ARs that we detected with very peculiar hard spectral indices ($\alpha_{T_{\rm ex}} > 2$).

3.5 Future works

Among future SRT/SDSA solar configurations, observing capabilities at new frequency bands will be implemented, simultaneously covering the X (8–9 GHz) and K (25.5–27.0 GHz) or X and Ka (31–33 GHz) bands that may play a crucial role to constrain the frequency range of AR gyro-resonance emission. To date, this component has been detected till 15–17 GHz (see Nindos, 2020 and references therein), while at 34 GHz Selhorst et al. 2008 modelled the emission as purely free-free. Thermal components will be further constrained through the

[6]For example, this is the case of SPoCA 24770 / SPoCA 24772 (on 29-Oct-2020 with $\alpha_{T_p} = 1.2$), SPoCA 24827 / SPoCA 24840 (on 28-Nov-2020 with $\alpha_{T_p} = 1.4$), and SPoCA 24827 / SPoCA 24850 / SPoCA 24851 / SPoCA 24853 (on 30-Nov-2020 with $\alpha_{T_p} = 1.5$), detected as a single AR.

upgrading of SRT with the new receivers in Q-band (33–50 GHz) and W-band (75–116 GHz) whose operations are expected to start in 2023. These instruments coupled with the new generation digital backend SKARAB (Square Kilometer Array Reconfigurable Application Board)[7] will offer a wider dynamic range best suited to detect strong gyro-magnetic and synchrotron emission in perspective of the growing solar activity.

Polarimetric mapping of solar disk emission features could allow us to correlate magnetic information with AR spectra, helpful in disentangling gyro-magnetic contributions from free-free emission. A very high degree of polarization ($> 30\,\%$) is expected in sporadic ARs dominated by a strong gyro-magnetic component Selhorst et al., 2008. Full-Stokes polarimetric information is already available for SRT solar observations, while at Medicina station only dual polarization observing mode is presently available in the K-band. The exploitation of such information will represent a next challenging milestone for this project, considering the expected low degree of polarization ($< 10\,\%$, Selhorst et al., 2005) of the QS component and most of disk features, and the need of dedicated polarimetric calibration procedure for solar observations.

AR radio observations will support empirical and physical models of spectral behavior that can anticipate an upcoming flare; the correlation between AR spectral index changes (due to incoming strong gyro-magnetic components from X to K bands) and subsequent flare occurrence in a few hours/days can be statistically investigated and it might represent a valuable forecasting probe for flare events contributing to the Space Weather warning/alert network.

The additional complex network of diffuse and weaker emission structures typically present in our images ("semi AR" as defined by Kallunki et al., 2020), as well as emission regions at lower temperature than the QS level possibly related to Coronal Holes, will require dedicated investigations. The cross-comparison of our simultaneous 7-feed images[8] provided by SRT observations clearly demonstrates the realm of such weak structures not related to instrumental gain fluctuations.

It will be interesting to monitor the evolution of the extension and intensity of ARs and the diffuse "semi AR" features during the progression of the solar cycle. This monitoring can be supported by the study of the secular evolution of the $\sigma_{\rm disk}$ parameter (see Sec 3.1, Figure 3.1), and its correlations with sunspot numbers (SSN) and other solar indices. Several papers report the correlation between AR parameters and the solar cycle in the radio domain. A recent work about spectral analysis with SST at 212 and 405 GHz during Cycles 23 and 24 Giménez de Castro et al., 2020 indicates that the temporal evolution of AR brightness ($T_{\rm ex}$) at these two frequencies follows the solar cycle, represented by the SSN. A similar result was obtained by Selhorst et al. 2014 at 17 GHz: a correlation between the AR brightness temperature and the solar cycle is attributed to the emergence of ARs characterized by strong magnetic fields ($\geq$ 2200 G at the photosphere; Vourlidas et al., 2006) and a gyro-resonance contribution, able to increase the AR brightness temperatures up to 10^5 K (and beyond), if the 17 GHz gyro-resonance third harmonic ($\sim$ 2000 G) occurs above the transition region Selhorst et al., 2008; Shibasaki et al., 1994, 2011; Vourlidas et al., 2006.

The study of the radio counterpart of other peculiar large-scale structures, such as Coronal Holes, loop systems, filaments, streamers and the coronal plateau, will also benefit from systematic long-term observations during the evolution of the solar cycle. For example, interesting solar disk features as polar brightening (see, e.g., Kosugi et al., 1986; Shibasaki, 1998) are clearly detected in our data (e.g. on September 17^{th} 2020 at SRT, Figure 3.8). The radio brightness in polar regions seems anti-correlated with solar activity as suggested by

[7] www.tauceti.caltech.edu/casper-workshop-2017/slides/12_moschella.pdf

[8] Accurate solar data calibration is presently available for the central feed only, despite image quality is good in most feeds.

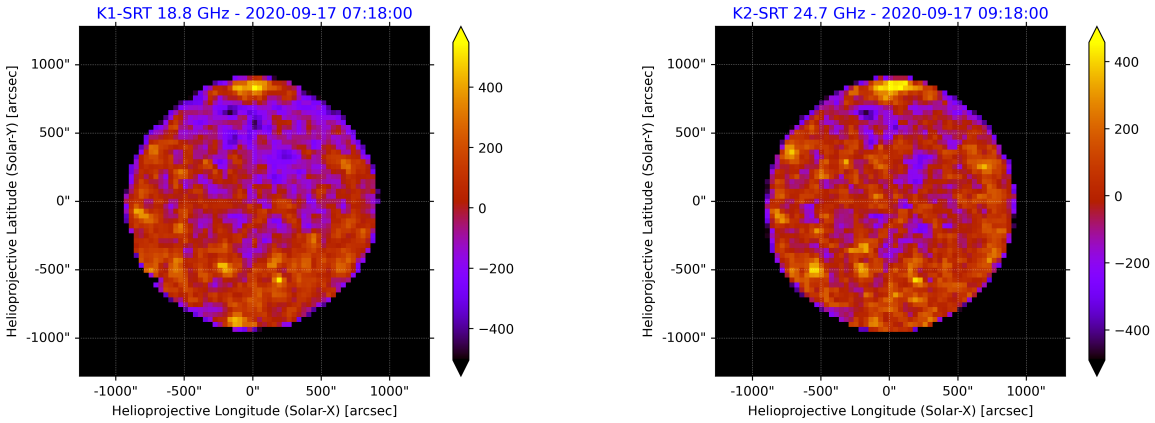

Figure 3.8: Total intensity map (T_{ex} brightness level) of the solar disk at 18.8 GHz (*left*) and 24.7 GHz (*right*) obtained with SRT on 17-Sep-2020, characterized by a typical episode of polar brightening (Pellizzoni et al. 2022).

NoRH images at 17 GHz in the epoch range 1992–2013. This effect could be related to the fact that around solar activity minimum – characterized by a reduced presence of ARs – polar regions are dominated by strong unipolar magnetic field that may enhance their brightness (see, e.g., Nitta et al., 2014; Shibasaki et al., 2011). For systematic studies of solar cycle dependence of polar brightening (as a probe of magnetic field variations during a solar cycle), long-term full-disk observations are required, and ideally starting from the present phase near minimum solar activity.

3.6 Future projects

To further expand our studies on the solar observations illustrated in Chapter 2 and 3 we are planning to observe at higher frequencies in the next future. This is possible thanks to the implementations of new SRT receivers in the context of the PON funding (see Sec 3.6.1) and the Solaris project, which has the aim to observe the Sun up to 100 GHz (see Sec 3.6.2).

3.6.1 PON receivers

SRT is currently equipped with radio astronomy receivers operating in the 305 MHz - 26.5 GHz frequency range. The PON (National Operational Program) funding, which the Italian Ministry of University and Research has recently assigned to INAF, has the aim to upgrade the SRT to allow observations at high radio frequencies (Govoni et al. 2021). In particular, two receivers are in project to be used for future solar studies which will help to further constrain the thermal components of the Sun:

1. A multi-beam cryogenic receiver operating in the 70-116 GHz frequency band (W Band) for SRT, composed of 16 double linear polarization beams;

2. A multi-beam cryogenic receiver operating in the 33-50 GHz frequency band (Q Band) for SRT, composed of 19 double circular polarization beams.

The working goal of the next few years is to acquire, install, and bringing in the operational phase these new high frequency radio astronomical receivers and others wich are indicated in violet boxes in Fig. 3.9.

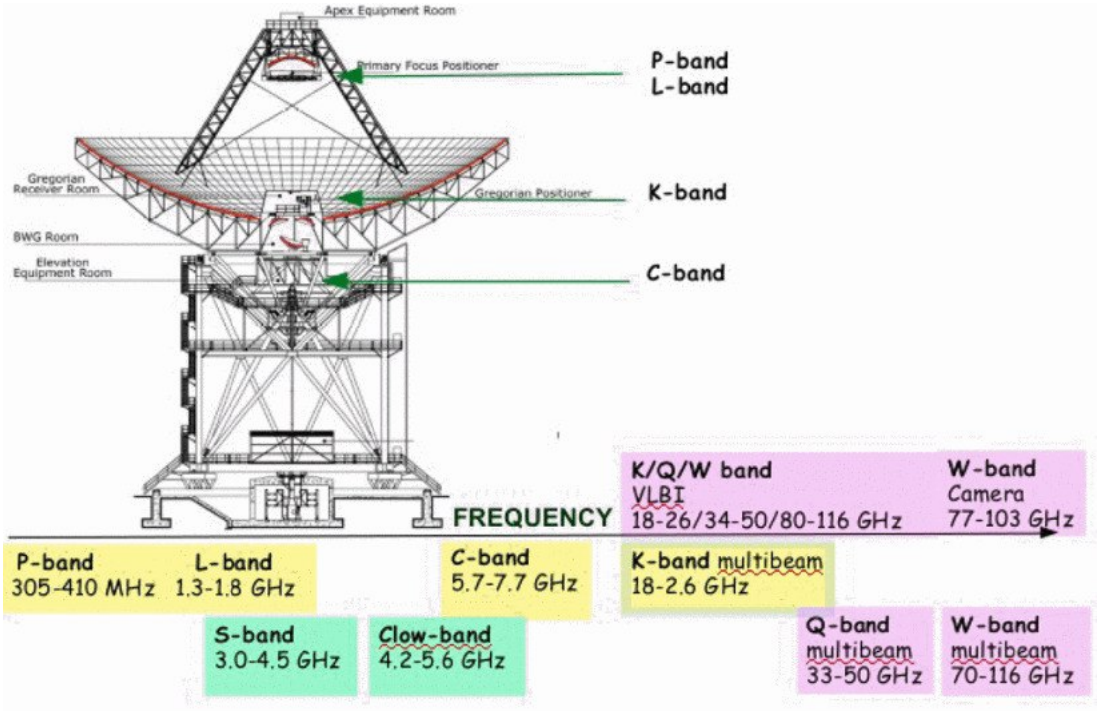

Figure 3.9: Receivers of the SRT and their focal position: current (yellow), under construction (green) and those expected from the PON project (violet) (Govoni et al. 2021)

3.6.2 Solaris

Solaris is a scientific and technological project aimed at the development of a smart Solar monitoring system at high radio frequencies based on single-dish imaging techniques. It combines the implementation of a dedicated and interchangeable 100 GHz receiver on existing small radio telescope systems (1.5/2.6m class) available in our laboratories in Milan and in Antarctica, to be adapted for Solar observations.

The Solaris Observatory is designed for operations in Antarctica, that will offer unique observing conditions (very low sky opacity and long Solar exposures) and unprecedented Solar monitoring in the radio W-band. This will be achieved through state-of-the-art single-dish imaging techniques at radio frequencies, that allows to map the entire Solar disk in less than 30 min with spatial resolution of a few arcminutes. This opens for the identification and spectral analysis of Active Regions before, after and during the occurrence of solar flares. These system features will allow Solaris to explore cutting-edge aspects of Solar Physics (e.g. chromosphere dynamic monitoring) and Space Weather applications (e.g. flare forecast). Solaris can perform continuous solar imaging observations nearly 20h/day during Antarctic summer exploiting the observation facility OASI (Osservatorio Antartico Submillimetrico ed Infrarosso dall'Oglio and de Bernardis 1987) existing in East Antarctica at Mario Zucchelli Station. The project mostly uses existing expertise and instrumentation yet available at the Universities and INAF laboratories of our collaboration. We intend to offer to the scientific community a very competitive tool and to young scientists a unique opportunity of professional growth in the challenging multi-disciplinary framework of Solar Physics and Space Weather science. The Solaris observatory will be the only Solar facility offering continuous monitoring at 100 GHz, and it will be able to collect and disseminate data in synergy with the existing national and international network of Space Weather facilities.

Part B:
The Sardinia Deep Space Antenna

Chapter 4

Space science with the SDSA

The Sardinia Deep Space Antenna (SDSA) is the space configuration of the Sardinia Radio Telescope that started its activity in 2017 with the aim to provide tracking and communication services for robotic/human exploration of near Earth, lunar, Deep Space missions and to support ambitious scientific experiments (Flamini et al. 2017). The main SDSA potentiality is related to its possible use for distinctive, not only routine activities. Its capabilities can be extended to have a station characterized by the versatility and high performance essential for research, in full compliance with international standards.

The Deep Space (distances from spacecraft more than 2 million km) communications are mostly performed by the antennas of the NASA Deep Space Network and ESA Estrack. They are networks of antennas distributed around the world aimed at tracking interplanetary spacecrafts. The NASA DSN[1] consists of three different complexes, located at Goldstone, Madrid and Canberra, hosting each one several 34-m and a 70-m antennas. The Estrack Network[2] consists of three complexes, located at Madrid, Malargue and Canberra, hosting one 35-m antenna. The strategic placement of these facilities permits constant communication with spacecraft as our planet rotates, as they are equidistant from each other approximately 120 degrees apart in longitude. They provide the crucial connection for commanding the spacecraft via a transmitted signal from the ground station to the spacecraft (uplink) and receiving scientific and engineering data from the spacecraft to the ground station (downlink). Another important activity carried out by these complexes is related to radio-science experiments, where the connection signal between the spacecraft and the antenna (uplink and/or downlink) is exploited for extracting scientific information, e.g. related to the composition of planetary atmospheres. In order to perform this kind of space science, a very stable connection link has to be established and ground segment equipment need to be be very performing and characterised by a very low noise level.

SDSA, thanks to its large dish and to its very innovative technology, is one of the few antennas in the world that could be potentially exploited to carry out very challenging space science experiments, using the radio science technique.

SDSA is managed by the Italian Space Agency (ASI) and shares with the Sardinia Radio Telescope (SRT) a part of the system and infrastructure, however it has its own specific equipment and a dedicated control center. The Initial Operational Capability of SDSA is related to the X-band receiving chain ($\sim$ 8.5 GHz), installed in 2017 and fully commissioned in 2021 (Valente et al. 2022b).

A study for future possible developments includes the capability to receive and transmit in particular at X ($\sim$ 8.5 GHz), and Ka (32 GHz) bands approaching the NASA-DSN and Estrack capabilities. The scientific use of these new capabilities has been studied in this

[1] https://www.jpl.nasa.gov/missions/dsn

[2] https://www.esa.int/Enabling_Support/Operations/ESA_Ground_Stations/Estrack_ground_stations

Thesis, assuming as driver missions JUICE[3] and BepiColombo[4] Deep Space missions. The two Missions carry-out very challenging radio-science experiments involving very stable communication links between the spacecraft and the Ground Station.

The BepiColombo Deep Space Missions will perform tests of general relativity, exploiting the measurement of the Shapiro delay (Shapiro 1964) and the corresponding Doppler shift affecting the propagation of radio-waves (Bertotti et al. 2003) as artistically represented in Fig. 4.1 left panel.

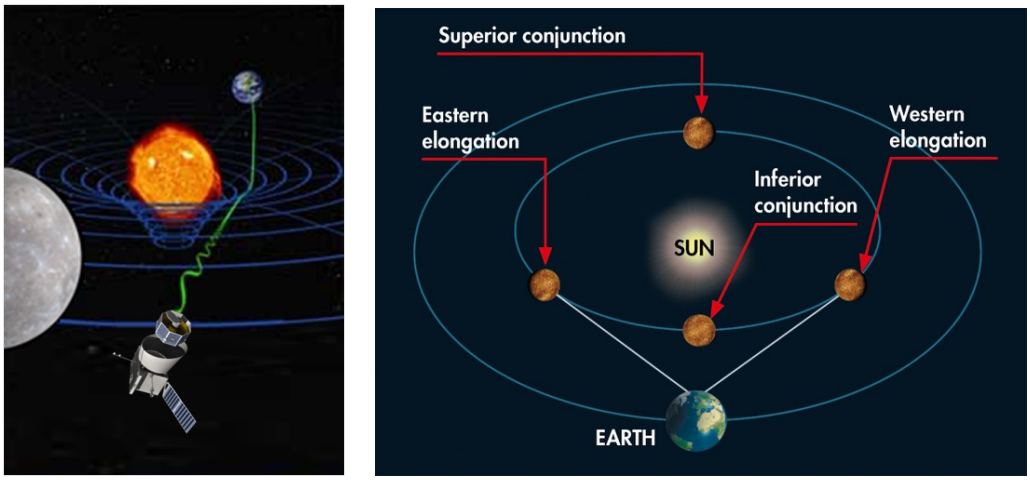

Figure 4.1: left panel: Representation of the Shapiro time delay science experiment with the BepiColombo spacecraft; right panel: an illustration of solar conjunctions geometry (Credit: BBC Sky at Night Magazine).

The spacecraft in its orbit will reach a peculiar position with respect to the Sun (see Iess et al. 2021) allowing to perform the radio science experiments in superior solar conjunction (see Fig. 4.1 right panel). This tracking modality is particularly challenging. There is the need of using a triple link at the X and Ka frequency bands, in particular for the elimination of the plasma noise (the dominant noise source in Doppler and range measurements near superior solar conjunctions, see Sec 4.2.2). Also, since the Deep Space Antenna instrumentation will have to observe extremely close to Sun, there is the need to protect the instrumentation from possible damages for receivers, as explained in Sec 2.1.2 in the context of the SunDish project. Therefore, we performed several studies on the solar emission in the X and Ka bands, also with the aid of the analysis and results obtained in Chapter 2 and 3.

This Chapter is focused on the studies performed to assess the most stringent frequency stability requirements for radio science experiments, collecting the values reported in the literature related to the most challenging radio-science experiments executed so far. The study is described in detail in Iacolina, Mulas et al. 2022 (work in progress), where the preliminary scientific and instrumental requirements are defined in detail.

4.1 Radio-science technique

A tracking experiment that exploits the radio science technique consists in an exchange of a radio signal between a deep space antenna and a spacecraft (see Fig. 4.2).

In general, the communication systems of all deep space probes have a dual use: control of the spacecraft from the ground via the uplink and return of telemetry from the probe, via the downlink. However, if the signal only derives from the onboard oscillator (e.g., an ultra stable oscillator) and it is transmitted to the ground, then the measurement is called

[3] https://sci.esa.int/web/juice
[4] https://www.esa.int/Science_Exploration/Space_Science/BepiColombo

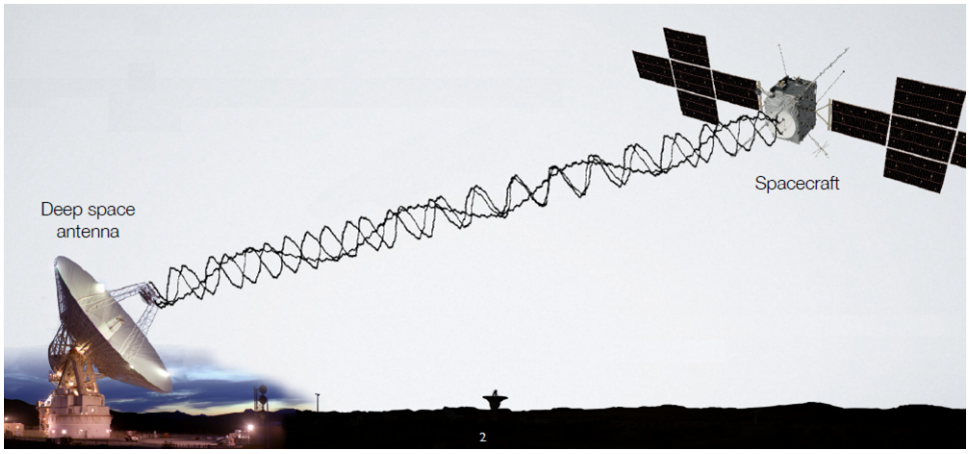

Figure 4.2: Schematic representation of a radio-science experiment (Di Ruscio et al. 2019)

one-way. If the spacecraft transponds a frequency signal transmitted from the ground and the ground-based reference for the Doppler is the same one that drives the transmitter, the observation is *two-way* (see Fig. 4.3, Pätzold et al. 2004). A precision frequency standard from the Frequency and Timing Subsystem (FTS) provides the frequency reference to both the transmitter and receiver chains (Asmar et al. 2005b).

These communications systems typically obtain the two observables: radio ranging and Earth- spacecraft Doppler shift, to determine probe position and velocity. Both these two observable serve at least two purposes: navigation and radio science; in particular the latter exploits the radio link explicitly for science purposes.

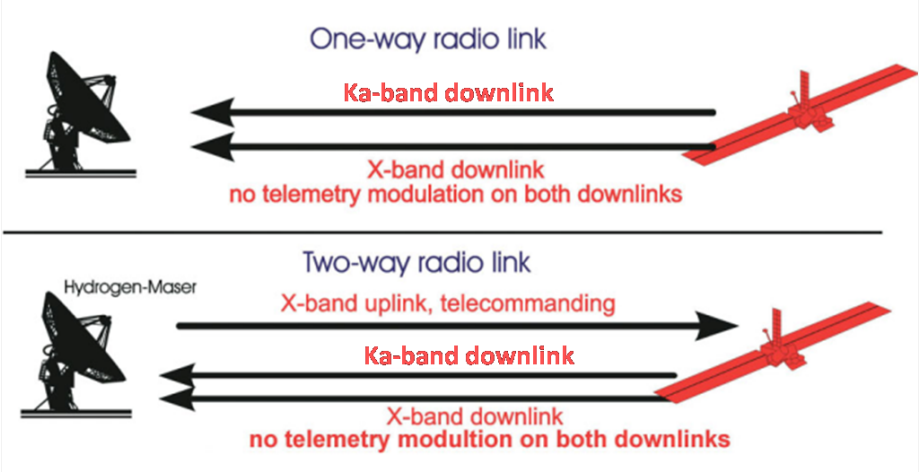

Figure 4.3: One way and two way radio-science experiment scheme from Pätzold et al. 2004 with two receiver, one in X-band and one in Ka-band.

Radio Science experiments are of different nature depending on the scientific purpose. The main types are related to the study of:

- planetary atmospheres and rings;
- planetary mass and interiors;
- planetary surfaces and shapes;
- planetary geodesy;
- planetary gravitational fields;

- solar corona and wind;
- fundamental physics and general relativity.

These scientific purposes translate into different operation modes that SDSA could aiming to perform, compatibly with specifications achievable by the station:

- gravity radio science;
- general relativity radio science;
- occultation radio science;
- bistatic radar radio science;
- same beam interferometry for radio science;
- gravitational waves radio science.

4.2 Principal noise sources affecting the signal

As in the future SDSA could be implemented to perform radio science experiments, it is necessary to inquire the instrumental performances needed to be fullled during the upgrade phase. Performances of radio science experiments typically depend on:

- Used link signal frequencies;
- Signal strength (signal to noise ratio);
- Intervening media (Earth atmosphere and interplanetary medium);
- Non-gravitational forces;
- Accuracy of trajectory reconstruction;
- Spacecraft and ground station (Electronic components, Mechanical components);
- Antenna pointing stability;

and are generally evaluated by measuring the following properties:

1. Frequency stability;
2. Phase noise;
3. Amplitude stability.

Typically, ranging and Doppler shift measurements are adopted, providing for a measure of the relative distance and motion between the spacecraft and the ground station (Di Ruscio et al. 2019). The precision of these observable directly affects the level of accuracy achievable in the estimation of the parameters, hence, a precise description of the error budget derived from the principal noise sources affecting the stability of the radio link becomes fundamental in assessing radio science experiments results.

The most adopted Doppler noise characterization in time-domain is the Allan deviation applied to the residuals from the expected frequency to the measured one. The Allan deviation is defined in Riley 2007 as:

$$\sigma(\tau) = \sqrt{\frac{1}{2(M-1)} \sum_{i=1}^{M-1} (y_{i+1} - y_i)^2} \tag{4.1}$$

where y_i is the i-th of M fractional frequency values averaged over the sampling interval τ. The Allan deviation can provide an estimate of the frequency stability of the signal link between the spacecraft and the ground station. The mission requirements related to the frequency stability of the end-to-end chain (Allan deviation evaluated on the two-way signal from its generation at ground station and return after transponding to the spacecraft) of the BepiColombo and JUICE Mission are listed in Tab 4.1.

Table 4.1: End-to-end value of the Allan deviation at 1000 s for the two driver missions ESA BepiColombo and Juice.

Mission	End-to-end Allan deviation at 1000s	Reference
Juice	$6.8 \cdot 10^{-15}$	De Vicente et al. 2019
BepiColombo	$1 \cdot 10^{-14}$	De Vicente et al. 2019

These values have to be compared with noise budget that affects the signal link. In particular, this is an essential study for considering the upgrade of the instrumentation.

Studying the literature we found that the principal noise sources come from in particular: the Spacecraft and its interaction with the surrounding medium, the interaction of the radio signal with the interplanetary medium and atmosphere and the ground station. In the following sub-sections we are going to analyse them and give, if available, a way to minimize them and reach the instrumental requirement to potentially perform radio science experiments with the JUICE and BepiColombo Deep Space Missions.

4.2.1 Spacecraft and interaction with the interplanetary medium

- the **spacecraft transponder noise**, which is generated mainly from the electronic systems of the onboard deep space transponders. For the BepiColombo mission it could also be attributed to the Ka/Ka radio science transponder. This effect has to be taken into account during mission planning phase.

- the **unmodeled motion of the spacecraft** derives from the difficulty in predicting the effects of different phenomena, such as the fluctuations in the solar wind hitting the spacecraft, fluctuations in solar radiation pressure, physical articulation of spacecraft parts, leaking thrusters, sloshing of fuel in the spacecrafts tanks, and so on. This effect has to be taken into account during mission operational phase.

- the **spacecraft thermal noise**. Usually the small size of the spacecraft menages to balance the negative effects of the spacecraft thermoelastic deformations. However, for some missions, it may become a non-negligible noise source. This effect has to be taken into account during mission planning and operational phase.

One can consult Armstrong 2006, Asmar et al. 2005a, Di Ruscio et al. 2019 for more details on these noise sources, that are not due to the performance of the ground station, but are anyway important in evaluation of the link stability in a radio science experiment.

4.2.2 Plasma perturbation and triple-link

The interaction of the radio signal with the interplanetary medium is one of the most important noise source, especially in the case of radio science experiments in superior solar conjunction (see Fig. 4.1 right panel) where the Solar Wind has a non-negligible impact in the Doppler measurement. The plasma perturbation is a dispersive type noise ($\propto \nu^{-2}$) and derives from the irregularities in the interplanetary medium. It is a complex phenomena, but for the scope of this study, we will not go into the mathematical details (see Bertotti et al. 1993 and Iess et al. 1983 for the a more theoretical discussion).

In a simple approach, the irregularities in the interplanetary plasma and solar wind cause a variation in the refractive index, that will in turn disrupt the radio signal phase. This perturbations mimic a time varying change, implying an error in the estimation of the spacecraft velocity and in the Doppler measurement. Its Allan deviation at 1000 s is evaluated at Ka band as $1.5 \cdot 10^{-15}$ at 160° Sun-Earth-Spacecraft angle (Su-E-Sp) (Armstrong et al. 1979).

A method to compensate and almost cancel the effect due to the plasma perturbation called triple-link (see Fig. 4.4), has been described in Bertotti et al. 1993.

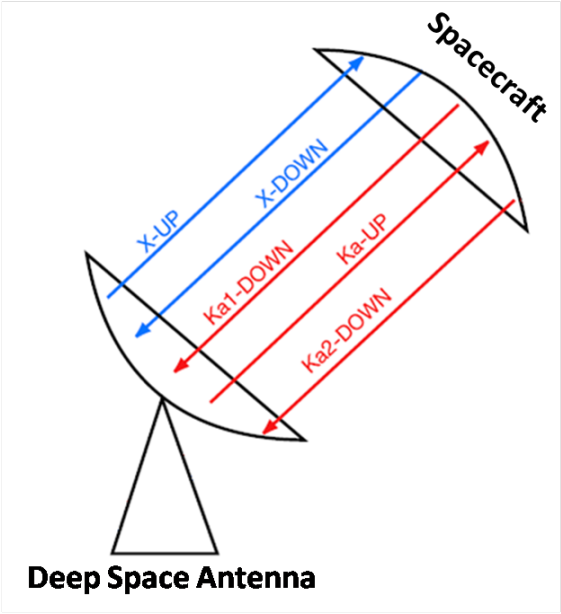

Figure 4.4: Triple link configuration from Armstrong 2006.

The system consists in a using multi-frequency radio system, usually in the X and Ka-band. In this configuration the ground station simultaneously transmits two uplink carriers at X and Ka-band that are coherently retransmitted to ground by means of the on-board transponder to form a triple downlink (X/X, X/Ka and Ka/Ka) Iess et al. 2012.

This configuration was implemented in the Cassini deep space mission[5]. The spacecraft had two transponders: KEX and KaT. The first one accepts the X-band uplink and produces two phase-coherent outputs, one at $f_X \cdot 880/749$ (= X-band downlink frequency) and another at $f_X \cdot 3344/749$ (= Ka1 downlink frequency), where fX is the frequency of the X-band uplink signal observed at the spacecraft. These signals are amplified, routed to the spacecraft high-gain antenna, and transmitted to the Earth. Another flight unit, the Ka-band Translator (KaT), accepts a Ka-band uplink signal and produces a phase coherent signal with frequency $f_k \cdot 14/15$ (= Ka2 downlink frequency), where fk is the Ka-band signal frequency observed at the spacecraft (Armstrong 2006). In Iess et al. 2012 they illustrated how this configuration has greatly improved the sensitivity of the Cassini deep space mission. This configuration will be

[5]https://www.nasa.gov/mission_pages/cassini/main/index.html

also used in the BepiColombo mission (De Vicente et al. 2019) and is also an instrumental methodology that need to be implemented for SDSA to be able to perform this type of experiments.

Also the Earth ionosphere introduces a dispersive type noise, therefore it can be reduced or cancelled with the same method.

4.2.3 Troposphere calibration

The Earth troposphere is another remarkable source of noise in the Doppler measurements, due to the fluctuations of the refractive index induced by the neutral component of the atmosphere. The main difference with respect to the plasma perturbation, is the non-dispersive nature at microwave frequencies. Therefore, the triple link can not compensate or cancel it (Armstrong 2006).

The troposphere is composed by a dry and wet component. The first one is homogeneous and is responsible for up to $\sim$ 90% of the tropospheric path delay. The frequency drift on range rate measurements is essentially a geometric effect due to elevation changes. With a suitable elevation models and ground readings of meteorological data, it is possible to compensate the error introduced in the measurements (Iess et al. 2012).

On the contrary, the wet part is non-homogeneous, and even if the wet path delay amounts to only a few centimetres (the dry path delay can be as large as $\sim 2\ m$), it is hardly predictable and difficult to calibrate (De Vicente et al. 2019). The Allan deviation typically measured is about $3 \cdot 10^{-14}$ at 1000s (Keihm et al. 2004), which represents one of the most impacting noise source in the noise budget.

An ultra stable microwave radiometer (MWR) is required to be part of the SDSA equipment in order to calibrate the wet tropospheric path delay with high accuracy. It has to be able to measure the sky brightness temperature T_b along the line of sight and for this reason it needs to be a directive instrument with the ability to point the same direction of the spacecraft. This instrument would be essential to meet the stringent requirements of the main driver mission illustrated at the beginning of Chapter 4. The Cassini mission exploited two water-vapor-radiometer-based Advanced Media Calibration (see Fig. 4.5) for the gravitational wave experiment and other Cassini Doppler tracking observation (Armstrong 2006).

Figure 4.5: Advanced Water Vapor Radiometer units next to the DSN 34-meter antennas (Buccino et al. 2021).

4.2.4 Ground noise and three way link

The noise from the ground station comes mainly from instrumental sources:

- **frequency standard form the frequency and time system (FTS)**: the coherence in two-way Doppler measurements is maintained by the frequency standard to which the up- and down-links are referenced. The presence of a Hydrogen Maser system is essential to reach Allan deviation due to FTS system of about $2 \cdot 10^{-15}$ (Kuhnle 1989). In this way the stability of the ground FTS is usually elevated, however, in some case there could be intermittent problems with an FTS distribution amplifier or other components that can cause a non negligible noise (Armstrong 2006), for this reason system redundancy is also required;

- **antenna thermal deformations**: thermal processes due to a variation in the temperature during a tracking can cause a variation in the radio path length. In some cases, the subreector could be continuously repositioned to compensate the error (Armstrong 2006);

- the **electronics components** should be carefully designed to minimize phase/frequency noise and produce only a small contribution to the overall error budget, Allan deviation due to this system can reach values of $3 \cdot 10^{-16}$ at 1000 s;

- **antenna mechanics** can introduce an error in the Doppler measurements (Di Ruscio et al. 2019). For example, the signal can be blue shifted if the antennas phase center suddenly moves toward the spacecraft, with an immediate effect in the Doppler measurements. This effects cause an echo in the transmitted signal which will in turn be blue shifted as well (Armstrong 2006). Measurements of this effect were performed in the NASA DSN deep space station 34-m DSS-25 at Goldstone complex reaching values of the Allan deviation of about $1 \cdot 10^{-14}/4 \cdot 10^{-15}$ at 1000 s, in bad and good conditions (e.g. high/low wind condition). SDSA need to characterize the effects of this noise source in order to compare performances with DSS-25.

In a two-way link configuration, Di Ruscio et al. 2019 articulated a possible solution to reduce the effect of the antenna mechanical noise in the data by exploiting a second antenna in a listen-only configuration, called three-way (Fig 4.6).

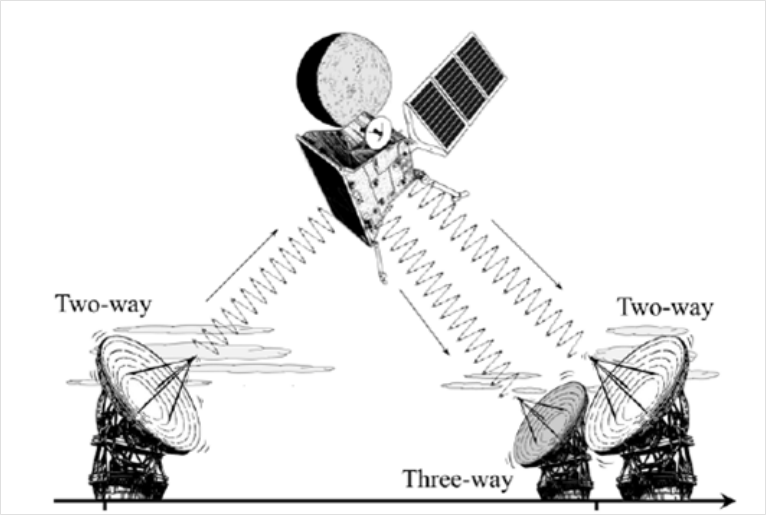

Figure 4.6: Illustration depicting two-way and three-way link configuration. The uplink is sent by the two-way station before the downlink signal is received-back by the same antenna and the three-way one (Di Ruscio et al. 2019).

They analysed the JUICE and BepiColombo missions and presented the potential improvements this configuration could bring, achieving an improvement of about 50% under favorable conditions. The second antenna should be stiffer with a better mechanical stability than the one implemented for the two-way link and possibly, located in a dry region with low tropospheric noise. For example, in the Di Ruscio et al. 2019 work they identify the 12 meter Large Latin American Millimeter Array (LLAMA) antenna in the Puna de Atacama desert as a reliable second listen only antenna.

SDSA could consider this technique in order to reach better performance for very challenging radio science experiments.

4.2.5 Beam squint

The beam squint phenomenon is not specifically a noise source which affects the acquired data, but generally occurs in radio science experiments that involves two-way link between the ground station and the spacecraft at Ka-band. This is due to the fact that targeted spacecraft is not only moving along the antenna line of sight but also in the transversal direction. Adding also the finite time of flight of the signal from the ground station to the space probe and back, the downlink and uplink directions are separated by an angular offset, usually referred as beam squint angle (Besso et al. 2010; Giannini et al. 2012; Iess et al. 2012), which at Ka band is higher than the half power beam width.

Fig. 4.7 depicts the geometry of the beam squint effect, with the received signal (RX) separated by the transmitted signal (TX) by the beam squint angle (θ). This effects can lead, especially at high frequency with a narrow beam as at Ka-band, to unacceptable pointing loss. Therefore, while upgrading a ground station for two-way link configuration, it is essential to take into consideration this aberration effect.

In Giannini et al. 2012 they presented a solution specifically for the Sardinia Radio Telescope beam squint effect at the Ka-band, considering a particular optical configuration of the mirrors inside the antenna. In upgrading the SDSA equipment, this configuration should be taken into account in order to avoid pointing losses at Ka frequencies.

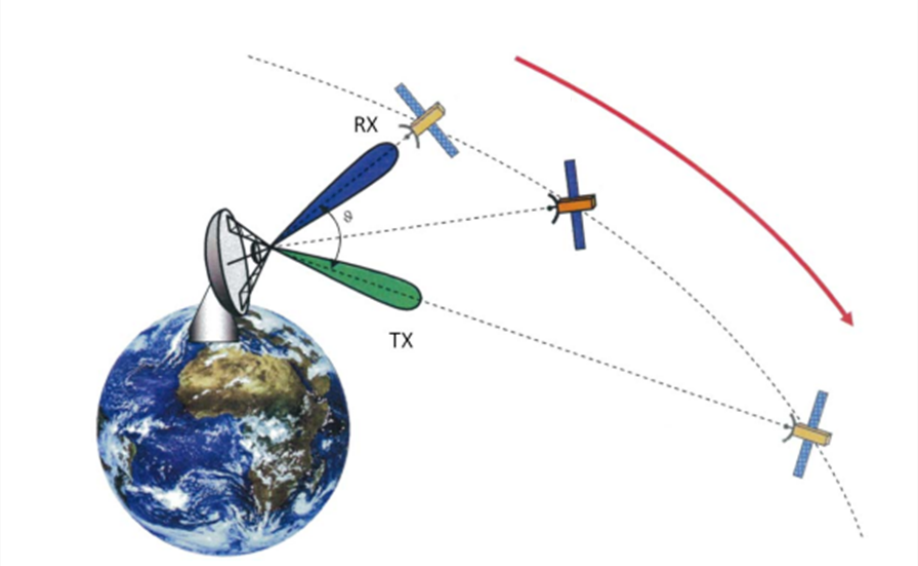

Figure 4.7: Illustration of the aberration effect. RX is the received signal, TX the transmitted one and θ is the beam squint angle (Giannini et al. 2012).

4.3 Instrumental requirements summary

In Tab 4.1 the mission requirements related to the frequency stability of the end-to-end chain (evaluated on the simulated two-way signal from its generation at ground station and return after transponding to the spacecraft) of the BepiColombo and JUICE Mission are listed. In Tab 4.2 and 4.3 we summarized the most stringent frequency stability requirements for radio science experiments cited throughout this chapter. The list selected in the Table is related to the requirement of possible implementation for SDSA. They constitute the state-of-the-art of the noise budget related to the different subsystems of the end-to-end chain is shown.

Table 4.2: State-of-the-art noise budget for radio science experiments.

Noise source	Allan deviation (Two-way, 1000s)	References
Ground FTS	$\sim 2 \cdot 10^{-15}$	Kuhnle 1989
Antenna mechanical noise	$\sim 1 \cdot 10^{-14} - 4 \cdot 10^{-15}$	Rochblatt et al. 1997
Ground electronics	$\sim 3 \cdot 10^{-16}$	Abbate et al. 2003
Plasma scintillation (Ka-band)	$< 1.5 \cdot 10^{-15}$ (160° Su-E-Sp)	Armstrong et al. 1979
Tropospheric scintillation	$< 1 to 3 \cdot 10^{-14}$	Keihm et al. 2004

Table 4.3: End-to-end stability requirements for the most common types of radio science (Asmar et al. 2021).

Radio science type	Method	Frequency Stability (Allan deviation)
Gravity and general relativity	Two-way	$\sim 1 \cdot 10^{-14}$ (at 1000s)
Occultation	One-/Two-way	$\sim 1 \cdot 10^{-13}$ (at 100s)
Bistatic Radar	One-way	$\sim 3 \cdot 10^{-12}$ (at 100s)

4.4 SDSA receivers implementations

Among future SDSA configurations, observing capabilities at new frequency bands will be implemented, simultaneously covering the X (8-9 GHz) and K (25.5-27.0 GHz) or X and Ka (31-33 GHz) bands.

With the aid of the studies and results obtained during these years, in the future we may be able to provide specific requirements for the instrumentation to perform science experiments like those carried out by the deep space missions JUNO and BepiColombo. In order to perform all the science experiments listed in Sec 4.1 we would also need the transmitters at X, K and Ka band (two-way configuration), however, we may still be able to perform a part of them with the only receiving component (one-way configuration).

In addition, we are also planning to use this new space configuration also to deepen the solar studies presented in Chapter 2 and 3, see 4.4.1.

4.4.1 Thermal characterization and solar studies

As mentioned at the beginning of Chapter 4, the BepiColombo mission will perform test of general relativity exploiting the mass of the Sun to study the Shapiro Delay Shapiro 1964. In order to investigate on requirements for the instrumentation to point close and to the Sun, we need to investigate the brightness temperature the receivers at X and Ka bands must withstand for the following emission components: quiet Sun, Active Regions and Flare

(see Chapter 1 for the description of each component). Hence, in the future, a set of signal attenuators to be installed in the receiver chain will be designed based on the value reported in Tab 4.4 and Tab 4.5, as done for the K-band in the SunDish project (see Sec. 2.1).

Once the solar attenuation set up is correctly installed, it will be also possible to make images of the Sun with the SDSA receivers. The simultaneous covering of the X and K or X and Ka bands, may play a crucial role in future solar studies:

- they may be crucial to constrain the frequency range of AR gyro-resonance emission. To date, this component has been detected till 15-17 GHz (see Nindos 2020 and references therein), while at 34 GHz Selhorst et al. 2008 modelled the emission as purely free-free. The K and Ka bands will help to understand better the non-thermal component as the results in these bands are still not conclusive (Nindos 2020). Thermal components will be further constrained through the upgrading of SRT with the new receivers in Q-band (33-50 GHz) and W-band (75-116 GHz) whose operations are expected to start in 2023 (see Sec 3.6.1). These instruments coupled with the new generation digital backend[6] SKARAB (Square Kilometer Array Reconfigurable Application Board) will offer a wider dynamic range best suited to detect strong gyro-magnetic and synchrotron emission in perspective of the growing solar activity;

- the simultaneous observation in multi-frequency band would be a powerful tool to study the spectral index of different parts of Sun, especially the ARs or the occasional observed flares;

- they will be extremely helpful for Space Weather applications: temporal variations of the ARs flux/brightness temperature at X-band and K-band spectral indexes studies can be used as a prognostic tool in the prediction of powerful eruptive events and flares that could be associated with geomagnetic disturbances (X-band: Borovik et al. 2012; K-band: Pellizzoni et al. 2022).

Table 4.4: Brightness temperatures of the different radio emission components in the X-band and near frequencies. ν is the observing frequency while T_b is the brightness temperature

Emission Component	ν [GHz]	T_b [K]	Reference
Quiet Sun	8.2	12900	Zirin et al. 1991
	9.37	12600	Borovik et al. 1992
	9.4	12200	Zirin et al. 1991
	9.5	11800	Shimabukuro and Stacey 1968
	10.6	11300	Zirin et al. 1991
Active Region	8-9	(Min) $\sim$ 17600	Silva et al. 2005
	8-9	(Max) $\sim$ 176000	Silva et al. 2005
	8	(Min) $\sim$ 35270	Borovik et al. 2012
	8	(Max) $\sim$ 308570	Borovik et al. 2012
	9	(Min) $\sim$ 19400	Borovik et al. 2012
	9	(Max) $\sim$ 290930	Borovik et al. 2012
Flare	8-9	$> 10^5$	Dulk 2001

In the Kundu 1970 work they found an excess of 1000 K in the brightness temperature of the ARs with respect to the QS level base. If one assume the Landi and Chiuderi Drago 2008 QS value as the correct one, then the brightness temperatures of the ARs at 33 GHz would be

[6] www.tauceti.caltech.edu/casper-workshop-2017/slides/12_moschella.pdf

Table 4.5: Brightness temperatures of the different radio emission components in the Ka-band and near frequencies. ν is the observing frequency while T_b is the brightness temperature

Emission Component	ν [GHz]	T_b [K]	Reference
Quiet Sun	32	8928	Landi and Chiuderi Drago 2008
Quiet Sun	33	8864	Landi and Chiuderi Drago 2008
Quiet Sun	35	8742	Landi and Chiuderi Drago 2008
Active Region	33	~ 9900	Kundu 1970
	35	~ 8900	Hachenberg et al. 1978
Flare	32	$10^5 - 10^6$	Dulk 2001

about 9900 K, as written in Tab 4.5. The value at 35 GHz value was calculated in the same way while considering an excess of 170 K with respect to the QS level base (Hachenberg et al. 1978).

4.4.2 X-band beam shape

The characterization of the beam shape of the Sardinia Radio Telescope in total intensity is an important tool for evaluating the possible variations/aberrations as a function of the elevation and for checking the pointing models for the different receivers.

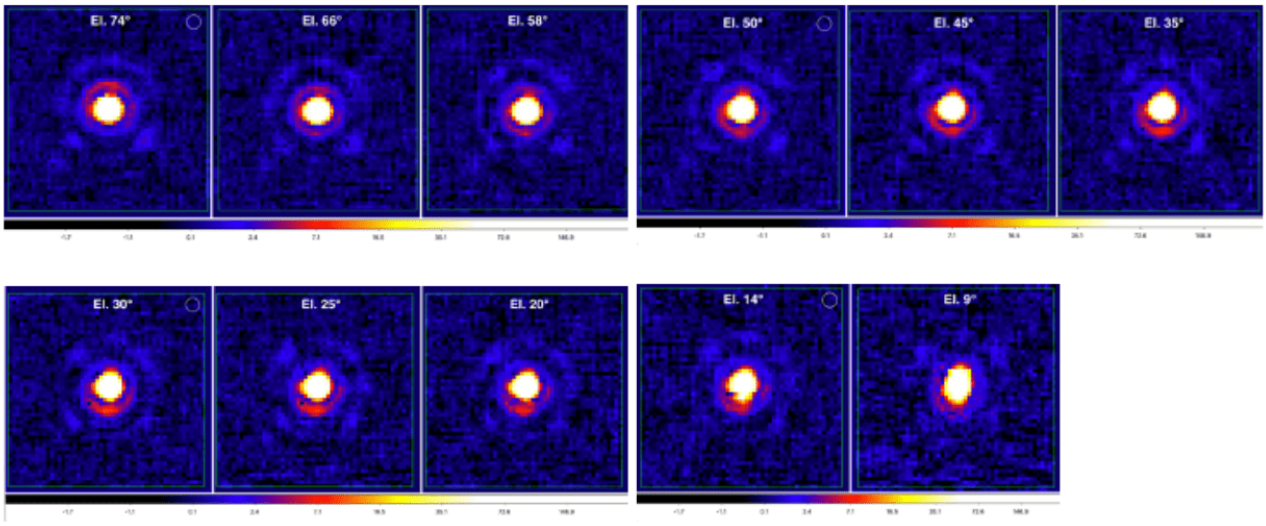

Figure 4.8: Maps of 3C84 at high, mean, low and very low elevations, taken on 23/03/2021 at 8.45 GHz (Egron et al. 2022)

The beam shape characterization was performed at C-band (5.7-7.7 GHz) and K-band during the commissioning (Bolli et al. 2015; Murgia et al. 2016) and during the Astronomical Validation (AV; Prandoni et al. 2017). Below only the results obtained for the X-band are illustrated, consult Egron et al. 2022 for a more in-depth analysis and information on the other SRT receivers.

The data were recently acquired during the recommissioning using the new pointing model (after the active surface actuators were replaced) in June 2018, and after the second stop of the antenna, in September 2020. Data reduction was performed using the Single Dish Imager software (see Sec 2.2).

For the X-band we carried out observations for the beam shape analysis of the X-band receiver on 23 March 2021 with 40 MHz bandwidth, using the Total Power backend. We obtained 11 3C84 Az-El maps ($0.5° \times 0.5°$). Each map covered an elevation range of about 5

deg. For each map we performed a 2D Gaussian fit obtaining the peak counts and the HPBW value, and we measured the background counts rms. Moreover, as the maps were very clean and with high exposition (antenna velocity of 4 deg/min), the side lobes were very clear and we measured count peaks of the second, the third and the fourth lobe (even if the last one was often represented by only few brighter pixels in the background). The results of data analysis are reported in Egron et al. 2022.

In Fig. 4.8 the final images at different elevations are depicted. It can be seen how the shape of the SRT beam at X-band changes its form depending on the elevation, especially at low and high elevations. This behaviour reflects the expectations of this kind of measurements, as the beam shape at the various elevations is affected by the effects of the antenna deformations mainly due to gravitational effects on the structure. By these measurements a deformation parameter has been derived as:

$$\epsilon = \sqrt{(\theta_{az} - \theta_e)^2 + (\theta_{el} - \theta_e)^2} \tag{4.2}$$

where θ_{az} and θ_{el} are the HPBWs of the 2D gaussian fit and θ_e is the theoretical HPBW ($\sim 1.2\ \lambda/\mathrm{D}{=}0.0381^\circ$, which is typical of most radio telescopes Condon and Ransom 2016). The mean beam deformation is $0.17{\pm}0.04$ arcmin, which corresponds to about 7.5% of the beam size, hence compatible with the theoretical value within 10%.

Chapter 5

P-band receiver analysis

The primary (parabolic) focus of the Sardinia Radio Telescope is equipped with a L-P receiver able to acquire the signal in double frequency band (L-band at 1300-1800 MHz and P-band at 305-410 MHz) and double linear polarization, but with the possibility to switch to circular polarization (Valente et al. 2010; Valente et al. 2022b).

The main goal of this chapter is to assess the performances of the P-band receiver and obtain the flux density of Cassiopeia A at this frequency. As said in Sec 2.5.3, we used the Vinyaikin 2014 spectral fit of this Supernova Remnant for the Sun absolute calibration. In the future we are planning to obtain ourselves calibrated measurements of Cas A and obtain other quiet Sun measurements. The P-band could be crucial to constrain the spectral fit model at low radio band.

The Italian Space Agency interests for the P-band receiver are relevant for the communication link by spacecraft of missions that lands in Solar System planets or satellites, during the Entry Descent and Landing (EDL) phases. In this last case, the spacecraft transmits a one-way signal to another spacecraft orbiting the planet/satellite and also to the Earth ground stations at UHF frequency (Maxia et al. 2021). In 2018 with the Sardinia Deep Space Antenna (the space configuration of the SRT Valente et al. 2022b), the Insight Mission 2 was successfully tracked during its EDL phase (Valente et al. 2019).

Analyzing the P-band data is not a trivial task, since they are heavily influenced by external interferences (see e.g. Fig. 5.1) coming from different sources (Zanichelli et al. 2022). In this chapter different analysis methods to reduce the Radio Frequency Interferences (RFI) effects in the P-band are described.

5.1 Radio Frequency Interferences

The L-P frequency receiver bands are strongly affected by the radio environment around the SRT site. In particular, the P-band spectrum is dominated by very strong RFIs, whose origin is of various nature (Zanichelli et al. 2022). Power line broadband radio emissions, broadcasting radio services and emission from electronic devices within the SRT site significantly reduce the usage of the P-band receiver for radio astronomy purposes and cause data loss. However, some countermeasures are usually adopted to limit, for instance, the effects of electronics emission from the antenna on the P-band observation. A metallic cover is usually placed on the Gregorian window to strongly attenuate the power level of the radio emissions coming from the inner rooms of the antenna (elevation equipment room). The implementation of this countermeasure during the P-band observations improves the P-band receiver sensitivity and the P-band spectrum turns out to be slightly cleaner, but it can be still recorded high power level signals coming from the radio environment outside the antenna. These remaining RFI features often are the result of the combination of different signals type having both large (this

is the case of power lines) and narrow band emissions (this is the case of radio broadcasting network). Within a data spectrum, they can generate a variable noise floor level, bump shaped features and comb-like signals, but even narrow spikes having power level much higher than the source signal power level. Two typical RFI spectra acquired in P-band at SRT site are reported in Fig. 5.1. Both the spectra are related to a data sample not containing the radio-source signal, but the result is the same when considering samples taken in the source direction. The spectra, recorded one after 16 minutes from the other and at two elevations differing of 5 degrees, show how the RFI scenario can change during a map acquisition.

In these conditions, the data analysis cannot be performed, as any signature of a radio-source is completely buried due to this RFI mask. Because of these very problematic issues, the characterization of the P-band has not been completed yet. Therefore, preparatory to the data analysis, it is mandatory to remove the effect of the RFI on the data spectrum. So, the data acquisition has been performed considering these two aspects:

- it is necessary to acquire data with a spectro-polarimetric backend;
- specific techniques of RFI excision have to be applied.

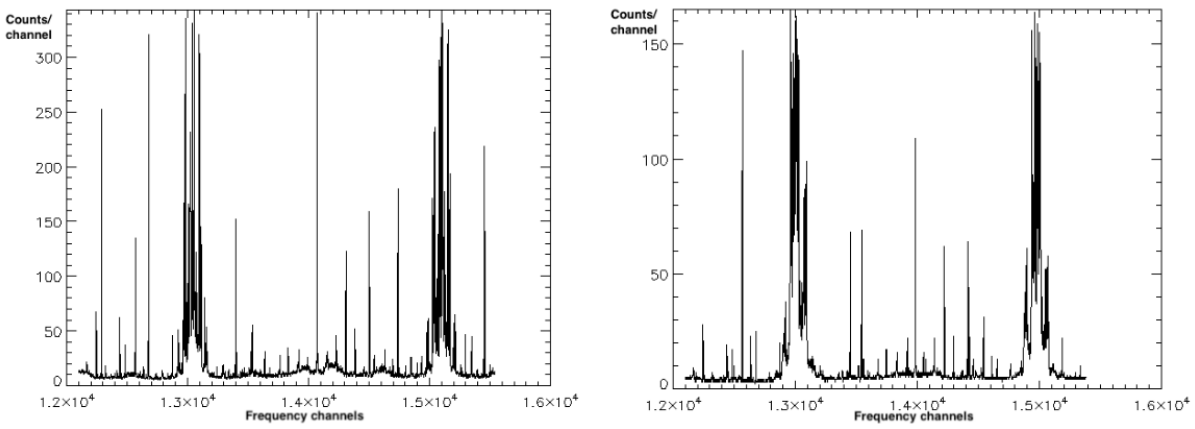

Figure 5.1: Two examples of P-band spectra taken from two map scan samples with 420 MHz bandwidth and 16384 frequency channels. In abscissa the frequency channel number is indicated, corresponding to the 305-410 MHz sky frequency. Both spectra are related to a data sample not containing the radio-source signal, but only the background signal (Iacolina et al. 2022)

As a first step in this direction, we planned a series of observations at P-band using the SARDARA backend (Melis et al. 2018), devoted to customize imaging techniques considering the peculiar features relevant to the spectral environment at this band (e.g., for beam shape analysis) including specific tests for RFI excision. This work was carried out in a collaboration with ASI and INAF personnel.

At the epoch of the observation, the polarization channel 1 of the P-band receiver presented a malfunctioning caused by instability in cables connections. Here, we describe also which has been the effect of this malfunctioning on the acquired data.

5.2 Observation parameters and acquired data

Observation has been performed on 2021/04/17. The selected radio-sources Cassiopeia A and Cygnus A (Cyg A hereafter) are among the brightest point-like sources at this radio frequency band, parameters are listed in Tab 5.1. The Flux density values at 350 MHz are fro the work of Perley and Butler 2017.

Table 5.1: Radio source parameters list.

Source	J2000 Coordinates [RA, Dec] (hh, deg)	Flux density at 350 MHz (Jy)	Angular size (arcmin)
Cassiopeia A	23:23:24.00, 58:48:54.0	~ 5000	~ 5
Cygnus A	19:59:28.36, 40:44:02.1	~ 5800	~ 2

The observing strategy was to perform maps of the two mentioned radio-sources for different front-end and backend settings, mainly considering: available bandwidth and number of frequency channels of the SARDARA backend, polarization filter, Stokes information. Map parameters of the observing strategy are listed in Tab 5.2. The list of the acquired map data with all the relevant backend and receiver configurations are shown in Tab 5.3, along with the elevation value of each map center. Totally, 8 maps were acquired: 3 of them were acquired with subscan direction in the two Horizontal coordinates (i.e., 1 scan with subscans with variable Azimuth and 1 scan with subscans with variable Elevation, with the same instrumental configuration), the other 5 were acquired only with subscans with variable Azimuth. The subscan interleave has been taken as HPBW/3. This choice has been made considering a trade-off between the minimum resolution for performing beam shape analysis (HPBW/4 is the standard value) and the time of the map execution, as multiple tests were planned in one single session. Moreover, at this phase that resolution was enough for performing these specific tests, mainly devoted to RFI excision.

Table 5.2: Map parameters.

Parameter	Value
HPBW at 350 MHz	55 arcmin
Subscan speed	7 deg/min
Subscan interleave	HPBW/3
Map size	5deg x 5deg

Table 5.3: Acquired maps on Cyg A and Cas A during observing session and front-end/backend configurations in azimuth (AZ) and elevation (EL). The Identification name contains the data information on the date/time of acquisition, the source and the scanning direction.

Data identification name	SARDARA Bandwidth [MHz]	Frequency channels number	Stokes	Elevation [deg]
20210417-085250-ASI-CygA_PmapAZ	1500	1024	No	52
20210417-091219-ASI-CygA_PmapEL	1500	1024	No	49
20210417-103616-ASI-CasA_PmapAZ	420	16384	No	65
20210417-105707-ASI-CasA_PmapEL	420	16384	No	63
20210417-112336-ASI-CasA_PmapAZ	420	16384	Yes	60
20210417-114329-ASI-CasA_PmapEL	420	16384	Yes	57
20210417-120754-ASI-CasA_PmapAZ	1500	16384	No	54
20210417-122827-ASI-CasA_PmapAZ	1500	16384	No	51
20210417-124957-ASI-CasA_PmapAZ	420	1024	No	49
20210417-131731-ASI-CasA_PmapAZ	1500	16384	Yes	45
20210417-151523-ASI-CasA_PmapAZ	420	16384	Yes	31

5.3 First data analysis, methodology and results

The data analysis has been performed using the SDI software (see Sec 2.2) and considering the strategies indicated by e.g. Egron et al. 2017 and Loru et al. 2021. The software takes in input a configuration file (inputpars), where parameters can be specified.

With SARDARA backend, the user can select two different backend bandwidths: 420 or 1500 MHz, which can be divided into 1024 or 16384 frequency channels, so increasing the frequency resolution. As the P-band receiver bandwidth is lower than the selectable backend filter bandwidths (105 MHz vs 420 MHz or 1500 MHz), the sky data will be available in a sub-band of the backend bandwidth which can be easily calculated, by recalling the starting and ending frequencies (310-405 MHz) of the receiver. In the case of a data taken at 420 MHz bandwidth divided in 1024 channels, the interval is between 756 and 987 frequency channels. The other possible combinations are listed in Tab 5.4.

Table 5.4: Range of frequency channels for the several combinations of SARDARA backend.

Bandwidth (MHz)	Number of channels	Channel bandwidth (MHz)	Channels range
1500	1024	1.465	215-275
1500	16384	0.092	3390-4420
420	1024	0.410	750-990
420	16384	0.026	12100-15800

Our analysis firstly focused on data taken with a familiar SARDARA configuration that we experienced during radio astronomy observations at other frequency bands with the SRT (i.e., C and K bands e.g., Loru et al. 2021) and without the acquisition of the Stokes parameters. We set the backend by selecting a bandwidth equal to 1500 MHz subdivided into 1024 frequency channels. Results of this first analysis were as expected and with no technical problems, hence after little customization of the imaging software to efficiently plot and visualize the spectrum, we continued to perform the simple production and visualization of the maps, changing backend configurations as listed in Tab 5.4.

All the acquired maps were investigated, obtaining about the same results. In particular, we focused our analysis on these three datasets, being the others with very similar features concerning the spectral situation. We identify the three dataset with the following configuration, considering the parameters indicated in Tab 5.3:

- **Configuration A**: 20210417-085250-ASI-CygA_PmapAZ at 1500 MHz bandwidth subdivided in 1024 frequency channels;
- **Configuration B**: 20210417-124957-ASI-CasA_PmapAZ at 420 MHz bandwidth subdivided in 1024 frequency channels;
- **Configuration C**: 20210417-103616-ASI-CasA_PmapAZ and 20210417-105707-ASI-CasA _PmapEL at 420 MHz bandwidth subdivided in 16384 frequency channels.

On all the three maps a deep analysis has been performed, however the map with 16384 frequency channels Configuration C would need a computer with higher performance in order to perform a deeper analysis in a reasonable amount of time. Here, we present the analysis strategy and the results mainly of the Cas A maps at 420 MHz bandwidth with 1024 channels and 16384 channels, that are the ones with the narrowest bandwidth and having a high number of frequency channels per bandwidth. Results for the Cas A map at 1500 MHz bandwidth with 1024 channels are also presented.

The first step to do after the acquisition of the maps, is to convert them into a ds9[1] readable FITS format. We call this procedure Quicklook and we use the SDI pipeline. The detailed description of the algorithm used and the Quicklook method are beyond the scope of this report. For a deeper insight of the computational procedure and the SDI pipeline, the reader can consult Marongiu et al. 2022.

To verify this result, as a first try, we performed a Quicklook image with no frequency filtering and checked if the real band was identifiable in the spectrum at the expected range. Once verified it, we filtered the frequency channels without the sky signal and made a Quicklook to compare the results, visualizing the total intensity image obtained as the mean of the two polarization signals. In Fig. 5.2, we report the total intensity images obtained after the spectral filtering.

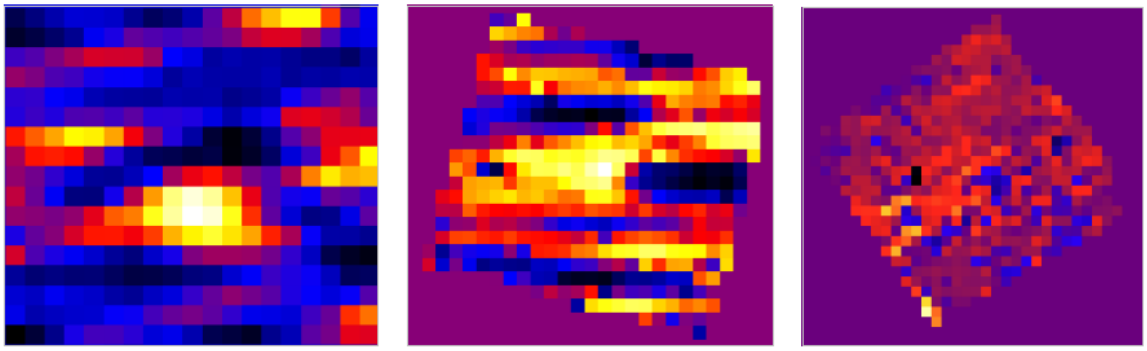

Figure 5.2: Total intensity images obtained simply plotting the quick look after filtering frequency channels with no sky data. Left panel: Cas A map with 420 MHz bandwidth/1024 channels. Centre panel: Cyg A map with 1500 MHz bandwidth/1024 channels. Right panel: Cas A map with 420 MHz bandwidth/16384 channels (this last map is the mean of the maps taken in the azimuth direction - AZ - and in the elevation direction - EL) (Iacolina et al. 2022).

As highlighted in Fig. 5.2, all the images present severe signatures of RFI. In the case of Cas A with 420 MHz bandwidth and 16384 channels, the source is not even visible. Therefore, we need to improve the cleanness of the final result by removing the most notable spikes that bury the signal of the source. This process was not enough to clean the image, since under the strongest RFI, other spikes and bumps were found in a shape similar to Fig. 5.1. A deeper understanding of the data was necessary to obtain the desired result.

In order to simplify the identification and removal of the frequency channels with the interferences, we executed an inspection of the noise behaviour, examining the variation of the spectrum feature in time, polarization and space. We concluded that:

1. the RFIs in the left and right polarization are not identical;

2. even for the same polarization, the RFIs frequency in the spectrum and the background noise level change during the map execution;

3. the RFI amplitude is not constant in time.

In the following, we firstly present the analysis of Cas A map with 420 MHz bandwidth and 1024 channels (Configuration B), and after we show the application of the cleaning strategy to the other two maps: Cyg A at 1500 MHz bandwidth with 1024 channels (Configuration A) and Cas A at 420 MHz bandwidth with 16384 channels (Configuration C), performing some optimizations.

[1] https://sites.google.com/cfa.harvard.edu/saoimageds9

5.3.1 Cas A map in configuration B

The aspects above mentioned made the RFI removal challenging, so we decided to simplify the procedure. Instead of examining both polarizations, we focused only on one of them, also because the polarization channel 1 chain was not working properly.

By examining the quicklook images of the two polarization channels we in fact noticed that the map in the polarization channel 0 (CH 0 hereafter) was looking better than the channel 1 (CH 1 hereafter), it is less noisy and the radio-source is almost visible. The result is reported in Fig 5.3 where a strong and clearly visible RFI signal is evident, highlighted by a black circle. This effect confirms the malfunctioning of the CH 1 channel chain, and hereafter the analysis is performed only by considering the CH 0 channel.

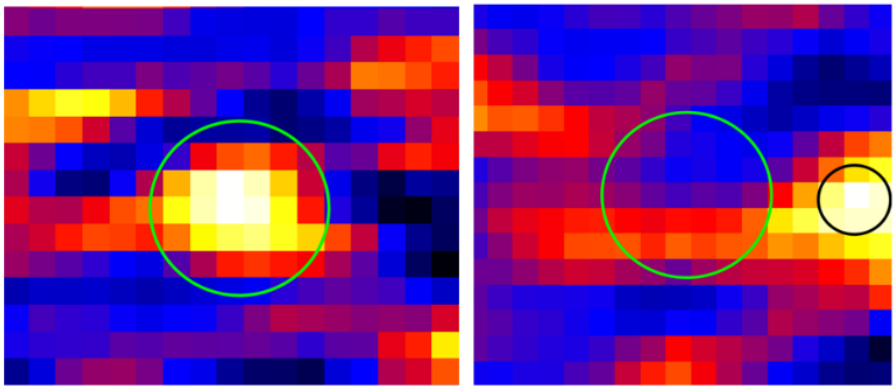

Figure 5.3: Image of the Cas A map in the two polarizations: left panel CH 0, right panel CH 1. The green circles indicate the area in which the source should be present. The black circle indicates the present of a strong RFI in the map (Iacolina et al. 2022).

We tried to isolate the channels with the spikes. We succeeded for the most part, however, some spikes were not easy to associate with the corresponding frequency channel. We hence customized the software by adding an interactive plot with the possibility of zooming the spectrum, view several plots at the same time, and other features. It was a very useful task, but it did not fix the issue. To improve the cleaning procedure, we hence activated the spatial filter option in the input parameters file. The spatial filter removes spikes signature in a specific region of the coordinates map whose maximum height and width can be set in the inputpars. However, not only it did not work as expected, but also sometimes the filter identified the source as an RFI and removed it from the images, while not eliminating the actual interferences.

We then took two different approaches to clean the image:

- a large spectrum flagging, removing all possible frequency ranges in which RFI signatures were present in the whole P-band spectrum;
- a selection of multiple sub-bands of the whole P-band spectrum identifying the cleaner frequency channels interval, with addition of flagging of subchannels inside this frequency range.

In Fig. 5.4, we plot the resulting map and a Table of a summary of the frequency channels flagged manually after a large cleaning.

From Fig. 5.5 to Fig. 5.9 we report the resulting maps obtained considering a selection of multiple sub-bands of 50 channels with addition of sub flagging and related Tables.

For the first approach, the only frequency channels that were saved from cleaning were 26 (about 11 MHz), which is about the 10% of the initial bandwidth. For the second method, we obtained the best results in the 850-900 and 900-940 interval (Fig 5.7 and Fig 5.8), and the

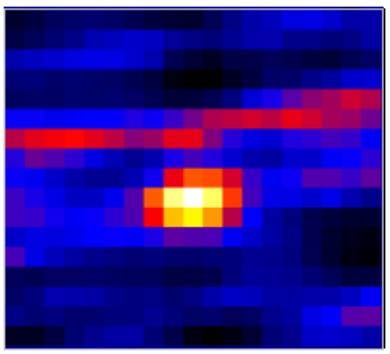

Channel interval	Flagged subchannels
750-990	752-781
	786-797
	800-846
	850-861
	867-909
	914-925
	931-990

Figure 5.4: Left panel: image of Cas A map with frequency channel range 750-990 and strongly filtered for any feature of RFI in the broad spectrum. Right panel: table with the frequency channel range and removed subchannels.

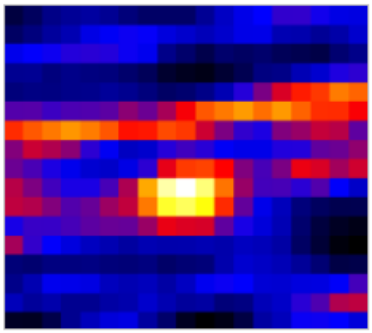

Channel interval	Flagged subchannels
750-800	753-757
	761-765
	771-774
	776-781
	786-789
	794-797

Figure 5.5: Left panel: image of Cas A map with channel range 750-800 of 50 channels. Right panel: table with the channel range and removed subchannels.

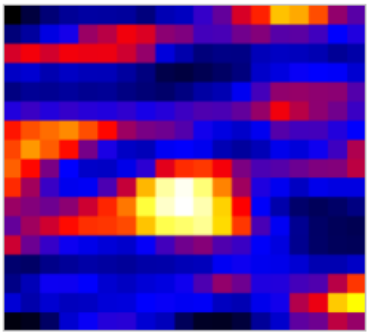

Channel interval	Flagged subchannels
800-850	803-806
	810-824
	826-829
	835-838
	843-846

Figure 5.6: Left panel: image of Cas A map with channel range 800-850 of 50 channels. Right panel: table with the channel range and removed subchannels.

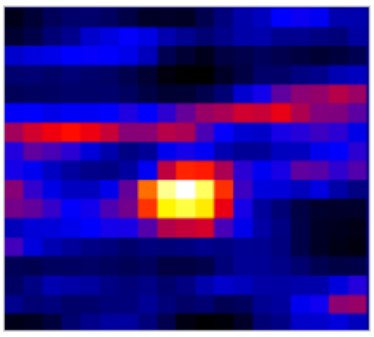

Channel interval	Flagged subchannels
850-900	850-852
	858-861
	854
	867-870
	874-878
	882-888
	890-895

Figure 5.7: Left panel: image of Cas A map with channel range 850-900 of 50 channels. Right panel: table with the channel range and removed subchannels.

band was reduced to 18 channels (7.4 MHz) and 15 channels (6.2 MHz) respectively, which is the 35% of the initial sub-band in both cases. By comparing images in Fig 5.7 and in Fig 5.8

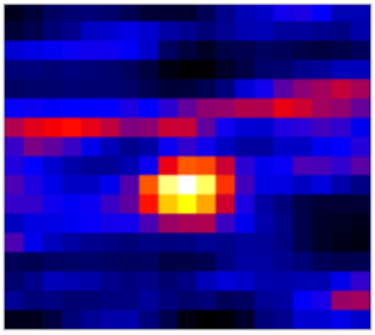

Channel interval	Flagged subchannels
900-940	901-906
	907-909
	914-917
	922-925
	931-934
	938-940

Figure 5.8: Left panel: image of Cas A map with channel range 900-940 of 40 channels. Right panel: table with the channel range and removed subchannels.

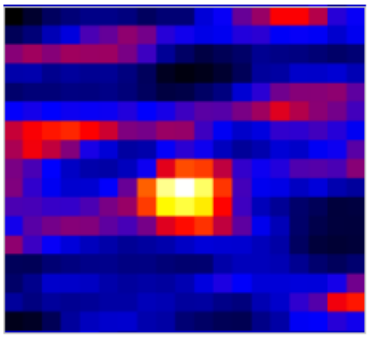

Channel interval	Flagged subchannels
940-990	940-944
	946-968
	971-974
	978-981
	987-990

Figure 5.9: Left panel: image of Cas A map with channel range 900-940 of 40 channels. Right panel: table with the channel range and removed subchannels.

it can be seen that there is no significant difference among the maps after the cleaning. The result is better than the one with no filtering, however some irregularities and noise are still present even with a large flagging.

5.4 The threshold spectral filter

The turning point came with the development of a special threshold in the spectral filtering of the SDI software (see Sec 2.2). A new option called *spike* was added in the input parameters file. The new process works with several steps: SDI calculates the mean of the 10% lower counts for each sample spectrum, then it multiplies the result for the spike factor (e.g., a value of 5). Finally, it removes all the frequency channels whose counts value is above this threshold. We considered the percentage of 10% of the lower counts as this resulted from the analysis explained above as the worst case of clean bandwidth after filtering, and hence represents the signal level of the source or the sky (depending on the direction). Moreover, this percentage, representative of the clean part of the spectrum baseline, has been obtained experimentally even in other RFI studies at this band. This method resulted in the best outcome so far, which is shown in Fig. 5.10.

In Fig. 5.11, we show a comparison of the results obtained during the three main phase of cleaning of the Cas A maps with 420 MHz bandwidth and 1024: in the left panel, the extrapolation of all the frequency channels within the real receiver band (750-990); in the central panel, the map after a large filtering; in the right panel, the map in the channel range 750-990 after the spectral threshold filter superimposed to a smoothing effect.

After the application of the spectral filtering, we observe a remarkable improvement in the image quality, but since it is an automatic process, which adjust the filtering at each data sample, it is difficult at this level, to have a precise estimation of the number of frequency

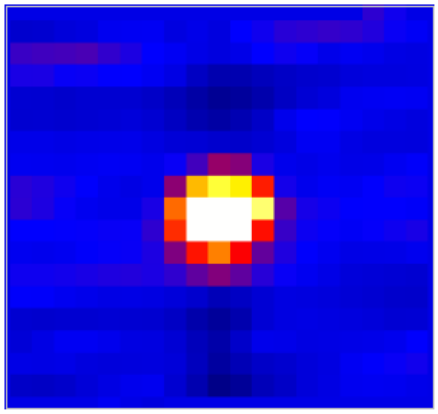

Figure 5.10: Image resulted from the map elaborated considering all the P-band frequency range (750-990 channel range) and filtered only with the threshold spectral filter.

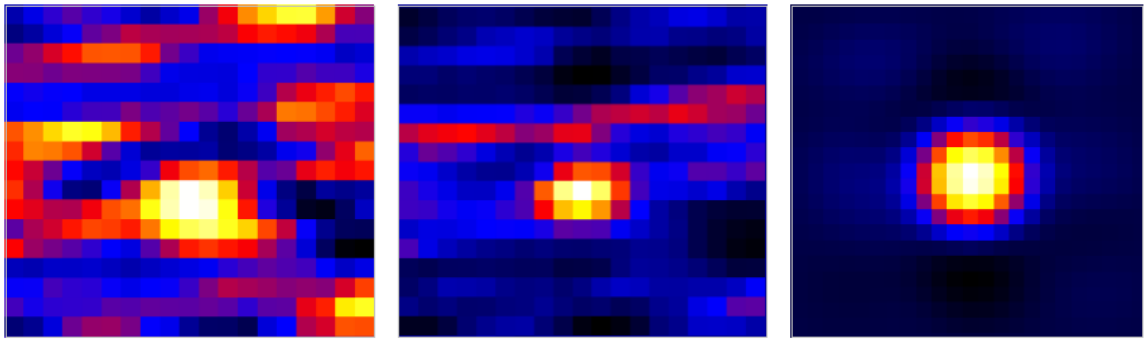

Figure 5.11: Cas A maps with 420 MHz bandwidth and 1024 channels obtained with cleaning considering: left panel, channels within all the real receiver band; central panel, large filtering of all RFI signatures; right panel, spectral threshold filtering and smoothing.

channels left after the cleaning. Also considering that the removed channels could be different for different data samples since, as mentioned above, the RFI spectrum is strongly variable. This aspect could lead to complications in case of a calibration analysis: since the final band available at the end of the cleaning could be different between the calibration source and the target, the physical quantity of interest could be wrongly calculated. Hence, further customization is needed. However, for other procedures (e.g., checking the P-band receiver working condition and beam shape characterization) it is already a powerful tool that can be greatly beneficial to the analysis procedure.

5.4.1 Application of the spectral filter to Cyg A map in configuration A

Once verified the powerful effect on the Cas A maps with 420 MHz bandwidth and 1024 channels, we applied the spectral threshold filter to the Cyg A map at 1500 MHz bandwidth with 1024 channels. The result is depicted in Fig. 5.12, Fig. 5.13 and Fig. 5.14. Again, most of the RFI signatures were easily removed from the map.

After the selection of the sky signal (channels 210-280) we thought that the CH 1 could be less affected from the RFI, in opposition to the Cas A case. On the contrary, after the spectral filtering procedure, we found again that the CH 0 is the cleaner one; it was only contaminated by RFIs and leads to a better result. The spectral filtering had no substantial effect on the quality of the map, as can be seen from Fig. 5.13, confirming the effects of the malfunctioning of CH 1 chain.

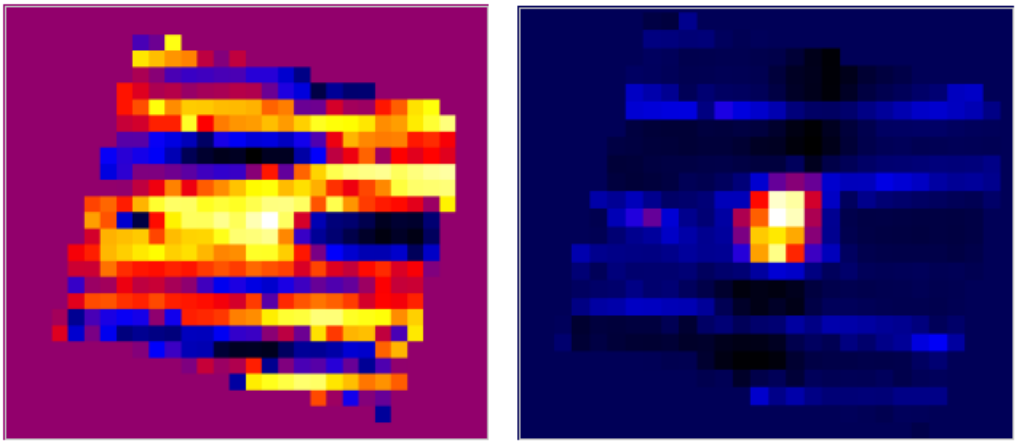

Figure 5.12: Comparison of the Cyg A maps at 1500 MHz bandwidth with 1024 channels CH 0 (obtained after selection of the P-band receiver, 210-280 channel range) before (left panel) and after (right panel) the application of the spectral threshold filter (Iacolina et al. 2022).

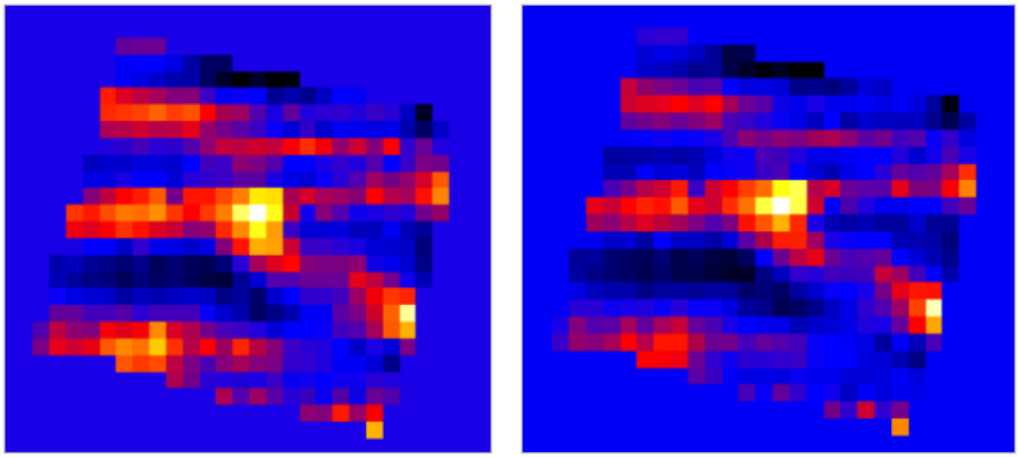

Figure 5.13: Comparison of the Cyg A maps at 1500 MHz bandwidth with 1024 channels CH 1 (obtained after selection of the P-band receiver, 210-280 channel range) before (left panel) and after (right panel) the application of the spectral threshold filter (Iacolina et al. 2022).

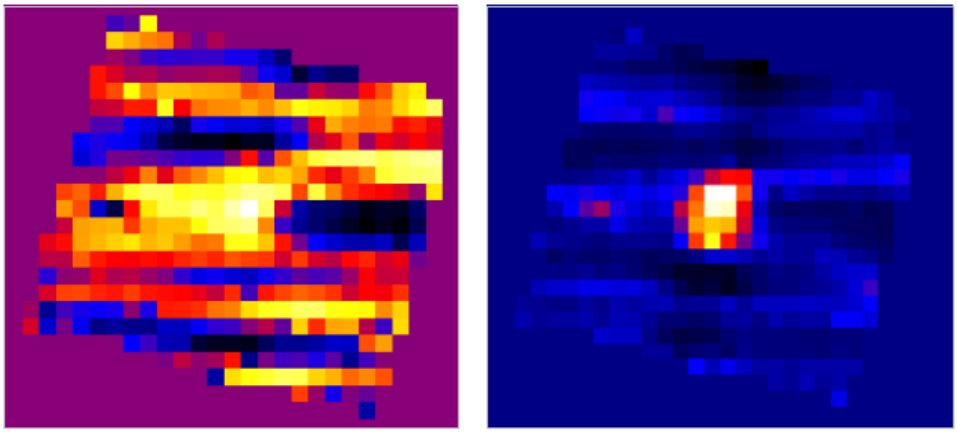

Figure 5.14: Comparison of the Cyg A maps at 1500 MHz bandwidth with 1024 channels Total Intensity (obtained after selection of the P-band receiver, 210-280 channel range) before (left panel) and after (right panel) the application of the spectral threshold filter (Iacolina et al. 2022).

5.4.2 Application of the spectral filter to Cas A map in configuration C

The Cas A maps at 420 MHz bandwidth with 16384 channels have been performed in both the Horizontal coordinates. The analysis started inspecting the two maps separately with

the aim to clean them once at time, and after merging them to increase the sensitivity of the measure. Unfortunately, the map with variable Azimuth was very dirty in both polarizations and no RFI excision technique was enough to obtain an acceptable result. Hence, we decided to focus our analysis on the map with variable Elevation, whose rough data were definitely cleaner. We attributed this difference to possible strong all-band RFIs that affected the data during the first map execution time and that disappeared almost at the end of the completion of this first map.

The Elevation map was inspected in both the polarizations. As for the maps presented in the previous Sections, we tried different settings of the RFI excision filters, trying to select and flag the frequency channels mostly affected by RFI signatures. The most effective RFI filter has been the spectral threshold filter since, even in this case, neither with the large flagging filtering nor with the spatial filter we obtained acceptable results.

In Fig. 5.15, the Cas A map at 420 MHz bandwidth with 16384 channels is depicted with no filtering (only the spectral selection of the receiver band frequency channels was applied). The figure shows the signal in the: total intensity (TI left panel), polarization channel 0 (CH 0 central panel), polarization channel 1 (CH 1 right panel).

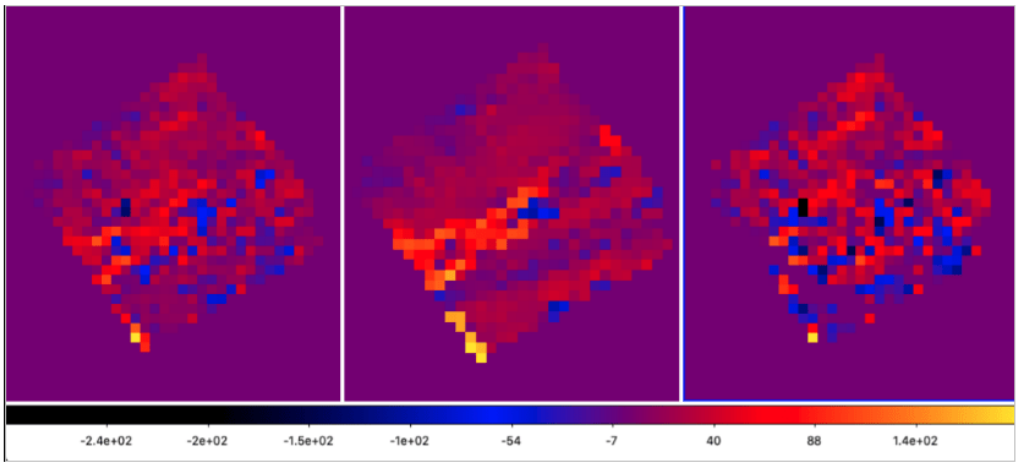

Figure 5.15: Cas A map at 420 MHz bandwidth with 16384 channels with no filtering (only P-band frequency channels selected): left panel: TI; central panel, CH 0; right panel, CH 1 (Iacolina et al. 2022).

In none of the images in Fig. 5.15 the source is minimally visible. The RFI signatures are completely burying the radio-source signal. We hence decided to apply the threshold spectral filter.

We tried different values of the *spike* parameter, and a deep analysis was made in order to optimize the result. We indeed applied the threshold filter and tried to flag specific spectral channels particularly compromised by strong RFI. Once applied it, we identified and removed channels in 2 main spectrum regions very polluted by strong RFI signatures. Channels involved are in these two ranges: [12500:13300] - [14650:15500]. Further frequency channel flagging did not significantly improve the result, on the contrary, it removed part of the source signal.

The spatial filtering (removal of RFI signature in the space/coordinates domain) was not effective on the data and besides resulted in a flagging of the source in some cases. Therefore, we decided to disable it.

The application of the above-mentioned indications was effective on the CH 0 map. While it could not effectively clean the signal of the CH 1 map. We, hence, decided to focus our analysis only on CH 0, confirming even in this case that CH 1 was not working properly.

In order to evaluate the goodness of the result and in particular the best value for the parameter *spike* of the threshold filter, the following aspects were taken into account:

- visual inspection of the map and of the spectrum after RFI filtering;
- 2D Gaussian fit parameters (Gaussian peak height, HPBW in the direction of the 2 axes of the elliptical section and their ratio);
- rms of the map background;
- signal to noise ratio (SNR) of the Gaussian maximum with respect to the background rms.

In this work I will report only the measurements when the best filter is applied, which resulted to be 15 for the *spike* parameter, and when the filter is not applied (see Tab 5.5). The results obtained with all the spike parameters we tried, including the one from Tab 5.5, are available in Iacolina et al. 2022.

Table 5.5: Results of the analysis for the inspection of the best value for the spike parameter. Other applied flagging was the filtering of the 2 very polluted zone - [12500:13300] [14650:15500]. The SNR was calculated by the formula: $10 \cdot log_{10}(Gauss\_max/rms)$.

	2D Gaussian fit Parameters					
Spike parameter (value)	X (arcmin)	Y (arcmin)	X/Y	Gauss Max (cts)	map rms (cts)	SNR (dB)
Not applied	74.3	65.6	1.1333	5.5	0.0108	27.06
15	70.4	53.6	1.3126	5.6	0.0075	28.76

Fig. 5.16 and 5.17 depict the spectra of a signal sample of the first map sub-scan for the various chosen RFI filter method. In the left panel of Fig. 5.16, the plot represents the spectrum related to the frequency band of the receiver with no other flag applied. Only a very strong (of the order of 108 counts) spike is visible as the rest of the spectra is flattened due to the high vertical scale. In the right panel of 5.16, the spectrum with flagging of the very polluted main 2 regions is shown. Again, strong spikes are present, and the sky spectrum is only slightly visible. Left panel of 5.17 shows the spectrum when the threshold filter with spike=15 was applied. The situation is strongly changed and even if several spikes are always present, the sky flat spectrum (in this frequency band) is significantly evaluable in about 10 counts per channel on average. Right panel of Fig. 5.17 show the spectrum where both the two flagging were applied.

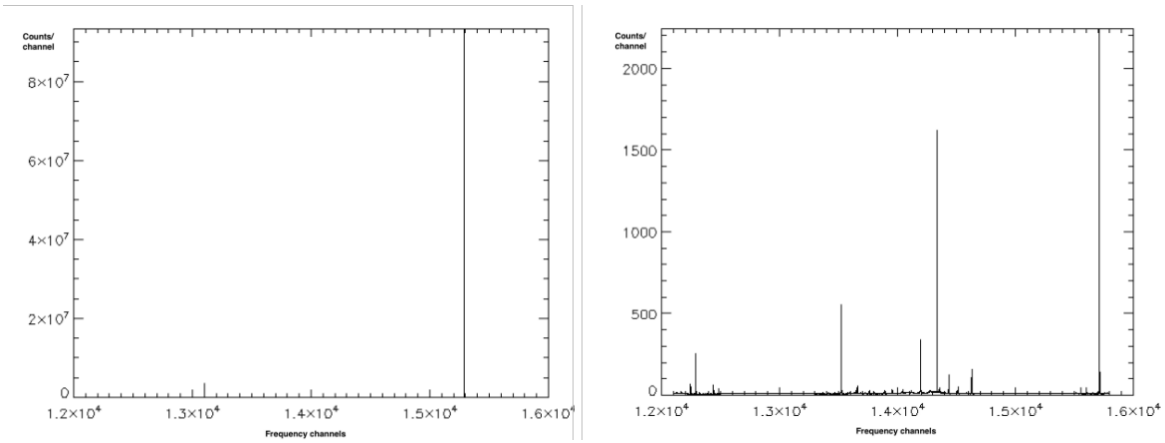

Figure 5.16: Spectra related to the various stages of RFI excision. Left panel No flagging. Right panel only 2 zone flagging (Iacolina et al. 2022).

Fig. 5.18 shows that the images in the various panels reflect the behavior of the related spectra just described for the spectra of Fig. 5.16 and 5.17. In particular, the maps of Fig.

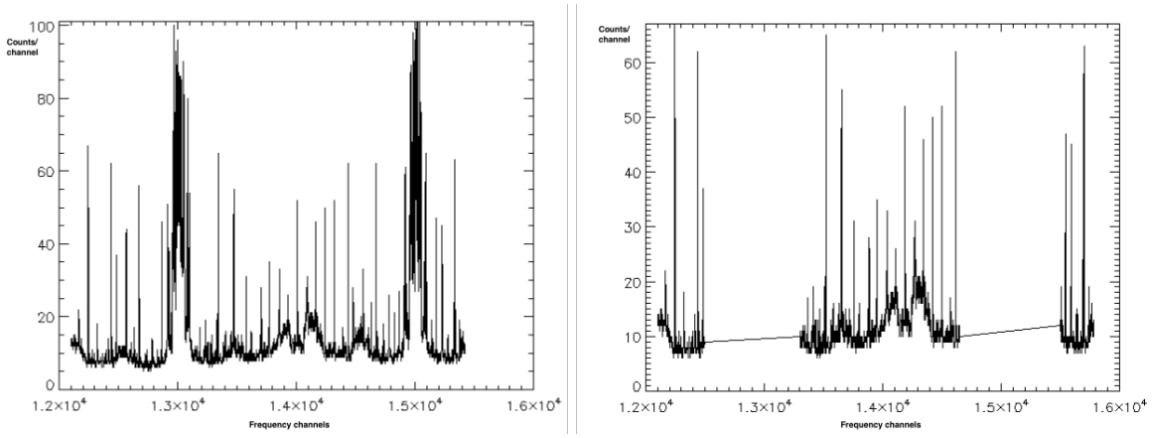

Figure 5.17: Spectra related to the various stages of RFI excision. Left panel Only threshold filter with spike=15. Right panel Threshold filter with spike=15 superimposed to 2 zone flagging (Iacolina et al. 2022).

5.18 panel c. and d. highlight the improvement in using both the threshold filter and the flagging of very polluted specific zones instead of using only the threshold filter, even if also the source brightness is slightly reduced. Further flagging of other spectrum channels did not significantly improve the result.

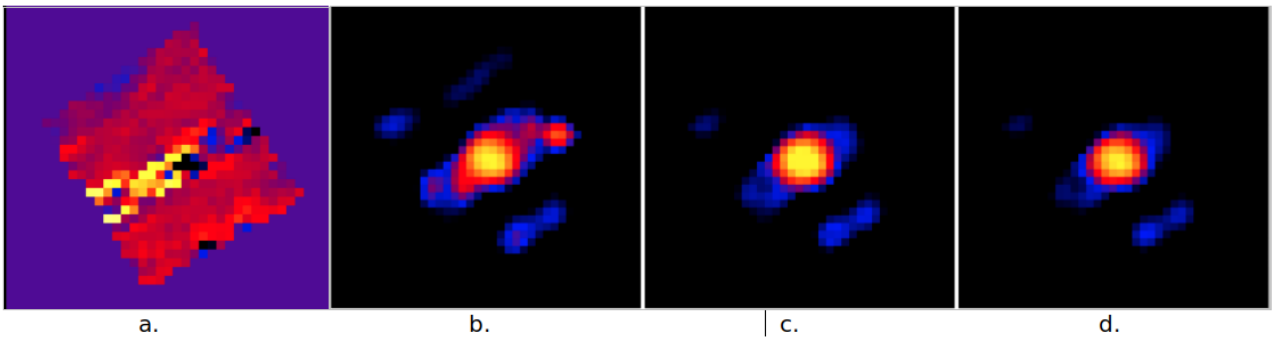

Figure 5.18: Comparison between the various stages of RFI excision. a. No flagging. b. Only 2 zone flagging. c. Only threshold filter with spike=15. d. Threshold filter with spike=15 superimposed to 2 zone flagging. All the images show the CH 0 signal represented in logarithmic scale. The last three maps have the same count limits and colorbar (Iacolina et al. 2022).

5.5 Results, conclusions and future developments

The main scope of this Chapter was to preliminary assess imaging technique in P-band using the SRT and obtain the flux density of Cassiopeia A at this frequency. Therefore, we planned an observing campaign of the strongest radio source calibrators at this band. Cygnus A and Cassiopeia A were chosen to this aim and data with different front-end and backend configurations were acquired.

As the P-band frequencies are strongly affected by RFI, the most problematic issue in performing the data analysis was to handle with the cleaning of the data. Different RFI excision techniques were tried and the most effective was the application of a threshold spectral filter, so removing all the frequency channels in which the signal exceeded the spike factor multiplied for the mean of the 10% lower counts for each sample spectrum. This work aimed also to find a method to optimize the spike factor. This threshold spectral filtering method was so effective that allowed the source to emerge from the noise and to have a preliminary evaluation of the beam shape at P-band.

The data analysis indicated an elliptical beam shape with HPBW in the larger axis to be about 70 arcmin instead of about 55 (i.e., as the theoretical HPBW for P-band at 350 MHz).

This so high discrepancy could be due to a lack of resolution in the maps which were acquired with only 3 sub-scans per beam with an interleave of about 18 arcmin. This choice was made to save time during the observation session in order to acquire maps with all the possible configurations in a reasonable amount of time, even because this imaging campaign was performed with the aim of testing technological (first maps acquired and analysed with this strategy, technique and software using the SARDARA backend at P-band) and data reduction capabilities.

Another issue that we faced on was related to the performance of the two P-band polarization channels. In all the examined maps, the CH 1 was strongly affected by an all-band noise that was impossible to clean with all the tried techniques. This all-band noise was also intermittent and buried the radio-source signal without any possibility to recover it after RFI excision. Therefore, as even a so strong radio source could not definitely emerge from the noise, we concluded that this behavior confirmed the malfunctioning of the CH 1 receiver chain that was present during the data acquisition.

Future specific observing campaign should be undertaken to complete and optimize this work in light of the results achieved here. Some considerations have to be taken into account for the future observations, which could be focused only to configurations with the narrowest bandwidth and the highest number of frequency channels. Higher spectral resolution will allow to perform a more effective RFI excision and a more accurate beam shape measurement. Four scans per beam will allow to obtain the desired information, but eight scan/beam could give better results as shown by Egron et al. 2022 at L-band.

Furthermore, an optimization of the threshold spectral filter should be done performing the identification of the removed frequency channels. This will allow to evaluate the effective bandwidth (the total bandwidth minus the removed channels) and the central frequency resulting after the RFI excision. In case of flux calibration of the data, specific techniques considering customized trade-offs will be evaluated. In order to perform an accurate flux calibration, the statistic of the flagged channels has to be taken into account during the calibration process with the calibration source.

L-P receiver will be upgraded in order to improve the performances of the system, taking into account the mitigation of the main radio frequency interferences (Ladu et al. 2022)

Chapter 6

Conclusions

In this Thesis I presented the results obtained during my three years of PhD dedicated to the study of the Sun environment and its emission mechanisms at radio frequencies.

Since 2018 we have been observing the Sun in K-band (18-26 GHz), in the context of the SunDish project, with Medicina and SRT. Both radio telescopes were not initially designed to perform solar observations, therefore, the team has developed an imaging configuration for such observations with both instruments. I took part in several phases of the research program. Firstly, I participated in the development and test of the software pipeline (SUNPIT) we implemented for the solar data. I dedicated a large part of my work to the data analysis, imaging of the Sun and provide the archive on the website devoted to the SunDish project. Currently, we have more than 300 maps uploaded, starting from 2018. I contributed in the planning and execution of the observing sessions during these three years, both at SRT and at Medicina. One of my main role in the project, apart from scientific data analysis development and operations, was to develop and optimize an innovative calibration procedure for the solar maps. At present, I am the coordinator of solar calibration operations (and related developments) within the SunDish project. This calibration procedure is based on the Supernova Remnant Cassiopeia A as a flux reference, instead of more standard calibrator like the New Moon (see Silva et al. 2005 or Fedoseev and Chernyshev 1998) which is usually used at these radio frequencies. This is a challenging procedure since this calibrator is an extended source (resolved at our frequencies) and it is currently in expansion. However, due to its strong flux, Cassiopeia A presents several advantages compared to other standard calibrators and its brightness variation is well studied in the literature.

Regarding the main results obtained in this Thesis work, in part A, I illustrated strategies, techniques and the scientific potentialities of the new solar observing system of INAF radio telescopes, with a focus on radio continuum imaging of ARs features and related statistics. Our observations show that the so-far poorly explored 18-26 GHz frequency range harbors very dynamical processes in the chromosphere that require smart and frequent mapping of the entire solar disk.

I obtained unprecedented and very precise calibrated measurements of the QS in the K-band and verified the trustworthiness of the SNR Cas A as a solar calibrator through an accurate error analysis. Our QS values are affected by a mean relative error of 3%. This is an extremely important result, since Cas A could be one of the few calibration source visible at higher frequencies where the opacity has an even greater impact on the map quality. We obtained a flatter trend in the QS spectrum with our values compared to the literature. At 18.8 GHz we have an almost perfect accordance with the theoretical value, while at 24.7 and 25.5 GHz we have a deviation up to 3.7% from the Landi and Chiuderi Drago 2008 fit. This deviation could derive from physical origins or external factors, such as the weather conditions, that could have affected our data. However, since we are within 2 σ of deviation

from the Landi and Chiuderi Drago 2008 fit, new dedicated observations are required to verify the significance of our deviations.

We encountered some anomalies in the QS calibrated measurements starting from 2021. The recent observations with the Medicina radio telescope suggest a possible strong contribution from the SRT LNA deterioration and a not ideal attenuation parameter set. However, even with the ideal conditions, the data from Medicina present a slight deviation from the expected values, which could be explained by the raising of the solar activities and the contribution from the semi active regions. If this last hypothesis will be conformed, the observations in K-band could be reviled to be a precious probe of the solar activity during the solar cycle.

Our ARs spectral data offer clues about the possible existence of sporadic gyro-resonance emission above ~ 26 GHz even around the solar minimum. Moreover, we found an interesting case of a possible correlation between an anomalous value of an AR spectral index and the origin of a flare. We will need further statistics, but it is still an indication of how the K-band continuous monitoring of the Sun could be a crucial tool for Space Weather applications.

In Part B, I presented the studies performed to assess the frequency stability requirements for SDSA in order to be able to perform a tracking experiment exploiting radio science technique like those planned with the BepiColombo and JUICE Mission. We started from the literature and found the principal noise sources which could affect the measurements. Then, we collected and presented the values reported in literature for the most stringent radio-science experiments requirements.

We also investigated the brightness temperature that the receivers at the X and Ka bands must withstand in order to observe the Sun and its near environment. These data will be useful to design a specific solar attenuation set up for each frequency range and allow us to perform solar observations in these bands.

For the P-band (305-410 MHz) I presented a new reliable method, a spectral filter, to remove the majority of the RFI afflicting this frequency rage. This technique was so effective that allowed the source to emerge from the noise and let us have a preliminary evaluation of the beam shape at P-band. Future specific observing campaign will be undertaken to complete and optimize this work in light of the results achieved in this Thesis. In the future we are going to further develop the spectral filter. We need to be able to valuate the effective bandwidth (the total bandwidth minus the removed channels) and the central frequency resulting after the RFI excision, in order to perform an accurate flux calibration of Cassiopeia A with Cygnus A.

The studies presented in my Thesis gave rise to several publications. I am the first author of the ASI technical report Mulas et al. 2022. Moreover I am co-author of: two papers Pellizzoni et al. 2022 and Valente et al. 2022a; three INAF internal reports Marongiu et al. 2021, Marongiu et al. 2022, Egron et al. 2022 and two other ASI technical reports Maxia et al. 2021 and Iacolina et al. 2022. I am also working on a new ASI technical report: Iacolina, Mulas et al. 2022 (work in progress).

For the future of SRT/SDSA solar observing capabilities, there is the plan to upgrade the system with new receivers and configurations that will help deepen our understanding of the solar phenomena presented in this work. For the SDSA, new receivers in K (25.5–27.0 GHz) and Ka (31–33 GHz) bands will be implemented, which will allow us to simultaneously covering the X (8–9 GHz) and K or X and Ka bands. With the installation of the apposite attenuation set ups, they may play a crucial role to constrain the frequency range of AR gyro-resonance emission. To date, this component has been detected till 15–17 GHz (see Nindos, 2020 and references therein). The K and Ka bands lie in the uncertainty range, where it is not clear the distinction of free-free and gyro-resonance emission (Nindos 2020; Pellizzoni et al. 2022). That is why there is the need of more imaging observations to better understand the

boundaries between the two components. At 34 GHz Selhorst et al. 2008 modelled the ARs emission as purely free-free. The new SRT receivers Q-band (33-50 GHz) and W-band (75-116 GHz) from the PON will help to further constrain the thermal components. In addition, the temporal variations of AR in the X-band can be used as a prognostic criterion in the prediction of Space Weather phenomena such as powerful eruptive events (Borovik et al. 2012) which could be associated with geomagnetic disturbances.

Last but not least, in order to expand the range of scientific applications of the SunDish project, I am also taking part in the new Solaris project. Its principal aim is to continuously monitor the Sun at high radio frequencies with single-dish imaging techniques by combining the implementation of a dedicated and interchangeable 100 GHz receiver on existing small radio telescope systems (1.5/2.6m class) available in the laboratories of our research groups and in national facilities in Antarctica.

Acknowledgements

I wish to express my sincere gratitude to all those who supported and helped me to achieve this important objective.

I would like to thank Prof. Andrea Possenti who allowed me to undertake this work.

A very special gratitude goes to Dr. Alberto Pellizzoni, Dr. Elise Egron and Dr. Noemi Iacolina, for their teachings during these years. Their guidance made me discover new challenging and interesting topics, from solar physics to space science. They strengthen my passion for radio astronomy and helped me greatly to improve my knowledge.

I very warmly thank Dr. Marco Marongiu and Dr. Giulia Murtas. It would have been extremely difficult to complete the work presented in this Thesis without their precious help.

I would like to thank Dr. Massimo Gervasi and Dr. Mauro Messerotti for their comments and suggestions that have helped me to improve my thesis.

I acknowledge contributions from the Italian Space Agency for ASI/Cagliari University grants no. N. 2019-13-HH.0 and no. 2020-34-HH.0.

I sincerely thanks the SunDish and SDSA teams for these years of fascinating and fruitful work.

I would like to thank all the staff from the University of Cagliari, the Department of Physics, and Observatory of Cagliari for their help during these years.

To all my friends and colleagues a special thanks for having shared the most beautiful moments of these years, you all contributed in making this PhD experience even better.

Last but not least, I am grateful to my family. Without their precious support, none of this would have been possible.

Appendix A: Summary of Medicina and SRT observations

Table 6.1: Summary of Medicina and SRT observations. *ID* indicates the identification number for each single map, where the letters *M* and *S* specify the radiotelescope (Medicina or SRT); an asterisk flag is shown for images presenting significant artifacts. *Epoch* indicates the observation date, *T* the acquisition time interval of the map, and $\nu_{\rm obs}$ the central observing frequency; $\sigma_{\rm disk}$ represents the standard deviation of the solar disk brightness distribution with respect to the QS level reported in Table 3 of the paper. AR_n indicates the number of identified ARs in each solar map.

ID	Epoch	T (UT)	$\nu_{\rm obs}$ (GHz)	$\sigma_{\rm disk}$ (K)	AR_n
*M*1	2018 Feb. 15	11:20-12:20	24.1	129.8 ± 4.0	1
*M*2	2018 Feb. 15	12:22-13:22	24.1	114.5 ± 3.6	1
*M*3	2018 Feb. 19	10:14-11:30	24.1	102.4 ± 3.8	1
*M*4	2018 Feb. 19	11:33-12:49	24.1	145.2 ± 3.5	0
*M*5	2018 Feb. 27	09:39-10:50	23.6	160.2 ± 4.2	1
$*M6$	2018 Feb. 27	10:52-12:02	23.6	269.4 ± 18.6	1
*M*7	2018 Mar. 7	13:50-15:00	23.6	129.5 ± 3.9	1
*M*8	2018 Mar. 7	15:02-16:05	23.6	148.0 ± 7.0	0
*M*9	2018 Mar. 9	12:11-13:20	23.6	180.5 ± 5.1	1
*M*10	2018 Mar. 9	13:22-14:33	23.6	134.0 ± 3.9	1
*M*11	2018 Mar. 28	10:05-11:20	23.6	103.1 ± 3.1	0
*M*12	2018 Mar. 28	11:22-12:37	23.6	126.3 ± 3.4	0
$*M13$	2018 Mar. 30	09:45-11:00	23.6	137.1 ± 4.3	1
$*M14$	2018 Mar. 30	11:02-12:18	23.6	121.9 ± 3.5	2
*M*15	2018 Apr. 2	09:45-11:00	23.6	145.5 ± 4.8	2
*M*16	2018 Apr. 2	11:02-12:18	23.6	171.6 ± 4.1	2
*M*17	2018 Apr. 6	10:34-11:50	23.6	163.8 ± 3.8	2
*M*18	2018 Apr. 6	11:52-13:07	23.6	156.3 ± 3.5	1
$*M19$	2018 Apr. 7	09:39-11:26	23.6	121.6 ± 3.3	2
*M*20	2018 Apr. 7	11:28-13:14	23.6	155.0 ± 4.0	0
*M*21	2018 Apr. 12	10:20-11:22	18.1	133.6 ± 3.1	3
$*M22$	2018 Apr. 12	11:24-12:26	26.1	228.3 ± 7.4	0
*M*23	2018 Apr. 13	07:30-08:39	18.1	103.5 ± 2.8	1
$*M24$	2018 Apr. 13	08:40-09:47	26.1	175.1 ± 5.2	1
$*M25$	2018 Apr. 13	10:00-11:09	22.1	132.8 ± 2.8	3
$*M26$	2018 Apr. 13	11:11-12:20	18.1	100.7 ± 3.1	3
*M*27	2018 Apr. 17	10:45-11:47	18.1	219.0 ± 8.4	1
*M*28	2018 Apr. 18	11:20-12:29	18.1	121.2 ± 2.4	5
*M*29	2018 Apr. 18	12:31-13:40	26.1	209.6 ± 5.1	1
*M*30	2018 Apr. 19	09:40-10:43	18.1	128.6 ± 3.8	2
$*M31$	2018 Apr. 19	10:45-11:48	26.1	264.2 ± 7.0	0
*M*32	2018 Apr. 20	07:40-08:58	18.1	108.8 ± 2.4	2

Table 6.1: Continued.

ID	Epoch	T (UT)	$\nu_{\rm obs}$ (GHz)	$\sigma_{\rm disk}$ (K)	AR_n
*M*33	2018 Apr. 20	09:25-10:39	26.1	217.8 ± 5.6	1
*M*34	2018 Apr. 20	10:45-12:03	23.6	153.8 ± 3.4	1
*M*35	2018 Apr. 23	09:31-10:48	18.1	144.3 ± 2.7	1
*M*36	2018 Apr. 23	10:51-12:08	18.1	70.3 ± 1.1	1
*M*37	2018 Apr. 25	10:45-12:02	18.1	112.9 ± 2.1	1
*M*38	2018 Apr. 26	09:00-10:17	18.1	122.5 ± 2.9	1
*M*39	2018 Jun. 10	10:15-11:30	18.1	126.2 ± 3.2	2
*M*40	2018 Jun. 10	11:32-12:47	26.1	204.1 ± 7.2	1
*M*41	2018 Jun. 17	08:56-10:10	18.3	90.0 ± 2.6	1
*M*42	2018 Jun. 17	10:12-11:27	26.1	258.7 ± 5.6	0
*M*43	2018 Jun. 23	09:00-10:15	18.3	169.6 ± 3.2	3
$*M$44	2018 Jun. 23	10:17-11:31	26.1	247.7 ± 4.0	4
*M*45	2018 Aug. 6	10:00-11:15	18.3	131.9 ± 3.3	3
*M*46	2018 Aug. 6	11:18-12:32	26.1	202.5 ± 4.1	2
*M*47	2018 Aug. 20	09:50-11:05	18.3	143.5 ± 2.5	3
*M*48	2018 Aug. 20	11:08-12:22	26.1	251.0 ± 4.7	1
*M*49	2018 Sep. 21	10:00-11:15	18.3	110.4 ± 3.6	1
*M*50	2018 Sep. 21	11:18-12:32	26.1	192.3 ± 6.4	0
*M*51	2018 Sep. 27	10:20-11:35	18.3	115.8 ± 3.8	2
*M*52	2018 Sep. 27	11:38-12:52	26.1	123.4 ± 3.8	0
*M*53	2018 Oct. 3	09:30-10:45	18.3	120.3 ± 2.5	2
*M*54	2018 Oct. 3	10:48-12:02	26.1	179.6 ± 4.3	2
*M*55	2018 Oct. 11	10:40-11:55	18.3	111.1 ± 3.2	1
$*M$56	2018 Oct. 11	11:57-13:12	18.3	195.7 ± 6.2	0
*M*57	2018 Oct. 22	11:35-12:50	18.3	97.8 ± 2.6	2
$*M$58	2018 Oct. 22	12:52-14:07	26.1	155.0 ± 4.7	0
$*M$59	2018 Oct. 27	09:50-11:02	18.3	146.3 ± 4.6	0
*M*60	2018 Oct. 31	09:45-10:59	18.3	98.9 ± 3.1	1
$*M$61	2018 Oct. 31	11:02-12:16	26.1	190.5 ± 5.5	1
*M*62	2018 Nov. 9	10:29-11:40	18.3	89.7 ± 2.7	1
$*M$63	2018 Nov. 9	11:42-12:57	26.1	147.8 ± 4.2	1
*M*64	2018 Nov. 12	10:07-11:20	18.3	109.5 ± 3.2	2
*M*65	2018 Nov. 12	11:23-12:37	26.1	177.6 ± 5.9	1
*M*66	2018 Nov. 26	10:05-11:20	18.3	108.3 ± 3.7	1
$*M$67	2018 Nov. 26	11:23-12:37	26.1	162.5 ± 4.9	1
*M*68	2018 Nov. 29	10:05-11:20	18.3	93.4 ± 2.9	1
*M*69	2018 Nov. 29	11:23-12:37	26.1	127.2 ± 4.1	0
*M*70	2018 Dec. 6	11:15-12:30	18.3	104.2 ± 3.2	1
$*M$71	2018 Dec. 6	12:33-13:47	26.1	348.5 ± 13.2	1
*S*72	2019 May 17	08:40-10:25	25.5	113.0 ± 1.0	1
*S*73	2019 May 17	10:25-12:10	25.5	101.7 ± 0.9	1
*M*74	2019 Jun. 12	08:30-09:45	18.3	113.9 ± 2.3	2
$*M$75	2019 Jun. 12	09:47-11:02	25.8	245.3 ± 6.1	0
*M*76	2019 Jun. 13	13:15-14:30	18.3	86.1 ± 2.9	2
*M*77	2019 Jun. 13	14:33-15:47	25.8	158.6 ± 5.1	1
*M*78	2019 Jun. 20	08:45-10:00	18.3	92.5 ± 3.2	2

Table 6.1: Continued.

ID	Epoch	T (UT)	$\nu_{\rm obs}$ (GHz)	$\sigma_{\rm disk}$ (K)	AR_n
*M*79	2019 Jun. 20	10:03-11:17	25.8	218.8 ± 6.5	0
*M*80	2019 Jun. 26	08:30-09:45	18.3	78.1 ± 2.9	1
*M*81	2019 Jun. 26	09:48-11:02	25.8	196.9 ± 6.5	0
*M*82	2019 Jul. 3	08:30-09:45	18.3	110. ± 2.7	3
∗*M*83	2019 Jul. 3	09:47-11:02	25.8	226.7 ± 5.5	1
*M*84	2019 Jul. 4	09:05-10:20	18.3	143.1 ± 2.9	3
∗*M*85	2019 Jul. 4	10:22-11:37	25.8	207.6 ± 3.7	2
*M*86	2019 Jul. 12	09:15-10:30	18.3	97.4 ± 2.2	1
∗*M*87	2019 Jul. 12	10:32-11:47	25.8	184.4 ± 5.4	0
*M*88	2019 Jul. 19	08:00-09:15	18.3	92.2 ± 2.3	1
∗*M*89	2019 Jul. 19	09:17-10:32	25.8	161.4 ± 4.9	1
*M*90	2019 Jul. 24	09:35-10:50	18.3	92.1 ± 2.4	2
∗*M*91	2019 Jul. 24	10:52-12:07	25.8	196.7 ± 5.1	0
*M*92	2019 Jul. 30	08:10-09:25	18.3	126.7 ± 2.7	1
*M*93	2019 Jul. 30	09:27-10:42	25.8	195.1 ± 5.5	1
*M*94	2019 Aug. 7	10:00-11:14	18.3	85.4 ± 2.2	2
*M*95	2019 Aug. 7	11:17-12:31	25.8	248.5 ± 5.0	1
*M*96	2019 Aug. 13	10:00-11:15	18.3	140.1 ± 4.0	0
*M*97	2019 Aug. 13	11:17-12:32	25.8	175.3 ± 6.6	0
*M*98	2019 Aug. 27	09:15-10:30	18.3	110.8 ± 3.5	0
*M*99	2019 Aug. 27	10:32-11:47	25.8	243.1 ± 8.0	0
*M*100	2019 Sep. 5	07:30-08:45	18.3	94.1 ± 3.7	1
*M*101	2019 Sep. 5	08:48-10:02	25.8	160.6 ± 6.0	0
*M*102	2019 Sep. 10	09:50-11:05	18.3	88.5 ± 2.3	1
*M*103	2019 Sep. 10	11:08-12:22	25.8	116.6 ± 3.9	0
*M*104	2019 Sep. 16	09:10-10:25	18.3	101.8 ± 2.7	0
*M*105	2019 Sep. 16	10:28-11:42	25.8	116.3 ± 3.7	0
*M*106	2019 Sep. 24	10:55-12:10	18.3	81.0 ± 2.2	1
∗*M*107	2019 Sep. 24	12:13-13:27	25.8	168.1 ± 7.1	0
*M*108	2019 Oct. 1	09:10-10:25	18.3	89.9 ± 2.7	1
*M*109	2019 Oct. 1	10:28-11:42	25.8	120.2 ± 4.1	1
*M*110	2019 Oct. 9	09:10-10:25	18.3	101.6 ± 3.5	3
*M*111	2019 Oct. 9	10:28-11:42	25.8	112.2 ± 3.9	0
*S*112	2019 Oct. 9	11:46-13:30	18.8	97.9 ± 1.0	3
*S*113	2019 Oct. 9	09:14-10:58	24.7	130.1 ± 1.1	1
*M*114	2019 Oct. 14	12:40-13:55	18.3	84.8 ± 2.6	1
*M*115	2019 Oct. 14	13:58-15:12	25.8	170.1 ± 5.8	0
*M*116	2019 Oct. 23	11:50-13:05	18.3	90.2 ± 2.5	1
*M*117	2019 Oct. 23	13:08-14:22	25.8	123.7 ± 4.7	0
*M*118	2019 Nov. 4	10:15-11:30	18.3	245.5 ± 9.4	1
∗*M*119	2019 Nov. 4	11:33-12:47	25.8	259.1 ± 8.7	0
*M*120	2019 Nov. 14	10:25-11:40	18.3	82.4 ± 2.4	2
*M*121	2019 Nov. 14	11:42-12:57	25.8	136.8 ± 4.3	1
*M*122	2019 Nov. 21	10:10-11:25	18.3	64.9 ± 1.9	2
∗*M*123	2019 Nov. 21	11:27-12:42	25.8	129.1 ± 4.3	1
*M*124	2019 Nov. 26	10:00-11:15	18.3	69.4 ± 2.6	1

Table 6.1: Continued.

ID	Epoch	T (UT)	$\nu_{\rm obs}$ (GHz)	$\sigma_{\rm disk}$ (K)	AR_n
$*M125$	2019 Nov. 26	11:17-12:32	25.8	100.8 ± 3.9	0
$S126$	2020 Jan. 28	09:41-11:25	18.8	162.7 ± 2.8	2
$*S127$	2020 Jan. 28	11:26-13:18	18.8	252.7 ± 3.8	2
$S128$	2020 Jan. 28	13:40-15:24	24.7	122.2 ± 1.0	3
$M129$	2020 Aug. 10	09:10-10:24	18.3	83.6 ± 1.9	3
$M130$	2020 Aug. 10	10:27-11:42	25.8	167.1 ± 5.5	1
$M131$	2020 Aug. 17	09:15-10:29	18.3	96.8 ± 2.1	3
$M132$	2020 Aug. 17	10:32-11:47	25.8	198.0 ± 5.5	2
$M133$	2020 Aug. 26	09:10-10:24	18.3	97.8 ± 2.9	1
$M134$	2020 Aug. 26	10:27-11:42	25.8	174.4 ± 5.2	0
$M135$	2020 Sep. 2	09:15-10:29	18.3	129.2 ± 4.9	1
$M136$	2020 Sep. 2	10:32-11:47	25.8	202.0 ± 5.4	0
$M137$	2020 Sep. 6	08:00-09:14	18.3	93.0 ± 3.1	3
$M138$	2020 Sep. 6	09:17-10:32	25.8	165.9 ± 5.0	0
$M139$	2020 Sep. 14	10:10-11:24	18.3	86.7 ± 2.1	2
$M140$	2020 Sep. 14	11:27-12:42	25.8	209.0 ± 6.0	0
$S141$	2020 Sep. 17	09:18-11:02	18.8	141.1 ± 1.8	3
$S142$	2020 Sep. 17	11:18-13:02	24.7	108.0 ± 1.1	5
$M143$	2020 Sep. 29	09:00-10:14	18.3	125.5 ± 3.9	2
$M144$	2020 Sep. 29	10:17-11:32	25.8	209.5 ± 6.0	2
$*M145$	2020 Oct. 5	09:40-10:54	18.3	192.2 ± 5.0	0
$*M146$	2020 Oct. 5	10:57-12:12	25.8	451.5 ± 16.5	0
$M147$	2020 Oct. 19	08:00-09:14	18.3	78.3 ± 2.9	1
$M148$	2020 Oct. 19	09:17-10:32	25.8	101.5 ± 3.6	2
$S149$	2020 Oct. 29	08:32-10:05	24.7	156.3 ± 1.8	4
$S150$	2020 Oct. 29	10:17-12:01	18.8	133.0 ± 1.6	2
$M151$	2020 Oct. 30	08:15-09:29	18.3	67.2 ± 1.9	2
$M152$	2020 Oct. 30	09:32-10:47	25.8	110.7 ± 3.9	3
$M153$	2020 Nov. 6	09:52-11:07	25.8	111.1 ± 3.8	3
$M154$	2020 Nov. 6	08:35-09:49	18.3	565.2 ± 19.4	1
$M155$	2020 Nov. 8	09:22-10:32	25.8	123.7 ± 4.1	2
$M156$	2020 Nov. 11	10:00-11:14	18.3	84.9 ± 2.8	4
$M157$	2020 Nov. 11	11:17-12:32	25.8	124.0 ± 4.1	1
$M158$	2020 Nov. 23	09:15-10:29	18.3	96.3 ± 3.7	4
$M159$	2020 Nov. 23	12:22-13:37	25.8	184.3 ± 6.4	2
$M160$	2020 Nov. 28	10:35-11:49	18.3	241.0 ± 10.8	2
$M161$	2020 Nov. 28	11:52-13:04	25.8	179.4 ± 6.6	1
$M162$	2020 Nov. 30	09:25-10:39	18.3	161.6 ± 5.3	3
$M163$	2020 Nov. 30	10:42-11:57	25.8	120.4 ± 6.0	3
$M164$	2020 Dec. 7	09:15-13:29	18.3	362.2 ± 15.3	2
$*M165$	2020 Dec. 7	10:32-11:47	25.8	1029.9 ± 63.2	0
$M166$	2020 Dec. 13	09:15-13:29	18.3	81.8 ± 2.9	4
$M167$	2020 Dec. 13	10:32-11:47	25.8	105.0 ± 3.9	1
$M168$	2020 Dec. 21	09:45-10:59	18.3	91.6 ± 3.9	4
$M169$	2020 Dec. 21	11:02-12:17	25.8	120.2 ± 5.4	2

Appendix B: Analysis results obtained through the automatic procedure of SUNDARA

Table 6.2: Analysis results obtained through the automatic procedure of SUNDARA. *ID* is the identification number for each single map, where the letters *M* and *S* specify the radiotelescope (Medicina or SRT); *ar_id* is the AR name (if present), *Epoch* the observation date, ν_{obs} the central observing frequency, *Size* the AR size, at twice the fitted semi-axes level (in units of arcmin^2); $T_{p,ex}$ indicates the peak of the excess brightness temperature T_{ex} for each AR; S_{sub} and S_{tot} indicate the AR flux density of the QS-subtracted image and the original image, respectively. *Notes* indicates further AR flags: b" indicates if the AR position is located outside of the 95%-level of the solar radius; k" indicates the distance between 2 different ARs $\leq$ 2 beams of the receiver; C" indicates a AR located inside a confused region (see Footnote 4 of the paper); sequential numbers are related to multiple AR detection for the same observing session. AR candidates without known HEK counterpart are labeled as *SD_AR_X12345* (lon, lat), where *SD* indicates SunDish project, *AR* Active Region, *X* the INAF radio telescope (*M* for Medicina, *S* for SRT, *N* for Noto), *12345* the number of AR (sorted by epoch), lon/lat indicate the Helioprojective Longitude/Latitude (in units of arcsec).

ID	*ar_id*	Epoch	T (UT)	ν_{obs} (GHz)	Size (arcmin^2)	$T_{p,tot}$ (K)	$T_{p,ex}$ (K)	S_{sub} (sfu)	S_{tot} (sfu)	Notes
*M*2	NOAA_12699, SPoCA_21552	2018 Feb. 15	12:22-13:22	24.1	3.60	10385 ± 262	545 ± 14	0.13 ± 0.003	5.47 ± 0.14	b1
*M*1	NOAA_12699, SPoCA_21552	2018 Feb. 15	11:20-12:20	24.1	-	10396 ± 263	556 ± 14	0.17 ± 0.004	6.58 ± 0.16	b1
*M*3	SD-AR_M00001 (-36.2, +334.2)	2018 Feb. 19	10:14-11:30	24.1	49.50	10062 ± 256	222 ± 6	0.70 ± 0.017	74.25 ± 1.86	C1
*M*4	SD-AR_M00001 (-36.2, +334.2)	2018 Feb. 19	11:33-12:49	24.1	-	< 10124.98	< 284.98	< 0.66	< 106.31	1
*M*5	NOAA_12700, SPoCA_21600	2018 Feb. 27	09:39-10:50	23.6	39.00	10440 ± 270	575 ± 14	0.97 ± 0.024	56.68 ± 1.42	C1
*M*6	NOAA_12700, SPoCA_21600	2018 Feb. 27	10:52-12:02	23.6	-	10472 ± 263	607 ± 15	1.75 ± 0.044	112.93 ± 2.82	1
*M*7	SPoCA_21612	2018 Mar. 7	13:50-15:00	23.6	51.50	10340 ± 265	475 ± 12	1.07 ± 0.027	74.55 ± 1.86	1
*M*8	SPoCA_21612	2018 Mar. 7	15:02-16:05	23.6	-	< 10081.00	< 216.00	< 0.25	< 72.70	1
*M*10	SPoCA_21612	2018 Mar. 9	13:22-14:33	23.6	49.50	10360 ± 261	495 ± 12	1.14 ± 0.028	71.79 ± 1.79	C1
*M*9	SPoCA_21612	2018 Mar. 9	12:11-13:20	23.6	-	10433 ± 265	568 ± 14	1.22 ± 0.030	70.82 ± 1.77	C1
*M*14	NOAA_12703, SPoCA_21684	2018 Mar. 30	11:02-12:18	23.6	3.75	10225 ± 257	360 ± 9	0.07 ± 0.002	5.41 ± 0.14	b1
*M*13	NOAA_12703, SPoCA_21684	2018 Mar. 30	09:45-11:00	23.6	-	< 10179.90	< 314.90	< 0.05	< 5.03	1
*M*15	SD-AR_M00002 (-726.9, +16.3)	2018 Apr. 2	09:45-11:00	23.6	18.62	10317 ± 261	452 ± 11	0.44 ± 0.011	27.03 ± 0.68	Ck1
*M*16	SD-AR_M00002 (-726.9, +16.3)	2018 Apr. 2	11:02-12:18	23.6	-	10399 ± 261	534 ± 13	0.41 ± 0.010	14.34 ± 0.36	k1
*M*16	NOAA_12703, SPoCA_21684	2018 Apr. 2	11:02-12:18	23.6	49.00	10800 ± 271	935 ± 23	1.85 ± 0.046	71.84 ± 1.80	k2
*M*15	NOAA_12703, SPoCA_21684	2018 Apr. 2	09:45-11:00	23.6	-	10628 ± 269	763 ± 19	2.18 ± 0.054	136.50 ± 3.41	k2
*M*17	NOAA_12703, SPoCA_21708	2018 Apr. 6	10:34-11:50	23.6	21.25	10235 ± 260	370 ± 9	0.41 ± 0.010	30.74 ± 0.77	Ck1
*M*18	NOAA_12703, SPoCA_21708	2018 Apr. 6	11:52-13:07	23.6	-	< 10173.35	< 308.35	< 0.46	< 31.51	1
*M*17	SD-AR_M00003 (+33.7, +20.4)	2018 Apr. 6	10:34-11:50	23.6	47.75	10241 ± 260	376 ± 9	0.98 ± 0.024	69.18 ± 1.73	Ck2
*M*18	SD-AR_M00003 (+33.7, +20.4)	2018 Apr. 6	11:52-13:07	23.6	-	10248 ± 258	383 ± 10	1.11 ± 0.028	70.38 ± 1.76	Ck2
*M*19	SPoCA_21710	2018 Apr. 7	09:39-11:26	23.6	17.75	10191 ± 257	326 ± 8	0.27 ± 0.007	25.61 ± 0.64	Ck1
*M*20	SPoCA_21710	2018 Apr. 7	11:28-13:14	23.6	-	< 10205.32	< 340.32	< 0.34	< 27.11	1
*M*19	SD-AR_M00004 (+243.1, -51.0)	2018 Apr. 7	09:39-11:26	23.6	49.25	10242 ± 258	377 ± 9	0.95 ± 0.024	71.28 ± 1.78	Ck2
*M*20	SD-AR_M00004 (+243.1, -51.0)	2018 Apr. 7	11:28-13:14	23.6	-	< 10203.01	< 338.01	< 0.74	< 70.37	2
*M*21	SD-AR_M00005 (+496.9, -24.1)	2018 Apr. 12	10:20-11:22	18.1	19.25	10445 ± 267	305 ± 8	0.18 ± 0.005	16.80 ± 0.42	Ck1
*M*22	SD-AR_M00005 (+496.9, -24.1)	2018 Apr. 12	11:24-12:26	26.1	-	< 9684.27	-[b]	-[b]	< 31.29	1
*M*21	NOAA_12704, SPoCA_21724	2018 Apr. 12	10:20-11:22	18.1	6.00	10937 ± 279	797 ± 20	0.19 ± 0.005	5.37 ± 0.13	bk2
*M*22	NOAA_12704, SPoCA_21724	2018 Apr. 12	11:24-12:26	26.1	-	< 9789.93	< 49.93	-[b]	< 10.16	2

[a] *This AR corresponds also to other 3 SPoCA targets: SPoCA_22276, SPoCA_22279, and SPoCA_22280.*
[b] *Unknown flux because the brightness temperature of the AR pixels is lower than the quiet-Sun.*
[c] *There are two very close ARs in this position. Our algorithm detected a unique AR.*
[d] *This AR corresponds also to other 3 SPoCA targets: SPoCA_24850, SPoCA_24851, and SPoCA_24853.*
[e] *The quality of the* 25.8 *GHz-solar map on December 7, 2020 is very low.*
[f] *Same region.*
[g] *There is a very close AR in this position (NOAA_12793/SPoCA_24935) that pollutes our measures.*
[h] *There is a very close AR in this position (NOAA_12792/SPoCA_24918) that pollutes our measures.*

Table 6.2: Continued.

ID	*ar_id*	Epoch	T (UT)	ν_{obs} (GHz)	Size (arcmin^2)	$T_{p,tot}$ (K)	$T_{p,ex}$ (K)	S_{sub} (sfu)	S_{tot} (sfu)	Notes
*M*21	SD-AR_M00006 (-472.4, +298.1)	2018 Apr. 12	10:20-11:22	18.1	42.50	10489 ± 268	349 ± 9	0.52 ± 0.013	37.21 ± 0.93	k3
*M*22	SD-AR_M00006 (-472.4, +298.1)	2018 Apr. 12	11:24-12:26	26.1	-	< 9878.96	< 138.96	< 0.13	< 72.92	3
*M*24	NOAA_12704, SPoCA_21724	2018 Apr. 13	08:40-09:47	26.1	14.00	10700 ± 275	960 ± 24	0.80 ± 0.020	24.94 ± 0.62	bk1
*M*26	NOAA_12704, SPoCA_21724	2018 Apr. 13	11:11-12:20	18.1	-	11465 ± 289	1325 ± 33	0.67 ± 0.017	18.05 ± 0.45	bk1
*M*25	NOAA_12704, SPoCA_21724	2018 Apr. 13	10:00-11:09	22.1	-	11492 ± 294	1552 ± 39	0.76 ± 0.019	19.36 ± 0.48	bk1
*M*23	NOAA_12704, SPoCA_21724	2018 Apr. 13	07:30-08:39	18.1	-	11694 ± 296	1554 ± 39	0.67 ± 0.017	12.55 ± 0.31	bk1
*M*25	SD-AR_M00007 (-516.4, +13.2)	2018 Apr. 13	10:00-11:09	22.1	42.50	10293 ± 264	353 ± 9	0.60 ± 0.015	54.21 ± 1.36	Ck2
*M*26	SD-AR_M00007 (-516.4, +13.2)	2018 Apr. 13	11:11-12:20	18.1	-	10857 ± 274	717 ± 18	0.53 ± 0.013	53.28 ± 1.33	k2
*M*24	SD-AR_M00007 (-516.4, +13.2)	2018 Apr. 13	08:40-09:47	26.1	-	< 10036.19	< 296.19	< 0.94	< 73.36	2
*M*23	SD-AR_M00007 (-516.4, +13.2)	2018 Apr. 13	07:30-08:39	18.1	-	< 10397.62	< 257.62	< 0.41	< 36.46	2
*M*25	SD-AR_M00008 (+227.4, -108.1)	2018 Apr. 13	10:00-11:09	22.1	27.50	10256 ± 263	316 ± 8	0.41 ± 0.010	35.08 ± 0.88	Ck3
*M*24	SD-AR_M00008 (+227.4, -108.1)	2018 Apr. 13	08:40-09:47	26.1	-	< 9980.29	< 240.29	< 0.23	< 45.44	3
*M*26	SD-AR_M00008 (+227.4, -108.1)	2018 Apr. 13	11:11-12:20	18.1	-	< 10317.97	< 177.97	< 0.19	< 33.12	3
*M*23	SD-AR_M00008 (+227.4, -108.1)	2018 Apr. 13	07:30-08:39	18.1	-	< 10289.62	< 149.62	< 0.13	< 23.22	3
*M*26	SD-AR_M00009 (+501.8, +176.8)	2018 Apr. 13	11:11-12:20	18.1	30.24	10370 ± 262	230 ± 6	0.20 ± 0.005	26.30 ± 0.66	Ck4
*M*24	SD-AR_M00009 (+501.8, +176.8)	2018 Apr. 13	08:40-09:47	26.1	-	< 10016.03	< 276.03	< 0.35	< 38.23	4
*M*25	SD-AR_M00009 (+501.8, +176.8)	2018 Apr. 13	10:00-11:09	22.1	-	< 10207.24	< 267.24	< 0.19	< 26.68	4
*M*23	SD-AR_M00009 (+501.8, +176.8)	2018 Apr. 13	07:30-08:39	18.1	-	< 10323.71	< 183.71	< 0.11	< 19.11	4
*M*27	NOAA_12704, SPoCA_21724	2018 Apr. 17	10:45-11:47	18.1	40.25	10997 ± 278	857 ± 21	0.77 ± 0.019	35.53 ± 0.89	k1
*M*28	SD-AR_M00010 (-115.9, -146.2)	2018 Apr. 18	11:20-12:29	18.1	32.00	10516 ± 266	376 ± 9	0.33 ± 0.008	27.96 ± 0.70	Ck1
*M*29	SD-AR_M00010 (-115.9, -146.2)	2018 Apr. 18	12:31-13:40	26.1	-	< 10066.41	< 326.41	< 1.19	< 110.87	1
*M*28	SPoCA_21739	2018 Apr. 18	11:20-12:29	18.1	28.00	10464 ± 264	324 ± 8	0.26 ± 0.007	24.44 ± 0.61	Ck2
*M*29	SPoCA_21739	2018 Apr. 18	12:31-13:40	26.1	-	< 10107.09	< 367.09	< 0.93	< 93.70	2
*M*28	NOAA_12704, SPoCA_21724	2018 Apr. 18	11:20-12:29	18.1	28.75	10743 ± 271	603 ± 15	0.50 ± 0.012	25.33 ± 0.63	Ck3
*M*29	NOAA_12704, SPoCA_21724	2018 Apr. 18	12:31-13:40	26.1	-	10371 ± 261	631 ± 16	1.99 ± 0.050	96.63 ± 2.42	Ck3
*M*28	SPoCA_21735	2018 Apr. 18	11:20-12:29	18.1	12.75	10602 ± 268	462 ± 12	0.18 ± 0.005	11.19 ± 0.28	k4
*M*29	SPoCA_21735	2018 Apr. 18	12:31-13:40	26.1	-	< 10107.09	< 367.09	< 0.33	< 43.36	4
*M*28	SPoCA_21741	2018 Apr. 18	11:20-12:29	18.1	45.00	10529 ± 266	389 ± 10	0.53 ± 0.013	39.38 ± 0.98	k5
*M*29	SPoCA_21741	2018 Apr. 18	12:31-13:40	26.1	-	< 10142.76	< 402.76	< 2.33	< 152.80	5
*M*30	NOAA_12706, SPoCA_21742	2018 Apr. 19	09:40-10:43	18.1	2.00	10729 ± 270	589 ± 15	0.04 ± 0.001	1.75 ± 0.04	b1
*M*31	NOAA_12706, SPoCA_21742	2018 Apr. 19	10:45-11:48	26.1	-	< 9430.92	-[b]	-[b]	< 6.98	1
*M*30	NOAA_12704, SPoCA_21724	2018 Apr. 19	09:40-10:43	18.1	49.75	10578 ± 267	438 ± 11	0.63 ± 0.016	43.56 ± 1.09	2
*M*31	NOAA_12704, SPoCA_21724	2018 Apr. 19	10:45-11:48	26.1	-	< 9730.37	-[b]	-[b]	< 159.11	2
*M*34	NOAA_12706, SPoCA_21742	2018 Apr. 20	10:45-12:03	23.6	6.00	11897 ± 300	2032 ± 51	0.60 ± 0.015	9.08 ± 0.23	b1
*M*33	NOAA_12706, SPoCA_21742	2018 Apr. 20	09:25-10:39	26.1	-	11314 ± 289	1574 ± 39	0.58 ± 0.014	11.08 ± 0.28	b1
*M*32	NOAA_12706, SPoCA_21742	2018 Apr. 20	07:40-08:58	18.1	-	12724 ± 321	2584 ± 65	0.58 ± 0.015	5.94 ± 0.15	b1
*M*32	NOAA_12704, SPoCA_21724	2018 Apr. 20	07:40-08:58	18.1	48.25	10489 ± 266	349 ± 9	0.54 ± 0.014	41.96 ± 1.05	2
*M*34	NOAA_12704, SPoCA_21724	2018 Apr. 20	10:45-12:03	23.6	-	< 10107.04	< 242.04	< 0.46	< 69.22	2

[a] *This AR corresponds also to other 3 SPoCA targets: SPoCA_22276, SPoCA_22279, and SPoCA_22280.*
[b] *Unknown flux because the brightness temperature of the AR pixels is lower than the quiet-Sun.*
[c] *There are two very close ARs in this position. Our algorithm detected a unique AR.*
[d] *This AR corresponds also to other 3 SPoCA targets: SPoCA_24850, SPoCA_24851, and SPoCA_24853.*
[e] *The quality of the* 25.8 *GHz-solar map on December 7, 2020 is very low.*
[f] *Same region.*
[g] *There is a very close AR in this position (NOAA_12793/SPoCA_24935) that pollutes our measures.*
[h] *There is a very close AR in this position (NOAA_12792/SPoCA_24918) that pollutes our measures.*

Table 6.2: Continued.

ID	*ar_id*	Epoch	T (UT)	ν_{obs} (GHz)	Size (arcmin^2)	$T_{p,tot}$ (K)	$T_{p,ex}$ (K)	S_{sub} (sfu)	S_{tot} (sfu)	Notes
*M*33	NOAA_12704, SPoCA_21724	2018 Apr. 20	09:25-10:39	26.1	-	< 10058.00	< 318.00	< 0.88	< 83.69	2
*M*35	NOAA_12706, SPoCA_21742	2018 Apr. 23	09:31-10:48	18.1	9.00	12332 ± 310	2192 ± 55	0.74 ± 0.019	8.52 ± 0.21	1
*M*36	NOAA_12706, SPoCA_21742	2018 Apr. 23	10:51-12:08	18.1	-	11418 ± 289	1278 ± 32	0.48 ± 0.012	8.04 ± 0.20	1
*M*37	NOAA_12706, SPoCA_21742	2018 Apr. 25	10:45-12:02	18.1	37.50	12441 ± 313	2301 ± 58	1.85 ± 0.046	34.24 ± 0.86	1
*M*38	NOAA_12706, SPoCA_21742	2018 Apr. 26	09:00-10:17	18.1	30.25	12365 ± 312	2225 ± 56	1.64 ± 0.041	27.76 ± 0.69	1
*M*39	SD-AR_M00011 (+219.3, +34.2)	2018 Jun. 10	10:15-11:30	18.1	31.00	10460 ± 263	320 ± 8	0.28 ± 0.007	27.03 ± 0.68	C1
*M*40	SD-AR_M00011 (+219.3, +34.2)	2018 Jun. 10	11:32-12:47	26.1	-	10198 ± 261	458 ± 11	1.35 ± 0.034	56.11 ± 1.40	1
*M*39	SD-AR_M00012 (-464.3, +348.9)	2018 Jun. 10	10:15-11:30	18.1	47.00	10414 ± 262	274 ± 7	0.46 ± 0.011	41.01 ± 1.03	2
*M*40	SD-AR_M00012 (-464.3, +348.9)	2018 Jun. 10	11:32-12:47	26.1	-	< 10022.72	< 282.72	< 0.69	< 79.88	2
*M*41	NOAA_12713, SPoCA_21840	2018 Jun. 17	08:56-10:10	18.3	37.00	12554 ± 317	2424 ± 61	2.00 ± 0.050	34.63 ± 0.87	1
*M*42	NOAA_12713, SPoCA_21840	2018 Jun. 17	10:12-11:27	26.1	-	< 11792.46	< 2052.46	< 6.76	< 129.31	1
*M*43	SPoCA_21867	2018 Jun. 23	09:00-10:15	18.3	9.50	10642 ± 269	512 ± 13	0.13 ± 0.003	8.49 ± 0.21	k1
*M*44	SPoCA_21867	2018 Jun. 23	10:17-11:31	26.1	-	10303 ± 260	563 ± 14	0.43 ± 0.011	15.96 ± 0.40	Ck1
*M*44	NOAA_12713, SPoCA_21840	2018 Jun. 23	10:17-11:31	26.1	2.75	11202 ± 283	1462 ± 37	0.39 ± 0.010	5.13 ± 0.13	b2
*M*43	NOAA_12713, SPoCA_21840	2018 Jun. 23	09:00-10:15	18.3	-	12607 ± 318	2477 ± 62	0.41 ± 0.010	2.83 ± 0.07	b2
*M*43	NOAA_12715, SPoCA_21859	2018 Jun. 23	09:00-10:15	18.3	13.00	12141 ± 307	2011 ± 50	0.72 ± 0.018	12.17 ± 0.30	k3
*M*44	NOAA_12715, SPoCA_21859	2018 Jun. 23	10:17-11:31	26.1	-	11793 ± 297	2053 ± 51	1.89 ± 0.047	24.75 ± 0.62	Ck3
*M*44	HMI_SHARP_7276	2018 Jun. 23	10:17-11:31	26.1	49.00	10391 ± 262	651 ± 16	2.17 ± 0.054	86.64 ± 2.17	Ck4
*M*43	HMI_SHARP_7276	2018 Jun. 23	09:00-10:15	18.3	-	< 10485.28	< 355.28	< 0.09	< 42.69	4
*M*45	NOAA_12717, SPoCA_21941	2018 Aug. 6	10:00-11:15	18.3	47.75	10963 ± 276	833 ± 21	0.70 ± 0.018	42.73 ± 1.07	1
*M*46	NOAA_12717, SPoCA_21941	2018 Aug. 6	11:18-12:32	26.1	-	10260 ± 260	520 ± 13	0.96 ± 0.024	83.17 ± 2.08	C1
*M*45	SD-AR_M00013 (-378.2, +38.4)	2018 Aug. 6	10:00-11:15	18.3	46.50	10484 ± 264	354 ± 9	0.56 ± 0.014	41.56 ± 1.04	Ck2
*M*46	SD-AR_M00013 (-378.2, +38.4)	2018 Aug. 6	11:18-12:32	26.1	-	< 10093.76	< 353.76	< 1.24	< 81.43	2
*M*45	SPoCA_21947	2018 Aug. 6	11:18-12:32	26.1	12.25	10212 ± 259	472 ± 12	0.48 ± 0.012	21.52 ± 0.54	bk3
*M*46	SPoCA_21947	2018 Aug. 6	10:00-11:15	18.3	-	11109 ± 280	979 ± 24	0.53 ± 0.013	10.83 ± 0.27	bk3
*M*47	NOAA_12718, SPoCA_21976	2018 Aug. 20	09:50-11:05	18.3	35.00	10594 ± 267	464 ± 12	0.46 ± 0.012	31.33 ± 0.78	1
*M*48	NOAA_12718, SPoCA_21976	2018 Aug. 20	11:08-12:22	26.1	-	< 10240.88	< 500.88	< 0.79	< 61.12	1
*M*48	NOAA_12719, SPoCA_21981	2018 Aug. 20	11:08-12:22	26.1	18.00	10804 ± 272	1064 ± 27	1.01 ± 0.025	32.04 ± 0.80	2
*M*47	NOAA_12719, SPoCA_21981	2018 Aug. 20	09:50-11:05	18.3	-	11526 ± 290	1396 ± 35	0.72 ± 0.018	17.04 ± 0.43	2
*M*47	SD-AR_M00014 (+332.1, +258.0)	2018 Aug. 20	09:50-11:05	18.3	50.75	10537 ± 266	407 ± 10	0.49 ± 0.012	45.11 ± 1.13	C3
*M*48	SD-AR_M00014 (+332.1, +258.0)	2018 Aug. 20	11:08-12:22	26.1	-	< 10190.94	< 450.94	< 1.53	< 89.84	3
*M*49	SPoCA_22078	2018 Sep. 21	10:00-11:15	18.3	62.25	10418 ± 262	288 ± 7	0.39 ± 0.010	55.04 ± 1.38	1
*M*50	SPoCA_22078	2018 Sep. 21	11:18-12:32	26.1	-	< 10120.04	< 380.04	< 1.38	< 108.09	1
*M*51	SD-AR_M00015 (-506.8, -227.3)	2018 Sep. 27	10:20-11:35	18.3	48.00	10405 ± 261	275 ± 7	0.44 ± 0.011	42.75 ± 1.07	1
*M*52	SD-AR_M00015 (-506.8, -227.3)	2018 Sep. 27	11:38-12:52	26.1	-	< 9929.90	< 189.90	< 0.44	< 82.21	1
*M*51	SD-AR_M00016 (+587.0, +15.0)	2018 Sep. 27	10:20-11:35	18.3	28.25	10379 ± 261	249 ± 6	0.20 ± 0.005	25.10 ± 0.63	2
*M*52	SD-AR_M00016 (+587.0, +15.0)	2018 Sep. 27	11:38-12:52	26.1	-	< 9924.11	< 184.11	< 0.29	< 50.68	2
*M*53	SD-AR_M00017 (-208.5, +68.3)	2018 Oct. 3	09:30-10:45	18.3	45.25	10575 ± 267	445 ± 11	0.66 ± 0.016	40.52 ± 1.01	1

[a] *This AR corresponds also to other 3 SPoCA targets: SPoCA_22276, SPoCA_22279, and SPoCA_22280.*
[b] *Unknown flux because the brightness temperature of the AR pixels is lower than the quiet-Sun.*
[c] *There are two very close ARs in this position. Our algorithm detected a unique AR.*
[d] *This AR corresponds also to other 3 SPoCA targets: SPoCA_24850, SPoCA_24851, and SPoCA_24853.*
[e] *The quality of the* 25.8 *GHz-solar map on December 7, 2020 is very low.*
[f] *Same region.*
[g] *There is a very close AR in this position (NOAA_12793/SPoCA_24935) that pollutes our measures.*
[h] *There is a very close AR in this position (NOAA_12792/SPoCA_24918) that pollutes our measures.*

Table 6.2: Continued.

ID	*ar_id*	Epoch	T (UT)	ν_{obs} (GHz)	Size (arcmin^2)	$T_{p,tot}$ (K)	$T_{p,ex}$ (K)	S_{sub} (sfu)	S_{tot} (sfu)	Notes
*M*54	SD-AR_M00017 (-208.5, +68.3)	2018 Oct. 3	10:48-12:02	26.1	-	10228 ± 259	488 ± 12	1.86 ± 0.046	82.93 ± 2.07	1
*M*54	NOAA_12723, SPoCA_22102	2018 Oct. 3	10:48-12:02	26.1	12.75	10419 ± 264	679 ± 17	0.48 ± 0.012	22.42 ± 0.56	C2
*M*53	NOAA_12723, SPoCA_22102	2018 Oct. 3	09:30-10:45	18.3	-	11001 ± 277	871 ± 22	0.35 ± 0.009	11.59 ± 0.29	2
*M*55	SPoCA_22124	2018 Oct. 11	10:40-11:55	18.3	55.50	10500 ± 264	370 ± 9	0.50 ± 0.012	49.43 ± 1.24	1
*M*56	SPoCA_22124	2018 Oct. 11	11:57-13:12	18.3	-	< 9554.46	-[b]	-[b]	< 64.24	1
*M*57	SPoCA_22122	2018 Oct. 22	11:35-12:50	18.3	18.25	10495 ± 264	365 ± 9	0.26 ± 0.007	16.32 ± 0.41	k1
*M*58	SPoCA_22122	2018 Oct. 22	12:52-14:07	26.1	-	< 9854.02	< 114.02	< 0.09	< 32.47	1
*M*57	SD-AR_M00018 (+526.1, +4.6)	2018 Oct. 22	11:35-12:50	18.3	50.50	10495 ± 264	365 ± 9	0.48 ± 0.012	45.00 ± 1.13	k2
*M*58	SD-AR_M00018 (+526.1, +4.6)	2018 Oct. 22	12:52-14:07	26.1	-	< 9959.84	< 219.84	< 0.46	< 86.66	2
*M*61	SD-AR_M00019 (+397.4, +154.7)	2018 Oct. 31	11:02-12:16	26.1	48.25	10229 ± 259	489 ± 12	1.92 ± 0.048	85.15 ± 2.13	1
*M*60	SD-AR_M00019 (+397.4, +154.7)	2018 Oct. 31	09:45-10:59	18.3	-	10524 ± 264	394 ± 10	0.58 ± 0.014	43.79 ± 1.09	1
*M*63	HMI_SHARP_7321	2018 Nov. 9	10:29-11:40	18.3	45.50	10399 ± 262	269 ± 7	0.26 ± 0.006	40.33 ± 1.01	1
*M*62	HMI_SHARP_7321	2018 Nov. 9	11:42-12:57	26.1	-	10171 ± 256	431 ± 11	1.73 ± 0.043	81.51 ± 2.04	1
*M*64	NOAA_12726, SPoCA_22221	2018 Nov. 12	10:07-11:20	18.3	16.50	10478 ± 264	348 ± 9	0.20 ± 0.005	14.75 ± 0.37	Ck1
*M*65	NOAA_12726, SPoCA_22221	2018 Nov. 12	11:23-12:37	26.1	-	< 10127.86	< 387.86	< 0.68	< 29.14	1
*M*64	SPoCA_22205	2018 Nov. 12	10:07-11:20	18.3	49.00	10584 ± 266	454 ± 11	0.63 ± 0.016	43.84 ± 1.10	k2
*M*65	SPoCA_22205	2018 Nov. 12	11:23-12:37	26.1	-	10139 ± 256	399 ± 10	1.59 ± 0.040	86.54 ± 2.16	2
*M*67	NOAA_12728, SPoCA_22251	2018 Nov. 26	11:23-12:37	26.1	44.50	10290 ± 260	550 ± 14	1.64 ± 0.041	78.40 ± 1.96	1
*M*66	NOAA_12728, SPoCA_22251	2018 Nov. 26	10:05-11:20	18.3	-	10763 ± 270	633 ± 16	0.85 ± 0.021	44.06 ± 1.10	1
*M*68	SD-AR_M00020 (+474.3, +48.7)	2018 Nov. 29	10:05-11:20	18.3	49.00	10458 ± 263	328 ± 8	0.52 ± 0.013	43.73 ± 1.09	1
*M*69	SD-AR_M00020 (+474.3, +48.7)	2018 Nov. 29	11:23-12:37	26.1	-	< 9988.13	< 248.13	< 0.71	< 86.50	1
*M*70	NOAA_12729[a]	2018 Dec. 6	11:15-12:30	18.3	18.75	11721 ± 294	1591 ± 40	0.73 ± 0.018	17.25 ± 0.43	1
*M*71	NOAA_12729[a]	2018 Dec. 6	12:33-13:47	26.1	-	10597 ± 269	857 ± 21	1.31 ± 0.033	34.08 ± 0.85	C1
*S*72	SPoCA_22691	2019 May 17	08:40-10:25	25.5	16.75	11012 ± 275	1248 ± 31	0.89 ± 0.022	29.34 ± 0.73	b1
*S*73	SPoCA_22691	2019 May 17	10:25-12:10	25.5	-	10723 ± 268	959 ± 24	1.10 ± 0.028	63.65 ± 1.59	b1
*M*74	SPoCA_22823	2019 Jun. 12	08:30-09:45	18.3	45.25	10593 ± 270	463 ± 12	0.50 ± 0.012	40.34 ± 1.01	1
*M*75	SPoCA_22823	2019 Jun. 12	09:47-11:02	25.8	-	< 10149.60	< 394.60	< 0.88	< 110.05	1
*M*74	SD-AR_M00021 (+88.3, -12.1)	2019 Jun. 12	08:30-09:45	18.3	43.50	10506 ± 268	376 ± 9	0.52 ± 0.013	38.88 ± 0.97	C2
*M*75	SD-AR_M00021 (+88.3, -12.1)	2019 Jun. 12	09:47-11:02	25.8	-	< 10131.83	< 376.83	< 2.02	< 108.36	2
*M*76	SD-AR_M00022 (-390.6, -32.1)	2019 Jun. 13	13:15-14:30	18.3	16.75	10375 ± 263	245 ± 6	0.12 ± 0.003	14.89 ± 0.37	Ck1
*M*77	SD-AR_M00022 (-390.6, -32.1)	2019 Jun. 13	14:33-15:47	25.8	-	< 10018.95	< 263.95	< 0.45	< 40.56	1
*M*76	SD-AR_M00023 (-27.7, +85.1)	2019 Jun. 13	13:15-14:30	18.3	10.50	10389 ± 263	259 ± 6	0.08 ± 0.002	9.34 ± 0.23	Ck2
*M*77	SD-AR_M00023 (-27.7, +85.1)	2019 Jun. 13	14:33-15:47	25.8	-	10166 ± 258	411 ± 10	0.50 ± 0.012	24.80 ± 0.62	2
*M*78	SD-AR_M00024 (+587.5, -133.2)	2019 Jun. 20	08:45-10:00	18.3	21.25	10335 ± 261	205 ± 5	0.12 ± 0.003	18.86 ± 0.47	C1
*M*79	SD-AR_M00024 (+587.5, -133.2)	2019 Jun. 20	10:03-11:17	25.8	-	< 9790.96	< 35.96	< 0.01	< 35.56	1
*M*80	SD-AR_M00025 (+504.9, +103.0)	2019 Jun. 26	08:30-09:45	18.3	12.00	10323 ± 261	193 ± 5	0.07 ± 0.002	10.66 ± 0.27	C1
*M*81	SD-AR_M00025 (+504.9, +103.0)	2019 Jun. 26	09:48-11:02	25.8	-	< 9985.54	< 230.54	< 0.26	< 19.67	1
*M*82	SPoCA_22886	2019 Jul. 3	08:30-09:45	18.3	40.00	10410 ± 263	280 ± 7	0.36 ± 0.009	35.58 ± 0.89	Ck1

[a] *This AR corresponds also to other 3 SPoCA targets: SPoCA_22276, SPoCA_22279, and SPoCA_22280.*
[b] *Unknown flux because the brightness temperature of the AR pixels is lower than the quiet-Sun.*
[c] *There are two very close ARs in this position. Our algorithm detected a unique AR.*
[d] *This AR corresponds also to other 3 SPoCA targets: SPoCA_24850, SPoCA_24851, and SPoCA_24853.*
[e] *The quality of the* 25.8 *GHz-solar map on December 7, 2020 is very low.*
[f] *Same region.*
[g] *There is a very close AR in this position (NOAA_12793/SPoCA_24935) that pollutes our measures.*
[h] *There is a very close AR in this position (NOAA_12792/SPoCA_24918) that pollutes our measures.*

Table 6.2: Continued.

ID	*ar_id*	Epoch	T (UT)	ν_{obs} (GHz)	Size (arcmin^2)	$T_{p,tot}$ (K)	$T_{p,ex}$ (K)	S_{sub} (sfu)	S_{tot} (sfu)	Notes
*M*83	SPoCA_22886	2019 Jul. 3	09:47-11:02	25.8	-	< 10320.22	< 565.22	< 2.10	< 67.51	1
*M*82	HMI_SHARP_7374	2019 Jul. 3	08:30-09:45	18.3	31.25	10536 ± 266	406 ± 10	0.38 ± 0.010	27.89 ± 0.70	Ck2
*M*83	HMI_SHARP_7374	2019 Jul. 3	09:47-11:02	25.8	-	10320 ± 263	565 ± 14	1.15 ± 0.029	54.70 ± 1.37	Ck2
*M*82	SD-AR_M00026 (-568.0, +200.0)	2019 Jul. 3	08:30-09:45	18.3	20.50	10458 ± 264	328 ± 8	0.27 ± 0.007	18.35 ± 0.46	3
*M*83	SD-AR_M00026 (-568.0, +200.0)	2019 Jul. 3	09:47-11:02	25.8	-	< 10050.63	< 295.63	< 0.39	< 34.13	3
*M*84	SD-AR_M00027 (-408.9, +202.9)	2019 Jul. 4	09:05-10:20	18.3	37.75	10477 ± 266	347 ± 9	0.41 ± 0.010	33.68 ± 0.84	Ck1
*M*85	SD-AR_M00027 (-408.9, +202.9)	2019 Jul. 4	10:22-11:37	25.8	-	< 10173.28	< 418.28	< 1.35	< 64.63	1
*M*85	SD-AR_M00028 (+51.1, +80.3)	2019 Jul. 4	10:22-11:37	25.8	48.75	10371 ± 264	616 ± 15	2.42 ± 0.061	84.71 ± 2.12	Ck2
*M*84	SD-AR_M00028 (+51.1, +80.3)	2019 Jul. 4	09:05-10:20	18.3	-	10544 ± 268	414 ± 10	0.66 ± 0.016	44.27 ± 1.11	Ck2
*M*85	HMI_SHARP_7374	2019 Jul. 4	10:22-11:37	25.8	48.75	10261 ± 261	506 ± 13	1.33 ± 0.033	83.60 ± 2.09	Ck3
*M*84	HMI_SHARP_7374	2019 Jul. 4	09:05-10:20	18.3	-	10571 ± 269	441 ± 11	0.58 ± 0.015	43.53 ± 1.09	Ck3
*M*86	NOAA_12744, SPoCA_22925	2019 Jul. 12	09:15-10:30	18.3	12.75	10559 ± 269	429 ± 11	0.16 ± 0.004	11.40 ± 0.28	1
*M*87	NOAA_12744, SPoCA_22925	2019 Jul. 12	10:32-11:47	25.8	-	< 10052.72	< 297.72	< 0.12	< 21.56	1
*M*88	SPoCA_22983	2019 Jul. 19	08:00-09:15	18.3	48.75	10436 ± 264	306 ± 8	0.45 ± 0.011	43.42 ± 1.09	C1
*M*89	SPoCA_22983	2019 Jul. 19	09:17-10:32	25.8	-	< 10088.08	< 333.08	< 0.91	< 83.57	1
*M*89	SD-AR_M00029 (+112.8, +70.0)	2019 Jul. 19	09:17-10:32	25.8	49.00	10147 ± 260	392 ± 10	1.36 ± 0.034	84.07 ± 2.10	C2
*M*88	SD-AR_M00029 (+112.8, +70.0)	2019 Jul. 19	08:00-09:15	18.3	-	< 10322.69	< 192.69	< 0.28	< 43.91	2
*M*90	SD-AR_M00030 (-82.5, +293.6)	2019 Jul. 24	09:35-10:50	18.3	20.75	10357 ± 262	227 ± 6	0.13 ± 0.003	18.42 ± 0.46	C1
*M*91	SD-AR_M00030 (-82.5, +293.6)	2019 Jul. 24	10:52-12:07	25.8	-	< 10027.11	< 272.11	< 0.47	< 33.81	1
*M*90	SPoCA_22998	2019 Jul. 24	09:35-10:50	18.3	9.50	10521 ± 266	391 ± 10	0.14 ± 0.003	8.51 ± 0.21	2
*M*91	SPoCA_22998	2019 Jul. 24	10:52-12:07	25.8	-	< 10025.05	< 270.05	< 0.09	< 17.29	2
*M*92	SD-AR_M00031 (+187.0, +45.2)	2019 Jul. 30	08:10-09:25	18.3	21.00	10485 ± 266	355 ± 9	0.22 ± 0.005	18.72 ± 0.47	C1
*M*93	SD-AR_M00031 (+187.0, +45.2)	2019 Jul. 30	09:27-10:42	25.8	-	10319 ± 263	564 ± 14	0.97 ± 0.024	36.84 ± 0.92	C1
*M*94	NOAA_12747, SPoCA_23064	2019 Aug. 7	10:00-11:14	18.3	28.00	10652 ± 268	522 ± 13	0.40 ± 0.010	25.09 ± 0.63	k1
*M*95	NOAA_12747, SPoCA_23064	2019 Aug. 7	11:17-12:31	25.8	-	10395 ± 264	640 ± 16	1.75 ± 0.044	49.02 ± 1.23	C1
*M*94	SD-AR_M00032 (-398.6, +333.1)	2019 Aug. 7	10:00-11:14	18.3	14.00	10344 ± 260	214 ± 5	0.11 ± 0.003	12.45 ± 0.31	Ck2
*M*95	SD-AR_M00032 (-398.6, +333.1)	2019 Aug. 7	11:17-12:31	25.8	-	< 10243.69	< 488.69	< 0.64	< 22.59	2
*M*100	SD-AR_M00033 (+178.3, -69.6)	2019 Sep. 5	07:30-08:45	18.3	26.25	10341 ± 262	211 ± 5	0.17 ± 0.004	23.32 ± 0.58	C1
*M*101	SD-AR_M00033 (+178.3, -69.6)	2019 Sep. 5	08:48-10:02	25.8	-	< 10008.62	< 253.62	< 0.51	< 45.24	1
*M*102	SD-AR_M00034 (+371.6, +383.7)	2019 Sep. 10	09:50-11:05	18.3	51.50	10353 ± 261	223 ± 6	0.32 ± 0.008	45.65 ± 1.14	C1
*M*103	SD-AR_M00034 (+371.6, +383.7)	2019 Sep. 10	11:08-12:22	25.8	-	< 9929.99	< 174.99	< 0.30	< 87.32	1
*M*106	SD-AR_M00035 (+175.6, +88.3)	2019 Sep. 24	10:55-12:10	18.3	22.00	10367 ± 261	237 ± 6	0.18 ± 0.004	19.58 ± 0.49	C1
*M*107	SD-AR_M00035 (+175.6, +88.3)	2019 Sep. 24	12:13-13:27	25.8	-	< 10072.67	< 317.67	< 0.76	< 38.74	1
*M*108	SD-AR_M00036 (-456.5, -204.0)	2019 Oct. 1	09:10-10:25	18.3	34.75	10324 ± 260	194 ± 5	0.23 ± 0.006	30.86 ± 0.77	1
*M*109	SD-AR_M00036 (-456.5, -204.0)	2019 Oct. 1	10:28-11:42	25.8	-	< 9927.49	< 172.49	< 0.30	< 57.99	1
*M*109	SD-AR_M00037 (+142.6, +86.9)	2019 Oct. 1	10:28-11:42	25.8	33.75	10014 ± 254	259 ± 6	0.65 ± 0.016	57.62 ± 1.44	C2
*M*108	SD-AR_M00037 (+142.6, +86.9)	2019 Oct. 1	09:10-10:25	18.3	-	< 10256.19	< 126.19	< 0.07	< 30.00	2
*M*110	SD-AR_M00038 (-485.1, +63.1)	2019 Oct. 9	09:10-10:25	18.3	29.50	10353 ± 263	223 ± 6	0.21 ± 0.005	26.22 ± 0.66	C1

[a] *This AR corresponds also to other 3 SPoCA targets: SPoCA_22276, SPoCA_22279, and SPoCA_22280.*
[b] *Unknown flux because the brightness temperature of the AR pixels is lower than the quiet-Sun.*
[c] *There are two very close ARs in this position. Our algorithm detected a unique AR.*
[d] *This AR corresponds also to other 3 SPoCA targets: SPoCA_24850, SPoCA_24851, and SPoCA_24853.*
[e] *The quality of the* 25.8 *GHz-solar map on December 7, 2020 is very low.*
[f] *Same region.*
[g] *There is a very close AR in this position (NOAA_12793/SPoCA_24935) that pollutes our measures.*
[h] *There is a very close AR in this position (NOAA_12792/SPoCA_24918) that pollutes our measures.*

Table 6.2: Continued.

ID	*ar_id*	Epoch	T (UT)	ν_{obs} (GHz)	Size (arcmin^2)	$T_{p,tot}$ (K)	$T_{p,ex}$ (K)	S_{sub} (sfu)	S_{tot} (sfu)	Notes
*M*111	SD-AR_M00038 (-485.1, +63.1)	2019 Oct. 9	10:28-11:42	25.8	-	< 8438.77	-[b]	-[b]	< 41.88	1
*M*110	SD-AR_M00039 (+245.3, -293.2)	2019 Oct. 9	09:10-10:25	18.3	50.50	10451 ± 265	321 ± 8	0.40 ± 0.010	44.92 ± 1.12	k2
*M*111	SD-AR_M00039 (+245.3, -293.2)	2019 Oct. 9	10:28-11:42	25.8	-	< 8301.79	-[b]	-[b]	< 70.07	2
*M*110	SPoCA_23273	2019 Oct. 9	09:10-10:25	18.3	26.75	10462 ± 266	332 ± 8	0.27 ± 0.007	23.86 ± 0.60	k3
*M*111	SPoCA_23273	2019 Oct. 9	10:28-11:42	25.8	-	< 8409.97	-[b]	-[b]	< 37.78	3
*S*112	SD-AR_S00001 (-381.2, -629.1)	2019 Oct. 9	11:46-13:30	18.8	13.68	10431 ± 261	332 ± 8	0.09 ± 0.002	12.76 ± 0.32	1
*S*113	SD-AR_S00001 (-381.2, -629.1)	2019 Oct. 9	09:14-10:58	24.7	-	< 10177.54	< 378.54	< 0.34	< 15.88	1
*S*112	SPoCA_23273	2019 Oct. 9	11:46-13:30	18.8	45.72	10740 ± 269	641 ± 16	0.57 ± 0.014	42.99 ± 1.07	2
*S*113	SPoCA_23273	2019 Oct. 9	09:14-10:58	24.7	-	< 10187.78	< 388.78	< 0.41	< 50.06	2
*S*112	SD-AR_S00002 (-59.9, +798.2)[f]	2019 Oct. 9	11:46-13:30	18.8	23.40	10524 ± 263	425 ± 11	0.43 ± 0.011	22.10 ± 0.55	bk3
*S*113	SD-AR_S00002 (-59.9, +798.2)[f]	2019 Oct. 9	09:14-10:58	24.7	-	< 10196.77	< 397.77	< 0.37	< 25.99	3
*S*113	SD-AR_S00002 (-165.9, +797.0)[f]	2019 Oct. 9	09:14-10:58	24.7	12.75	10197 ± 255	398 ± 10	0.31 ± 0.008	20.06 ± 0.50	bk3
*S*112	SD-AR_S00002 (-165.9, +797.0)[f]	2019 Oct. 9	11:46-13:30	18.8	-	< 10524.27	< 425.27	< 0.32	< 16.54	3
*M*114	SD-AR_M00040 (+195.9, -109.9)	2019 Oct. 14	12:40-13:55	18.3	48.75	10327 ± 261	197 ± 5	0.32 ± 0.008	43.32 ± 1.08	1
*M*115	SD-AR_M00040 (+195.9, -109.9)	2019 Oct. 14	13:58-15:12	25.8	-	< 10039.64	< 284.64	< 1.47	< 83.34	1
*M*116	SD-AR_M00041 (-599.7, -226.6)	2019 Oct. 23	11:50-13:05	18.3	29.75	10381 ± 266	251 ± 6	0.23 ± 0.006	26.45 ± 0.66	1
*M*117	SD-AR_M00041 (-599.7, -226.6)	2019 Oct. 23	13:08-14:22	25.8	-	< 9803.18	< 48.18	< 0.01	< 48.74	1
*M*118	SPoCA_23409	2019 Nov. 4	10:15-11:30	18.3	43.00	10632 ± 270	502 ± 13	0.70 ± 0.018	38.62 ± 0.97	1
*M*119	SPoCA_23409	2019 Nov. 4	11:33-12:47	25.8	-	< 9897.42	< 142.42	< 0.08	< 70.47	1
*M*120	SD-AR_M00042 (+298.5, +25.1)	2019 Nov. 14	10:25-11:40	18.3	36.00	10360 ± 263	230 ± 6	0.34 ± 0.008	32.08 ± 0.80	1
*M*121	SD-AR_M00042 (+298.5, +25.1)	2019 Nov. 14	11:42-12:57	25.8	-	10103 ± 256	348 ± 9	1.27 ± 0.032	62.46 ± 1.56	1
*M*120	NOAA_12752, SPoCA_23461	2019 Nov. 14	10:25-11:40	18.3	10.00	10755 ± 273	625 ± 16	0.19 ± 0.005	8.98 ± 0.22	b2
*M*121	NOAA_12752, SPoCA_23461	2019 Nov. 14	11:42-12:57	25.8	-	< 9853.87	< 98.87	< 0.01	< 17.64	2
*M*122	SPoCA_23479	2019 Nov. 21	10:10-11:25	18.3	31.25	10314 ± 260	184 ± 5	0.21 ± 0.005	27.76 ± 0.69	1
*M*123	SPoCA_23479	2019 Nov. 21	11:27-12:42	25.8	-	< 9875.47	< 120.47	< 0.08	< 53.37	1
*M*122	SD-AR_M00043 (+201.2, -376.0)	2019 Nov. 21	10:10-11:25	18.3	19.25	10269 ± 259	139 ± 3	0.09 ± 0.002	17.07 ± 0.43	2
*M*123	SD-AR_M00043 (+201.2, -376.0)	2019 Nov. 21	11:27-12:42	25.8	-	< 9909.36	< 154.36	< 0.22	< 32.70	2
*M*123	SD-AR_M00044 (+83.6, +73.3)	2019 Nov. 21	11:27-12:42	25.8	48.75	10047 ± 254	292 ± 7	1.36 ± 0.034	83.66 ± 2.09	3
*M*122	SD-AR_M00044 (+83.6, +73.3)	2019 Nov. 21	10:10-11:25	18.3	-	< 10242.39	< 112.39	< 0.14	< 44.21	3
*M*124	SD-AR_M00045 (-404.2, +203.9)	2019 Nov. 26	10:00-11:15	18.3	20.52	10293 ± 259	163 ± 4	0.13 ± 0.003	18.23 ± 0.46	1
*M*125	SD-AR_M00045 (-404.2, +203.9)	2019 Nov. 26	11:17-12:32	25.8	-	< 9934.34	< 179.34	< 0.23	< 22.59	1
*S*128	SPoCA_23783	2020 Jan. 28	13:40-15:24	24.7	13.00	11373 ± 284	1574 ± 39	0.80 ± 0.020	21.00 ± 0.52	1
*S*127	SPoCA_23783	2020 Jan. 28	11:26-13:18	18.8	-	12321 ± 308	2222 ± 56	0.66 ± 0.016	12.94 ± 0.32	1
*S*126	SPoCA_23783	2020 Jan. 28	09:41-11:25	18.8	-	12472 ± 312	2373 ± 59	1.41 ± 0.035	32.29 ± 0.81	1
*S*128	NOAA_12757, SPoCA_23779	2020 Jan. 28	13:40-15:24	24.7	7.75	11791 ± 295	1992 ± 50	0.52 ± 0.013	12.56 ± 0.31	2
*S*127	NOAA_12757, SPoCA_23779	2020 Jan. 28	11:26-13:18	18.8	-	12489 ± 312	2390 ± 60	0.48 ± 0.012	7.44 ± 0.19	2
*S*126	NOAA_12757, SPoCA_23779	2020 Jan. 28	09:41-11:25	18.8	-	12457 ± 312	2358 ± 59	0.66 ± 0.017	20.85 ± 0.52	2

[a] *This AR corresponds also to other 3 SPoCA targets: SPoCA_22276, SPoCA_22279, and SPoCA_22280.*
[b] *Unknown flux because the brightness temperature of the AR pixels is lower than the quiet-Sun.*
[c] *There are two very close ARs in this position. Our algorithm detected a unique AR.*
[d] *This AR corresponds also to other 3 SPoCA targets: SPoCA_24850, SPoCA_24851, and SPoCA_24853.*
[e] *The quality of the* 25.8 *GHz-solar map on December 7, 2020 is very low.*
[f] *Same region.*
[g] *There is a very close AR in this position (NOAA_12793/SPoCA_24935) that pollutes our measures.*
[h] *There is a very close AR in this position (NOAA_12792/SPoCA_24918) that pollutes our measures.*

Table 6.2: Continued.

ID	*ar_id*	Epoch	T (UT)	ν_{obs} (GHz)	Size (arcmin^2)	$T_{p,tot}$ (K)	$T_{p,ex}$ (K)	S_{sub} (sfu)	S_{tot} (sfu)	Notes
*S*128	SPoCA_23787	2020 Jan. 28	13:40-15:24	24.7	4.00	10238 ± 256	439 ± 11	0.14 ± 0.003	6.35 ± 0.16	b3
*S*126	SPoCA_23787	2020 Jan. 28	09:41-11:25	18.8	-	< 10364.69	< 265.69	< 0.11	< 10.16	3
*S*127	SPoCA_23787	2020 Jan. 28	11:26-13:18	18.8	-	< 10691.34	< 592.34	< 0.08	< 3.54	3
*M*129	NOAA_12770, SPoCA_24500	2020 Aug. 10	09:10-10:24	18.3	25.20	11433 ± 288	1303 ± 33	0.70 ± 0.017	22.92 ± 0.57	k1
*M*130	NOAA_12770, SPoCA_24500	2020 Aug. 10	10:27-11:42	25.8	-	10713 ± 270	958 ± 24	1.17 ± 0.029	46.13 ± 1.15	k1
*M*129	NOAA_12769, SPoCA_24497	2020 Aug. 10	09:10-10:24	18.3	48.24	10829 ± 273	699 ± 17	0.87 ± 0.022	43.27 ± 1.08	k2
*M*130	NOAA_12769, SPoCA_24497	2020 Aug. 10	10:27-11:42	25.8	-	< 10123.60	< 368.60	< 0.86	< 84.20	2
*M*129	SD-AR_M00046 (-594.6, -380.8)	2020 Aug. 10	09:10-10:24	18.3	20.52	10385 ± 262	255 ± 6	0.21 ± 0.005	18.27 ± 0.46	3
*M*130	SD-AR_M00046 (-594.6, -380.8)	2020 Aug. 10	10:27-11:42	25.8	-	< 9946.44	< 191.44	< 0.19	< 35.32	3
*M*132	SPoCA_24514	2020 Aug. 17	10:32-11:47	25.8	7.56	10159 ± 256	404 ± 10	0.22 ± 0.006	12.98 ± 0.32	k1
*M*131	SPoCA_24514	2020 Aug. 17	09:15-10:29	18.3	-	10656 ± 268	526 ± 13	0.16 ± 0.004	6.19 ± 0.15	k1
*M*131	SPoCA_24533	2020 Aug. 17	09:15-10:29	18.3	52.20	10465 ± 263	335 ± 8	0.54 ± 0.014	46.58 ± 1.16	Ck2
*M*132	SPoCA_24533	2020 Aug. 17	10:32-11:47	25.8	-	< 10017.36	< 262.36	< 0.63	< 89.83	2
*M*131	NOAA_12772, SPoCA_24530	2020 Aug. 17	09:15-10:29	18.3	27.36	10685 ± 269	555 ± 14	0.36 ± 0.009	24.48 ± 0.61	3
*M*132	NOAA_12772, SPoCA_24530	2020 Aug. 17	10:32-11:47	25.8	-	10289 ± 260	534 ± 13	0.87 ± 0.022	47.65 ± 1.19	C3
*M*133	SD-AR_M00047 (+89.5, -321.3)	2020 Aug. 26	09:10-10:24	18.3	27.00	10367 ± 261	237 ± 6	0.19 ± 0.005	24.00 ± 0.60	1
*M*134	SD-AR_M00047 (+89.5, -321.3)	2020 Aug. 26	10:27-11:42	25.8	-	< 10099.77	< 344.77	< 0.75	< 46.32	1
*M*135	HMI_SHARP_7443	2020 Sep. 2	09:15-10:29	18.3	27.72	10528 ± 265	398 ± 10	0.24 ± 0.006	24.60 ± 0.62	1
*M*136	HMI_SHARP_7443	2020 Sep. 2	10:32-11:47	25.8	-	< 10160.03	< 405.03	< 0.62	< 48.53	1
*M*137	SD-AR_M00048 (+248.3, -73.5)	2020 Sep. 6	08:00-09:14	18.3	16.92	10361 ± 261	231 ± 6	0.15 ± 0.004	15.08 ± 0.38	C1
*M*138	SD-AR_M00048 (+248.3, -73.5)	2020 Sep. 6	09:17-10:32	25.8	-	< 10026.62	< 271.62	< 0.40	< 30.79	1
*M*137	SD-AR_M00049 (-464.4, +391.4)	2020 Sep. 6	08:00-09:14	18.3	24.12	10337 ± 260	207 ± 5	0.17 ± 0.004	21.42 ± 0.54	2
*M*138	SD-AR_M00049 (-464.4, +391.4)	2020 Sep. 6	09:17-10:32	25.8	-	< 9971.76	< 216.76	< 0.42	< 41.12	2
*M*137	SPoCA_24604	2020 Sep. 6	08:00-09:14	18.3	23.04	10418 ± 262	288 ± 7	0.17 ± 0.004	20.44 ± 0.51	3
*M*138	SPoCA_24604	2020 Sep. 6	09:17-10:32	25.8	-	< 10033.27	< 278.27	< 0.37	< 39.74	3
*M*139	SD-AR_M00050 (-472.0, -411.1)	2020 Sep. 14	10:10-11:24	18.3	7.92	10328 ± 259	198 ± 5	0.06 ± 0.001	7.04 ± 0.18	1
*M*140	SD-AR_M00050 (-472.0, -411.1)	2020 Sep. 14	11:27-12:42	25.8	-	< 9635.91	-[b]	-[b]	< 14.82	1
*M*139	SPoCA_24651	2020 Sep. 14	10:10-11:24	18.3	16.20	10449 ± 262	319 ± 8	0.17 ± 0.004	14.45 ± 0.36	2
*M*140	SPoCA_24651	2020 Sep. 14	11:27-12:42	25.8	-	< 9856.64	< 101.64	< 0.06	< 27.72	2
*S*141	SD-AR_S00003 (-109.6, -862.2)	2020 Sep. 17	09:18-11:02	18.8	11.88	10544 ± 264	445 ± 11	0.18 ± 0.004	11.15 ± 0.28	bk1
*S*142	SD-AR_S00003 (-109.6, -862.2)	2020 Sep. 17	11:18-13:02	24.7	-	< 10072.00	< 273.00	< 0.17	< 19.17	1
*S*142	SD-AR_S00004 (-195.9, -503.2)	2020 Sep. 17	11:18-13:02	24.7	10.08	10132 ± 253	333 ± 8	0.18 ± 0.005	15.84 ± 0.40	Ck2
*S*141	SD-AR_S00004 (-195.9, -503.2)	2020 Sep. 17	09:18-11:02	18.8	-	10547 ± 264	448 ± 11	0.15 ± 0.004	10.17 ± 0.25	Ck2
*S*141	SD-AR_S00005 (-8.7, +828.8)	2020 Sep. 17	09:18-11:02	18.8	19.44	10648 ± 266	549 ± 14	0.31 ± 0.008	18.31 ± 0.46	b3
*S*142	SD-AR_S00005 (-8.7, +828.8)	2020 Sep. 17	11:18-13:02	24.7	-	10256 ± 257	457 ± 11	0.59 ± 0.015	30.69 ± 0.77	b3
*S*142	SD-AR_S00006 (-546.4, -503.5)	2020 Sep. 17	11:18-13:02	24.7	15.84	10209 ± 255	410 ± 10	0.35 ± 0.009	24.95 ± 0.62	k4
*S*141	SD-AR_S00006 (-546.4, -503.5)	2020 Sep. 17	09:18-11:02	18.8	-	< 10432.85	< 333.85	< 0.19	< 14.89	4
*S*142	SD-AR_S00007 (-193.6, -342.2)	2020 Sep. 17	11:18-13:02	24.7	10.80	10133 ± 254	334 ± 8	0.20 ± 0.005	16.97 ± 0.42	Ck5

[a] *This AR corresponds also to other 3 SPoCA targets: SPoCA_22276, SPoCA_22279, and SPoCA_22280.*
[b] *Unknown flux because the brightness temperature of the AR pixels is lower than the quiet-Sun.*
[c] *There are two very close ARs in this position. Our algorithm detected a unique AR.*
[d] *This AR corresponds also to other 3 SPoCA targets: SPoCA_24850, SPoCA_24851, and SPoCA_24853.*
[e] *The quality of the* 25.8 *GHz-solar map on December 7, 2020 is very low.*
[f] *Same region.*
[g] *There is a very close AR in this position (NOAA_12793/SPoCA_24935) that pollutes our measures.*
[h] *There is a very close AR in this position (NOAA_12792/SPoCA_24918) that pollutes our measures.*

Table 6.2: Continued.

ID	*ar_id*	Epoch	T (UT)	ν_{obs} (GHz)	Size (arcmin^2)	$T_{p,tot}$ (K)	$T_{p,ex}$ (K)	S_{sub} (sfu)	S_{tot} (sfu)	Notes
*S*141	SD-AR_S00007 (-193.6, -342.2)	2020 Sep. 17	09:18-11:02	18.8	-	< 10350.94	< 251.94	< 0.10	< 10.45	5
*S*142	SD-AR_S00008 (-712.7, +358.8)	2020 Sep. 17	11:18-13:02	24.7	10.08	10189 ± 255	390 ± 10	0.22 ± 0.006	15.88 ± 0.40	bk6
*S*141	SD-AR_S00008 (-712.7, +358.8)	2020 Sep. 17	09:18-11:02	18.8	-	< 10400.01	< 301.01	< 0.12	< 10.13	6
*M*143	SPoCA_24702	2020 Sep. 29	09:00-10:14	18.3	57.96	10698 ± 269	568 ± 14	0.66 ± 0.016	51.74 ± 1.29	1
*M*144	SPoCA_24702	2020 Sep. 29	10:17-11:32	25.8	-	10345 ± 261	590 ± 15	1.38 ± 0.035	99.01 ± 2.48	C1
*M*144	NOAA_12773, SPoCA_24694	2020 Sep. 29	10:17-11:32	25.8	54.00	10764 ± 271	1009 ± 25	2.86 ± 0.071	94.01 ± 2.35	2
*M*143	NOAA_12773, SPoCA_24694	2020 Sep. 29	09:00-10:14	18.3	-	11738 ± 295	1608 ± 40	1.67 ± 0.042	49.28 ± 1.23	2
*M*147	NOAA_12776, SPoCA_24743	2020 Oct. 19	08:00-09:14	18.3	25.20	11604 ± 292	1474 ± 37	1.00 ± 0.025	23.22 ± 0.58	k1
*M*148	NOAA_12776, SPoCA_24743	2020 Oct. 19	09:17-10:32	25.8	-	10566 ± 265	811 ± 20	1.11 ± 0.028	43.00 ± 1.08	k1
*M*148	SD-AR_M00051 (+106.5, +10.3)	2020 Oct. 19	09:17-10:32	25.8	71.28	10095 ± 253	340 ± 8	1.34 ± 0.034	121.64 ± 3.04	Ck2
*M*147	SD-AR_M00051 (+106.5, +10.3)	2020 Oct. 19	08:00-09:14	18.3	-	< 10282.61	< 152.61	< 0.21	< 62.05	2
*S*150	SPoCA_24770, SPoCA_24772[c]	2020 Oct. 29	10:17-12:01	18.8	34.79	17756 ± 444	7657 ± 191	4.17 ± 0.104	37.46 ± 0.94	1
*S*149	SPoCA_24770, SPoCA_24772[c]	2020 Oct. 29	08:32-10:05	24.7	-	14241 ± 356	4442 ± 111	3.82 ± 0.096	56.63 ± 1.42	1
*S*149	SPoCA_24760	2020 Oct. 29	08:32-10:05	24.7	6.37	11044 ± 276	1245 ± 31	0.45 ± 0.011	10.31 ± 0.26	b2
*S*150	SPoCA_24760	2020 Oct. 29	10:17-12:01	18.8	-	11540 ± 289	1441 ± 36	0.38 ± 0.010	6.30 ± 0.16	b2
*M*152	NOAA_12778, SPoCA_24770	2020 Oct. 30	09:32-10:47	25.8	13.68	10860 ± 273	1105 ± 28	0.85 ± 0.021	23.56 ± 0.59	b1
*M*151	NOAA_12778, SPoCA_24770	2020 Oct. 30	08:15-09:29	18.3	-	13102 ± 329	2972 ± 74	1.40 ± 0.035	12.48 ± 0.31	b1
*M*151	SD-AR_M00052 (-21.8, +487.4)	2020 Oct. 30	08:15-09:29	18.3	32.04	10341 ± 260	211 ± 5	0.23 ± 0.006	28.49 ± 0.71	C2
*M*152	SD-AR_M00052 (-21.8, +487.4)	2020 Oct. 30	09:32-10:47	25.8	-	10000 ± 252	245 ± 6	0.54 ± 0.014	52.78 ± 1.32	C2
*M*152	SD-AR_M00053 (-87.9, -192.3)	2020 Oct. 30	09:32-10:47	25.8	52.92	9988 ± 251	233 ± 6	0.69 ± 0.017	90.00 ± 2.25	C3
*M*151	SD-AR_M00053 (-87.9, -192.3)	2020 Oct. 30	08:15-09:29	18.3	-	< 10243.98	< 113.98	< 0.12	< 46.42	3
*M*153	NOAA_12781, SPoCA_24790	2020 Nov. 6	09:52-11:07	25.8	21.96	14133 ± 355	4378 ± 109	4.50 ± 0.113	41.57 ± 1.04	k1
*M*154	NOAA_12781, SPoCA_24790	2020 Nov. 6	08:35-09:49	18.3	-	19203 ± 481	9073 ± 227	6.31 ± 0.158	26.00 ± 0.65	k1
*M*153	NOAA_12780, SPoCA_24778	2020 Nov. 6	09:52-11:07	25.8	69.48	10382 ± 262	627 ± 16	1.92 ± 0.048	119.14 ± 2.98	k2
*M*154	NOAA_12780, SPoCA_24778	2020 Nov. 6	08:35-09:49	18.3	-	< 11014.13	< 884.13	< 0.77	< 61.97	2
*M*153	SPoCA_24797	2020 Nov. 6	09:52-11:07	25.8	29.52	10176 ± 256	421 ± 11	0.95 ± 0.024	50.78 ± 1.27	Ck3
*M*154	SPoCA_24797	2020 Nov. 6	08:35-09:49	18.3	-	< 10718.80	< 588.80	< 0.53	< 27.15	3
*M*155	NOAA_12781, SPoCA_24790	2020 Nov. 8	09:22-10:32	25.8	33.48	12058 ± 303	2303 ± 58	3.42 ± 0.085	59.93 ± 1.50	1
*M*155	NOAA_12780, SPoCA_24778	2020 Nov. 8	09:22-10:32	25.8	71.64	10469 ± 263	714 ± 18	2.89 ± 0.072	123.82 ± 3.10	2
*M*157	NOAA_12781, SPoCA_24790	2020 Nov. 11	11:17-12:32	25.8	32.04	11567 ± 291	1812 ± 45	2.68 ± 0.067	56.71 ± 1.42	k1
*M*156	NOAA_12781, SPoCA_24790	2020 Nov. 11	10:00-11:14	18.3	-	13570 ± 341	3440 ± 86	2.65 ± 0.066	29.95 ± 0.75	k1
*M*156	NOAA_12782, SPoCA_24807	2020 Nov. 11	10:00-11:14	18.3	4.68	10573 ± 266	443 ± 11	0.03 ± 0.001	4.10 ± 0.10	b2
*M*157	NOAA_12782, SPoCA_24807	2020 Nov. 11	11:17-12:32	25.8	-	< 9419.44	-[b]	-[b]	< 6.79	2
*M*156	SD-AR_M00054 (+24.6, -404.7)	2020 Nov. 11	10:00-11:14	18.3	28.44	10398 ± 261	268 ± 7	0.30 ± 0.007	25.38 ± 0.63	Ck3
*M*157	SD-AR_M00054 (+24.6, -404.7)	2020 Nov. 11	11:17-12:32	25.8	-	< 9964.03	< 209.03	< 0.75	< 48.76	3
*M*156	NOAA_12780, SPoCA_24778	2020 Nov. 11	10:00-11:14	18.3	10.44	10609 ± 267	479 ± 12	0.17 ± 0.004	9.36 ± 0.23	b4
*M*157	NOAA_12780, SPoCA_24778	2020 Nov. 11	11:17-12:32	25.8	-	< 9909.88	< 154.88	< 0.11	< 18.76	4
*M*158	NOAA_12783, SPoCA_24812	2020 Nov. 23	09:15-10:29	18.3	31.68	12483 ± 313	2353 ± 59	1.67 ± 0.042	29.61 ± 0.74	k1

[a] *This AR corresponds also to other 3 SPoCA targets: SPoCA_22276, SPoCA_22279, and SPoCA_22280.*
[b] *Unknown flux because the brightness temperature of the AR pixels is lower than the quiet-Sun.*
[c] *There are two very close ARs in this position. Our algorithm detected a unique AR.*
[d] *This AR corresponds also to other 3 SPoCA targets: SPoCA_24850, SPoCA_24851, and SPoCA_24853.*
[e] *The quality of the* 25.8 *GHz-solar map on December 7, 2020 is very low.*
[f] *Same region.*
[g] *There is a very close AR in this position (NOAA_12793/SPoCA_24935) that pollutes our measures.*
[h] *There is a very close AR in this position (NOAA_12792/SPoCA_24918) that pollutes our measures.*

Table 6.2: Continued.

ID	*ar_id*	Epoch	T (UT)	ν_{obs} (GHz)	Size (arcmin^2)	$T_{p,tot}$ (K)	$T_{p,ex}$ (K)	S_{sub} (sfu)	S_{tot} (sfu)	Notes
*M*159	NOAA_12783, SPoCA_24812	2020 Nov. 23	12:22-13:37	25.8	-	10676 ± 269	921 ± 23	1.85 ± 0.046	57.16 ± 1.43	k1
*M*158	NOAA_12784, SPoCA_24823	2020 Nov. 23	09:15-10:29	18.3	41.04	11037 ± 277	907 ± 23	0.84 ± 0.021	37.03 ± 0.93	2
*M*159	NOAA_12784, SPoCA_24823	2020 Nov. 23	12:22-13:37	25.8	-	10171 ± 257	416 ± 10	1.05 ± 0.026	70.27 ± 1.76	C2
*M*158	SPoCA_24821	2020 Nov. 23	09:15-10:29	18.3	52.20	12256 ± 308	2126 ± 53	1.75 ± 0.044	47.78 ± 1.19	k3
*M*159	SPoCA_24821	2020 Nov. 23	12:22-13:37	25.8	-	< 10675.83	< 920.83	< 2.65	< 92.57	3
*M*158	NOAA_12786, SPoCA_24827	2020 Nov. 23	09:15-10:29	18.3	8.28	12227 ± 307	2097 ± 52	0.57 ± 0.014	7.69 ± 0.19	4
*M*159	NOAA_12786, SPoCA_24827	2020 Nov. 23	12:22-13:37	25.8	-	< 9101.55	-[b]	-[b]	< 9.37	4
*M*160	SPoCA_24827, SPoCA_24840[c]	2020 Nov. 28	10:35-11:49	18.3	63.36	15007 ± 376	4877 ± 122	7.53 ± 0.188	63.31 ± 1.58	1
*M*161	SPoCA_24827, SPoCA_24840[c]	2020 Nov. 28	11:52-13:04	25.8	-	12074 ± 303	2319 ± 58	7.25 ± 0.181	112.81 ± 2.82	1
*M*160	NOAA_12783, SPoCA_24812	2020 Nov. 28	10:35-11:49	18.3	5.76	10904 ± 274	774 ± 19	0.16 ± 0.004	5.24 ± 0.13	b2
*M*161	NOAA_12783, SPoCA_24812	2020 Nov. 28	11:52-13:04	25.8	-	< 9882.84	< 127.84	< 0.03	< 8.40	2
*M*163	NOAA_12789, SPoCA_24834	2020 Nov. 30	10:42-11:57	25.8	22.32	10401 ± 263	646 ± 16	0.83 ± 0.021	38.40 ± 0.96	k1
*M*162	NOAA_12789, SPoCA_24834	2020 Nov. 30	09:25-10:39	18.3	-	11624 ± 291	1494 ± 37	1.03 ± 0.026	20.08 ± 0.50	k1
*M*163	SPoCA_24827[d]	2020 Nov. 30	10:42-11:57	25.8	67.68	11299 ± 285	1544 ± 39	5.83 ± 0.146	119.83 ± 3.00	k2
*M*162	SPoCA_24827[d]	2020 Nov. 30	09:25-10:39	18.3	-	13273 ± 333	3143 ± 79	6.58 ± 0.164	67.15 ± 1.68	k2
*M*163	NOAA_12787, SPoCA_24849	2020 Nov. 30	10:42-11:57	25.8	13.68	10044 ± 254	289 ± 7	0.30 ± 0.007	23.38 ± 0.58	3
*M*162	NOAA_12787, SPoCA_24849	2020 Nov. 30	09:25-10:39	18.3	-	10524 ± 264	394 ± 10	0.21 ± 0.005	12.26 ± 0.31	C3
*M*164	NOAA_12790, SPoCA_24848[e]	2020 Dec. 7	09:15-13:29	18.3	65.16	11676 ± 293	1546 ± 39	1.66 ± 0.042	58.78 ± 1.47	k1
*M*165	NOAA_12790, SPoCA_24848[e]	2020 Dec. 7	10:32-11:47	25.8	-	< 11001.09	< 1246.09	< 2.72	< 111.93	1
*M*164	NOAA_12791, SPoCA_24870[e]	2020 Dec. 7	09:15-13:29	18.3	41.76	12296 ± 309	2166 ± 54	2.06 ± 0.051	38.84 ± 0.97	k2
*M*165	NOAA_12791, SPoCA_24870[e]	2020 Dec. 7	10:32-11:47	25.8	-	< 10218.71	< 463.71	< 0.34	< 66.32	2
*M*166	NOAA_12792, SPoCA_24918	2020 Dec. 13	09:15-13:29	18.3	10.08	11024 ± 277	894 ± 22	0.21 ± 0.005	9.02 ± 0.23	bk1
*M*167	NOAA_12792, SPoCA_24918	2020 Dec. 13	10:32-11:47	25.8	-	< 9745.24	-[b]	-[b]	< 15.86	1
*M*166	SPoCA_24905	2020 Dec. 13	09:15-13:29	18.3	21.24	10417 ± 261	287 ± 7	0.19 ± 0.005	18.87 ± 0.47	Ck2
*M*167	SPoCA_24905	2020 Dec. 13	10:32-11:47	25.8	-	< 9938.67	< 183.67	< 0.17	< 35.22	2
*M*166	SD-AR_M00055 (+183.2, -545.2)	2020 Dec. 13	09:15-13:29	18.3	31.68	10376 ± 260	246 ± 6	0.26 ± 0.007	28.16 ± 0.70	Ck3
*M*167	SD-AR_M00055 (+183.2, -545.2)	2020 Dec. 13	10:32-11:47	25.8	-	< 9885.66	< 130.66	< 0.17	< 52.78	3
*M*167	NOAA_12791, SPoCA_24917	2020 Dec. 13	10:32-11:47	25.8	6.12	9972 ± 252	217 ± 5	0.12 ± 0.003	10.45 ± 0.26	k4
*M*166	NOAA_12791, SPoCA_24917	2020 Dec. 13	09:15-13:29	18.3	-	10422 ± 262	292 ± 7	0.09 ± 0.002	5.81 ± 0.15	k4
*M*169	NOAA_12792, SPoCA_24918[g]	2020 Dec. 21	11:02-12:17	25.8	24.12	10359 ± 261	604 ± 15	0.92 ± 0.023	41.60 ± 1.04	k1
*M*168	NOAA_12792, SPoCA_24918[g]	2020 Dec. 21	09:45-10:59	18.3	-	11331 ± 285	1201 ± 30	0.98 ± 0.024	21.93 ± 0.55	k1
*M*168	NOAA_12793, SPoCA_24935[h]	2020 Dec. 21	09:45-10:59	18.3	70.92	11331 ± 285	1201 ± 30	1.89 ± 0.047	64.43 ± 1.61	k2
*M*169	NOAA_12793, SPoCA_24935[h]	2020 Dec. 21	11:02-12:17	25.8	-	10359 ± 261	604 ± 15	2.33 ± 0.058	123.80 ± 3.09	k2
*M*168	NOAA_12794, SPoCA_24943	2020 Dec. 21	09:45-10:59	18.3	9.72	10431 ± 262	301 ± 8	0.09 ± 0.002	8.64 ± 0.22	b3
*M*169	NOAA_12794, SPoCA_24943	2020 Dec. 21	11:02-12:17	25.8	-	< 9978.45	< 223.45	< 0.07	< 15.99	3
*M*168	SPoCA_24945	2020 Dec. 21	09:45-10:59	18.3	64.08	10490 ± 264	360 ± 9	0.58 ± 0.015	57.09 ± 1.43	Ck4
*M*169	SPoCA_24945	2020 Dec. 21	11:02-12:17	25.8	-	< 10063.51	< 308.51	< 1.13	< 109.28	4

[a] *This AR corresponds also to other 3 SPoCA targets: SPoCA_22276, SPoCA_22279, and SPoCA_22280.*
[b] *Unknown flux because the brightness temperature of the AR pixels is lower than the quiet-Sun.*
[c] *There are two very close ARs in this position. Our algorithm detected a unique AR.*
[d] *This AR corresponds also to other 3 SPoCA targets: SPoCA_24850, SPoCA_24851, and SPoCA_24853.*
[e] *The quality of the* 25.8 *GHz-solar map on December 7, 2020 is very low.*
[f] *Same region.*
[g] *There is a very close AR in this position (NOAA_12793/SPoCA_24935) that pollutes our measures.*
[h] *There is a very close AR in this position (NOAA_12792/SPoCA_24918) that pollutes our measures.*

Appendix C: Spectral indices obtained through the automatic procedure of SUNDARA

Table 6.3: Spectral indices obtained through the automatic procedure of SUNDARA. α_{T_p}, $\alpha_{T_{ex}}$, and α_{tot} indicate the spectral indices referred to $T_{p,tot}$, T_{ex}, and S_{tot}, respectively. Sequential numbers in the column *n"* are related to multiple AR detection for the same observing session. See the caption of Table 6.2 for a full description of the other parameters.

ID	*ar_id*	Epoch	T (UT)	ν_{obs} (GHz)	Size (arcmin^2)	α_{T_p}	$\alpha_{T_{ex}}$	α_{tot}	n
*M*21	SD-AR_M00005 (+496.9, -24.1)	2018 Apr. 12	10:20-11:22	18.1	19.25	< 1.79	-[b]	< 1.70	1
*M*22	SD-AR_M00005 (+496.9, -24.1)	2018 Apr. 12	11:24-12:26	26.1	-	–	–	–	1
*M*21	NOAA_12704, SPoCA_21724	2018 Apr. 12	10:20-11:22	18.1	6.00	< 1.70	< -5.57	< 1.74	2
*M*22	NOAA_12704, SPoCA_21724	2018 Apr. 12	11:24-12:26	26.1	-	–	–	–	2
*M*21	SD-AR_M00006 (-472.4, +298.1)	2018 Apr. 12	10:20-11:22	18.1	42.50	< 1.84	< -0.52	< 1.84	3
*M*22	SD-AR_M00006 (-472.4, +298.1)	2018 Apr. 12	11:24-12:26	26.1	-	–	–	–	3
*M*23	NOAA_12704, SPoCA_21724	2018 Apr. 13	07:30-08:39	18.1	14.00	1.76 ± 0.10	0.68 ± 0.10	1.88 ± 0.10	1
*M*24	NOAA_12704, SPoCA_21724	2018 Apr. 13	08:40-09:47	26.1	-	–	–	–	1
*M*23	NOAA_12704, SPoCA_21724	2018 Apr. 13	07:30-08:39	18.1	14.00	1.91 ± 0.18	1.99 ± 0.18	2.17 ± 0.18	1
*M*25	NOAA_12704, SPoCA_21724	2018 Apr. 13	10:00-11:09	22.1	-	–	–	–	1
*M*24	NOAA_12704, SPoCA_21724	2018 Apr. 13	08:40-09:47	26.1	14.00	1.57 ± 0.22	-0.89 ± 0.21	1.52 ± 0.21	1
*M*25	NOAA_12704, SPoCA_21724	2018 Apr. 13	10:00-11:09	22.1	-	–	–	–	1
*M*24	NOAA_12704, SPoCA_21724	2018 Apr. 13	08:40-09:47	26.1	14.00	1.81 ± 0.10	1.12 ± 0.10	0.88 ± 0.10	1
*M*26	NOAA_12704, SPoCA_21724	2018 Apr. 13	11:11-12:20	18.1	-	–	–	–	1
*M*25	NOAA_12704, SPoCA_21724	2018 Apr. 13	10:00-11:09	22.1	14.00	2.01 ± 0.18	2.79 ± 0.18	0.35 ± 0.18	1
*M*26	NOAA_12704, SPoCA_21724	2018 Apr. 13	11:11-12:20	18.1	-	–	–	–	1
*M*25	SD-AR_M00007 (-516.4, +13.2)	2018 Apr. 13	10:00-11:09	22.1	42.50	1.73 ± 0.18	-1.55 ± 0.18	0.09 ± 0.18	2
*M*26	SD-AR_M00007 (-516.4, +13.2)	2018 Apr. 13	11:11-12:20	18.1	-	–	–	–	2
*M*25	SD-AR_M00007 (-516.4, +13.2)	2018 Apr. 13	10:00-11:09	22.1	42.50	> 1.95	> 3.58	> 1.99	2
*M*23	SD-AR_M00007 (-516.4, +13.2)	2018 Apr. 13	07:30-08:39	18.1	-	–	–	–	2
*M*25	SD-AR_M00007 (-516.4, +13.2)	2018 Apr. 13	10:00-11:09	22.1	42.50	< 1.85	< 0.95	< 1.82	2
*M*24	SD-AR_M00007 (-516.4, +13.2)	2018 Apr. 13	08:40-09:47	26.1	-	–	–	–	2
*M*25	SD-AR_M00008 (+227.4, -108.1)	2018 Apr. 13	10:00-11:09	22.1	27.50	> 1.98	> 5.74	> 2.07	3
*M*23	SD-AR_M00008 (+227.4, -108.1)	2018 Apr. 13	07:30-08:39	18.1	-	–	–	–	3
*M*25	SD-AR_M00008 (+227.4, -108.1)	2018 Apr. 13	10:00-11:09	22.1	27.50	> 1.97	> 4.87	> 0.29	3
*M*26	SD-AR_M00008 (+227.4, -108.1)	2018 Apr. 13	11:11-12:20	18.1	-	–	–	–	3
*M*25	SD-AR_M00008 (+227.4, -108.1)	2018 Apr. 13	10:00-11:09	22.1	27.50	< 1.84	< 0.36	< 1.56	3
*M*24	SD-AR_M00008 (+227.4, -108.1)	2018 Apr. 13	08:40-09:47	26.1	-	–	–	–	3
*M*26	SD-AR_M00009 (+501.8, +176.8)	2018 Apr. 13	11:11-12:20	18.1	30.24	< 1.92	< 2.76	< 0.07	4
*M*25	SD-AR_M00009 (+501.8, +176.8)	2018 Apr. 13	10:00-11:09	22.1	-	–	–	–	4
*M*26	SD-AR_M00009 (+501.8, +176.8)	2018 Apr. 13	11:11-12:20	18.1	30.24	< 1.91	< 2.50	< 1.02	4
*M*24	SD-AR_M00009 (+501.8, +176.8)	2018 Apr. 13	08:40-09:47	26.1	-	–	–	–	4
*M*28	SD-AR_M00010 (-115.9, -146.2)	2018 Apr. 18	11:20-12:29	18.1	32.00	< 1.88	< 1.61	< 3.76	1

[a] *This AR corresponds also to other 3 SPoCA targets: SPoCA_22276, SPoCA_22279, and SPoCA_22280.*
[b] *Unknown flux because the brightness temperature of the AR pixels is lower than the quiet-Sun.*
[c] *There are two very close ARs in this position. Our algorithm detected a unique AR.*
[d] *This AR corresponds also to other 3 SPoCA targets: SPoCA_24850, SPoCA_24851, and SPoCA_24853.*
[e] *The quality of the* 25.8 *GHz-solar map on December 7, 2020 is very low.*
[f] *Same region.*
[g] *There is a very close AR in this position (NOAA_12793/SPoCA_24935) that pollutes our measures.*
[h] *There is a very close AR in this position (NOAA_12792/SPoCA_24918) that pollutes our measures.*

Table 6.3: Continued.

ID	*ar_id*	Epoch	T (UT)	ν_{obs} (GHz)	Size (arcmin^2)	α_{T_p}	$\alpha_{T_{ex}}$	α_{tot}	n
*M*29	SD-AR_M00010 (-115.9, -146.2)	2018 Apr. 18	12:31-13:40	26.1	-	–	–	–	1
*M*28	SPoCA_21739	2018 Apr. 18	11:20-12:29	18.1	28.00	< 1.91	< 2.34	< 3.67	2
*M*29	SPoCA_21739	2018 Apr. 18	12:31-13:40	26.1	-	–	–	–	2
*M*28	NOAA_12704, SPoCA_21724	2018 Apr. 18	11:20-12:29	18.1	28.75	1.90 ± 0.10	2.13 ± 0.10	3.66 ± 0.10	3
*M*29	NOAA_12704, SPoCA_21724	2018 Apr. 18	12:31-13:40	26.1	-	–	–	–	3
*M*28	SPoCA_21735	2018 Apr. 18	11:20-12:29	18.1	12.75	< 1.87	< 1.37	< 3.70	4
*M*29	SPoCA_21735	2018 Apr. 18	12:31-13:40	26.1	-	–	–	–	4
*M*28	SPoCA_21741	2018 Apr. 18	11:20-12:29	18.1	45.00	< 1.90	< 2.09	< 3.70	5
*M*29	SPoCA_21741	2018 Apr. 18	12:31-13:40	26.1	-	–	–	–	5
*M*30	NOAA_12706, SPoCA_21742	2018 Apr. 19	09:40-10:43	18.1	2.00	< 1.65	-[b]	< 3.77	1
*M*31	NOAA_12706, SPoCA_21742	2018 Apr. 19	10:45-11:48	26.1	-	–	–	–	1
*M*30	NOAA_12704, SPoCA_21724	2018 Apr. 19	09:40-10:43	18.1	49.75	< 1.77	-[b]	< 3.54	2
*M*31	NOAA_12704, SPoCA_21724	2018 Apr. 19	10:45-11:48	26.1	-	–	–	–	2
*M*32	NOAA_12706, SPoCA_21742	2018 Apr. 20	07:40-08:58	18.1	6.00	1.68 ± 0.10	0.65 ± 0.10	1.70 ± 0.10	1
*M*33	NOAA_12706, SPoCA_21742	2018 Apr. 20	09:25-10:39	26.1	-	–	–	–	1
*M*32	NOAA_12706, SPoCA_21742	2018 Apr. 20	07:40-08:58	18.1	6.00	1.75 ± 0.13	1.09 ± 0.13	1.60 ± 0.13	1
*M*34	NOAA_12706, SPoCA_21742	2018 Apr. 20	10:45-12:03	23.6	-	–	–	–	1
*M*33	NOAA_12706, SPoCA_21742	2018 Apr. 20	09:25-10:39	26.1	6.00	1.50 ± 0.36	-0.53 ± 0.35	1.98 ± 0.35	1
*M*34	NOAA_12706, SPoCA_21742	2018 Apr. 20	10:45-12:03	23.6	-	–	–	–	1
*M*32	NOAA_12704, SPoCA_21724	2018 Apr. 20	07:40-08:58	18.1	48.25	< 1.89	< 1.75	< 1.89	2
*M*33	NOAA_12704, SPoCA_21724	2018 Apr. 20	09:25-10:39	26.1	-	–	–	–	2
*M*32	NOAA_12704, SPoCA_21724	2018 Apr. 20	07:40-08:58	18.1	48.25	< 1.86	< 0.62	< 1.89	2
*M*34	NOAA_12704, SPoCA_21724	2018 Apr. 20	10:45-12:03	23.6	-	–	–	–	2
*M*39	SD-AR_M00011 (+219.3, +34.2)	2018 Jun. 10	10:15-11:30	18.1	31.00	1.93 ± 0.10	2.99 ± 0.10	2.00 ± 0.10	1
*M*40	SD-AR_M00011 (+219.3, +34.2)	2018 Jun. 10	11:32-12:47	26.1	-	–	–	–	1
*M*39	SD-AR_M00012 (-464.3, +348.9)	2018 Jun. 10	10:15-11:30	18.1	47.00	< 1.90	< 2.09	< 1.82	2
*M*40	SD-AR_M00012 (-464.3, +348.9)	2018 Jun. 10	11:32-12:47	26.1	-	–	–	–	2
*M*41	NOAA_12713, SPoCA_21840	2018 Jun. 17	08:56-10:10	18.3	37.00	< 1.82	< 1.53	< 3.71	1
*M*42	NOAA_12713, SPoCA_21840	2018 Jun. 17	10:12-11:27	26.1	-	–	–	–	1
*M*43	SPoCA_21867	2018 Jun. 23	09:00-10:15	18.3	9.50	1.91 ± 0.10	2.27 ± 0.10	1.78 ± 0.10	1
*M*44	SPoCA_21867	2018 Jun. 23	10:17-11:31	26.1	-	–	–	–	1
*M*43	NOAA_12713, SPoCA_21840	2018 Jun. 23	09:00-10:15	18.3	2.75	1.67 ± 0.10	0.52 ± 0.10	1.67 ± 0.10	2
*M*44	NOAA_12713, SPoCA_21840	2018 Jun. 23	10:17-11:31	26.1	-	–	–	–	2
*M*43	NOAA_12715, SPoCA_21859	2018 Jun. 23	09:00-10:15	18.3	13.00	1.92 ± 0.10	2.06 ± 0.10	2.00 ± 0.10	3
*M*44	NOAA_12715, SPoCA_21859	2018 Jun. 23	10:17-11:31	26.1	-	–	–	–	3
*M*44	HMI_SHARP_7276	2018 Jun. 23	10:17-11:31	26.1	49.00	> 1.97	> 3.70	> 1.99	4
*M*43	HMI_SHARP_7276	2018 Jun. 23	09:00-10:15	18.3	-	–	–	–	4
*M*45	NOAA_12717, SPoCA_21941	2018 Aug. 6	10:00-11:15	18.3	47.75	1.81 ± 0.10	0.67 ± 0.10	1.88 ± 0.10	1

[a] *This AR corresponds also to other 3 SPoCA targets: SPoCA_22276, SPoCA_22279, and SPoCA_22280.*
[b] *Unknown flux because the brightness temperature of the AR pixels is lower than the quiet-Sun.*
[c] *There are two very close ARs in this position. Our algorithm detected a unique AR.*
[d] *This AR corresponds also to other 3 SPoCA targets: SPoCA_24850, SPoCA_24851, and SPoCA_24853.*
[e] *The quality of the* 25.8 *GHz-solar map on December 7, 2020 is very low.*
[f] *Same region.*
[g] *There is a very close AR in this position (NOAA_12793/SPoCA_24935) that pollutes our measures.*
[h] *There is a very close AR in this position (NOAA_12792/SPoCA_24918) that pollutes our measures.*

Table 6.3: Continued.

ID	*ar_id*	Epoch	T (UT)	$\nu_{\rm obs}$ (GHz)	Size (arcmin^2)	α_{T_p}	$\alpha_{\rm T_{ex}}$	$\alpha_{\rm tot}$	n
*M*46	NOAA_12717, SPoCA_21941	2018 Aug. 6	11:18-12:32	26.1	-	–	–	–	1
*M*45	SD-AR_M00013 (-378.2, +38.4)	2018 Aug. 6	10:00-11:15	18.3	46.50	< 1.89	< 2.00	< 1.89	2
*M*46	SD-AR_M00013 (-378.2, +38.4)	2018 Aug. 6	11:18-12:32	26.1	-	–	–	–	2
*M*45	SPoCA_21947	2018 Aug. 6	10:00-11:15	18.3	12.25	1.76 ± 0.10	-0.06 ± 0.10	1.93 ± 0.10	3
*M*46	SPoCA_21947	2018 Aug. 6	11:18-12:32	26.1	-	–	–	–	3
*M*47	NOAA_12718, SPoCA_21976	2018 Aug. 20	09:50-11:05	18.3	35.00	< 1.90	< 2.21	< 1.88	1
*M*48	NOAA_12718, SPoCA_21976	2018 Aug. 20	11:08-12:22	26.1	-	–	–	–	1
*M*47	NOAA_12719, SPoCA_21981	2018 Aug. 20	09:50-11:05	18.3	18.00	1.82 ± 0.10	1.24 ± 0.10	1.78 ± 0.10	2
*M*48	NOAA_12719, SPoCA_21981	2018 Aug. 20	11:08-12:22	26.1	-	–	–	–	2
*M*47	SD-AR_M00014 (+332.1, +258.0)	2018 Aug. 20	09:50-11:05	18.3	50.75	< 1.91	< 2.29	< 1.94	3
*M*48	SD-AR_M00014 (+332.1, +258.0)	2018 Aug. 20	11:08-12:22	26.1	-	–	–	–	3
*M*49	SPoCA_22078	2018 Sep. 21	10:00-11:15	18.3	62.25	< 1.92	< 2.78	< 1.90	1
*M*50	SPoCA_22078	2018 Sep. 21	11:18-12:32	26.1	-	–	–	–	1
*M*51	SD-AR_M00015 (-506.8, -227.3)	2018 Sep. 27	10:20-11:35	18.3	48.00	< 1.87	< 0.96	< 1.84	1
*M*52	SD-AR_M00015 (-506.8, -227.3)	2018 Sep. 27	11:38-12:52	26.1	-	–	–	–	1
*M*51	SD-AR_M00016 (+587.0, +15.0)	2018 Sep. 27	10:20-11:35	18.3	28.25	< 1.87	< 1.15	< 1.98	2
*M*52	SD-AR_M00016 (+587.0, +15.0)	2018 Sep. 27	11:38-12:52	26.1	-	–	–	–	2
*M*53	SD-AR_M00017 (-208.5, +68.3)	2018 Oct. 3	09:30-10:45	18.3	45.25	1.91 ± 0.10	2.26 ± 0.10	2.02 ± 0.10	1
*M*54	SD-AR_M00017 (-208.5, +68.3)	2018 Oct. 3	10:48-12:02	26.1	-	–	–	–	1
*M*53	NOAA_12723, SPoCA_22102	2018 Oct. 3	09:30-10:45	18.3	12.75	1.85 ± 0.10	1.30 ± 0.10	1.86 ± 0.10	2
*M*54	NOAA_12723, SPoCA_22102	2018 Oct. 3	10:48-12:02	26.1	-	–	–	–	2
*M*57	SPoCA_22122	2018 Oct. 22	11:35-12:50	18.3	18.25	< 1.82	< -1.28	< 1.94	1
*M*58	SPoCA_22122	2018 Oct. 22	12:52-14:07	26.1	-	–	–	–	1
*M*57	SD-AR_M00018 (+526.1, +4.6)	2018 Oct. 22	11:35-12:50	18.3	50.50	< 1.85	< 0.57	< 1.85	2
*M*58	SD-AR_M00018 (+526.1, +4.6)	2018 Oct. 22	12:52-14:07	26.1	-	–	–	–	2
*M*61	SD-AR_M00019 (+397.4, +154.7)	2018 Oct. 31	11:02-12:16	26.1	48.25	1.92 ± 0.10	2.61 ± 0.10	1.87 ± 0.10	1
*M*60	SD-AR_M00019 (+397.4, +154.7)	2018 Oct. 31	09:45-10:59	18.3	-	–	–	–	1
*M*62	HMI_SHARP_7321	2018 Nov. 9	11:42-12:57	26.1	45.50	1.94 ± 0.10	3.33 ± 0.10	1.98 ± 0.10	1
*M*63	HMI_SHARP_7321	2018 Nov. 9	10:29-11:40	18.3	-	–	–	–	1
*M*64	NOAA_12726, SPoCA_22221	2018 Nov. 12	10:07-11:20	18.3	16.50	< 1.90	< 2.30	< 1.92	1
*M*65	NOAA_12726, SPoCA_22221	2018 Nov. 12	11:23-12:37	26.1	-	–	–	–	1
*M*64	SPoCA_22205	2018 Nov. 12	10:07-11:20	18.3	49.00	1.88 ± 0.10	1.64 ± 0.10	1.92 ± 0.10	2
*M*65	SPoCA_22205	2018 Nov. 12	11:23-12:37	26.1	-	–	–	–	2
*M*67	NOAA_12728, SPoCA_22251	2018 Nov. 26	11:23-12:37	26.1	44.50	1.87 ± 0.10	1.60 ± 0.10	1.62 ± 0.10	1
*M*66	NOAA_12728, SPoCA_22251	2018 Nov. 26	10:05-11:20	18.3	-	–	–	–	1
*M*68	SD-AR_M00020 (+474.3, +48.7)	2018 Nov. 29	10:05-11:20	18.3	49.00	< 1.87	< 1.21	< 1.92	1
*M*69	SD-AR_M00020 (+474.3, +48.7)	2018 Nov. 29	11:23-12:37	26.1	-	–	–	–	1
*M*70	NOAA_12729[a]	2018 Dec. 6	11:15-12:30	18.3	18.75	1.72 ± 0.10	0.26 ± 0.10	1.92 ± 0.10	1

[a] *This AR corresponds also to other 3 SPoCA targets: SPoCA_22276, SPoCA_22279, and SPoCA_22280.*
[b] *Unknown flux because the brightness temperature of the AR pixels is lower than the quiet-Sun.*
[c] *There are two very close ARs in this position. Our algorithm detected a unique AR.*
[d] *This AR corresponds also to other 3 SPoCA targets: SPoCA_24850, SPoCA_24851, and SPoCA_24853.*
[e] *The quality of the* 25.8 *GHz-solar map on December 7, 2020 is very low.*
[f] *Same region.*
[g] *There is a very close AR in this position (NOAA_12793/SPoCA_24935) that pollutes our measures.*
[h] *There is a very close AR in this position (NOAA_12792/SPoCA_24918) that pollutes our measures.*

Table 6.3: Continued.

ID	*ar_id*	Epoch	T (UT)	ν_{obs} (GHz)	Size (arcmin^2)	α_{T_p}	$\alpha_{T_{ex}}$	α_{tot}	n
*M*71	NOAA_12729[a]	2018 Dec. 6	12:33-13:47	26.1	-	–	–	–	1
*M*74	SPoCA_22823	2019 Jun. 12	08:30-09:45	18.3	45.25	< 1.88	< 1.54	< 2.92	1
*M*75	SPoCA_22823	2019 Jun. 12	09:47-11:02	25.8	-	–	–	–	1
*M*74	SD-AR_M00021 (+88.3, -12.1)	2019 Jun. 12	08:30-09:45	18.3	43.50	< 1.89	< 2.01	< 2.98	2
*M*75	SD-AR_M00021 (+88.3, -12.1)	2019 Jun. 12	09:47-11:02	25.8	-	–	–	–	2
*M*76	SD-AR_M00022 (-390.6, -32.1)	2019 Jun. 13	13:15-14:30	18.3	16.75	< 1.90	< 2.22	< 2.92	1
*M*77	SD-AR_M00022 (-390.6, -32.1)	2019 Jun. 13	14:33-15:47	25.8	-	–	–	–	1
*M*76	SD-AR_M00023 (-27.7, +85.1)	2019 Jun. 13	13:15-14:30	18.3	10.50	1.94 ± 0.10	3.34 ± 0.10	2.84 ± 0.10	2
*M*77	SD-AR_M00023 (-27.7, +85.1)	2019 Jun. 13	14:33-15:47	25.8	-	–	–	–	2
*M*78	SD-AR_M00024 (+587.5, -133.2)	2019 Jun. 20	08:45-10:00	18.3	21.25	< 1.84	< -3.06	< 1.85	1
*M*79	SD-AR_M00024 (+587.5, -133.2)	2019 Jun. 20	10:03-11:17	25.8	-	–	–	–	1
*M*80	SD-AR_M00025 (+504.9, +103.0)	2019 Jun. 26	08:30-09:45	18.3	12.00	< 1.90	< 2.51	< 1.79	1
*M*81	SD-AR_M00025 (+504.9, +103.0)	2019 Jun. 26	09:48-11:02	25.8	-	–	–	–	1
*M*82	SPoCA_22886	2019 Jul. 3	08:30-09:45	18.3	40.00	< 1.97	< 4.05	< 1.86	1
*M*83	SPoCA_22886	2019 Jul. 3	09:47-11:02	25.8	-	–	–	–	1
*M*82	HMI_SHARP_7374	2019 Jul. 3	08:30-09:45	18.3	31.25	1.94 ± 0.10	2.97 ± 0.10	1.96 ± 0.10	2
*M*83	HMI_SHARP_7374	2019 Jul. 3	09:47-11:02	25.8	-	–	–	–	2
*M*82	SD-AR_M00026 (-568.0, +200.0)	2019 Jul. 3	08:30-09:45	18.3	20.50	< 1.88	< 1.70	< 1.81	3
*M*83	SD-AR_M00026 (-568.0, +200.0)	2019 Jul. 3	09:47-11:02	25.8	-	–	–	–	3
*M*84	SD-AR_M00027 (-408.9, +202.9)	2019 Jul. 4	09:05-10:20	18.3	37.75	< 1.91	< 2.54	< 1.90	1
*M*85	SD-AR_M00027 (-408.9, +202.9)	2019 Jul. 4	10:22-11:37	25.8	-	–	–	–	1
*M*84	SD-AR_M00028 (+51.1, +80.3)	2019 Jul. 4	09:05-10:20	18.3	48.75	1.95 ± 0.10	3.15 ± 0.10	1.89 ± 0.10	2
*M*85	SD-AR_M00028 (+51.1, +80.3)	2019 Jul. 4	10:22-11:37	25.8	-	–	–	–	2
*M*84	HMI_SHARP_7374	2019 Jul. 4	09:05-10:20	18.3	48.75	1.91 ± 0.10	2.40 ± 0.10	1.90 ± 0.10	3
*M*85	HMI_SHARP_7374	2019 Jul. 4	10:22-11:37	25.8	-	–	–	–	3
*M*86	NOAA_12744, SPoCA_22925	2019 Jul. 12	09:15-10:30	18.3	12.75	< 1.86	< 0.93	< 1.86	1
*M*87	NOAA_12744, SPoCA_22925	2019 Jul. 12	10:32-11:47	25.8	-	–	–	–	1
*M*88	SPoCA_22983	2019 Jul. 19	08:00-09:15	18.3	48.75	< 1.90	< 2.24	< 1.91	1
*M*89	SPoCA_22983	2019 Jul. 19	09:17-10:32	25.8	-	–	–	–	1
*M*89	SD-AR_M00029 (+112.8, +70.0)	2019 Jul. 19	09:17-10:32	25.8	49.00	> 1.95	> 4.07	> 1.89	2
*M*88	SD-AR_M00029 (+112.8, +70.0)	2019 Jul. 19	08:00-09:15	18.3	-	–	–	–	2
*M*90	SD-AR_M00030 (-82.5, +293.6)	2019 Jul. 24	09:35-10:50	18.3	20.75	< 1.91	< 2.52	< 1.77	1
*M*91	SD-AR_M00030 (-82.5, +293.6)	2019 Jul. 24	10:52-12:07	25.8	-	–	–	–	1
*M*90	SPoCA_22998	2019 Jul. 24	09:35-10:50	18.3	9.50	< 1.86	< 0.92	< 2.06	2
*M*91	SPoCA_22998	2019 Jul. 24	10:52-12:07	25.8	-	–	–	–	2
*M*92	SD-AR_M00031 (+187.0, +45.2)	2019 Jul. 30	08:10-09:25	18.3	21.00	1.95 ± 0.10	3.35 ± 0.10	1.97 ± 0.10	1
*M*93	SD-AR_M00031 (+187.0, +45.2)	2019 Jul. 30	09:27-10:42	25.8	-	–	–	–	1
*M*94	NOAA_12747, SPoCA_23064	2019 Aug. 7	10:00-11:14	18.3	28.00	1.93 ± 0.10	2.59 ± 0.10	1.95 ± 0.10	1

[a] *This AR corresponds also to other 3 SPoCA targets: SPoCA_22276, SPoCA_22279, and SPoCA_22280.*
[b] *Unknown flux because the brightness temperature of the AR pixels is lower than the quiet-Sun.*
[c] *There are two very close ARs in this position. Our algorithm detected a unique AR.*
[d] *This AR corresponds also to other 3 SPoCA targets: SPoCA_24850, SPoCA_24851, and SPoCA_24853.*
[e] *The quality of the* 25.8 *GHz-solar map on December 7, 2020 is very low.*
[f] *Same region.*
[g] *There is a very close AR in this position (NOAA_12793/SPoCA_24935) that pollutes our measures.*
[h] *There is a very close AR in this position (NOAA_12792/SPoCA_24918) that pollutes our measures.*

Table 6.3: Continued.

ID	*ar_id*	Epoch	T (UT)	ν_{obs} (GHz)	Size (arcmin^2)	α_{T_p}	$\alpha_{T_{ex}}$	α_{tot}	n
*M*95	NOAA_12747, SPoCA_23064	2019 Aug. 7	11:17-12:31	25.8	-	–	–	–	1
*M*94	SD-AR_M00032 (-398.6, +333.1)	2019 Aug. 7	10:00-11:14	18.3	14.00	< 1.97	< 4.41	< 1.73	2
*M*95	SD-AR_M00032 (-398.6, +333.1)	2019 Aug. 7	11:17-12:31	25.8	-	–	–	–	2
*M*100	SD-AR_M00033 (+178.3, -69.6)	2019 Sep. 5	07:30-08:45	18.3	26.25	< 1.90	< 2.54	< 1.93	1
*M*101	SD-AR_M00033 (+178.3, -69.6)	2019 Sep. 5	08:48-10:02	25.8	-	–	–	–	1
*M*102	SD-AR_M00034 (+371.6, +383.7)	2019 Sep. 10	09:50-11:05	18.3	51.50	< 1.88	< 1.30	< 1.89	1
*M*103	SD-AR_M00034 (+371.6, +383.7)	2019 Sep. 10	11:08-12:22	25.8	-	–	–	–	1
*M*106	SD-AR_M00035 (+175.6, +88.3)	2019 Sep. 24	10:55-12:10	18.3	22.00	< 1.92	< 2.85	< 1.99	1
*M*107	SD-AR_M00035 (+175.6, +88.3)	2019 Sep. 24	12:13-13:27	25.8	-	–	–	–	1
*M*108	SD-AR_M00036 (-456.5, -204.0)	2019 Oct. 1	09:10-10:25	18.3	34.75	< 1.89	< 1.66	< 1.84	1
*M*109	SD-AR_M00036 (-456.5, -204.0)	2019 Oct. 1	10:28-11:42	25.8	-	–	–	–	1
*M*109	SD-AR_M00037 (+142.6, +86.9)	2019 Oct. 1	10:28-11:42	25.8	33.75	> 1.93	> 4.09	> 1.90	2
*M*108	SD-AR_M00037 (+142.6, +86.9)	2019 Oct. 1	09:10-10:25	18.3	-	–	–	–	2
*M*110	SD-AR_M00038 (-485.1, +63.1)	2019 Oct. 9	09:10-10:25	18.3	29.50	< 1.40	-[b]	< 1.36	1
*M*111	SD-AR_M00038 (-485.1, +63.1)	2019 Oct. 9	10:28-11:42	25.8	-	–	–	–	1
*M*110	SD-AR_M00039 (+245.3, -293.2)	2019 Oct. 9	09:10-10:25	18.3	50.50	< 1.33	-[b]	< 1.29	2
*M*111	SD-AR_M00039 (+245.3, -293.2)	2019 Oct. 9	10:28-11:42	25.8	-	–	–	–	2
*M*110	SPoCA_23273	2019 Oct. 9	09:10-10:25	18.3	26.75	< 1.36	-[b]	< 1.34	3
*M*111	SPoCA_23273	2019 Oct. 9	10:28-11:42	25.8	-	–	–	–	3
*S*112	SD-AR_S00001 (-381.2, -629.1)	2019 Oct. 9	11:46-13:30	18.8	13.68	< 1.91	< 2.48	< 0.80	1
*S*113	SD-AR_S00001 (-381.2, -629.1)	2019 Oct. 9	09:14-10:58	24.7	-	–	–	–	1
*S*112	SPoCA_23273	2019 Oct. 9	11:46-13:30	18.8	45.72	< 1.81	< 0.17	< 0.56	2
*S*113	SPoCA_23273	2019 Oct. 9	09:14-10:58	24.7	-	–	–	–	2
*S*112	SD-AR_S00002 (-59.9, +798.2)[f]	2019 Oct. 9	11:46-13:30	18.8	23.40	< 1.88	< 1.76	< 0.59	3
*S*113	SD-AR_S00002 (-59.9, +798.2)[f]	2019 Oct. 9	09:14-10:58	24.7	-	–	–	–	3
*S*113	SD-AR_S00002 (-165.9, +797.0)[f]	2019 Oct. 9	09:14-10:58	24.7	12.75	> 1.88	> 1.76	> 0.71	4
*S*112	SD-AR_S00002 (-165.9, +797.0)[f]	2019 Oct. 9	11:46-13:30	18.8	-	–	–	–	4
*M*114	SD-AR_M00040 (+195.9, -109.9)	2019 Oct. 14	12:40-13:55	18.3	48.75	< 1.92	< 3.06	< 1.91	2
*M*115	SD-AR_M00040 (+195.9, -109.9)	2019 Oct. 14	13:58-15:12	25.8	-	–	–	–	2
*M*116	SD-AR_M00041 (-599.7, -226.6)	2019 Oct. 23	11:50-13:05	18.3	29.75	< 1.83	< -2.81	< 1.78	1
*M*117	SD-AR_M00041 (-599.7, -226.6)	2019 Oct. 23	13:08-14:22	25.8	-	–	–	–	1
*M*118	SPoCA_23409	2019 Nov. 4	10:15-11:30	18.3	43.00	< 1.79	< -1.67	< 1.75	1
*M*119	SPoCA_23409	2019 Nov. 4	11:33-12:47	25.8	-	–	–	–	1
*M*120	SD-AR_M00042 (+298.5, +25.1)	2019 Nov. 14	10:25-11:40	18.3	36.00	1.93 ± 0.10	3.21 ± 0.10	1.94 ± 0.10	1
*M*121	SD-AR_M00042 (+298.5, +25.1)	2019 Nov. 14	11:42-12:57	25.8	-	–	–	–	1
*M*120	NOAA_12752, SPoCA_23461	2019 Nov. 14	10:25-11:40	18.3	10.00	< 1.75	< -3.37	< 1.96	2
*M*121	NOAA_12752, SPoCA_23461	2019 Nov. 14	11:42-12:57	25.8	-	–	–	–	2

[a] *This AR corresponds also to other 3 SPoCA targets: SPoCA_22276, SPoCA_22279, and SPoCA_22280.*
[b] *Unknown flux because the brightness temperature of the AR pixels is lower than the quiet-Sun.*
[c] *There are two very close ARs in this position. Our algorithm detected a unique AR.*
[d] *This AR corresponds also to other 3 SPoCA targets: SPoCA_24850, SPoCA_24851, and SPoCA_24853.*
[e] *The quality of the* 25.8 *GHz-solar map on December 7, 2020 is very low.*
[f] *Same region.*
[g] *There is a very close AR in this position (NOAA_12793/SPoCA_24935) that pollutes our measures.*
[h] *There is a very close AR in this position (NOAA_12792/SPoCA_24918) that pollutes our measures.*

Table 6.3: Continued.

ID	*ar_id*	Epoch	T (UT)	$\nu_{\rm obs}$ (GHz)	Size (arcmin^2)	α_{T_p}	$\alpha_{\rm T_{ex}}$	$\alpha_{\rm tot}$	n
*M*122	SPoCA_23479	2019 Nov. 21	10:10-11:25	18.3	31.25	< 1.87	< 0.76	< 1.90	1
*M*123	SPoCA_23479	2019 Nov. 21	11:27-12:42	25.8	-	–	–	–	1
*M*122	SD-AR_M00043 (+201.2, -376.0)	2019 Nov. 21	10:10-11:25	18.3	19.25	< 1.90	< 2.30	< 1.89	2
*M*123	SD-AR_M00043 (+201.2, -376.0)	2019 Nov. 21	11:27-12:42	25.8	-	–	–	–	2
*M*123	SD-AR_M00044 (+83.6, +73.3)	2019 Nov. 21	11:27-12:42	25.8	48.75	> 1.94	> 4.78	> 1.86	3
*M*122	SD-AR_M00044 (+83.6, +73.3)	2019 Nov. 21	10:10-11:25	18.3	-	–	–	–	3
*M*124	SD-AR_M00045 (-404.2, +203.9)	2019 Nov. 26	10:00-11:15	18.3	20.52	< 1.90	< 2.27	< 0.63	1
*M*125	SD-AR_M00045 (-404.2, +203.9)	2019 Nov. 26	11:17-12:32	25.8	-	–	–	–	1
*S*128	SPoCA_23783	2020 Jan. 28	13:40-15:24	24.7	13.00	1.66 ± 0.13	0.50 ± 0.13	-1.58 ± 0.13	1
*S*126	SPoCA_23783	2020 Jan. 28	09:41-11:25	18.8	-	–	–	–	1
*S*128	SPoCA_23783	2020 Jan. 28	13:40-15:24	24.7	13.00	1.71 ± 0.13	0.74 ± 0.13	1.77 ± 0.13	1
*S*127	SPoCA_23783	2020 Jan. 28	11:26-13:18	18.8	-	–	–	–	1
*S*128	NOAA_12757, SPoCA_23779	2020 Jan. 28	13:40-15:24	24.7	7.75	1.80 ± 0.13	1.38 ± 0.13	-1.86 ± 0.13	2
*S*126	NOAA_12757, SPoCA_23779	2020 Jan. 28	09:41-11:25	18.8	-	–	–	–	2
*S*128	NOAA_12757, SPoCA_23779	2020 Jan. 28	13:40-15:24	24.7	7.75	1.79 ± 0.13	1.33 ± 0.13	1.92 ± 0.13	2
*S*127	NOAA_12757, SPoCA_23779	2020 Jan. 28	11:26-13:18	18.8	-	–	–	–	2
*S*128	SPoCA_23787	2020 Jan. 28	13:40-15:24	24.7	4.00	> 1.84	> 0.90	> 2.14	3
*S*127	SPoCA_23787	2020 Jan. 28	11:26-13:18	18.8	-	–	–	–	3
*S*128	SPoCA_23787	2020 Jan. 28	13:40-15:24	24.7	4.00	> 1.95	> 3.84	> -1.72	3
*S*126	SPoCA_23787	2020 Jan. 28	09:41-11:25	18.8	-	–	–	–	3
*M*129	NOAA_12770, SPoCA_24500	2020 Aug. 10	09:10-10:24	18.3	25.20	1.81 ± 0.10	1.11 ± 0.10	2.04 ± 0.10	1
*M*130	NOAA_12770, SPoCA_24500	2020 Aug. 10	10:27-11:42	25.8	-	–	–	–	1
*M*129	NOAA_12769, SPoCA_24497	2020 Aug. 10	09:10-10:24	18.3	48.24	< 1.80	< 0.14	< 1.94	2
*M*130	NOAA_12769, SPoCA_24497	2020 Aug. 10	10:27-11:42	25.8	-	–	–	–	2
*M*129	SD-AR_M00046 (-594.6, -380.8)	2020 Aug. 10	09:10-10:24	18.3	20.52	< 1.87	< 1.17	< 1.92	3
*M*130	SD-AR_M00046 (-594.6, -380.8)	2020 Aug. 10	10:27-11:42	25.8	-	–	–	–	3
*M*132	SPoCA_24514	2020 Aug. 17	10:32-11:47	25.8	7.56	1.86 ± 0.10	1.23 ± 0.10	2.15 ± 0.10	1
*M*131	SPoCA_24514	2020 Aug. 17	09:15-10:29	18.3	-	–	–	–	1
*M*131	SPoCA_24533	2020 Aug. 17	09:15-10:29	18.3	52.20	< 1.87	< 1.29	< 1.91	2
*M*132	SPoCA_24533	2020 Aug. 17	10:32-11:47	25.8	-	–	–	–	2
*M*131	NOAA_12772, SPoCA_24530	2020 Aug. 17	09:15-10:29	18.3	27.36	1.89 ± 0.10	1.88 ± 0.10	1.94 ± 0.10	3
*M*132	NOAA_12772, SPoCA_24530	2020 Aug. 17	10:32-11:47	25.8	-	–	–	–	3
*M*133	SD-AR_M00047 (+89.5, -321.3)	2020 Aug. 26	09:10-10:24	18.3	27.00	< 1.92	< 3.10	< 1.91	1
*M*134	SD-AR_M00047 (+89.5, -321.3)	2020 Aug. 26	10:27-11:42	25.8	-	–	–	–	1
*M*135	HMI_SHARP_7443	2020 Sep. 2	09:15-10:29	18.3	27.72	< 1.90	< 2.05	< 1.98	1
*M*136	HMI_SHARP_7443	2020 Sep. 2	10:32-11:47	25.8	-	–	–	–	1
*M*137	SD-AR_M00048 (+248.3, -73.5)	2020 Sep. 6	08:00-09:14	18.3	16.92	< 1.90	< 2.47	< 2.08	1
*M*138	SD-AR_M00048 (+248.3, -73.5)	2020 Sep. 6	09:17-10:32	25.8	-	–	–	–	1

[a] *This AR corresponds also to other 3 SPoCA targets: SPoCA_22276, SPoCA_22279, and SPoCA_22280.*
[b] *Unknown flux because the brightness temperature of the AR pixels is lower than the quiet-Sun.*
[c] *There are two very close ARs in this position. Our algorithm detected a unique AR.*
[d] *This AR corresponds also to other 3 SPoCA targets: SPoCA_24850, SPoCA_24851, and SPoCA_24853.*
[e] *The quality of the* 25.8 *GHz-solar map on December 7, 2020 is very low.*
[f] *Same region.*
[g] *There is a very close AR in this position (NOAA_12793/SPoCA_24935) that pollutes our measures.*
[h] *There is a very close AR in this position (NOAA_12792/SPoCA_24918) that pollutes our measures.*

Table 6.3: Continued.

ID	*ar_id*	Epoch	T (UT)	ν_{obs} (GHz)	Size (arcmin^2)	α_{T_p}	$\alpha_{T_{ex}}$	α_{tot}	n
*M*137	SD-AR_M00049 (-464.4, +391.4)	2020 Sep. 6	08:00-09:14	18.3	24.12	< 1.90	< 2.14	< 1.90	2
*M*138	SD-AR_M00049 (-464.4, +391.4)	2020 Sep. 6	09:17-10:32	25.8	-	–	–	–	2
*M*137	SPoCA_24604	2020 Sep. 6	08:00-09:14	18.3	23.04	< 1.89	< 1.90	< 1.94	3
*M*138	SPoCA_24604	2020 Sep. 6	09:17-10:32	25.8	-	–	–	–	3
*M*139	SD-AR_M00050 (-472.0, -411.1)	2020 Sep. 14	10:10-11:24	18.3	7.92	< 1.80	-[b]	< 2.17	1
*M*140	SD-AR_M00050 (-472.0, -411.1)	2020 Sep. 14	11:27-12:42	25.8	-	–	–	–	1
*M*139	SPoCA_24651	2020 Sep. 14	10:10-11:24	18.3	16.20	< 1.83	< -1.33	< 1.90	2
*M*140	SPoCA_24651	2020 Sep. 14	11:27-12:42	25.8	-	–	–	–	2
*S*141	SD-AR_S00003 (-109.6, -862.2)	2020 Sep. 17	09:18-11:02	18.8	11.88	< 1.83	< 0.21	< 1.99	1
*S*142	SD-AR_S00003 (-109.6, -862.2)	2020 Sep. 17	11:18-13:02	24.7	-	–	–	–	1
*S*142	SD-AR_S00004 (-195.9, -503.2)	2020 Sep. 17	11:18-13:02	24.7	10.08	1.85 ± 0.13	0.91 ± 0.13	1.62 ± 0.13	2
*S*141	SD-AR_S00004 (-195.9, -503.2)	2020 Sep. 17	09:18-11:02	18.8	-	–	–	–	2
*S*141	SD-AR_S00005 (-8.7, +828.8)	2020 Sep. 17	09:18-11:02	18.8	19.44	1.86 ± 0.13	1.33 ± 0.13	1.89 ± 0.13	3
*S*142	SD-AR_S00005 (-8.7, +828.8)	2020 Sep. 17	11:18-13:02	24.7	-	–	–	–	3
*S*142	SD-AR_S00006 (-546.4, -503.5)	2020 Sep. 17	11:18-13:02	24.7	15.84	> 1.92	> 2.75	> 1.89	4
*S*141	SD-AR_S00006 (-546.4, -503.5)	2020 Sep. 17	09:18-11:02	18.8	-	–	–	–	4
*S*142	SD-AR_S00007 (-193.6, -342.2)	2020 Sep. 17	11:18-13:02	24.7	10.80	> 1.92	> 3.03	> 1.78	5
*S*141	SD-AR_S00007 (-193.6, -342.2)	2020 Sep. 17	09:18-11:02	18.8	-	–	–	–	5
*S*142	SD-AR_S00008 (-712.7, +358.8)	2020 Sep. 17	11:18-13:02	24.7	10.08	> 1.92	> 2.95	> 1.65	6
*S*141	SD-AR_S00008 (-712.7, +358.8)	2020 Sep. 17	09:18-11:02	18.8	-	–	–	–	6
*M*143	SPoCA_24702	2020 Sep. 29	09:00-10:14	18.3	57.96	1.90 ± 0.10	2.11 ± 0.10	1.89 ± 0.10	1
*M*144	SPoCA_24702	2020 Sep. 29	10:17-11:32	25.8	-	–	–	–	1
*M*143	NOAA_12773, SPoCA_24694	2020 Sep. 29	09:00-10:14	18.3	54.00	1.75 ± 0.10	0.64 ± 0.10	1.88 ± 0.10	2
*M*144	NOAA_12773, SPoCA_24694	2020 Sep. 29	10:17-11:32	25.8	-	–	–	–	2
*M*147	NOAA_12776, SPoCA_24743	2020 Oct. 19	08:00-09:14	18.3	25.20	1.73 ± 0.10	0.26 ± 0.10	1.79 ± 0.10	1
*M*148	NOAA_12776, SPoCA_24743	2020 Oct. 19	09:17-10:32	25.8	-	–	–	–	1
*M*148	SD-AR_M00051 (+106.5, +10.3)	2020 Oct. 19	09:17-10:32	25.8	71.28	> 1.95	> 4.33	> 1.96	2
*M*147	SD-AR_M00051 (+106.5, +10.3)	2020 Oct. 19	08:00-09:14	18.3	-	–	–	–	2
*S*150	SPoCA_24770, SPoCA_24772[c]	2020 Oct. 29	10:17-12:01	18.8	34.79	1.19 ± 0.13	0.01 ± 0.13	1.51 ± 0.13	1
*S*149	SPoCA_24770, SPoCA_24772[c]	2020 Oct. 29	08:32-10:05	24.7	-	–	–	–	1
*S*149	SPoCA_24760	2020 Oct. 29	08:32-10:05	24.7	6.37	1.84 ± 0.13	1.46 ± 0.13	1.81 ± 0.13	2
*S*150	SPoCA_24760	2020 Oct. 29	10:17-12:01	18.8	-	–	–	–	2
*M*152	NOAA_12778, SPoCA_24770	2020 Oct. 30	09:32-10:47	25.8	13.68	1.45 ± 0.10	-0.88 ± 0.10	1.85 ± 0.10	1
*M*151	NOAA_12778, SPoCA_24770	2020 Oct. 30	08:15-09:29	18.3	-	–	–	–	1
*M*151	SD-AR_M00052 (-21.8, +487.4)	2020 Oct. 30	08:15-09:29	18.3	32.04	1.90 ± 0.10	2.44 ± 0.10	1.80 ± 0.10	2
*M*152	SD-AR_M00052 (-21.8, +487.4)	2020 Oct. 30	09:32-10:47	25.8	-	–	–	–	2
*M*152	SD-AR_M00053 (-87.9, -192.3)	2020 Oct. 30	09:32-10:47	25.8	52.92	> 1.93	> 4.08	> 1.93	3
*M*151	SD-AR_M00053 (-87.9, -192.3)	2020 Oct. 30	08:15-09:29	18.3	-	–	–	–	3

[a] *This AR corresponds also to other 3 SPoCA targets: SPoCA_22276, SPoCA_22279, and SPoCA_22280.*
[b] *Unknown flux because the brightness temperature of the AR pixels is lower than the quiet-Sun.*
[c] *There are two very close ARs in this position. Our algorithm detected a unique AR.*
[d] *This AR corresponds also to other 3 SPoCA targets: SPoCA_24850, SPoCA_24851, and SPoCA_24853.*
[e] *The quality of the* 25.8 *GHz-solar map on December 7, 2020 is very low.*
[f] *Same region.*
[g] *There is a very close AR in this position (NOAA_12793/SPoCA_24935) that pollutes our measures.*
[h] *There is a very close AR in this position (NOAA_12792/SPoCA_24918) that pollutes our measures.*

Table 6.3: Continued.

ID	*ar_id*	Epoch	T (UT)	ν_{obs} (GHz)	Size (arcmin^2)	α_{T_p}	$\alpha_{T_{ex}}$	α_{tot}	n
*M*153	NOAA_12781, SPoCA_24790	2020 Nov. 6	09:52-11:07	25.8	21.96	1.11 ± 0.10	-0.12 ± 0.10	1.37 ± 0.10	1
*M*154	NOAA_12781, SPoCA_24790	2020 Nov. 6	08:35-09:49	18.3	-	–	–	–	1
*M*153	NOAA_12780, SPoCA_24778	2020 Nov. 6	09:52-11:07	25.8	69.48	> 1.83	> 1.00	> 1.90	2
*M*154	NOAA_12780, SPoCA_24778	2020 Nov. 6	08:35-09:49	18.3	-	–	–	–	2
*M*153	SPoCA_24797	2020 Nov. 6	09:52-11:07	25.8	29.52	> 1.85	> 1.02	> 1.82	3
*M*154	SPoCA_24797	2020 Nov. 6	08:35-09:49	18.3	-	–	–	–	3
*M*157	NOAA_12781, SPoCA_24790	2020 Nov. 11	11:17-12:32	25.8	32.04	1.54 ± 0.10	0.13 ± 0.10	1.86 ± 0.10	1
*M*156	NOAA_12781, SPoCA_24790	2020 Nov. 11	10:00-11:14	18.3	-	–	–	–	1
*M*156	NOAA_12782, SPoCA_24807	2020 Nov. 11	10:00-11:14	18.3	4.68	< 1.66	-[b]	< 1.47	2
*M*157	NOAA_12782, SPoCA_24807	2020 Nov. 11	11:17-12:32	25.8	-	–	–	–	2
*M*156	SD-AR_M00054 (+24.6, -404.7)	2020 Nov. 11	10:00-11:14	18.3	28.44	< 1.88	< 1.27	< 1.90	3
*M*157	SD-AR_M00054 (+24.6, -404.7)	2020 Nov. 11	11:17-12:32	25.8	-	–	–	–	3
*M*156	NOAA_12780, SPoCA_24778	2020 Nov. 11	10:00-11:14	18.3	10.44	< 1.80	< -1.29	< 2.02	4
*M*157	NOAA_12780, SPoCA_24778	2020 Nov. 11	11:17-12:32	25.8	-	–	–	–	4
*M*158	NOAA_12783, SPoCA_24812	2020 Nov. 23	09:15-10:29	18.3	31.68	1.54 ± 0.10	-0.73 ± 0.10	1.91 ± 0.10	1
*M*159	NOAA_12783, SPoCA_24812	2020 Nov. 23	12:22-13:37	25.8	-	–	–	–	1
*M*158	NOAA_12784, SPoCA_24823	2020 Nov. 23	09:15-10:29	18.3	41.04	1.76 ± 0.10	-0.27 ± 0.10	1.87 ± 0.10	2
*M*159	NOAA_12784, SPoCA_24823	2020 Nov. 23	12:22-13:37	25.8	-	–	–	–	2
*M*158	SPoCA_24821	2020 Nov. 23	09:15-10:29	18.3	52.20	< 1.60	< -0.44	< 1.93	3
*M*159	SPoCA_24821	2020 Nov. 23	12:22-13:37	25.8	-	–	–	–	3
*M*158	NOAA_12786, SPoCA_24827	2020 Nov. 23	09:15-10:29	18.3	8.28	< 1.14	-[b]	< 0.57	4
*M*159	NOAA_12786, SPoCA_24827	2020 Nov. 23	12:22-13:37	25.8	-	–	–	–	4
*M*160	SPoCA_24827, SPoCA_24840[c]	2020 Nov. 28	10:35-11:49	18.3	63.36	1.37 ± 0.10	-0.16 ± 0.10	1.68 ± 0.10	1
*M*161	SPoCA_24827, SPoCA_24840[c]	2020 Nov. 28	11:52-13:04	25.8	-	–	–	–	1
*M*160	NOAA_12783, SPoCA_24812	2020 Nov. 28	10:35-11:49	18.3	5.76	< 1.71	< -3.24	< 1.37	2
*M*161	NOAA_12783, SPoCA_24812	2020 Nov. 28	11:52-13:04	25.8	-	–	–	–	2
*M*163	NOAA_12789, SPoCA_24834	2020 Nov. 30	10:42-11:57	25.8	22.32	1.68 ± 0.10	-0.44 ± 0.10	1.89 ± 0.10	1
*M*162	NOAA_12789, SPoCA_24834	2020 Nov. 30	09:25-10:39	18.3	-	–	–	–	1
*M*163	SPoCA_24827[d]	2020 Nov. 30	10:42-11:57	25.8	67.68	1.53 ± 0.10	-0.07 ± 0.10	1.69 ± 0.10	2
*M*162	SPoCA_24827[d]	2020 Nov. 30	09:25-10:39	18.3	-	–	–	–	2
*M*163	NOAA_12787, SPoCA_24849	2020 Nov. 30	10:42-11:57	25.8	13.68	1.86 ± 0.10	1.10 ± 0.10	1.88 ± 0.10	3
*M*162	NOAA_12787, SPoCA_24849	2020 Nov. 30	09:25-10:39	18.3	-	–	–	–	3
*M*164	NOAA_12790, SPoCA_24848[e]	2020 Dec. 7	09:15-13:29	18.3	65.16	< 1.83	< 1.37	< 1.88	1
*M*165	NOAA_12790, SPoCA_24848[e]	2020 Dec. 7	10:32-11:47	25.8	-	–	–	–	1
*M*164	NOAA_12791, SPoCA_24870[e]	2020 Dec. 7	09:15-13:29	18.3	41.76	< 1.46	< -2.49	< 1.56	2
*M*165	NOAA_12791, SPoCA_24870[e]	2020 Dec. 7	10:32-11:47	25.8	-	–	–	–	2
*M*166	NOAA_12792, SPoCA_24918	2020 Dec. 13	09:15-13:29	18.3	10.08	< 1.64	-[b]	< 1.64	1

[a] *This AR corresponds also to other 3 SPoCA targets: SPoCA_22276, SPoCA_22279, and SPoCA_22280.*
[b] *Unknown flux because the brightness temperature of the AR pixels is lower than the quiet-Sun.*
[c] *There are two very close ARs in this position. Our algorithm detected a unique AR.*
[d] *This AR corresponds also to other 3 SPoCA targets: SPoCA_24850, SPoCA_24851, and SPoCA_24853.*
[e] *The quality of the* 25.8 *GHz-solar map on December 7, 2020 is very low.*
[f] *Same region.*
[g] *There is a very close AR in this position (NOAA_12793/SPoCA_24935) that pollutes our measures.*
[h] *There is a very close AR in this position (NOAA_12792/SPoCA_24918) that pollutes our measures.*

Table 6.3: Continued.

ID	*ar_id*	Epoch	T (UT)	$\nu_{\rm obs}$ (GHz)	Size (arcmin^2)	α_{T_p}	$\alpha_{\rm T_{ex}}$	$\alpha_{\rm tot}$	n
*M*167	NOAA_12792, SPoCA_24918	2020 Dec. 13	10:32-11:47	25.8	-	–	–	–	1
*M*166	SPoCA_24905	2020 Dec. 13	09:15-13:29	18.3	21.24	< 1.86	< 0.70	< 1.82	2
*M*167	SPoCA_24905	2020 Dec. 13	10:32-11:47	25.8	-	–	–	–	2
*M*166	SD-AR_M00055 (+183.2, -545.2)	2020 Dec. 13	09:15-13:29	18.3	31.68	< 1.86	< 0.16	< 1.83	3
*M*167	SD-AR_M00055 (+183.2, -545.2)	2020 Dec. 13	10:32-11:47	25.8	-	–	–	–	3
*M*167	NOAA_12791, SPoCA_24917	2020 Dec. 13	10:32-11:47	25.8	6.12	1.87 ± 0.10	1.14 ± 0.10	1.71 ± 0.10	4
*M*166	NOAA_12791, SPoCA_24917	2020 Dec. 13	09:15-13:29	18.3	-	–	–	–	4
*M*169	NOAA_12792, SPoCA_24918[g]	2020 Dec. 21	11:02-12:17	25.8	24.12	1.74 ± 0.10	-0.001 ± 0.10	1.86 ± 0.10	1
*M*168	NOAA_12792, SPoCA_24918[g]	2020 Dec. 21	09:45-10:59	18.3	-	–	–	–	1
*M*168	NOAA_12793, SPoCA_24935[h]	2020 Dec. 21	09:45-10:59	18.3	70.92	1.74 ± 0.10	-0.001 ± 0.10	1.90 ± 0.10	2
*M*169	NOAA_12793, SPoCA_24935[h]	2020 Dec. 21	11:02-12:17	25.8	-	–	–	–	2
*M*168	NOAA_12794, SPoCA_24943	2020 Dec. 21	09:45-10:59	18.3	9.72	< 1.87	< 1.13	< 1.79	3
*M*169	NOAA_12794, SPoCA_24943	2020 Dec. 21	11:02-12:17	25.8	-	–	–	–	3
*M*168	SPoCA_24945	2020 Dec. 21	09:45-10:59	18.3	64.08	< 1.88	< 1.55	< 1.89	4
*M*169	SPoCA_24945	2020 Dec. 21	11:02-12:17	25.8	-	–	–	–	4

[a] *This AR corresponds also to other 3 SPoCA targets: SPoCA_22276, SPoCA_22279, and SPoCA_22280.*
[b] *Unknown flux because the brightness temperature of the AR pixels is lower than the quiet-Sun.*
[c] *There are two very close ARs in this position. Our algorithm detected a unique AR.*
[d] *This AR corresponds also to other 3 SPoCA targets: SPoCA_24850, SPoCA_24851, and SPoCA_24853.*
[e] *The quality of the* 25.8 *GHz-solar map on December 7, 2020 is very low.*
[f] *Same region.*
[g] *There is a very close AR in this position (NOAA_12793/SPoCA_24935) that pollutes our measures.*
[h] *There is a very close AR in this position (NOAA_12792/SPoCA_24918) that pollutes our measures.*

Contents of Figures

Contents of Tables

Bibliography

S. F. Abbate, J. W. Armstrong, S. W. Asmar, E. Barbinis, B. Bertotti, D. U. Fleischman, M. S. Gatti, G. L. Goltz, R. G. Herrera, L. Iess, K. J. Lee, T. L. Ray, M. Tinto, P. Tortora, and H. D. Wahlquist. The Cassini gravitational wave experiment. In M. Cruise and P. Saulson, editors, Gravitational-Wave Detection, volume 4856 of Society of Photo-Optical Instrumentation Engineers (SPIE) Conference Series, pages 90–97, Mar. 2003. doi: 10.1117/12.458566.

V. E. Abramov-maximov, V. I. Efremov, L. D. Parfinenko, A. A. Solov'ev, and K. Shibasaki. Long-Term Oscillations of Sunspots from Simultaneous Observations with the Nobeyama Radioheliograph and Solar Dynamics Observatory. *Pub.* Astron. Soc. Japan, 65:S12, Dec. 2013. doi: 10.1093/pasj/65.sp1.S12.

S. B. Akhmedov, G. B. Gelfreikh, V. M. Bogod, and A. N. Korzhavin. The Measurement of Magnetic Fields in the Solar Atmosphere above Sunspots Using Gyro-Resonance Emission. *Solar* Phys., 79(1):41–58, July 1982. doi: 10.1007/BF00146972.

C. E. Alissandrakis. Structure of the solar atmosphere: a radio perspective. Frontiers in Astronomy and Space Sciences, 7:74, Oct. 2020. doi: 10.3389/fspas.2020.574460.

C. E. Alissandrakis, G. B. Gel'Frejkh, V. N. Borovik, A. N. Korzhavin, V. M. Bogod, A. Nindos, and M. R. Kundu. Spectral observations of active region sources with RATAN-600 and WSRT. *Astron.* Astrophys., 270(1-2):509–515, Mar. 1993.

J. W. Armstrong. Low-frequency gravitational wave searches using spacecraft doppler tracking. Living Reviews in Relativity, 9, 01 2006. doi: 10.12942/lrr-2006-1.

J. W. Armstrong, R. Woo, and F. B. Estabrook. Interplanetary phase scintillation and the search for very low frequency gravitational radiation. *Astrophys.* J., 230:570–574, June 1979. doi: 10.1086/157114.

S. Asmar, J. Armstrong, L. Iess, and P. Tortora. Spacecraft doppler tracking: Noise budget and accuracy achievable in precision radio science observations. RADIO SCIENCE, 40, 04 2005a. doi: 10.1029/2004RS003101.

S. Asmar, J. Armstrong, L. Iess, and P. Tortora. Spacecraft doppler tracking: Noise budget and accuracy achievable in precision radio science observations. RADIO SCIENCE, 40, 04 2005b. doi: 10.1029/2004RS003101.

S. Asmar, R. A. Preston, P. Vergados, D. H. Atkinson, T. Andert, H. Ando, C. O. Ao, J. W. Armstrong, N. Ashby, J.-P. Barriot, P. M. Beauchamp, D. J. Bell, P. L. Bender, M. D. Benedetto, B. G. Bills, M. K. Bird, T. M. Bocanegra-Bahamon, G. K. Botteon, S. Bruinsma, D. R. Buccino, K. L. Cahoy, P. Cappuccio, R. K. Choudhary, V. Dehant, C. Dumoulin, D. Durante, C. D. Edwards, H. M. Elliott, T. A. Ely, A. I. Ermakov, F. Ferri, F. M. Flasar, R. G. French, A. Genova, S. J. Goossens, B. Häusler, R. Helled, D. P. Hinson, M. D. Hofstadter, L. Iess, T. Imamura, A. P. Jongeling, Ö. Karatekin, Y. Kaspi, M. M. Kobayashi, A. Komjathy, A. S. Konopliv,

E. R. Kursinski, T. J. W. Lazio, S. L. Maistre, F. G. Lemoine, R. J. Lillis, I. R. Linscott, A. J. Mannucci, E. A. Marouf, J.-C. Marty, S. E. Matousek, K. Matsumoto, E. M. Mazarico, V. Notaro, M. Parisi, R. S. Park, M. Pätzold, G. G. Peytaví, M. P. Pugh, N. O. Rennó, P. Rosenblatt, D. Serra, R. A. Simpson, D. E. Smith, P. G. Steffes, B. D. Tapley, S. Tellmann, P. Tortora, S. G. Turyshev, T. V. Hoolst, A. K. Verma, M. M. Watkins, W. Williamson, M. A. Wieczorek, P. Withers, M. Yseboodt, N. Yu, M. Zannoni, and M. T. Zuber. Solar System Interiors, Atmospheres, and Surfaces Investigations via Radio Links: Goals for the Next Decade. Bulletin of the AAS, 53(4), mar 18 2021. https://baas.aas.org/pub/2021n4i109.

E. H. Avrett and R. Loeser. Models of the Solar Chromosphere and Transition Region from SUMER and HRTS Observations: Formation of the Extreme-Ultraviolet Spectrum of Hydrogen, Carbon, and Oxygen. *ApJS*, 175(1):229–276, Mar. 2008. doi: 10.1086/523671.

V. Barra, V. Delouille, J. F. Hochedez, and P. Chainais. Segmentation of EIT Images Using Fuzzy Clustering: a Preliminary Study. In D. Danesy, S. Poedts, A. de Groof, and J. Andries, editors, The Dynamic Sun: Challenges for Theory and Observations, volume 11 of ESA Special Publication, page 77.1, Dec. 2005.

B. Bertotti, G. Comoretto, and L. Iess. Doppler tracking of spacecraft with multi-frequency links. Astronomy and Astrophysics, 269:608–616, 02 1993.

B. Bertotti, L. Iess, and P. Tortora. A test of general relativity using radio links with the Cassini spacecraft. *Nature*, 425(6956):374–376, Sept. 2003. doi: 10.1038/nature01997.

P. Besso, M. Bozzi, M. Formaggi, and L. Perregrini. Pointing enhancement techniques for deep-space antennas. International Journal of Microwave and Wireless Technologies, 2(2): 211218, 2010. doi: 10.1017/S1759078710000139.

V. M. Bogod, A. G. Stupishin, and L. V. Yasnov. On Magnetic Fields of Active Regions at Coronal Heights. *Solar* Phys., 276(1-2):61–73, Feb. 2012. doi: 10.1007/s11207-011-9850-2.

P. Bolli, A. Orlati, L. Stringhetti, A. Orfei, S. Righini, R. Ambrosini, M. Bartolini, C. Bortolotti, F. Buffa, M. Buttu, A. Cattani, N. D'Amico, G. Deiana, A. Fara, F. Fiocchi, F. Gaudiomonte, A. Maccaferri, S. Mariotti, P. Marongiu, A. Melis, C. Migoni, M. Morsiani, M. Nanni, F. Nasyr, A. Pellizzoni, T. Pisanu, M. Poloni, S. Poppi, I. Porceddu, I. Prandoni, J. Roda, M. Roma, A. Scalambra, G. Serra, A. Trois, G. Valente, G. P. Vargiu, and G. Zacchiroli. Sardinia radio telescope: General description, technical commissioning and first light. Journal of Astronomical Instrumentation, 04(03n04):1550008, 2015. doi: 10.1142/S2251171715500087. URL https://doi.org/10.1142/S2251171715500087.

P. Bolli, M. T. Beltran Sorolla, M. Burgay, P. Marongiu, T. Pisanu, C. Contavalle, A. Orfei, C. Stanghellini, G. Zacchiroli, and A. Zanichelli. Receivers for Radio Astronomy: current status and future developments at the Italian Radio Telescopes. Technical report, OA@INAF, 2017. URL http://pulsar.oa-cagliari.inaf.it/~pulsar/RX2017/review.html.

V. N. Borovik, M. S. Kurbanov, and V. V. Makarov. Distribution of Radio Brightness of the Quiet Sun in the 2-CENTIMETER to 32-CENTIMETER Range. *Soviet* Astron., 36:656, Dec. 1992.

V. N. Borovik, I. Y. Grigor'eva, and A. N. Korzhavin. Local maximum in the microwave spectrum of solar active regions as a factor in predicting powerful flares. volume 52, pages 1032–1043, Dec. 2012. doi: 10.1134/S001679321208004X.

L. Bradley, B. Sipőcz, T. Robitaille, E. Tollerud, Z. Vinícius, C. Deil, K. Barbary, H. M. Günther, M. Cara, I. Busko, S. Conseil, M. Droettboom, A. Bostroem, E. M. Bray, L. A. Bratholm, T. Wilson, M. Craig, G. Barentsen, S. Pascual, A. Donath, J. Greco, G. Perren, P. L. Lim, and W. Kerzendorf. astropy/photutils: v0.6, Jan. 2019. URL https://doi.org/10.5281/zenodo.2533376.

D. R. Buccino, D. S. Kahan, M. Parisi, M. Paik, E. Barbinis, O. Yang, R. S. Park, A. Tanner, S. Bryant, and A. Jongeling. Performance of Earth Troposphere Calibration Measurements With the Advanced Water Vapor Radiometer for the Juno Gravity Science Investigation. Radio Science, 56(12):e07387, Dec. 2021. doi: 10.1029/2021RS007387.

F. Buffa, G. Serra, P. Bolli, A. Fara, G. Deiana, F. Nasir, C. Castiglia, and A. Delitala. K-band system temperature forecast for the sardinia radio telescope. 04 2016. doi: 10.13140/RG.2.1.3306.5361.

E. P. Carley, C. Baldovin, P. Benthem, M. M. Bisi, R. A. Fallows, P. T. Gallagher, M. Olberg, H. Rothkaehl, R. Vermeulen, N. Vilmer, and D. Barnes. Radio observatories and instrumentation used in space weather science and operations. Journal of Space Weather and Space Climate, 10:7, Jan. 2020. doi: 10.1051/swsc/2020007.

J. P. Castelli and J. Clemens. Radio spectrum of ail active solar region determined from the 20 July 1963 eclipse. *Astron.* J., 71:652, Sept. 1966. doi: 10.1086/109976.

J. Cheng, Y. Yan, D. Zhao, and L. Xu. Scale sequentially CLEAN for Mingantu Spectral Radioheliograph. Solar-Terrestrial Physics, 5(2):50–57, June 2019. doi: 10.12737/stp-52201908.

J. J. Condon and S. M. Ransom. Essential Radio Astronomy. 2016.

G. dall'Oglio and P. de Bernardis. The OASI project: far infrared astronomy from Antarctica. *Mem.* Soc. Astron. Italiana, 58(2-3):371–375, Jan. 1987.

J. De Vicente, M. Lanucara, M. Mercolino, J. Villalvilla, and P. Cappuccio. The implementation of radio science capability in the esa deep space network of antennae. In 8th ESA International Workshop on Tracking, Telemtry and Command System for Space Applications, 2019.

V. Delouille, B. Mampaey, C. Verbeeck, and R. de Visscher. The SPOCA-suite: a software for extraction and tracking of Active Regions and Coronal Holes on EUV images. arXiv e-prints, art. arXiv:1208.1483, Aug. 2012.

A. Di Ruscio, P. Cappuccio, V. Notaro, and M. Di Benedetto. Improvements in bepicolombo and juice radio science experiments with a multi-station tracking configuration for the reduction of doppler noise. 10 2019.

G. A. Dulk. Solar radio emissions. pages 429–436, Wien, 2001. Verlag der sterreichischen Akademie der Wissenschaften. ISBN 978-3-7001-3048-2.

V. A. Efanov, A. G. Kislyakov, and I. G. Moiseev. Slowly Varying Component Spectrum of the Solar Radio Emission at Millimetre Wavelengths. *Solar* Phys., 24(1):142–153, May 1972. doi: 10.1007/BF00231092.

E. Egron, A. Pellizzoni, M. N. Iacolina, S. Loru, M. Marongiu, S. Righini, M. Cardillo, A. Giuliani, S. Mulas, G. Murtas, D. Simeone, R. Concu, A. Melis, A. Trois, M. Pilia, A. Navarrini, V. Vacca, R. Ricci, G. Serra, M. Bachetti, M. Buttu, D. Perrodin, F. Buffa, G. L. Deiana,

F. Gaudiomonte, A. Fara, A. Ladu, F. Loi, P. Marongiu, C. Migoni, T. Pisanu, S. Poppi, A. Saba, E. Urru, G. Valente, and G. P. Vargiu. Imaging of SNR IC443 and W44 with the Sardinia Radio Telescope at 1.5 and 7 GHz. *Mon.* Not. Roy. Astron. Soc., 470(2):1329–1341, Sept. 2017. doi: 10.1093/mnras/stx1240.

E. Egron, V. Vacca, and G. Carboni. Srt performance measurements (2018-2021). Technical Report 178, OA Cagliari, 2022. URL http://hdl.handle.net/20.500.12386/32536.

L. I. Fedoseev and V. I. Chernyshev. The millimeter spectrum of the quiet sun. Astronomy Reports, 42(1):105–109, Jan. 1998.

E. Flamini, L. Garramone, M. N. Iacolina, G. Parca, E. Russo, G. Valente, and S. Viviano. Deep space communication services provided by Sardinia Deep Space Antenna - SDSA: program status and capabilities - International Astronautical Conference - Adelaide (Australia) - IAC-17,B2,8-GTS.3,4,x41239. Sept. 2017. URL https://iafastro.directory/iac/paper/id/41239/abstract-pdf/IAC-17,B2,8-GTS.3,4,x41239.brief.pdf?2017-03-23.12:59:22.

D. E. Gary, T. S. Bastian, B. Chen, G. D. Fleishman, and L. Glesener. Radio Observations of Solar Flares. In E. Murphy, editor, Science with a Next Generation Very Large Array, volume 517 of Astronomical Society of the Pacific Conference Series, page 99, Dec. 2018.

A. Giannini, S. Moscato, M. Pasian, L. Perregrini, M. Bozzi, and P. Besso. Beam squint compensation technique for the sardinia radio telescope. In 2012 42nd European Microwave Conference, pages 683–686, 2012. doi: 10.23919/EuMC.2012.6459145.

C. G. Giménez de Castro, A. L. G. Pereira, J. F. Valle Silva, C. L. Selhorst, C. H. Mandrini, G. D. Cristiani, J.-P. Raulin, and A. Valio. The Submillimeter Active Region Excess Brightness Temperature during Solar Cycles 23 and 24. *Astrophys.* J., 902(2):136, Oct. 2020. doi: 10.3847/1538-4357/abb59e.

L. Golub, E. Deluca, G. Austin, J. Bookbinder, D. Caldwell, P. Cheimets, J. Cirtain, M. Cosmo, P. Reid, A. Sette, M. Weber, T. Sakao, R. Kano, K. Shibasaki, H. Hara, S. Tsuneta, K. Kumagai, T. Tamura, M. Shimojo, J. McCracken, J. Carpenter, H. Haight, R. Siler, E. Wright, J. Tucker, H. Rutledge, M. Barbera, G. Peres, and S. Varisco. The X-Ray Telescope (XRT) for the Hinode Mission. *Solar* Phys., 243(1):63–86, June 2007. doi: 10.1007/s11207-007-0182-1.

N. Gopalswamy. Solar activity studies using microwave imaging observations. In 2016 URSI Asia-Pacific Radio Science Conference (URSI AP-RASC), pages 1075–1078, 2016. doi: 10.1109/URSIAP-RASC.2016.7601382.

N. Gopalswamy, S. Yashiro, Y. Liu, G. Michalek, A. Vourlidas, M. L. Kaiser, and R. A. Howard. Coronal mass ejections and other extreme characteristics of the 2003 October-November solar eruptions. Journal of Geophysical Research (Space Physics), 110(A9):A09S15, Sept. 2005. doi: 10.1029/2004JA010958.

F. Govoni, P. Bolli, F. Buffa, L. Caito, E. Carretti, G. Comoretto, D. Fierro, A. Melis, M. Murgia, A. Navarrini, A. Orfei, A. Orlati, T. Pisanu, S. Poppi, A. Possenti, A. Attoli, U. Becciani, C. Belli, G. Carboni, M. T. Caria, A. Cattani, R. Concu, L. Cresci, A. Fara, F. Fiocchi, F. Gaudiomonte, A. Ladu, A. Maccaferri, S. Mariotti, P. Marongiu, C. Migoni, E. Molinari, M. Morsiani, R. Nesti, L. Olmi, I. Porceddu, S. Righini, P. Ortu, S. Palmas, M. Pili, A. Poddighe, M. Poloni, J. Roda, A. Scalambra, F. Schillir, L. Schirru, G. Serra, R. Smareglia, G. P. Vargiu, and F. Vitello. The high-frequency upgrade of the sardinia radio telescope. In 2021 XXXIVth General Assembly and Scientific Symposium of the International Union of Radio Science (URSI GASS), pages 1–4, 2021. doi: 10.23919/URSIGASS51995.2021.9560570.

V. V. Grechnev, S. V. Lesovoi, G. Y. Smolkov, B. B. Krissinel, V. G. Zandanov, A. T. Altyntsev, N. N. Kardapolova, R. Y. Sergeev, A. M. Uralov, V. P. Maksimov, and B. I. Lubyshev. The Siberian Solar Radio Telescope: the current state of the instrument, observations, and data. *Solar* Phys., 216(1):239–272, Sept. 2003. doi: 10.1023/A:1026153410061.

O. Hachenberg, P. Steffen, and W. Harth. The Sun at 8.5 mm wavelength — results of observations with high angular resolution. *Solar* Phys., 60(1):105–118, Nov. 1978. doi: 10.1007/BF00152335.

Y. A. Hafez, R. D. Davies, R. J. Davis, C. Dickinson, E. S. Battistelli, F. Blanco, K. Cleary, T. Franzen, R. Genova-Santos, K. Grainge, M. P. Hobson, M. E. Jones, K. Lancaster, A. N. Lasenby, C. P. Padilla-Torres, J. A. Rubiño-Martin, R. Rebolo, R. D. E. Saunders, P. F. Scott, A. C. Taylor, D. Titterington, M. Tucci, and R. A. Watson. Radio source calibration for the Very Small Array and other cosmic microwave background instruments at around 30 GHz. *Mon.* Not. Roy. Astron. Soc., 388(4):1775–1786, Aug. 2008. doi: 10.1111/j.1365-2966.2008.13515.x.

N. Hurlburt, M. Cheung, C. Schrijver, L. Chang, S. Freeland, S. Green, C. Heck, A. Jaffey, A. Kobashi, D. Schiff, J. Serafin, R. Seguin, G. Slater, A. Somani, and R. Timmons. Heliophysics Event Knowledgebase for the Solar Dynamics Observatory (SDO) and Beyond. *Solar* Phys., 275(1-2):67–78, Jan. 2012. doi: 10.1007/s11207-010-9624-2.

M. Iacolina, A. Pellizzoni, and S. Righini. Testing technological and astronomical SDSA/SRT capabilities for solar and near-Sun observations - International Astronautical Congress - Washington - IAC -19,A7,2,3,x52814. Oct. 2019. URL https://iafastro.directory/iac/paper/id/52814/summary/.

N. M. Iacolina, S. Mulas, A. Pellizzoni, E. Egron, G. Serra, G. Valente, A. Saba, E. Urru, and A. Melis. Preliminary results in the rfi excision applied to srt/sdsa p-band imaging data. Technical report, 2022.

N. M. S. Iacolina, Mulas, , A. Saba, G. Serra, P. Tortora, E. Urru, G. Valente, and S. Viviano. Radio science mission requirements assessment for sdsa, (in progress). Technical report, 2022.

L. Iess, B. Bertotti, and M. Dobrowolny. Plasma effects on doppler measurements of interplanetary spacecraft. i - discontinuities and waves. Astronomy and Astrophysics, 121:203–210, 04 1983.

L. Iess, M. Di Benedetto, M. Marabucci, and P. Racioppa. Improved doppler tracking systems for deep space navigation. 01 2012.

L. Iess, S. W. Asmar, P. Cappuccio, and a. et. Gravity, geodesy and fundamental physics with bepicolombos more investigation. Space Science Reviews, 217, 02 2021. doi: https://doi.org/10.1007/s11214-021-00800-3.

S. A. Jaeggli and A. A. Norton. The Magnetic Classification of Solar Active Regions 1992-2015. *Astrophys.* J. Lett., 820(1):L11, Mar. 2016. doi: 10.3847/2041-8205/820/1/L11.

N. L. Johnson. Systems of Frequency Curves Generated by Methods of Translation. Biometrika, 36(1/2):149–176, 1949a. ISSN 00063444. URL http://www.jstor.org/stable/2332539.

N. L. Johnson. Bivariate distributions based on simple translation systems. Biometrika, 36 (3-4):297–304, 12 1949b. ISSN 0006-3444. doi: 10.1093/biomet/36.3-4.297. URL https://doi.org/10.1093/biomet/36.3-4.297.

T. Kakinuma and G. Swarup. A Model for the Sources of the Slowly Varying Component of Microwave Solar Radiation. *Astrophys.* J., 136:975, Nov. 1962. doi: 10.1086/147450.

J. Kallunki and M. Tornikoski. Eruptive Solar Prominence at 37 GHz. *Solar* Phys., 292(7):84, July 2017. doi: 10.1007/s11207-017-1110-7.

J. Kallunki, M. Tornikoski, and I. Björklund. Identifying 8 mm Radio Brightenings During the Solar Activity Minimum. *Solar* Phys., 295(7):105, July 2020. doi: 10.1007/s11207-020-01673-5.

T. I. Kaltman, V. M. Bogod, A. G. Stupishin, and L. V. Yasnov. The altitude structure of the coronal magnetic field of AR 10933. Astronomy Reports, 56(10):790–799, Oct. 2012. doi: 10.1134/S1063772912100022.

S. R. Kane. Impulsive (flash) phase of solar flares: Hard x-ray, microwave, euv and optical observations. Symposium - International Astronomical Union, 57:105141, 1974. doi: 10.1017/S0074180900234165.

P. Kaufmann. Some Characteristics of an S-Component of Solar Radiation identified on November 1966 Eclipse at 4.28-cm Wavelength. *Solar* Phys., 4(1):58–66, May 1968. doi: 10.1007/BF00146998.

P. Kaufmann, H. Levato, M. M. Cassiano, E. Correia, J. E. R. Costa, C. G. Giménez de Castro, R. Godoy, R. K. Kingsley, J. S. Kingsley, A. S. Kudaka, R. Marcon, R. Martin, A. Marun, A. M. Melo, P. Pereyra, J.-P. Raulin, T. Rose, A. Silva Valio, A. Walber, P. Wallace, A. Yakubovich, and M. B. Zakia. New telescopes for ground-based solar observations at submillimeter and mid-infrared. In L. M. Stepp and R. Gilmozzi, editors, Ground-based and Airborne Telescopes II, volume 7012 of Society of Photo-Optical Instrumentation Engineers (SPIE) Conference Series, page 70120L, July 2008. doi: 10.1117/12.788889.

M. D. Kazachenko and H. S. Hudson. Active Region Irradiance during Quiescent Periods: New Insights from Sun-as-a-star Spectra. *Astrophys.* J., 901(1):64, Sept. 2020. doi: 10.3847/1538-4357/abada6.

S. J. Keihm, A. Tanner, and H. Rosenberger. Measurements and Calibration of Tropospheric Delay at Goldstone from the Cassini Media Calibration System. Interplanetary Network Progress Report, 42-158:1–17, Aug. 2004.

A. Kerdraon and J.-M. Delouis. The Nançay Radioheliograph, volume 483, page 192. 1997. doi: 10.1007/BFb0106458.

H. E. J. Koskinen, D. N. Baker, A. Balogh, T. Gombosi, A. Veronig, and R. von Steiger. Achievements and Challenges in the Science of Space Weather. *Space* Sci. Rev., 212(3-4):1137–1157, Nov. 2017. doi: 10.1007/s11214-017-0390-4.

T. Kosugi, M. Ishiguro, and K. Shibasaki. Polar-cap and coronal-hole-associated brightenings of the sun at millimeter wavelengths. *Pub.* Astron. Soc. Japan, 38(1):1–11, Jan. 1986.

T. Kosugi, K. Matsuzaki, T. Sakao, T. Shimizu, Y. Sone, S. Tachikawa, T. Hashimoto, K. Minesugi, A. Ohnishi, T. Yamada, S. Tsuneta, H. Hara, K. Ichimoto, Y. Suematsu, M. Shimojo,

T. Watanabe, S. Shimada, J. M. Davis, L. D. Hill, J. K. Owens, A. M. Title, J. L. Culhane, L. K. Harra, G. A. Doschek, and L. Golub. The Hinode (Solar-B) Mission: An Overview. *Solar* Phys., 243(1):3–17, June 2007. doi: 10.1007/s11207-007-9014-6.

P. Kuhnle. Nasa/jpl deep space network frequency and timing. 1989.

M. R. Kundu. Solar Active Regions at Millimeter Wavelengths. *Solar* Phys., 13(2):348–356, Aug. 1970. doi: 10.1007/BF00153556.

M. R. Kundu, S. M. White, K. Shibasaki, and J. P. Raulin. A Radio Study of the Evolution of Spatial Structure of an Active Region and Flare Productivity. *ApJS*, 133(2):467–482, Apr. 2001. doi: 10.1086/320351.

A. Ladu, L. Schirru, F. Gaudiomonte, P. Marongiu, G. Angius, F. Perini, and G. P. Vargiu. Upgrading of the l-p band cryogenic receiver of the sardinia radio telescope: A feasibility study. Sensors, 22(11), 2022. ISSN 1424-8220. doi: 10.3390/s22114261. URL https://www.mdpi.com/1424-8220/22/11/4261.

E. Landi and F. Chiuderi Drago. The Quiet-Sun Differential Emission Measure from Radio and UV Measurements. *Astrophys.* J., 675(2):1629–1636, Mar. 2008. doi: 10.1086/527285.

J. Lee. Radio Emissions from Solar Active Regions. *Space* Sci. Rev., 133(1-4):73–102, Dec. 2007. doi: 10.1007/s11214-007-9206-2.

J. Lee, A. N. McClymont, Z. Mikić, S. M. White, and M. R. Kundu. Coronal Currents, Magnetic Fields, and Heating in a Solar Active Region. *Astrophys.* J., 501(2):853–865, July 1998. doi: 10.1086/305851.

J. R. Lemen, A. M. Title, D. J. Akin, P. F. Boerner, C. Chou, J. F. Drake, D. W. Duncan, C. G. Edwards, F. M. Friedlaender, G. F. Heyman, N. E. Hurlburt, N. L. Katz, G. D. Kushner, M. Levay, R. W. Lindgren, D. P. Mathur, E. L. McFeaters, S. Mitchell, R. A. Rehse, C. J. Schrijver, L. A. Springer, R. A. Stern, T. D. Tarbell, J.-P. Wuelser, C. J. Wolfson, C. Yanari, J. A. Bookbinder, P. N. Cheimets, D. Caldwell, E. E. Deluca, R. Gates, L. Golub, S. Park, W. A. Podgorski, R. I. Bush, P. H. Scherrer, M. A. Gummin, P. Smith, G. Auker, P. Jerram, P. Pool, R. Soufli, D. L. Windt, S. Beardsley, M. Clapp, J. Lang, and N. Waltham. The Atmospheric Imaging Assembly (AIA) on the Solar Dynamics Observatory (SDO). *Solar* Phys., 275(1-2): 17–40, Jan. 2012. doi: 10.1007/s11207-011-9776-8.

J. L. Linsky. A Recalibration of the Quiet Sun Millimeter Spectrum Based on the Moon as an Absolute Radiometric Standard. *Solar* Phys., 28(2):409–418, Feb. 1973. doi: 10.1007/BF00152312.

S. Loru, A. Pellizzoni, E. Egron, S. Righini, M. N. Iacolina, S. Mulas, M. Cardillo, M. Marongiu, R. Ricci, M. Bachetti, M. Pilia, A. Trois, A. Ingallinera, O. Petruk, G. Murtas, G. Serra, F. Buffa, R. Concu, F. Gaudiomonte, A. Melis, A. Navarrini, D. Perrodin, and G. Valente. Investigating the high-frequency spectral features of SNRs Tycho, W44, and IC443 with the Sardinia Radio Telescope. *Mon.* Not. Roy. Astron. Soc., 482(3):3857–3867, Jan. 2019. doi: 10.1093/mnras/sty1194.

S. Loru, A. Pellizzoni, E. Egron, A. Ingallinera, G. Morlino, S. Celli, G. Umana, C. Trigilio, P. Leto, M. N. Iacolina, S. Righini, P. Reich, S. Mulas, M. Marongiu, M. Pilia, A. Melis, R. Concu, F. Bufano, C. Buemi, F. Cavallaro, S. Riggi, and F. Schillirò. New high-frequency radio observations of the Cygnus Loop supernova remnant with the Italian radio telescopes. *Mon.* Not. Roy. Astron. Soc., 500(4):5177–5194, Jan. 2021. doi: 10.1093/mnras/staa2868.

M. Loukitcheva. First solar observations with ALMA. Advances in Space Research, 63(4): 1396–1403, Feb. 2019. doi: 10.1016/j.asr.2018.08.030.

W. Manchester, E. K. J. Kilpua, Y. D. Liu, N. Lugaz, P. Riley, T. Török, and B. Vršnak. The Physical Processes of CME/ICME Evolution. *Space* Sci. Rev., 212(3-4):1159–1219, Nov. 2017. doi: 10.1007/s11214-017-0394-0.

M. Marongiu, A. Pellizzoni, E. Egron, T. Laskar, M. Giroletti, S. Loru, A. Melis, G. Carboni, C. Guidorzi, S. Kobayashi, N. Jordana-Mitjans, A. Rossi, C. G. Mundell, R. Concu, R. Martone, and L. Nicastro. Methods for detection and analysis of weak radio sources with single-dish radio telescopes. Experimental Astronomy, 49(3):159–182, May 2020. doi: 10.1007/s10686-020-09658-9.

M. Marongiu, A. P. Pellizzoni, S. Mulas, and G. Murtas. A python approach for solar data analysis: Sundara (sundish active region analyser), preliminary development. Technical Report 81, OA@INAF, 2021. URL http://hdl.handle.net/20.500.12386/30719.

M. Marongiu, A. Pellizzoni, M. Bachetti, S. Mulas, S. Righini, G. Murtas, S. Loru, E. Egron, and I. M.N. A dedicated pipeline to analyse solar data with inaf radio telescopes: Sunpit (sundish pipeline tool). Technical Report 137, OA@INAF, 2022. URL http://hdl.handle.net/20.500.12386/31426.

S. Masuda. Twenty-seven years of Nobeyama Radioheliograph: Its contribution to understanding of particle acceleration in solar flares. In AGU Fall Meeting Abstracts, volume 2019, pages SH13D–3410, Dec. 2019.

P. Maxia, N. M. Iacolina, G. Serra, G. Valente, S. Mulas, R. Ghiani, A. Saba, and E. Urru. Pianificazione dell'attivit di tracking per la fase EDL della missione Mars 2020 - Perseverance. Technical report, 2021.

P. S. McIntosh. The Classification of Sunspot Groups. *Solar* Phys., 125(2):251–267, Sept. 1990. doi: 10.1007/BF00158405.

A. Melis, R. Concu, A. Trois, A. Possenti, A. Bocchinu, P. Bolli, M. Burgay, E. Carretti, P. Castangia, S. Casu, C. C. Pestellini, A. Corongiu, N. D'Amico, E. Egron, F. Govoni, M. N. Iacolina, M. Murgia, A. Pellizzoni, D. Perrodin, M. Pilia, T. Pisanu, A. Poddighe, S. Poppi, I. Porceddu, A. Tarchi, V. Vacca, G. Aresu, M. Bachetti, M. Barbaro, A. Casula, A. Ladu, S. Leurini, F. Loi, S. Loru, P. Marongiu, P. Maxia, G. Mazzarella, C. Migoni, G. Montisci, G. Valente, and G. Vargiu. SArdinia Roach2-based Digital Architecture for Radio Astronomy (SARDARA). Journal of Astronomical Instrumentation, 7(1):1850004, Mar. 2018. doi: 10.1142/S2251171718500046.

S. Mulas, A. Pellizzoni, N. M. Iacolina, E. Egron, M. Marongiu, G. Valente, A. Melis, S. Righini, and G. Murtas. A New Method for Accurate Calibration of Solar Disk Emission in the Radio Band. Technical report, 2022.

S. Mumford, N. Freij, S. Christe, J. Ireland, F. Mayer, V. Hughitt, A. Shih, D. Ryan, S. Liedtke, D. Pérez-Suárez, P. Chakraborty, V. K, A. Inglis, P. Pattnaik, B. Sipőcz, R. Sharma, A. Leonard, D. Stansby, R. Hewett, A. Hamilton, L. Hayes, A. Panda, M. Earnshaw, N. Choudhary, A. Kumar, P. Chanda, M. Haque, M. Kirk, M. Mueller, S. Konge, R. Srivastava, Y. Jain, S. Bennett, A. Baruah, W. Barnes, M. Charlton, S. Maloney, N. Chorley, Himanshu, S. Modi, J. Mason, Naman, J. I. Campos Rozo, L. Manley, A. Chatterjee, J. Evans, M. Malocha, M. Bobra, S. Ghosh, Airmansmith, D. Stańczak, R. De Visscher, S. Verma, A. Agrawal, D. Buddhika, S. Sharma, J. Park, M. Bates, D. Goel, G. Taylor, G. Cetusic,

Jacob, M. Inchaurrandieta, S. Dacie, S. Dubey, D. Sharma, E. Bray, J. Rideout, S. Zahniy, T. Meszaros, A. Bose, A. Chicrala, Ankit, C. Guennou, D. D'Avella, D. Williams, J. Ballew, N. Murphy, P. Lodha, T. Robitaille, Y. Krishan, A. Hill, A. Eigenbrot, B. Mampaey, B. Wiedemann, C. Molina, D. Keşkek, I. Habib, J. Letts, J. Bazán, Q. Arbolante, R. Gomillion, Y. Kothari, Y. Sharma, A. Stevens, A. Price-Whelan, A. Mehrotra, A. Kustov, B. Stone, T. Dang, E. Arias, F. Dover, F. Verstringe, G. Kumar, H. Mathur, I. Babuschkin, J. Wimbish, J. Buitrago-Casas, K. Krishna, K. Hiware, M. Mangaonkar, M. Mendero, M. Schoentgen, N. Gyenge, O. Streicher, R. Mekala, R. Mishra, S. Srikanth, S. Jain, T. Yadav, T. Wilkinson, T. Pereira, Y. Agrawal, Jamescalixto, Yasintoda, and S. Murray. SunPy: A Python package for Solar Physics. The Journal of Open Source Software, 5(46):1832, Feb. 2020. doi: 10.21105/joss.01832.

M. Murgia, F. Govoni, E. Carretti, A. Melis, R. Concu, A. Trois, F. Loi, V. Vacca, A. Tarchi, P. Castangia, A. Possenti, A. Bocchinu, M. Burgay, S. Casu, A. Pellizzoni, T. Pisanu, A. Poddighe, S. Poppi, N. D'Amico, M. Bachetti, A. Corongiu, E. Egron, N. Iacolina, A. Ladu, P. Marongiu, C. Migoni, D. Perrodin, M. Pilia, G. Valente, and G. Vargiu. Sardinia Radio Telescope wide-band spectral-polarimetric observations of the galaxy cluster 3C129. Monthly Notices of the Royal Astronomical Society, 461(4):3516–3532, 07 2016. ISSN 0035-8711. doi: 10.1093/mnras/stw1552. URL https://doi.org/10.1093/mnras/stw1552.

F. T. Nasir, C. Castiglia, F. Buffa, G. L. Deiana, A. Delitala, and A. Tarchi. Weather forecasting and dynamic scheduling for a modern cm/mm wave radiotelescope. Experimental Astronomy, 36(1-2):407–424, Aug. 2013. doi: 10.1007/s10686-013-9339-0.

A. Navarrini, A. Orfei, R. Nesti, G. Valente, S. Mariotti, P. Bolli, T. Pisanu, J. Roda, L. Cresci, P. Marongiu, A. Scalambra, D. Panella, A. Ladu, A. Cattani, L. Carbonaro, E. Urru, A. Cremonini, F. Fiocchi, A. Maccaferri, M. Morsiani, and M. Poloni. The sardinia radio telescope front-ends. In 27th International Symposium on Space Terahertz Technology, ISSTT 2016, 2017. URL www.scopus.com.

A. Navarrini, L. Olmi, R. Nesti, P. Ortu, P. Marongiu, A. Orlati, A. Scalambra, A. Orfei, J. Roda, A. Cattani, S. Leurini, F. Govoni, M. Murgia, E. Carretti, D. Fierro, and A. Pellizzoni. Feasibility study of a w-band multibeam heterodyne receiver for the gregorian focus of the sardinia radio telescope. IEEE Access, 10:26369–26403, 2022. doi: 10.1109/ACCESS.2022.3153492.

A. Nindos. Incoherent Solar Radio Emission. Frontiers in Astronomy and Space Sciences, 7:57, Nov. 2020. doi: 10.3389/fspas.2020.00057.

A. Nindos, M. R. Kundu, S. M. White, K. Shibasaki, and N. Gopalswamy. Soft X-Ray and Gyroresonance Emission above Sunspots. *ApJS*, 130(2):485–499, Oct. 2000. doi: 10.1086/317355.

A. Nindos, C. E. Alissandrakis, G. B. Gelfreikh, V. M. Bogod, and C. Gontikakis. Spatially resolved microwave oscillations above a sunspot. *Astron.* Astrophys., 386:658–673, May 2002. doi: 10.1051/0004-6361:20020252.

G. M. Nita, N. M. Viall, J. A. Klimchuk, M. A. Loukitcheva, D. E. Gary, A. A. Kuznetsov, and G. D. Fleishman. Dressing the Coronal Magnetic Extrapolations of Active Regions with a Parameterized Thermal Structure. *Astrophys.* J., 853(1):66, Jan. 2018. doi: 10.3847/1538-4357/aaa4bf.

N. V. Nitta, X. Sun, J. T. Hoeksema, and M. L. DeRosa. Solar Cycle Variations of the Radio Brightness of the Solar Polar Regions as Observed by the Nobeyama Radioheliograph. *Astrophys.* J. Lett., 780(2):L23, Jan. 2014. doi: 10.1088/2041-8205/780/2/L23.

A. Orfei, L. Carbonaro, A. Cattani, A. Cremonini, L. Cresci, F. Fiocchi, A. Maccaferri, G. Maccaferri, S. Mariotti, J. Monari, M. Morsiani, V. Natale, R. Nesti, D. Panella, M. Poloni, J. Roda, A. Scalambra, and G. Tofani. A Multi-Feed Receiver in the 18 to 26.5 GHz Band for Radio Astronomy. IEEE Antennas and Propagation Magazine, 52(4):62–72, Aug. 2010. doi: 10.1109/MAP.2010.5638236.

C. O'Sullivan and D. A. Green. Constraints on the secular decrease in the flux density of CAS A at 13.5, 15.5 and 16.5 GHz. *Mon.* Not. Roy. Astron. Soc., 303(3):575–578, Mar. 1999. doi: 10.1046/j.1365-8711.1999.02259.x.

B. D. Patel, B. Joshi, K.-S. Cho, R.-S. Kim, and Y.-J. Moon. Near-Earth Interplanetary Coronal Mass Ejections and Their Association with DH Type II Radio Bursts During Solar Cycles 23 and 24. arXiv e-prints, art. arXiv:2210.14535, Oct. 2022.

M. Pätzold, F. M. Neubauer, L. Carone, A. Hagermann, C. Stanzel, B. Häusler, S. Remus, J. Selle, D. Hagl, D. P. Hinson, R. A. Simpson, G. L. Tyler, S. W. Asmar, W. I. Axford, T. Hagfors, J. P. Barriot, J. C. Cerisier, T. Imamura, K. I. Oyama, P. Janle, G. Kirchengast, and V. Dehant. MaRS: Mars Express Orbiter Radio Science. In A. Wilson and A. Chicarro, editors, Mars Express: the Scientific Payload, volume 1240 of ESA Special Publication, pages 141–163, Aug. 2004.

A. Pellizzoni, S. Righini, G. Murtas, F. Buffa, R. Concu, E. Egron, M. N. Iacolina, S. Loru, A. Maccaferri, A. Melis, A. Navarrini, A. Orfei, P. Ortu, T. Pisanu, A. Saba, G. Serra, G. Valente, A. Zanichelli, P. Zucca, and M. Messerotti. Imaging of the solar atmosphere in the centimetre-millimetre band through single-dish observations. Nuovo Cimento C Geophysics Space Physics C, 42(1):9, Jan. 2019. doi: 10.1393/ncc/i2019-19009-x.

A. Pellizzoni, M. N. Righini, S. Iacolina, M. and Marongiu, G. Mulas, G. Murtas, E. Valente, M. Egron, F. Bachetti, R. Buffa, G. L. Concu, S. L. Deiana, A. Guglielmino, S. Ladu, A. Loru, P. Maccaferri, A. Marongiu, A. Melis, A. Navarrini, P. Orfei, M. Ortu, T. Pili, G. Pisanu, A. Pupillo, L. Saba, G. Schirru, C. Serra, A. Tiburzi, P. Zanichelli, M. Zucca, and Messerotti. Solar Observations with Single-Dish INAF Radio Telescopes: Continuum Imaging in the 1826 GHz Range. Solar Physics, July 2022. doi: 10.1007/s11207-022-02013-5.

R. A. Perley and B. J. Butler. An Accurate Flux Density Scale from 50 MHz to 50 GHz. *ApJS*, 230(1):7, May 2017. doi: 10.3847/1538-4365/aa6df9.

C. Plainaki, M. Antonucci, A. Bemporad, F. Berrilli, B. Bertucci, M. Castronuovo, P. De Michelis, M. Giardino, R. Iuppa, M. Laurenza, F. Marcucci, M. Messerotti, L. Narici, B. Negri, F. Nozzoli, S. Orsini, V. Romano, E. Cavallini, G. Polenta, and A. Ippolito. Current state and perspectives of Space Weather science in Italy. Journal of Space Weather and Space Climate, 10:6, Dec. 2020. doi: 10.1051/swsc/2020003.

A. I. Podgorny and I. M. Podgorny. Magnetohydrodynamic simulation of a solar flare: 2. Flare model and simulation using active-region magnetic maps. Geomagnetism and Aeronomy, 52(2):162–175, Apr. 2012. doi: 10.1134/S0016793212020119.

I. Prandoni, M. Murgia, A. Tarchi, M. Burgay, P. Castangia, E. Egron, F. Govoni, A. Pellizzoni, R. Ricci, S. Righini, M. Bartolini, S. Casu, A. Corongiu, M. N. Iacolina, A. Melis, F. T. Nasir, A. Orlati, D. Perrodin, S. Poppi, A. Trois, V. Vacca, A. Zanichelli, M. Bachetti, M. Buttu,

G. Comoretto, R. Concu, A. Fara, F. Gaudiomonte, F. Loi, C. Migoni, A. Orfei, M. Pilia, P. Bolli, E. Carretti, N. D'Amico, D. Guidetti, S. Loru, F. Massi, T. Pisanu, I. Porceddu, A. Ridolfi, G. Serra, C. Stanghellini, C. Tiburzi, S. Tingay, and G. Valente. The Sardinia Radio Telescope . From a technological project to a radio observatory. *Astron.* Astrophys., 608:A40, Dec. 2017. doi: 10.1051/0004-6361/201630243.

E. Priest. Magnetohydrodynamics of the Sun. Cambridge University Press, 2014. doi: 10.1017/CBO9781139020732.

R. Ramesh, K. R. Subramanian, M. S. Sundararajan, and C. V. Sastry. The Gauribidanur Radioheliograph. *Solar* Phys., 181(2):439–453, Aug. 1998. doi: 10.1023/A:1005075003370.

G. Righini-Cohen and M. Simon. Submillimeter observations of solar active regions. *Astrophys.* J., 217:999–1005, Nov. 1977. doi: 10.1086/155646.

W. Riley. Handbook of frequency stability analysis. NIST, 1065:1–123, 01 2007.

D. Rochblatt, P. Richter, and T. Otoshi. A microwave performance calibration system for nasa's deep space network antennas .2. holography, alignment, and frequency stability. pages 150 – 155 vol.1, 05 1997. ISBN 0-85296-686-5. doi: 10.1049/cp:19970227.

R. Schwartz. Das RATAN-600-Radioteleskop. Sterne und Weltraum, 17:242–245, Aug. 1978.

C. L. Selhorst, A. V. R. Silva, and J. E. R. Costa. Solar atmospheric model with spicules applied to radio observation. *Astron.* Astrophys., 433(1):365–374, Apr. 2005. doi: 10.1051/0004-6361:20042043.

C. L. Selhorst, A. Silva-Válio, and J. E. R. Costa. Solar atmospheric model over a highly polarized 17 GHz active region. *Astron.* Astrophys., 488(3):1079–1084, Sept. 2008. doi: 10.1051/0004-6361:20079217.

C. L. Selhorst, J. E. R. Costa, C. G. Giménez de Castro, A. Valio, A. A. Pacini, and K. Shibasaki. The 17 GHz Active Region Number. *Astrophys.* J., 790(2):134, Aug. 2014. doi: 10.1088/0004-637X/790/2/134.

I. I. Shapiro. Fourth Test of General Relativity. *Phys.* Rev. Lett., 13(26):789–791, Dec. 1964. doi: 10.1103/PhysRevLett.13.789.

K. Shibasaki. Radio Synoptic Maps and Polar CAP Brightening. In K. S. Balasubramaniam, J. Harvey, and D. Rabin, editors, Synoptic Solar Physics, volume 140 of Astronomical Society of the Pacific Conference Series, page 373, Jan. 1998.

K. Shibasaki. Long-Term Global Solar Activity Observed by the Nobeyama Radioheliograph. 65:S17, Dec. 2013. doi: 10.1093/pasj/65.sp1.S17.

K. Shibasaki, S. Enome, H. Nakajima, M. Nishio, T. Takano, Y. Hanaoka, C. Torii, H. Sekiguchi, S. Kawashima, T. Bushimata, N. Shinohara, H. Koshiishi, Y. Shiomi, Y. Irimajiri, K. D. Leka, and R. C. Canfield. A Purely Polarized S-Component at 17 GHz. 46:L17–L20, Apr. 1994.

K. Shibasaki, C. E. Alissandrakis, and S. Pohjolainen. Radio Emission of the Quiet Sun and Active Regions (Invited Review). *Solar* Phys., 273(2):309–337, Nov. 2011. doi: 10.1007/s11207-011-9788-4.

F. I. Shimabukuro and J. M. Stacey. Brightness Temperature of the Quiet Sun at Centimeter and Millimeter Wavelengths. *Astrophys.* J., 152:777, June 1968. doi: 10.1086/149594.

A. V. R. Silva, T. F. Laganá, C. G. Gimenez Castro, P. Kaufmann, J. E. R. Costa, H. Levato, and M. Rovira. Diffuse Component Spectra of Solar Active Regions at Submillimeter Wavelengths. *Solar* Phys., 227(2):265–281, Apr. 2005. doi: 10.1007/s11207-005-2787-6.

G. Y. Smolkov, A. A. Pistolkors, T. A. Treskov, B. B. Krissinel, V. A. Putilov, and N. N. Potapov. The Siberian Solar Radio Telescope - Parameters and Principle of Operation Objectives and Results of First Observations of Spatio-Temporal Properties of Development of Active Regions and Flares. *Astrophys. Space Sci.*, 119(1):1–4, Feb. 1986. doi: 10.1007/BF00648801.

B. V. Somov. Non-neutral current sheets and solar flare energetics. *Astron.* Astrophys., 163 (1-2):210–218, July 1986.

E. A. Spiegel and J. P. Zahn. The solar tachocline. *Astron.* Astrophys., 265:106–114, Nov. 1992.

J. R. Stallcop. Absorption of Infrared Radiation by Electrons in the Field of a Neutral Hydrogen Atom - I. *Astrophys.* J., 187:179–184, Jan. 1974. doi: 10.1086/152607.

A. G. Stupishin, T. I. Kaltman, V. M. Bogod, and L. V. Yasnov. Modeling of Solar Atmosphere Parameters Above Sunspots Using RATAN-600 Microwave Observations. *Solar* Phys., 293 (1):13, Jan. 2018. doi: 10.1007/s11207-017-1228-7.

K. F. Tapping and C. Zwaan. Sources of the Slowly-Varying Component of Solar Microwave Emission and their Relationship with their Host Active Regions. *Solar* Phys., 199(2): 317–344, Apr. 2001. doi: 10.1023/A:1010342823034.

M. J. Thompson. Grand challenges in the physics of the sun and sun-like stars. Frontiers in Astronomy and Space Sciences, 1, 2014. ISSN 2296-987X. doi: 10.3389/fspas.2014.00001. URL https://www.frontiersin.org/articles/10.3389/fspas.2014.00001.

W. T. Thompson. Coordinate systems for solar image data. *Astron.* Astrophys., 449(2): 791–803, Apr. 2006. doi: 10.1051/0004-6361:20054262.

S. D. Tun, D. E. Gary, and M. K. Georgoulis. Three-dimensional Structure of a Solar Active Region from Spatially and Spectrally Resolved Microwave Observations. *Astrophys.* J., 728 (1):1, Feb. 2011. doi: 10.1088/0004-637X/728/1/1.

G. Valente, T. Pisanu, P. Bolli, S. Mariotti, P. Marongiu, A. Navarrini, R. Nesti, A. Orfei, and J. Roda. The dual-band LP feed system for the Sardinia Radio Telescope prime focus. In W. S. Holland and J. Zmuidzinas, editors, Millimeter, Submillimeter, and Far-Infrared Detectors and Instrumentation for Astronomy V, volume 7741, page 774126. International Society for Optics and Photonics, SPIE, 2010. doi: 10.1117/12.857306. URL https://doi.org/10.1117/12.857306.

G. Valente, P. Marongiu, A. Navarrini, A. Saba, G. Montisci, A. Ladu, T. Pisanu, M. Pili, S. Dessi, A. Uccheddu, M. N. Iacolina, D. Perrodin, M. Buttu, E. Egron, A. Melis, C. Tiburzi, and V. Vacca. The 7-beam S-band cryogenic receiver for the SRT primary focus: project status. In W. S. Holland and J. Zmuidzinas, editors, Millimeter, Submillimeter, and Far-Infrared Detectors and Instrumentation for Astronomy VIII, volume 9914, page 991422. International Society for Optics and Photonics, SPIE, 2016. doi: 10.1117/12.2232625. URL https://doi.org/10.1117/12.2232625.

G. Valente, N. M. Iacolina, V. Salvatore, A. Saba, G. Serra, G. Parca, G. Impresario, G. D'Amore, S. W. Asmar, G. Montisci, P. Ortu, D. Perrodin, F. Gaudiomonte, and A. Melis. Sardinia deep space antenna: Current program status and results. IAF, 2019. doi: IAC-19,B6,IP,1,x52799.

G. Valente, M. N. Iacolina, R. Ghiani, A. Saba, G. Serra, E. Urru, G. Montisci, S. Mulas, S. W. Asmar, T. T. Pham, J. De Vicente, and S. Viviano. The sardinia space communication asset: Performance of the sardinia deep space antenna x-band downlink capability. IEEE Access, 10:64525–64534, 2022a. doi: 10.1109/ACCESS.2022.3183745.

G. Valente, T. Pisanu, A. Navarrini, P. Marongiu, A. Orfei, S. Mariotti, R. Nesti, J. Roda, A. Cattani, P. Bolli, and G. Montisci. The coaxial l-p cryogenic receiver of the sardinia radio telescope. IEEE Access, 10:2631–2645, 2022b. doi: 10.1109/ACCESS.2021.3139744.

A. Valio, E. Spagiari, M. Marengoni, and C. L. Selhorst. Correlations of Sunspot Physical Characteristics during Solar Cycle 23. *Solar* Phys., 295(9):120, Sept. 2020. doi: 10.1007/s11207-020-01691-3.

J. F. ValleSilva, C. G. GimnezdeCastro, C. L. Selhorst, J.-P. Raulin, and A. Valio. Spectral signature of solar active region in millimetre and submillimetre wavelengths. Monthly Notices of the Royal Astronomical Society, 500(2):1964–1969, 10 2020. ISSN 0035-8711. doi: 10.1093/mnras/staa3354. URL https://doi.org/10.1093/mnras/staa3354.

L. van Driel-Gesztelyi and L. M. Green. Evolution of Active Regions. Living Reviews in Solar Physics, 12(1):1, Sept. 2015. doi: 10.1007/lrsp-2015-1.

S. M. Vatrushin and A. N. Korzhavin. Sci. Proc. of VI Sem. In B. V. Somov, V. V. Fomichev, and A. V. Stepanov, editors, Physics of the solar plasma, Moscow Izdatel Nauka, pages 100–106, Jan. 1989.

C. Verbeeck, V. Delouille, B. Mampaey, and R. De Visscher. The SPoCA-suite: Software for extraction, characterization, and tracking of active regions and coronal holes on EUV images. *Astron.* Astrophys., 561:A29, Jan. 2014. doi: 10.1051/0004-6361/201321243.

R. Verma, G. Maccaferri, A. Orfei, I. Prandoni, and L. Gregorini. A new k-band (18-26 ghz) 7-horn multi-feed receiver: Calibration campaign at medicina 32 m dish, 2009. URL https://openaccess.inaf.it/handle/20.500.12386/25753?mode=simple.

J. E. Vernazza, E. H. Avrett, and R. Loeser. Structure of the Solar Chromosphere. Basic Computations and Summary of the Results. *Astrophys.* J., 184:605–632, Sept. 1973. doi: 10.1086/152353.

J. E. Vernazza, E. H. Avrett, and R. Loeser. Structure of the solar chromosphere. III. Models of the EUV brightness components of the quiet sun. *ApJS*, 45:635–725, Apr. 1981. doi: 10.1086/190731.

E. N. Vinyaikin. Frequency dependence of the evolution of the radio emission of the supernova remnant Cas A. Astronomy Reports, 58(9):626–639, Sept. 2014. doi: 10.1134/S1063772914090078.

A. Vourlidas, D. E. Gary, and K. Shibasaki. Sunspot Gyroresonance Emission at 17 GHz: A Statistical Study. *Pub.* Astron. Soc. Japan, 58(1):11–20, Feb. 2006. doi: 10.1093/pasj/58.1.11.

J. L. Weiland, N. Odegard, R. S. Hill, E. Wollack, G. Hinshaw, M. R. Greason, N. Jarosik, L. Page, C. L. Bennett, J. Dunkley, B. Gold, M. Halpern, A. Kogut, E. Komatsu, D. Larson, M. Limon, S. S. Meyer, M. R. Nolta, K. M. Smith, D. N. Spergel, G. S. Tucker, and E. L. Wright. Seven-year Wilkinson Microwave Anisotropy Probe (WMAP) Observations: Planets and Celestial Calibration Sources. *ApJS*, 192(2):19, Feb. 2011. doi: 10.1088/0067-0049/192/2/19.

F. J. Wentz and T. Meissner. Atmospheric absorption model for dry air and water vapor at microwave frequencies below 100ghz derived from spaceborne radiometer observations. Radio Science, 51(5):381–391, 2016. doi: https://doi.org/10.1002/2015RS005858. URL https://agupubs.onlinelibrary.wiley.com/doi/abs/10.1002/2015RS005858.

S. M. White. Coronal Magnetic Field Measurements Through Gyroresonance Emission, volume 314, page 89. 2004. doi: 10.1007/1-4020-2814-8_5.

S. M. White and M. R. Kundu. Radio Observations of Gyroresonance Emission from Coronal Magnetic Fields. *Solar* Phys., 174(1-2):31–52, Aug. 1997. doi: 10.1023/A:1004975528106.

S. M. White, M. R. Kundu, T. Shimizu, K. Shibasaki, and S. Enome. The Radio Properties of Solar Active Region Soft X-Ray Transient Brightenings. *Astrophys.* J., 450:435, Sept. 1995. doi: 10.1086/176153.

S. M. White, K. Iwai, N. M. Phillips, R. E. Hills, A. Hirota, P. Yagoubov, G. Siringo, M. Shimojo, T. S. Bastian, A. S. Hales, T. Sawada, S. Asayama, M. Sugimoto, R. G. Marson, W. Kawasaki, E. Muller, T. Nakazato, K. Sugimoto, R. Brajša, I. Skokić, M. Bárta, S. Kim, A. J. Remijan, I. de Gregorio, S. A. Corder, H. S. Hudson, M. Loukitcheva, B. Chen, B. De Pontieu, G. D. Fleishmann, D. E. Gary, A. Kobelski, S. Wedemeyer, and Y. Yan. Observing the Sun with the Atacama Large Millimeter/submillimeter Array (ALMA): Fast-Scan Single-Dish Mapping. *Solar* Phys., 292(7):88, July 2017. doi: 10.1007/s11207-017-1123-2.

T. L. Wilson, K. Rohlfs, and S. Hüttemeister. Tools of Radio Astronomy. 2013. doi: 10.1007/978-3-642-39950-3.

A. Wootten and A. R. Thompson. The atacama large millimeter/submillimeter array. Proceedings of the IEEE, 97(8):1463–1471, 2009. doi: 10.1109/JPROC.2009.2020572.

A. Zanichelli, G. Serra, K.-H. Mack, G. Nicotra, M. Bartolini, F. Cantini, M. De Biaggi, F. Gaudiomonte, C. Bortolotti, M. Roma, S. Poppi, F. Bedosti, S. Righini, P. Bolli, A. Orlati, R. Ambrosini, C. Buemi, M. Buttu, P. Cassaro, P. Leto, A. Mattana, C. Migoni, L. Moscadelli, P. Raffaele Platania, and C. Trigilio. Towards coordinated site monitoring and common strategies for mitigation of Radio Frequency Interference at the Italian radio telescopes. arXiv e-prints, art. arXiv:2207.07571, July 2022.

P. Zhang, P. Zucca, S. S. Sridhar, C. Wang, M. M. Bisi, B. Dabrowski, A. Krankowski, G. Mann, J. Magdalenic, D. E. Morosan, and C. Vocks. Interferometric imaging with LOFAR remote baselines of the fine structures of a solar type-IIIb radio burst. *Astron.* Astrophys., 639: A115, July 2020. doi: 10.1051/0004-6361/202037733.

P. Zhang, P. Zucca, K. Kozarev, E. Carley, C. Wang, T. Franzen, B. Dabrowski, A. Krankowski, J. Magdalenic, and C. Vocks. Imaging of the quiet sun in the frequency range of 20–80 MHz. The Astrophysical Journal, 932(1):17, jun 2022. doi: 10.3847/1538-4357/ac6b37. URL https://doi.org/10.3847/1538-4357/ac6b37.

H. Zirin, B. M. Baumert, and G. J. Hurford. The Microwave Brightness Temperature Spectrum of the Quiet Sun. *Astrophys.* J., 370:779, Apr. 1991. doi: 10.1086/169861.

P. Zucca, D. E. Morosan, A. P. Rouillard, R. Fallows, P. T. Gallagher, J. Magdalenic, K. L. Klein, G. Mann, C. Vocks, E. P. Carley, M. M. Bisi, E. P. Kontar, H. Rothkaehl, B. Dabrowski, A. Krankowski, J. Anderson, A. Asgekar, M. E. Bell, M. J. Bentum, P. Best, R. Blaauw, F. Breitling, J. W. Broderick, W. N. Brouw, M. Brüggen, H. R. Butcher, B. Ciardi, E. de Geus, A. Deller, S. Duscha, J. Eislöffel, M. A. Garrett, J. M. Grießmeier, A. W. Gunst, G. Heald,

M. Hoeft, J. Hörandel, M. Iacobelli, E. Juette, A. Karastergiou, J. van Leeuwen, D. McKay-Bukowski, H. Mulder, H. Munk, A. Nelles, E. Orru, H. Paas, V. N. Pandey, R. Pekal, R. Pizzo, A. G. Polatidis, W. Reich, A. Rowlinson, D. J. Schwarz, A. Shulevski, J. Sluman, O. Smirnov, C. Sobey, M. Soida, S. Thoudam, M. C. Toribio, R. Vermeulen, R. J. van Weeren, O. Wucknitz, and P. Zarka. Shock location and CME 3D reconstruction of a solar type II radio burst with LOFAR. *Astron.* Astrophys., 615:A89, July 2018. doi: 10.1051/0004-6361/201732308.